



N° d'ordre NNT : xxx

THÈSE DE DOCTORAT DE L'UNIVERSITÉ DE LYON
opérée au sein de
l'Université Claude Bernard Lyon 1

École Doctorale ED52
Physique et Astrophysique de Lyon

Spécialité de doctorat :
Discipline : Physique médicale

Soutenue publiquement **à huis clos le 14/12/2018**, par :
Mattia Fontana

Tests and characterization of gamma cameras for medical applications

Test et caractérisation de caméras gamma pour 
médical

Devant le jury composé de :

Llosá Gabriela, Professeur associée, IFIC - Institut de Fisica Corpuscolar, Paterna, Espagne
Rapportrice

Thirolf Peter, Professeur associé, Fakultät für Physik der LMU München - Lehrstuhl für Experimentalphysik - Medizinhce Physik, Garching, Allemagne
Rapporteur

Augier Corinne, Professeur, IPNL - Institut de Physique Nucléaire de Lyon, France
Examinateuse

Cerello Piergiorgio, INFN - Istituto Nazionale di Fisica Nucleare, sezione di Torino, Italie
Examinateur

Morel Christian, Professeur, CPPM - Centre de Physique de Particules de Marseille - Aix-Marseille Université, Marseille, France
Examinateur

Rafecas Magdalena, Professeur, Institut für Medizintechnik - Universität zu Lübeck, Allemagne
Examinateuse

Létang Jean Michel, maître de conférences, CREATIS - Centre de Recherche en Acquisition et Traitement de l'Image pour la Santé, Lyon, France
Co-directeur de thèse

Testa Étienne, maître de conférences, IPNL - Institut de Physique Nucléaire de Lyon, France
Directeur de thèse

Dauvergne Denis, Directeur de Recherche CNRS, LPSC - Laboratoire de Physique Corpusculaire de Grenoble, France
Invité

Tests and characterization of gamma cameras for medical applications

PhD Candidate

MATTIA FONTANA

Thesis directors

ÉTIENNE TESTA and JEAN MICHEL LÉTANG

Université Claude Bernard
Lyon 1
Physics department
Doctoral school ED52:
Physics and Astrophysics

Defended on December the 14th
2018

Abstract

The application of nuclear and particle physics techniques in the field of medical diagnosis and pathology treatment is nowadays well-established in the clinical routine. In particular, several medical imaging techniques are based on the exploitation of elementary particles (Positron Emission Tomography (PET), Single Photon Emission Computed Tomography (SPECT), Computed Tomography (CT) scans, etc.), as well as treatment methods, mainly concerning cancer, which causes about 9 millions deaths per year all over the world.

In this context, ion beam therapy is a promising technique in cancer treatment because of the ion defined range and favorable dose delivery features with respect to standard photon radiotherapy. Strict and precise treatment planning and monitoring are now key points for the method developments and full exploitation. In particular, with the aim of optimizing the ion treatment effectiveness, the ion range monitoring is mandatory: different solutions have been explored, but an online treatment check is still a challenge. The ion beam treatment monitoring is mainly performed by means of secondary charged or neutral particles. In this context, the detection of the Prompt-Gammas (PGs) emitted during treatments has proven its potential in the ion range control in real time. Since the first evidence of the existing correlation between the emitted gamma profile fall-off and the Bragg peak position, several groups are involved in research activities in order to develop and optimize instruments and methods with the aim of improving this monitoring technique. Among the others, collimated and Compton cameras are being studied and optimized for this application. The same detectors can also be employed in nuclear medicine for the detection of the radioactive elements decay products.

A collaboration of 4 laboratories in France, called *Contrôle en Ligne de l'hadronthérapie par Rayonnements Secondaires* (CLaRyS), is involved in the parallel development of two composite detectors for ion beam monitoring and nuclear medicine applications, and this thesis is carried out within this collaboration with the detectors clinical trial as final aim.

The development project started a few years ago and is now at the final stage. The two cameras have been designed according to simulation studies, and the different components are now under tests. The collimated camera is composed of a multi-slit tungsten mechanical collimator, set in front of an absorber composed of 30 Bismuth Germanium Oxide - $\text{Bi}_{12}\text{GeO}_{20}$ (BGO) blocks, for a total size of $210 \times 175 \times 30 \text{ mm}^3$; each block presents a streaked structure with a 8×8 pseudo-pixel matrix and the signal is read-out by 4 photomultipliers. A $\sim 3 \text{ ns}$ time resolution can be achieved on average for the prompt-gamma detection. The same absorber is part of the Compton camera, in addition to a scatterer section composed of 7 Double-sided Silicon Strip Detectors (DSSDs) $96 \times 96 \times 2 \text{ mm}^3$ each.

With the collimated camera, the parallel emitted photons are selected by the collimator and a mono-dimensional emission profile can be reconstructed. The Compton camera has a more efficient detection technique, thanks to the absence of a mechanical collimation system, and could potentially lead to 3D information via the reconstruction of the Compton cones. These features make it suitable for the application in nuclear medicine, in particular as an alternative to the present SPECT collimated cameras, allowing for accurate and efficient image reconstructions with the usage of high energy gamma source  which should reduce image

blurring effects due to attenuation in the patient and the total released dose with respect to the present clinical routine.

Concerning the monitoring of ion beam therapy treatments, an additional detector component is needed to temporally and spatially tag the incoming beam ions and help rejecting the relevant background (mostly due to neutrons) which strongly affects the prompt-gamma yield. A scintillating fiber tagging hodoscope, which can be coupled to both collimated and Compton camera, is under development: it is composed of 2 perpendicular planes of 128 scintillating fibers, read-out from both sides by 8 64-channel photomultipliers by Hamamatsu.

The thesis work consists in the critical evaluation, characterization and tuning of the different components, together with the associated electronics, and of the complete detectors on beam. In parallel, simulation studies can improve the detection technique and optimize the detector structure, as well as pave the way for further applications.

After a general introduction devoted to expose the thesis context in chapter 1, an overview of the instrumental and technical state of the art of the gamma cameras is given in chapter 2. Chapter 3 focuses on the two cameras developed by the CLaRyS[®] camera components are described in details, and all the characterization measurements performed during the three years of my PhD thesis are explained. Chapter 4 and 5 presents the simulation studies I performed with the aim of investigating the potential of the developed detectors for the application on ion beam therapy monitoring and nuclear medicine, respectively. The entire chapter 6 is dedicated to the description of the tests performed on proton beams for the detector characterization measurements. The final chapter 7 is used to summarize and discuss all the results obtained in this thesis work; furthermore, the perspectives of the project are fixed on a timeline for the next future, and new research directions emerging from the obtained results are proposed.

Contents

Prologue	1
1 Context	3
1.1 Ion beam therapy	5
1.1.1 Physics of ion beam therapy	6
1.1.2 Biological effects of ion beam therapy	13
1.1.3 Accelerators and beam delivery	14
1.1.3.1 Accelerators for ion beam therapy	14
1.1.3.2 Beam time structure	18
1.1.3.3 Beam delivery systems	18
1.1.4 Treatment planning	21
1.1.5 Ion beam therapy uncertainties and treatment monitoring	24
1.1.5.1 Positron Emission Tomography	25
1.1.5.2 Prompt-gamma detection	25
1.1.5.3 Interaction vertex imaging	25
1.1.5.4 Other techniques	25
1.2 Nuclear medicine	25
1.2.1 PET and SPECT	25
1.2.2 State of the art of PET and SPECT	25
2 Prompt gamma detection and imaging	27
2.1 Photons	28
2.1.1 Photon interactions in matter	28
2.1.2 Photon detection	28
2.2 Prompt gammas	28
2.2.1 Ion range monitoring with prompt gamma radiation	28
2.3 Gamma cameras	28
2.3.1 Applications in medicine	28
2.3.2 Ion beam range monitoring	28
2.3.3 Nuclear medicine	28
2.4 Gamma cameras state of the art	28
3 CLaRyS prototypes	29
3.1 CLaRyS gamma camera components	30
3.1.1 Scatterer	31
3.1.1.1 Scatterer Front-End card	34
3.1.1.2 Scatterer thermal regulated box	35
3.1.2 Collimator	36
3.1.3 Absorber	36
3.1.3.1 Absorber Front-End and read-out cards	38
3.1.3.2 Absorber mechanical support	41
3.1.4 Beam tagging hodoscope	41
3.1.4.1 Hodoscope Front-End card	43
3.1.4.2 Hodoscope mechanical support	45
3.1.4.3 Small hodoscope prototypes	46
3.1.5 Camera acquisition system	47

3.1.6 Camera acquisition, monitoring and slow control software	50
3.1.7 Camera integration and mechanical support	51
3.1.8 Data analysis and image reconstruction	52
3.2 Camera component characterization and development status	55
3.2.1 Scatterer silicon layer characterization	55
3.2.2 Absorber Bismuth Germanium Oxide - Bi ₁₂ GeO ₂₀ (BGO) blocks characterization	57
3.2.2.1 Space and energy calibration and characterization	58
3.2.2.2 Qualitative test of spatial reconstruction accuracy	59
3.2.2.3 Pixel identification and energy calibration algorithm	60
3.2.2.4 Time response characterization method	61
3.2.2.5 Results: Photo-Multiplier (PM) gain equalization	62
3.2.2.6 Results: block spatial precision	64
3.2.2.7 Pixel identification	67
3.2.2.8 Pixel energy calibration	67
3.2.2.9 Time characterization	73
3.2.2.10 Results for the 30 blocks	73
3.2.3 Hodoscope PMs characterization	73
3.2.4 Hodoscope fiber test with electron source	78
3.3 Summary and perspectives	81
3.3.1 Silicon scatterer	82
3.3.2 BGO absorber	83
3.3.2.1 Absorber upgrade	84
3.3.3 Scintillating fiber hodoscope	84
3.3.3.1 Hodoscope upgrade	85
3.3.4 Acquisition and software	85
3.4 Conclusions	86
4 Compton camera application for ion beam therapy monitoring	89
5 Compton camera application in nuclear medicine	91
5.1 Introduction	92
5.2 Material and methods	93
5.2.1 Radioactive sources	93
5.2.2 Compton camera simulation and data analysis	93
5.2.2.1 Simulation settings	93
5.2.2.2 Data collection and analysis	96
5.2.2.3 Compton camera study for SPECT application	96
5.2.3 Anger camera simulation and data analysis	98
5.2.3.1 Simulation settings	98
5.2.3.2 Data analysis	98
5.2.4 Figures of merit for the comparison study	104
5.3 Results: Compton camera study for SPECT application	104
5.3.1 Influence of Compton camera scatterer detector energy resolution	105
5.3.2 Compton camera coincidence study	106
5.3.3 Compton camera desing study	107
5.4 Results: Benchmark of Compton camera and Anger camera performance	108
5.5 Summary and discussion	110

6 Beam tests	113
6.1 Hodoscope: december 2017	114
6.2 Hodoscope: may 2018	114
6.3 Collimated camera: august 2018	114
6.4 Collimated camera: september 2018	114
7 Conclusions and discussion	115
Appendices	117
Appendix A Compton camera data format	119
A.1 Introduction	119
A.2 General features	119
A.2.1 Common information	119
A.2.1.1 Front End number	119
A.2.1.2 Pre-trigger and trigger	121
A.2.1.3 Mode number	121
A.2.3 Physical data format	123
A.2.3.1 Scatterer detector data format	123
A.2.3.2 Absorber detector data format	123
A.2.3.3 Beam hodoscope data format	126
A.2.4 Slow control, trigger and monitoring data format	126
A.2.4.1 Communication architecture	126
A.2.4.2 Transport protocol and processor packets	127
A.2.4.2.1 Definitions	127
A.2.4.2.2 Data encoding	128
A.2.4.2.3 Packets format	128
A.2.4.2.4 Possible control symbols	129
A.2.4.3 Transport layer	129
A.2.4.3.1 Control packet	129
A.2.4.3.2 Configuration packets	130
A.2.4.3.3 Monitoring process (Front End cards → Micro Advanced Telecommunications Computing Architecture (μ -TCA))	131
A.2.4.3.4 Special command process (μ -TCA → Front End cards)	133
A.2.4.4 Data packets (Front End card → μ -TCA)	133
A.2.5 UDP packets format	135
A.6 Data throughput expected in clinical conditions	136
A.6.1 Clinical intensities	136
A.6.1.1 Review: detector and target sizes	136
A.6.2 Coincidence rate	137
A.6.3 Data flow (Front End cards → μ -TCA)	137
A.6.4 Acquisition data flow (μ -TCA → Acquisition PC)	138
A.6.5 Conclusions	139
List of abbreviations	141
Bibliography	147

List of Figures

1.1	Treatment planning of lung cancer for the irradiation with x-rays (left) or carbon ions (right) (in Durante et al. 2016).	7
1.2	Relative dose as a function of the particle depth in water for different particle species. In Paganetti 2012b.	7
1.3	Schematic view of an example of the three main interactions mechanics of protons in matter: Coulomb interaction with atomic electrons (a), Coulomb interactions with atomic nucleus (b), nuclear reactions(c). In Newhauser et al. 2015.	8
1.4	Schematic view of the nuclear reaction between a projectile and a target nucleus. The two steps are defined as “collision” and “de-excitation” processes.	11
1.5	Effects of nuclear interactions on the primary beam and resulting dose distribution.	12
1.6	Schematic view of the main components of a cyclotron accelerator. On the left side the magnet is sketched together with the radio-frequency elements (“Dees”), which are also shown on the section depicted on the right side, with the ion source in the center. In Paganetti 2012b.	15
1.7	Comparison of the size of various ion accelerators for hadrontherapy. CABOTO is a cyclinac studied by the TERA Foundation; the superconducting cyclotron, designed by Ion Beam Applications, Belgium (IBA), is under installation in Caen, France, within the ARCHADE project; Heidelberg Ion Therapy Center, Germany (HIT) and Centro Nazionale di Adroterapia Oncologica, Italy (CNAO) are in operation in Heidelberg, Germany and Pavia, Italy, respectively; the SIEMENS synchrotron is installed in Marburg and Shangai. In Amaldi et al. 2010.	17
1.8	Example of Spree-Out Bragg Peak (SOBP). The target region is highlighted and the discrete pristine peaks composing the SOBP are sketched in red. In Durante et al. 2016.	18
1.9	Schematic view of a fully passive beam delivery system. In Schardt et al. 2010.	19
1.10	Schematic view of a fully active beam delivery system. In particular, here the GSI Helmholtz Centre for Heavy Ion Research, Germany (GSI) raster scanning system is depicted. In Schulz-Ertner et al. 2006.	20
1.11	Schemes of a standard gantry design (left) and of the carbon-ion rotating gantry installed at HIT (right).	21
1.12	The treatment planning system process is based on anatomical information about the patient, given by Computed Tomography (CT) scans, and physician treatment prescription. The CT values must be converted to Relative Stopping Power (RSP) and tabulated experimental data are used (left), while biological dose calculation models are applied to optimize the biological dose distribution to be delivered during the treatment (right).	23

3.1 Schematic view of the two CLaRyS gamma camera prototypes: the multi-collimated camera (a) and the Compton camera (b), both coupled to the beam tagging hodoscope. The ion beam is represented by the red line, and some beam bunches has been highlighted. The detection principle is also sketched for the two detectors: the tungsten collimator select the parallel incoming photons for the multi-slit collimated camera (a), while the Compton cone is reconstructed with the two interactions in scatterer and absorber in the Compton camera (b).	31
3.2 Overview of the scatterer layers, with its working principle (a) and a picture of the detector connected to the Front-End (FE) card in the thermal regulated box (b).	33
3.3 Scatterer silicon layers equipment: final version of the Front-End (FE) card (a) and scheme of the detector integration in the thermal regulated box (b).	36
3.4 Tungsten collimator and its setup in the multi-slit collimated camera. Two identical collimators are available, with $1.5 \times 120 \times 170$ mm ³ tungsten slabs and a pitch of 8 mm. The two tungsten multi-slit collimators are placed in front of a 6×5 Bismuth Germanium Oxide - Bi ₁₂ GeO ₂₀ (BGO) block absorber setup in its mechanical support (see section 3.1.3). Both the single collimator setup (size and pitch) and the two collimators configuration can be easily modified to adapt the system to peculiar applications.	37
3.5 Components of an absorber module and its working principle.	39
3.6 Absorber read-out electronics: FE card (a) and Analog Sampling Module (ASM) board (b).	40
3.7 Details of the temporary absorber acquisition based on the Altera development card.	41
3.8 Absorber front view with the BGO block lines arranged in the mechanical support (a). Scheme of the BGO absorber with its mechanical support (b).	42
3.9 128×128 scintillating fiber hodoscope on its 2-dimensional moving support.	43
3.10 Details of the scintillating fiber hodoscope setup.	44
3.11 HODOPIC board (a) and scheme of the beam-tagging hodoscope two-dimensional moving support (b).	44
3.12 Hodoscope small prototypes.	46
3.13 Acquisition system components: Micro Advanced Telecommunications Computing Architecture (μ -TCA) crate (a), Advanced Mezzanine Card (AMC)40 board (b) and Trigger et HORloge (THOR) card (c).	48
3.14 Schematic view of the Compton camera acquisition system. For the multi-collimated camera, the trigger and pre-trigger signals are the same.	49
3.15 Software tools: user interface of the acquisition C++ software (a) and example of the ROOT (Brun et al. 1997) monitoring software visualization for the beam tagging hodoscope 32×32 fiber prototype.	50
3.16 Details of the gamma camera integration and mechanical support.	52
3.17 Complete Compton camera with beam tagging hodoscope on the developed mechanical supports.	53
3.18 Scheme of the spatial and energy characterization test-bench.	58
3.19 Details about the BGO block time response characterization.	59

3.20 Logic for the event assignment to a single pixel. The dual pseudo-pixel grid is displayed: in white the mid points on the pseudo-pixel edges along rows, in red along columns. The sign of the outer products detailed in the red box are used to define the column and row (so that the pseudo-pixel) where to assign the reconstructed event.	60
3.21 Reference BGO block raw signals collected with the Wave Catcher acquisition system. The four outputs of the single PMTs are shown together with the sum signal.	62
3.22 Photo-Multiplier (PM) signal amplitude spectra before (a) and after (b) the PM gain equalization.	63
3.23 1D integrated position distribution on the two transverse dimensions before (a) and after (b) the PM gain equalization. Blue curves: horizontal dimension. Green curves: vertical dimension.	63
3.24 Block energy spectrum before (a) and after (b) the PM gain equalization.	64
3.25 2D reconstructed position map before (a) and after (b) the PM gain equalization.	64
3.26 2D reconstructed position maps during a 2-mm step scan performed with the Cobalt-60 (^{60}Co) source with the line aperture from the left to the right size of the block surface. 4 reference measurements points, the position of the aperture is shown by the semi-transparent yellow band.	65
3.27 2D reconstructed position maps during a 2-mm step scan performed with the ^{60}Co source with the line aperture from the bottom to the top side of the block surface. 4 reference measurements points, the position of the aperture is shown by the semi-transparent yellow band.	66
3.28 2D reconstructed position maps during a 1-mm step scan performed with the ^{60}Co source with the line aperture. 9 reference measurements points, the position of the aperture is shown by the semi-transparent yellow band.	68
3.29 1D integrated position distributions on the two transverse dimensions with the retrieved position of the pseudo-pixel average center (a). Reconstructed 2D map with the identified pseudo-pixels positions and surfaces.	69
3.30 Auxiliary position map used for the assignment of the reconstructed events to a single pixel. The highlighted points represent the “valleys” between neighboring pixels on their separation borders.	69
3.31 2D map of the reconstructed event assignations to pseudo-pixels.	70
3.32 Single pseudo-pixels (a) and whole block (b) energy spectra with the Sodium-22 (^{22}Na) source before (left) and after (right) the calibration process. The whole block spectra are reported in logarithmic scale. Three non calibrated spectra of pixels in reference positions (border, mid-center and center area) on the block are also reported with the non calibrated spectrum (a normalization factor has been applied for visualization purpose).	71
3.33 Relative number of entries for each pseudo-pixel as a function of the pixel relative position, represented by the row and column numbers (0 to 8 from left to right and bottom to top of the block surface). Figure(a) shows the entries in a selected energy window around 511 keV, Figure(b) in an energy window around 1275 keV. All the entries are normalized to the maximum collected number of entries, corresponding to 511 keV events in the central section of the block.	72
3.34 Distribution of arrival time differences between reference scintillator (a Barium Fluoride (BaF_2) monoblock detector with 1 ns time resolution) and BGO block.	73
3.35 Test-bench and tools for the characterization measurements performed on the Hamamatsu PMs of the beam tagging hodoscope.	76

3.36 Details of the hodoscope PMs and of the performed characterization measurements.	77
3.37 Two-dimensional response maps of one of the Hamamatsu PMs for the scintillating fiber hodoscope readout, obtained with the irradiation with a blue Light Emitting Diode (LED). The signal amplitude is normalized to the reference PM response.	78
3.38 Two-dimensional response maps of the Hamamatsu PMs for the scintillating fiber hodoscope readout, obtained with the irradiation with a blue LED. The signal amplitude is normalized to the reference PM response and then to each PM maximum detected amplitude.	79
3.39 Cross-talk study on neighboring PM pixels. The experimental results obtained with the irradiation with a blue LED through the plastic fiber mask on a reference PM (right) are compared to the specifications provided by the producer, measured in similar conditions (left). The cross-talk is expressed in % with respect to the irradiated anode, which is represented by the light-blue cell with 100% of the signal.	80
3.40 Comparison of the simulated distribution of energy deposited by electrons from the ^{90}Sr source on a single hodoscope fiber to the experimental signal amplitude distribution from a scintillating fiber irradiated with the ^{90}Sr source.	81
5.1 Sketch of the simulated geometry of the two systems: Anger camera (left) and Compton camera (right), in 3 dimensions (top line) and side projection (bottom line).	94
5.2 Radial event distribution normalized by the circular surface corresponding to each bin for 4 representative source energies, with the linear fit performed for background rejection. The total number of simulated primaries for each data set is 10^8	100
5.3 Comparison between expected entries in the central collimator hole (blue dashed curve) calculated according to pure geometrical factors and detector interaction cross section and simulated detected entries after background rejection (red solid curve) with null spatial resolution (ideal detector) to avoid resolution effects and lower energy threshold set to 80 keV.	101
5.4 Normalized radial distribution with background rejection (red solid lines) compared to normalized radial distribution for infinite density collimator (blue dashed lines).	102
5.5 Normalized radial distribution with no event selection (red solid lines) compared to normalized radial distribution for full collimator (green dashed lines). Both curves are normalized to the maximum of the raw radial distribution.	103
5.6 Reconstructed radial distribution standard deviation as a function of the source energy. Two energy resolution values are set to the silicon detectors ($\sigma_E = 2\text{ keV}$ - red dots solid line - and $\sigma_E = 4\text{ keV}$ - blue dots dashed line), the Doppler broadening effect has been removed (green horizontal triangles dashed line) and the scatterer material has been changed with Cadmium Telluride (CdTe) solid state detectors (black vertical triangles dashed line), for a fixed energy resolution of $\sigma_E = 2\text{ keV}$	105

5.7 (a): number of true (green) and random (red) coincidences as a function of the source activity in the range 1-500 MBq, for the reference energy of 555 keV. (b): Percentage of random coincidences as a function of the source energy, with a fixed source activity of 200 MBq. Compton camera parameters: time resolution Full Width at Half Maximum (FWHM) of 20 ns for silicon detectors, 3 ns for BGO and a coincidence window of 40 ns. The source branching ratio has been set to 100% for all sources for simplicity in the comparison of results.	106
5.8 Results of the Compton camera design study: reconstructed events efficiency (left) and standard deviation of the radial event distribution (right) as a function of the primary gamma energies for four reference energies and five scatterer stack configurations, with seven, six, five, four and three layers.	107
5.9 Overlap of the normalized radial distributions for 4 selected source energies. . .	108
5.10 Detection efficiency as a function of the source energy. Source activity = 200 MBq, Compton camera silicon detector $\sigma_E = 2 \text{ keV}$	109
5.11 Standard deviation of the radial event distributions as a function of the source energy. Source activity = 200 MBq, Compton camera silicon detector $\sigma_E = 2 \text{ keV}$.109	
5.12 Signal-to-background ratio as a function of the source energy. Source activity = 200 MBq, Compton camera silicon detector $\sigma_E = 2 \text{ keV}$	110
A.1 Data acquisition logic: pre-trigger and trigger generation and readout process. .	122
A.2 Scatterer detector data format.	124
A.3 Absorber detector data format.	125
A.4 Beam hodoscope data format.	126
A.5 Architecture of communication between DAQ cards and μ -TCA.	127

List of Tables

3.1 Comparison of the results obtained with the two pixel-assignment methods.	70
3.2 Calibration and characterization results for 10 tested Bismuth Germanium Oxide - $\text{Bi}_{12}\text{GeO}_{20}$ (BGO) blocks.	74
5.1 Radioactive sources used in the comparison study. Decay mode list: EC for electron capture, $\beta-$ for electron emission, $\beta+$ for positron emission, IT for isomeric transition. Half-life expressed in days (d), hours (h) or minutes (m). Data extracted using the National Nuclear Data Center On-Line Data Service from the Evaluated Nuclear Structure Data File database, file revised as of (2017-05-17) (Bhat 1992).	94
A.1 Front End number associated to each Front End card.	120
A.2 Packet with an even byte number cargo.	128
A.3 Packet with an odd byte number cargo.	128
A.4 Control symbol definition.	129
A.5 Control symbol definition.	130
A.6 Definition of the acknowledgement packet.	130
A.7 Writing register packet.	131
A.8 Reading register packet.	131
A.9 Two special registers(Micro Advanced Telecommunications Computing Architecture (μ -TCA) → Front End cards)	132
A.10 Measurement packet (Front End cards → μ -TCA)	132
A.11 Monitoring packet.	132
A.12 Monitoring messages.	133
A.13 Special command packets	133
A.14 Special commands examples	134
A.15 Control symbol for pre-trigger, trigger and physical data.	134
A.16 Pre-trigger packet	135
A.17 Trigger packet	135
A.18 Physical data packet	135
A.19 Coincidence and single rate as a function of the beam intensity. The BGO single rate corresponds to the pre-trigger rate.	137
A.20 Data flux between Front-End (FE) cards and μ -TCA.	138
A.21 Data flow between μ -TCA and acquisition PC.	138
7.22 Acquisition format of the Compton camera data.	140

Prologue

1

Context

Contents

1.1 Ion beam therapy	5
1.1.1 Physics of ion beam therapy	6
1.1.2 Biological effects of ion beam therapy	13
1.1.3 Accelerators and beam delivery	14
1.1.4 Treatment planning	21
1.1.5 Ion beam therapy uncertainties and treatment monitoring	24
1.2 Nuclear medicine	25
1.2.1 PET and SPECT	25
1.2.2 State of the art of PET and SPECT	25

1 Context

The application of physics concepts and techniques to the field of health-care is nowadays well-established in the clinical routine. Even if physical techniques have been used in medicine from the earliest time (Duck 2014), the discipline today known as “medical physics” emerged and grew in the past century thanks to the increasing knowledge and use of ionizing radiations both for diagnosis and disease treatment. In the late 19th century, the x-ray discovery by Röntgen, the radioactivity discovery by Henri Becquerel, and the radium and radioactive isotopes studies by Pierre and Marie Curie paved the way to the whole medical physics practice of the next century, where x-ray imaging and radiotherapy were soon established. Only three weeks after the discovery of the x-rays, Robert Jones and Oliver Lodge imaged with x-rays a boy’s hand (Cantor 1988), officially starting the diagnostic application of such a radiation. Following the first successes, more attention **were** given to radio-protection and dosimetry studies, and the investigations focused on new ways to use radioactive tracers for imaging purpose; this finally led to the birth of nuclear medicine, with the clinical use of the radioisotope Indium-131 (¹³¹In) in 1939 (Kereiakes 1987). Nuclear medicine rapidly gained importance in the diagnosis clinical panorama, also thanks to the introduction of new detectors, such as the Anger camera introduced in the ’60s, and new imaging techniques, such as the detection of photons from positron annihilation (Positron Emission Tomography (PET)). Moreover, several alternative methods were proposed or implemented for diagnosis (Magnetic Resonance Imaging (MRI), ultrasounds, etc.). In parallel, x-rays were soon employed also for tumor treatment: already in 1896, Emil Grubbe irradiated a woman with breast cancer (Evans 1951), and in the same year in Lyon a patient with a stomach cancer has been treated by Victor Despeignes (Despeignes 1896; Foray 2016). One year later, a skin tumor **were** successfully irradiated in Vienna using x-rays. Thanks to the invention of the klystron, and, later, of the so-called “magnetron”, by the Varian brothers with William Webster Hansen, the radiotherapy could spread and become a clinical reality; more refined treatment techniques were then introduced with the development of commercial particle accelerators after World War 2 (Keevil 2012).

At present days, the medical physics progress strongly relies on technological development and computer science, which already revolutionized several fields of science. In particular, cancer research is now a key area for technical and technological development, concerning both diagnosis and treatment (Webb 2009). Cancer continues to be one of the major issues in the medical scenario: it is at present the second cause of death worldwide, but it is expected to surpass heart diseases and become the main killer in the next tens of years (Jemal et al. 2010; Thun et al. 2010). The last two decades saw important improvements in radiotherapy techniques and machines, with more precise dose planning and delivery, which enhanced the patient survival and strongly reduced the impact of radiations on healthy tissues. This was possible also thanks to refined imaging technologies, allowing for an accurate tumor volume definition, as well as for image-guided treatments. In this scenario, ion beam therapy, already proposed in the middle of the past century, is rapidly spreading thanks to novel beam delivery technologies, able to relatively reduce the treatment costs and allowing for a commercial diffusion of this treatment method (which is still very limited with respect to standard radiotherapy). Notwithstanding the remarkable steps forward disclosed in the last years, there is still wide room for improvements in this field, which mainly requires strong imaging basis in order to fully profit of the treatment technique potential.

The work presented in this document **have** been carried out in this context and mainly deals with the development of gamma imaging detectors to be applied in the field of quality assurance for ion beam treatment. Furthermore, the same detectors have been applied to the

nuclear medicine field in simulation, with the aim of assessing its possible clinical implementation for a future development of the nuclear medicine clinical routine.

In the following sections, a general overview of the two main domains concerned in this thesis work is given.

1.1 Ion beam therapy

Radiation treatment is an essential component of the tumor therapy, being the second most applied and successful kind of therapy after surgery (Schardt et al. 2010). The majority of patients with localized malignant tumors are treated with radiations (Baskar et al. 2012; Durante et al. 2009; Moding et al. 2013), applied in several fractions in different days in order to reduce the damages to normal tissues (Bentzen 2006). The most of the patients treated with radio-therapy techniques receives standard photon treatments, with x-rays coming from linear electron accelerators, while a small percentage undergoes specialized gamma treatments like brachytherapy or gamma knife radiations. About 1 % of the radiotherapy patients are irradiated with charged particle beams, with the so-called ion beam therapy (Durante et al. 2016).

Ion beam therapy, or “hadrontherapy”, is a cancer radiation treatment method based on light ion beams instead of photons. It was first proposed by Wilson in 1946 in a famous seminal paper (R. R. Wilson 1946); the author was asked by its director Ernest Lawrence to clarify the stopping process of protons in matter. Thanks to measurements at the Berkeley cyclotron, he highlighted the physical principles and the possible benefits driven by the implementation of such a kind of radiation in clinical treatments, with particular focus on the simple case of protons and some considerations about heavier ions, like alpha particles and carbon ions. At that time, the accelerator technologies were still under development after the invention of the cyclotron by Ernest O. Lawrence in 1930, which allowed to increase the range of charged particles in matter, in particular in cells and human tissues, and the treatment required beam energy were about to be reached. Pioneering studies of the biomedical applications of accelerated hadron beams were performed by Cornelius Tobias in 1948 (Blakely et al. 2009) in Berkeley (USA), and the first patients have been treated almost ten years later in the same laboratory by Lawrence and Tobias (Tobias et al. 1958, 1955) with protons and, later on, with He ions (Halperin 2006). New accelerators in four continents were used to continue the quest started in Berkeley, and the experience were extended to carbon ion beams from 1994 in Japan (Chiba), and Germany (Heidelberg - Heidelberg Ion Therapy Center, Germany (HIT)).

Nowadays clinical adapted machines are well-established on the market, making ion beam therapy emerging as a wide-spread technique in the every-day cancer treatment routine all over the world. Starting from the early 2000's, many new treatment centers have been designed and built, mainly in Europe and Japan. An intense research effort has been dedicated to this field in the last decades; in addition to considerable improvements achieved in the accelerator technologies, new and refined imaging techniques allowed for important enhancement in the treatment planning, also supported by the continuous development of computer science and the growth of calculation power. In parallel, the biological implications of ion irradiation has been deeply investigated (Brahme 2004; Friedrich et al. 2012; Tobias et al. 1982). Moreover, since more and more patients are treated every year with this technique, more

clinical data are at present available for further study and the connection between physicists and physicians is strongly progressing both in the research field and in treatment practice. Several advancements are expected in the next years, following the extensive research work carried out by several groups in the world. In the following paragraph, the basic physical principles and features of this treatment method are explained, and advantages and drawbacks with respect to standard radiotherapy techniques are analyzed. After that, the need for ion range verification is discussed and detailed in order to reach the main topic for this thesis: the prompt-gamma detection.

1.1.1 Physics of ion beam therapy

Charged nuclear particle beams at relatively high energy show a characteristic depth-dose distribution in matter which makes them suitable for the application in cancer treatment as a valid alternative to standard photon therapy (x-ray or megavolt beams), bringing several advantages to the patient side. The peculiar energy deposition profile (“Bragg curve”) is named for Sir William Henri Bragg, who investigated the slowing-down process of α particles in air (Bragg et al. 1904, 1905). Low-energy (x-rays) and high-energy photons traversing the patient body deposit their energy by interacting with the target atomic electrons (mainly by Compton interaction), with the deposited dose decreasing at increasing depth after a build-up region (mainly due to forward scattered Compton electrons). Even if the entrance surface (the skin for a patient) can be spared thanks to this build-up region, with a dose peak shift of a few centimeters, a high relative dose is delivered to the tissues along the whole beam path. In order to maximize the tumor volume-to-healthy tissue dose ratio, a standard photon treatment always foresees several irradiation fields from different entrance points and angles (see Figure 1.1, left). This energy deposit behavior is common to all neutral particles, as shown in the first two boxes in Figure 1.2 where the depth-dose profiles of photons at various energies and neutrons in water is presented. In contrast to neutral particles, the energy deposited per track unit increases for increasing depth for the charged ones: in Figure 1.2 the depth-dose profile in water is shown for electrons, pions, protons and neon ions; it is characterized by an entrance low relative dose *plateau* and by a narrow high deposited dose peak at the end of the range (in the last few millimeters), called “Bragg peak”. The high-dose peak is sharper the more massive is the particle, as clear from Figure 1.2, where the different species are arranged by increasing mass. For what concerns ions and heavier ions, their clinical interest for the treatment of deep-seated tumors appears clear from the above considerations: a nuclear particle beam is able to deliver a reduced dose to the healthy tissues surrounding the target volume, where the dose is concentrated. This allows for the treatment of tumor volumes close to Organs At Risk (OsAR), also with limited irradiation angles with respect to photons, as shown in Figure 1.1, right.

The nuclear charged particle interactions in matter can be described by three main mechanisms: Electromagnetic (EM) inelastic interaction with the atomic electrons, EM elastic interactions with the atomic nuclei, and nuclear reactions. In addition to the listed interactions, also Bremsstrahlung is theoretically possible, but its effect is negligible at ion energies of clinical interest.

The EM inelastic interactions with atomic electrons cause an energy loss which is generally approximated with a Continuous Slowing Down Approach (CSDA) for simplicity, assuming a mono-dimensional ion path and an average, continuous energy loss rate. This is justified by

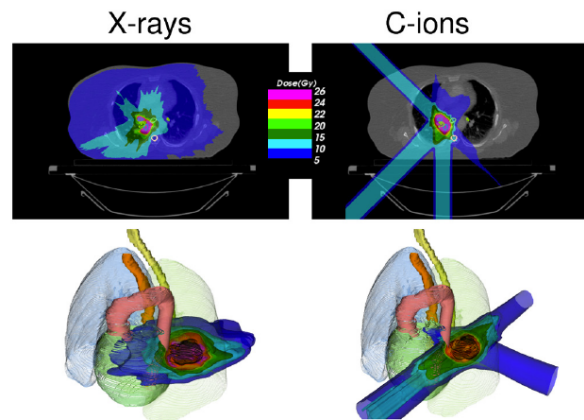


Figure 1.1: Treatment planning of lung cancer for the irradiation with x-rays (left) or carbon ions (right) (in Durante et al. 2016).

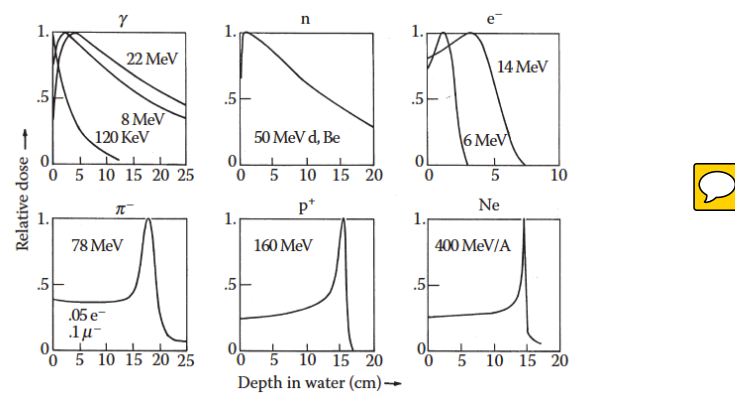


Figure 1.2: Relative dose as a function of the particle depth in water for different particle species. In Paganetti 2012b.



the mass difference between electrons and ions (as an example, the proton mass is 1832 times greater than that of an electron). The elastic repulsion caused by an atomic nucleus is able to deflect the projectile ion, with an angle which depends on the target-projectile relative mass. The inelastic nuclear reactions are less frequent, but reduce the intensity of the primary beam (the primary particle is destroyed) and cause the emission of secondary nuclear fragments. A schematic view of the three main interaction mechanisms described is given in Figure 1.3 for the example case of protons, while in the following the effects of these interactions are detailed.

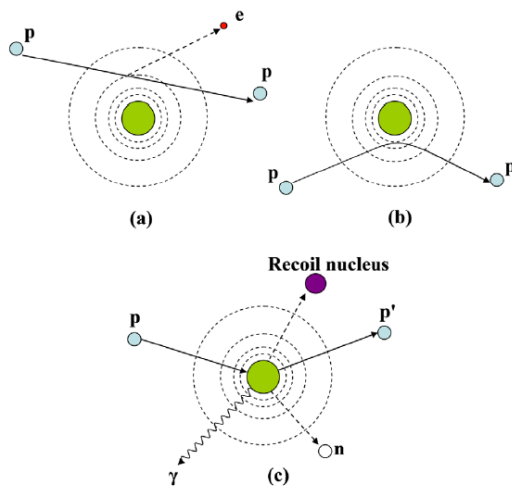
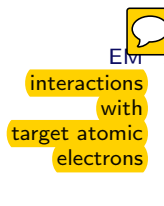


Figure 1.3: Schematic view of an example of the three main interactions mechanics of protons in matter: Coulomb interaction with atomic electrons (a), Coulomb interactions with atomic nucleus (b), nuclear reactions(c). In Newhauser et al. 2015.



At the primary particle velocities of clinical interest, the ion energy loss rate is dominated by inelastic collisions with the target atomic electrons and is well described by the formula attributed to Bethe (Bethe 1930) and Bloch (Bloch 1933), often referred as Bethe-Bloch formula, reported in equation 1.1 in its form independent of the mass density. This expression is also known as mass stopping power.

$$\frac{S}{\rho} = -\frac{dE}{\rho dx} = 4\pi N_A r_e^2 m_e c^2 \frac{z^2}{\beta^2 A} \left[\ln \frac{2m_e c^2 \beta^2 \gamma^2}{I} - \beta^2 - \frac{\delta}{2} - \frac{C}{Z} \right] \quad (1.1)$$

where N_A is the Avogadro's number ($6.022 \times 10^{23} \text{ mol}^{-1}$), r_e is the classical electron radius, m_e is the electron mass, z is the charge of the projectile, Z and A are the atomic number and weight of the target material, respectively, c is the speed of light, $\beta = v/c$ is the projectile velocity, $\gamma = (1 - \beta^2)^{-1/2}$, I is the mean excitation potential of the target material. The last two terms represent corrections for high energies (δ density effect correction term) and low energies (C shell correction term) incident ions. By observing equation 1.1, it clearly emerges how the energy loss rate is proportional to the inverse square of the projectile velocity and charge. The target material composition also plays a major role. The energy loss rate is directly proportional to the mass density: to be noticed, for clinical applications, that the density in a patient can vary by almost three orders of magnitude, ranging from the air cavity in the lungs to the most dense bones. As already mentioned, the energy loss increases for decreasing ion



energy due to the $1/\beta^2$ dependence, and the maximum energy-loss rate, corresponding to the Bragg peak depth, is reached at the projectile velocity expresses as

$$v_p = z^{2/3} v_0 \quad (1.2)$$

where $v_0 = e^2/\hbar$ is the Bohr velocity ($\beta = 1/137$).  

The energy loss rate equation directly leads to the definition of the ion beam range in matter (if we neglect nuclear interactions which cause a modification of the projectile nature), which is the integral over the incident energy of the energy loss per track unit, reported in equation 1.3. This formulation assumes a 1D ion trajectory with negligible lateral scattering (discussed below) and uses the CSDA.

$$R(E) = \int_0^E \left(\frac{dE'}{dx} \right)^{-1} dE' \quad (1.3)$$

E is the ion beam incident energy. To be noticed that the range is not a deterministic value, but it is intended as an average value and defined for the whole beam, not for single incident particles, which are affected by statistical fluctuations in the energy loss, leading to the so-called range straggling (described by different theoretical models, such as the ones in [Bohr 1915; Landau 1944; Vavilov 1957](#), and detailed below). Integration of the Bethe-Bloch is often a hard task, but, as realized by Bragg and Kleeman ([Bragg et al. 1905](#)), the range dependence on the incident particle energy can be practically expressed with an analytic approach as the power law in equation 1.4. This approximation directly derives from studies on alpha particles which anticipated the formulation of equation 1.1.

$$R(E) = \alpha E^p \quad (1.4)$$

E is again the ion beam initial energy, the constant α depends on the target material and the constant p is related to the projectile energy (or velocity). The proton range can be easily scaled to other ions at the same energy per nucleon in the same material with a factor M/z^2 .  The range of ions with the same specific energy scales from water to other homogeneous material with a factor of A/Z^2 .

The ion range predicted by equations 1.3 or 1.4 is an average value, calculated by considering a smooth and continuous energy loss process and neglecting the individual ion paths. The actual range suffers from statistical fluctuations in the primaries initial energy loss that broaden the Bragg peak, in the so called “range straggling”. In general, the longitudinal beam straggling can be described by an asymmetric distribution ([Vavilov 1957](#)), which is approximated to a Gaussian in the limit of many collisions, leading to the expression of the relative straggling in equation 1.5:

$$\frac{\sigma_R}{R} = (M^{-\frac{1}{2}}) \phi \frac{E}{Mc^2} \quad (1.5)$$

1 Context

The ratio of the straggling width σ_R and mean range R is then all the more reduced as the ion mass (M) increases, with ϕ a slowly varying function which depends on the target material (Rossi 1952) and E the ion energy. According to equation 1.5, it is interesting to notice how the relative straggling for carbon ions is about 3.5 times smaller with respect to protons (e.g. 7 mm and 25 mm at 18 cm of average range for carbon ions and protons, respectively - see Durante et al. 2016). 

EM interactions with target nuclei In addition to the energy loss process considered till here, which shapes the beam in the longitudinal direction (range variations), the actual delivered dose also depends on the lateral beam profile, which is mainly governed by elastic Coulomb scattering with atomic nuclei and by secondary particles produced by nuclear fragmentation. In case an ion passes close to a target atomic nucleus, it is elastically scattered by the repulsive electromagnetic force: the projectile loses a negligible amount of energy, so that this kind of interaction can be neglected when calculating the energy loss rate described above, but the change in its trajectory must be estimated for range and dose predictions. Starting from the single scattering model by Rutherford (Rutherford 1911), and moving to the calculation of the statistical distribution function for the scattering angle at a certain penetration depth given by Bothe 1921, a complete theory allowing for the calculation of the scattering angle probability in case of Multiple Coulomb Scattering (MCS) has been proposed by Molière (Molière 1948) (confirmed to provide good predictions thanks to a large set of proton beam spread data - see Gottschalk et al. 1993). 

The Molière MCS description allows to retrieve the main parameters contributing to this effect: in particular, heavier particles have more  grow lateral beam shape  and the scattering effect increases at increasing ion range (but is inversely proportional to the beam energy) and for high-Z materials. A more precise model of the lateral beam spread should involve nuclear reactions and the produced secondary particles, but an analytic approach is difficult and Monte Carlo based calculations are  time consuming. The empirical parametrizations are still strongly based on experimental data: as an example, measurements of the lateral beam spread in a water column for different beam energies (ranges) are reported in Pedroni et al. 2005. 

Nuclear reactions In addition to the electromagnetic interactions with electrons and nuclei which mainly govern the stopping process, primary ions impinging on a target also undergo nuclear reactions with the target nuclei which may cause the disintegration of the projectile and the target nucleus or a partial fragmentation. In general, nuclear reactions induce modifications in the beam composition and cause variations in the longitudinal and lateral beam structure which must be taken into account for the delivered physical and biological dose estimate. Moreover, this kind of reactions leads to the production of secondary particles, such as secondary protons, neutrons, hydrogen and helium isotopes and other ions (mainly with heavy ion irradiation), and gammas.

 nuclear interactions occurring between projectile ions and target nuclei can be described by a two-step process. At the “collision” stage, depending on the distance between projectile and target centers (impact parameter b), a variable number of nucleons is involved in the interaction and composes the reaction zone generally defined “fireball”. The so-called “spectator” nucleons are almost not affected and create projectile and target-like fragments (“fragmentation” process), often in excited states . After the collision, the excited fireball and fragments decay through the emission of secondary light particles, in the so-called “de-excitation” process, and the lighter fragments continue their path through the target. A schematic view of a typical nuclear reaction is given in Figure 1.4. Several models have been proposed to de-

scribe the two steps, and a complete description of the overall process is given by the so-called abrasion-ablation model (Hüfner et al. 1975; Serber 1947) generally used in therapy transport codes, where the abrasion phase describes the collision and the ablation one models the de-excitation stage. To be noticed that the ablation description is more adapted to peripheral collisions (high b), where the fragments are excited after the collision and decay to the ground state by emitting light particles and gamma rays.

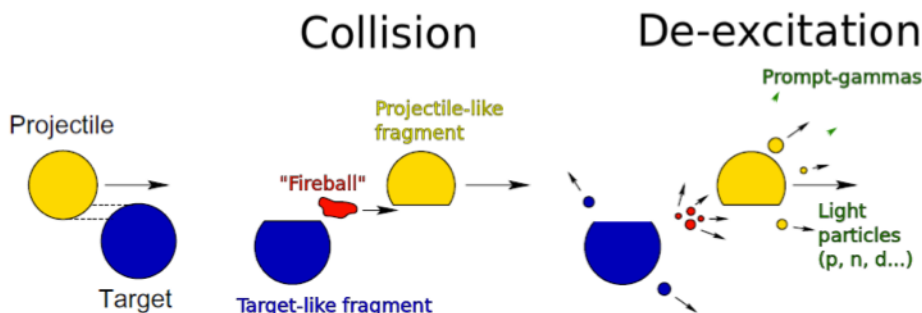
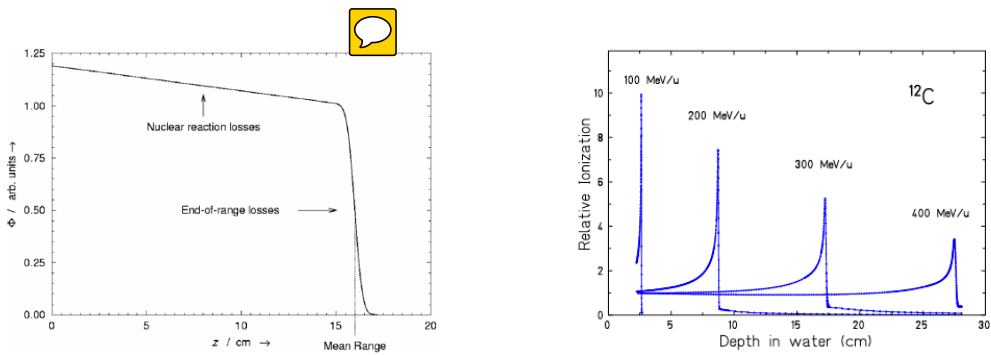


Figure 1.4: Schematic view of the nuclear reaction between a projectile and a target nucleus. The two steps are defined as “collision” and “de-excitation” processes.

Two main effects of fragmentation processes are relevant to ion beam therapy. First, the described nuclear reactions cause a loss of primary beam particles; this effect is all the more important for increasing penetration depth. It is clear that peripheral collisions (high b) lead to smaller loss of primaries with respect to central collision (small b), where projectile and target are most likely completely destroyed. Figure 1.5a shows the primary particle fluence loss in a proton beam as a function of the depth in water (Newhauser et al. 2015). In the entrance region before the falloff the fluence loss is caused by nuclear reactions, while close to the Bragg peak the fluence falloff is mainly due to absorption of primary particles with limited residual energy. In addition, the range straggling effect is visible. Concerning carbon ion beams, as reported in Durante et al. 2016, during a standard treatment only 50% of the primary ions reaches the Bragg peak region while the others undergo fragmentation processes and are lost. Second, lower-mass and Z fragments result from the nuclear interactions in case of irradiation with ions heavier than protons (with proton beams, only secondary protons and neutrons are produced). The projectile velocity determines the velocity of the secondary fragments, which can travel with longer ranges with respect to the primaries due to their reduced mass and charge (remember the range scaling factor M/z^2): this produces a tail in the dose distribution (for ions heavier than protons). The features of this tail have been deeply studied for different primary ions species (^{10}B , ^{12}C , ^{14}N , ^{16}O , ^{20}Ne), and shell-structure effects have been verified with a non-direct relationship between proton number Z and tails extension (Schall et al. 1996). Figure 1.5b shows the effects of nuclear reactions on the Bragg curves related to carbon ion beams at different energies stopping in water, measured in a water column (Schardt et al. 2008). With increasing primary energy and, consequently, beam penetration depth, the ratio between Bragg peak and entrance plateau dose is reduced by the decreased number of primary ions, while the tail after the Bragg peak is wider due to the increased number of lower-Z fragments traveling with longer range. In addition to this, the energy loss stochastic fluctuations is clearly visible in the broadening of the Bragg peak.



(a) Primary particle fluence loss in a proton beam as a function of the depth in water (in Newhauser et al. 2015).

(b) Measured relative ionizations for carbon ion beams stopping in water (in Schardt et al. 2008).

Figure 1.5: Effects of nuclear interactions on the primary beam and resulting dose distribution.

Further, interesting results about ion fragmentation in nuclear interactions can be found in Gunzenhäuser et al. 2008; Haettner et al. 2013, 2006; Matsufuji et al. 2003; Wroe et al. n.d.

Detailed information about fragmentation can be retrieved via Monte Carlo simulations and used to evaluate the impact on the delivered dose. As an example, simulations published in (Grassberger et al. 2011) of 160 MeV protons in water allowed to estimate the dose contributions given by primary particles (between 90% and more than 99% of the total depending on the range), with the remaining fraction of dose mainly connected to secondary protons and α particles: negligible dose is given by heavier fragments. A more intense dose contribution from heavier fragments is expected for carbon ion irradiation, but an accurate Monte Carlo simulation of these processes is still a challenge.

As mentioned, in addition to charged fragments, nuclear interactions also produce gammas, mainly originating from atomic de-excitation processes (prompt-gammas) or from the annihilation of positrons emitted by beta-emitter fragments (^{10}C , ^{11}C , ^{13}N , ^{14}O , ^{15}O), and neutrons. All the secondary particles which can be absorbed by the target contribute to the total dispensed dose, while the others (with the exception of neutrons), escaping the target volume, can be exploited for non-invasive measurements of beam and target features. In particular, different techniques have been proposed and tested to measure secondary protons and gamma rays (both prompt-gammas and positron-annihilation gammas) with the aim of retrieving information about the ion range and obtain an online treatment verification. A detailed discussion about this topic will be given in section ??.

Focusing on neutrons, which are produced in large quantities and over a wide energy range, they cannot be exploited for primary ion range monitoring since they are not correlated with the ion path in matter (“Real-time monitoring of the Bragg-peak position in ion therapy by means of single photon detection.” 2010) any case, they must be modeled with care in order to evaluate the safety measures to be implemented in treatment centers (Newhauser et al. 2002), as well as the implications in the delivered dose and secondary cancer probability (Newhauser et al. 2011). The dose contribution caused by secondary neutrons strongly depends on the beam delivery system (see section 1.1.3 for the description of the beam de-

livery systems), as demonstrated in Gottschalk 2006. In particular, passive elements used for beam shaping have been identified as one of the main source of secondary neutrons contributing to the total delivered dose to the patient (Yan et al. 2002), so that in modern facilities deflecting elements are set after the passive modules in order to limit the neutron flux towards the target. It is interesting to notice that the amount of produced neutrons and resulting dose is compatible for protons and carbon ion irradiation, even if the neutron yield is higher for carbon ions: this is due to the different beam intensities used in clinics for the two species, with more than a factor 20 in favour of protons. Finally, if compared to photon standard radiotherapy, the neutron dose associated to ion beam therapy treatments results to be smaller, as demonstrated in recent studies (Schneider et al. 2015).

More details about the physics of proton and, more generally, ion beam therapy, can be found in (Belkić 2010; Bichsel 2013; Durante et al. 2016; Lomax 2009; Newhauser et al. 2015; NuPECC 2014; Schardt et al. 2010). In the following section, the attention is focused on the biological aspects of this cancer treatment modality.



1.1.2 Biological effects of ion beam therapy

In addition to the already presented physical differences between photon radiation therapy and ion beam therapy treatments, a fundamental aspect of the game in the biological effect of such radiations. In the following, the main biological implications of radiation therapy are summarized with the aim of highlighting the favorable contribution given by charged particles with respect to photons and, at the same time, discuss some controversial points (Paganetti et al. 2013).

Absorbed dose, defined in ICRU 1980, 1998 as



$$D = \frac{d\bar{\epsilon}}{dm} \quad (1.6)$$

where $d\bar{\epsilon}$ is the mean energy imparted by ionizing radiation to matter of mass dm . To be precise, the imparted energy must also be defined: in the same ICRU reports we find that

$$\epsilon = R_{\text{in}} - R_{\text{out}} + \sum Q \quad (1.7)$$

with R_{in} and R_{out} the sum of the energies of all ionizing particles entering or leaving the volume, respectively, $\sum Q$ the sum of all changes of the rest mass energy of nuclei and elementary particles in any nuclear transformations occurred in the volume due to the ionizing radiation.

LET TO BE DEFINED: number of ionizations which radiation causes per unit distance as it traverses the target.

In order to transfer the experience from photon data to ion irradiation and to create a common evaluation parameter, the Relative Biological Effectiveness (RBE) has been introduced and defined as the ratio between the photon and ion equivalent dose:

$$RBE = \frac{D_{\text{photon}}}{D_{\text{ion}}} \quad (1.8)$$

where D_{photon} and D_{ion} are the absorbed dose for photon and ion irradiation causing the same biological effect. Notwithstanding the apparently simple definition, RBE results to be a very complex quantity, but for the moment the only one really used in clinics. It depends on several physical and biological parameters, such as Linear Energy Transfer (LET), does, dose rate, fractionation, particle type, target biological features (radiosensitivity, oxygen concentration, etc.) (Durante et al. 2009).

Cell survival studies (Blakely et al. 1984; Tobias et al. 1982) showed that heavy charged particles have an increased RBE compared to x-rays. *vedi Durante 2016*

Clinical trials for different ions to study LET and RBE variations, He, Ne, N, O, C, Si, Ar (**Castro1995**). *vedi Durante 2016*

Many simulation results and models on proton RBE 1.1 (Giantsoudi et al. 2013; Giovannini et al. 2016; Guan et al. 2015; Jones 2015; McNamara et al. 2015; Sethi et al. 2014). *vedi Durante 2016* 

1.1.3 Accelerators and beam delivery

The goal of ion beam therapy is to treat deep-seated tumors with a conform dose distribution. Different ion species, hadrons and charged particles in general have been and are under study for the clinical application (neutrons, charged pions, antiprotons, helium ions - i.e. alpha particles -, heavier ions like lithium, oxygen, up to silicon ions), but only two are at present implemented for the patient treatments: protons and fully stripped carbon ions (Degiovanni et al. 2015). The ability of treating any kind of tumor at any depth in human body relies on the possibility of providing the employed particles enough energy to obtain a range of about 25 cm in soft tissues. The ions employed in treatment must be then accelerated to about 60-70% of the speed of light ($\beta = 0.6-0.7$, see Durante et al. 2016) via different acceleration techniques and machines. This translates into maximum energy values of the order of 200-250 MeV and 4500 MeV (i.e. 375 MeV/u) for protons and carbon ions, respectively (Braccini 2010). In order to achieve the desired ion energy, sizable accelerators are needed and different solutions have been explored; at present, cyclotrons and synchrotrons are clinically implemented and available on the market. In the following, after a brief historical introduction, we sketch the main characteristics of the accelerators used in clinics, and we highlight the main features which are reflected in the treatment delivery. In addition to this, the beam delivery systems are described. Moreover, an overview of the main directions followed for the future acceleration and beam delivery techniques upgrade is provided.

1.1.3.1 Accelerators for ion beam therapy



Cyclotrons The way towards the possible application of ion beams in therapy (proposed only later by Wilson - see R. R. Wilson 1946) was opened by the invention of the cyclotron by Ernest Orlando

Lawrence in 1929 (Lawrence et al. 1932), which added a magnetic field to the recently proposed linear accelerator (Wideröe 1928). A cyclotron is composed of two hollow electrodes with a frequency-alternating voltage applied between them, which accelerates the charged particles at each revolution. The circular trajectory is obtained thanks to a fixed vertical magnetic field. A scheme of the main components of a cyclotron is sketched in Figure 1.6.

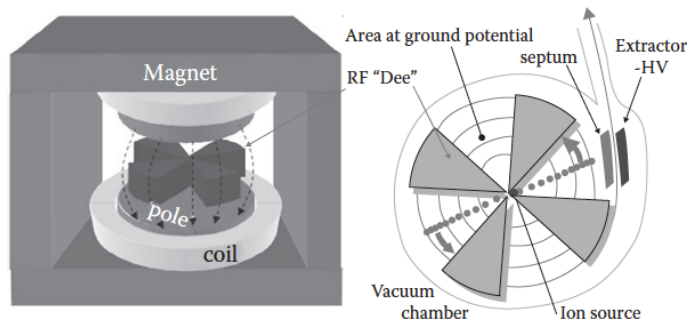


Figure 1.6: Schematic view of the main components of a cyclotron accelerator. On the left side the magnet is sketched together with the radio-frequency elements (“Dees”), which are also shown on the section depicted on the right side, with the ion source in the center. In Paganetti 2012b.

Nuclear physics saw a paramount development thanks to this invention, but also in the medical field the impact was remarkable. Already in 1935, Lawrence produced the first cyclotron-originated radionuclides, then used for radiotracing, diagnosis and treatment. The first cyclotron-based treatment was performed with fast neutrons (i.e. with kinetic energies between a few MeV and a few tens of MeV) in 1938, following a paper by Gordon Locher who underlined the therapeutic potentialities of neutrons (Locher 1936); the neutrons were produced by bombarding a beryllium target with cyclotron-accelerated deuterons (Stone et al. 1940). The unfavorable depth-dose distribution of neutrons and the difficulties linked to their collimation finally led to abandon the neutron treatments in 1948 (Stone 1948) and move towards proton-beam treatments in the 50’s: neutrons were revised in 1965 by Catterall in London (Catterall et al. 1971) and are still used today in Boron Neutron Capture Therapy (BNCT) techniques (Barth et al. 2005; Nedunchezhian et al. 2016). As already mentioned in section 1.1, the first proton therapy treatment was conducted by Cornelius Tobias, and John Lawrence with the Lawrence cyclotron in 1954 (Tobias et al. 1958, 1955). Between 1954 and 1974, more than 100 patients were treated in Berkeley with cyclotron-accelerated protons. In parallel, in 1957 the first tumor was irradiated with protons at the Uppsala cyclotron in Sweden (Larsson 1962), and an intensive proton therapy program, leaded by Robert Wilson, was started in Harvard with a new-built cyclotron (R. Wilson 2004). Following these first experiences, new physics laboratories decided to set up proton beams for therapy (USSR, Japan, Switzerland), until the creation of the first hospital-based center, built at the Clatterbridge Oncology Center in the United Kingdom, which started operating in 1989 with a 62.5 MeV cyclotron. This historical overview shows how the cyclotron technology has soon spread all over the world, not only in research centers, but also for therapy purpose. The present cyclotron

machines, which are now commercially available by different providers, still rely on the same accelerating principle as the first Lawrence system, but the technology has greatly advanced. In particular, the vertical magnetic fields in charge of bending the particles on a spiral trajectory has been improved, giving the beam the desired transverse compactness. Moreover, the beam extraction efficiency has been improved, and multiple extractions are now possible to supply different transport lines. Moreover, synchrocyclotrons are a solution compatible with hadrontherapy applications. Based on the cyclotron accelerating principle, a synchrocyclotron presents a variable frequency for the alternating voltage which is used to compensate for relativistic effects when the accelerated ions approach the speed of light. Such a solution has the advantage of allowing for the creation of more compact systems with high magnetic fields, and is at present exploited for commercial accelerators by the main providers.

Synchrotrons In addition to cyclotrons and synchrocyclotrons, other accelerating machines initially developed for fundamental research have been translated to medical applications and are nowadays knowing a large diffusion: the synchrotrons. While the cyclotron present a fixed-value magnetic field, so that the radius of the beam trajectory increases during the acceleration process, in the synchrotron the trajectory radius is kept constant thanks to the variation of the bending magnetic field. The boost is provided by radio-frequency cavities, based on the same principle as the one composing linear accelerators: the radio-frequency increases to follow the particle revolution speed, and this acceleration principle allows to overcome the cyclotron energy limitation, as well as to obtain beam at different energies by tuning the extraction process. The invention is based on the independent ideas of Vladimir Veksler ([Veksler 1944](#)) and Edwin McMillan ([McMillan 1945](#)): the latter both coined the name of the machine in its letter, and constructed the first electron synchrotron in 1945 in Berkeley. Some years later, the first proton synchrotron was designed in 1952 by Sir Marcus Oliphant, who already published a preliminary sketch of the machine in 1943 ([Oliphant 1943](#)). As for the cyclotron case, several years have been required to see the construction of the first hospital-based hadrontherapy facility using a synchrotron. The first center was built at Loma Linda University in California, where a 7-m-diameter synchrotron constructed by Fermilab was installed and started treating patients in 1990. The center has been a pioneer in the field also for the presence of three 10-m-diameter rotating gantries. After the clinical studies performed at the University of Tsukuba, in Japan, between 1983 and 2000, with the treatment of about 700 patients with synchrotron proton beams, a second hospital-based center was built and equipped with an Hitachi synchrotron and two rotating gantries. Since the first use of synchrotrons for treatment purpose, several improvements have been achieved in the accelerator technology to better adapt its features to the hadrontherapy needs. In particular, the beam size can be now reduced with strong focusing optics, and the beam energy can be varied on a single spill basis, in contrast to the first machines for which 1-2 s were needed to modify the spill energy. At present, all the hadrontherapy facilities in operation are based on circular accelerators (cyclotrons and synchrotrons): proton beams are produced with both the solutions, while only synchrotron-produced carbon-ion beams are used. In Figure 1.7 the size of different accelerators design is compared (CABOTO is still at the design stage, the Ion Beam Applications, Belgium (IBA) superconducting synchrotron is under installation in France, while HIT, Centro Nazionale di Adroterapia Oncologica, Italy (CNAO) and the SIEMENS accelerator are at present in operation).

Novel acceleration approaches

In the last years, novel approaches have been proposed to improve the present accelerators and beam features, mainly for what concerns the beam quality and the machine size and cost. It is worth to mention the Fixed Field Alternating Gradient (FFAG) accelerator, which combines the fixed magnetic field and variable radio-frequency with separated sector magnets ([Sheehy](#)

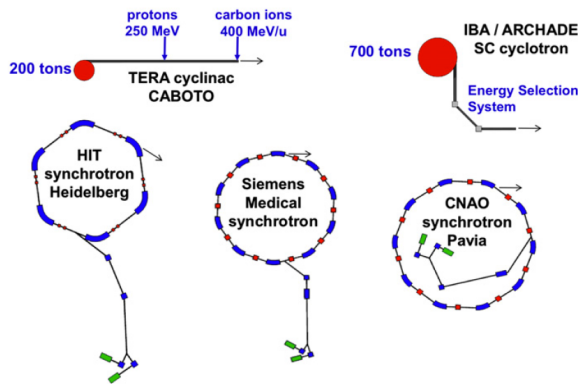


Figure 1.7: Comparison of the size of various ion accelerators for hadrontherapy. CABOTO is a cyclinac studied by the TERA Foundation; the superconducting cyclotron, designed by IBA, is under installation in Caen, France, within the ARCHADE project; HIT and CNAO are in operation in Heidelberg, Germany and Pavia, Italy, respectively; the SIEMENS synchrotron is installed in Marburg and Shangai. In Amaldi et al. 2010.

2017). This approach allows for the production of higher intensity beams with respect to synchrocyclotrons, and for the variation of the extracted beam energy at high repetition rate. Some design have been proposed for hadrontherapy applications in the last decade (Antoine et al. 2009; Peach et al. 2010), but the present machine size still limit its spread in treatment centers. Furthermore, linear acceleration approaches has been proposed since 1991 in both “all-linac” (Hamm et al. 1991; Lennox 1991) and “cyclinac” (Amaldi 2009) solutions. In addition to the compactness, the main advantage of linacs is the possibility to continuously vary the output beam energy on a pulse to pulse basis; in addition to this, there is neither the need for complex injection or extraction systems, such the ones used in synchrotrons, nor the need of an energy passive modulation technique as the one used in cyclotrons (see section 1.1.3.3). An extended description of linear accelerators for hadrontherapy is given in Amaldi et al. 2009. Following the first successful prototypes tested by the TERA Foundation and the Italian Istituto Nazionale di Fisica Nucleare, Italy (INFN) in the last twenty years (Amaldi et al. 2004; Roncivale et al. 2011), the Conseil Européen pour la Recherche Nucléaire, Geneva, Switzerland (CERN) spin-off company Advanced Oncotherapy (A.D.A.M.) is proposing a commercial solution called Linac for Image Guided HadronTherapy (LIGHT). A further solution can be given by the Dielectric Wall Accelerator (DWA) (Caporaso et al. 2009), where the acceleration tube is made of High Gradient Insulator disks alternated with conducting elements. A laser pulse is used to activate the switching units connected to these conducting modules. Very interesting thanks to a reduced size, this acceleration scheme still suffers beam focusing issues; moreover, it presents very short pulses which force a very precise selection of the number of ion per pulses at the source level. Finally, the electric field needed for reducing the machine size till 2-2.5 m is of the order of 100 MV/m; this challenging value has not been achieved yet, even if a prototype is under study at the Lawrence Livermore National Laboratory, USA (LLNL), with promising results (Zografos et al. 2013). Another attractive technique is the so-called “laser driven” acceleration, based on the use of short and powerful laser pulses irradiating a thin target, with the generation of a plasma field (Tajima et al. 2009). The electrons emerg-

ing form this plasma are able to induce a strong electric field which accelerates the protons (or ions). Again, this solution would allow for the creation of very compact systems, with relatively simple and light beam optics, but some issues are still under study to be solved; in particular, the accelerated beam has an almost continuous energy spectrum which forces to implement energy modulation solutions to be adapted to treatment purposes.

1.1.3.2 Beam time structure



1.1.3.3 Beam delivery systems

Once accelerated, the high-energetic ions must be delivered to the patient in order to be conform to the treatment specification, focusing the provided dose on the Planned Target Volume (PTV). As described and detailed in section 1.1.1, the beam range can be varied by modulating the primary particle energy with the aim of covering the whole tumor volume. The Bragg curve obtained with a monoenergetic beam is called “pristine Bragg curve”, and can be used to irradiate a section of the target volume at a given depth. The superposition of several pristine Bragg curve is necessary to deliver the prescribed dose to the tumor, which has been previously modeled in three dimensions. In particular, the beam energy spectrum has to be spread in order to increase the axial dimension of the peak region, in the so-called Spread-Out Bragg Peak (SOBP). At the same time, the beam fluence must be adapted to avoid over-irradiation of the entrance region. An example of SOBP is given in Figure 1.8.

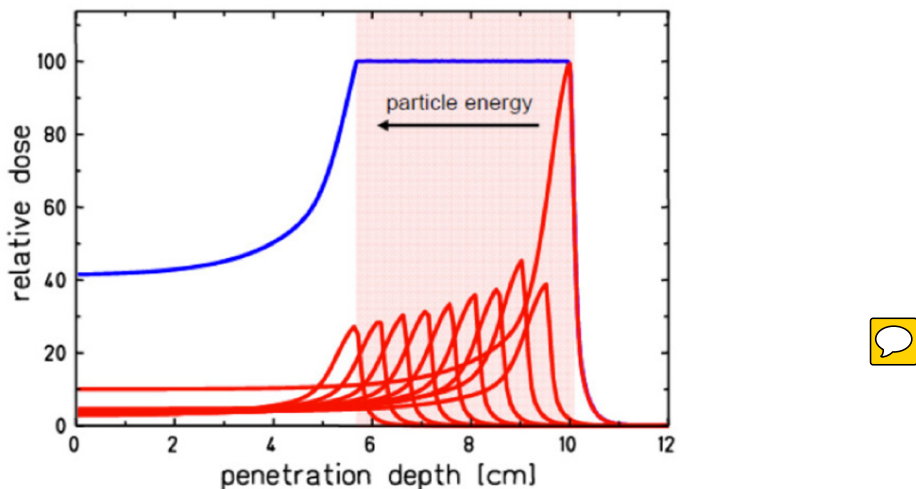


Figure 1.8: Example of SOBP. The target region is highlighted and the discrete pristine peaks composing the SOBP are sketched in red. In Durante et al. 2016.

All these tasks are in charge of the beam delivery system, which must be optimized to interface with the accelerator and to the patient by transporting the beam to the treatment area and adjusting its features to obtain the desired dose distribution. The delivery systems implemented in clinics are based on two main strategies: passive beam modulation and active scanning. For an extensive presentation of this topic, refer to Gottshalk et al. 2008. The chosen technique must be chosen according to the accelerator machine: it is important to remember that cyclotrons

provide fixed energy beams with pulses separated by about 10-20 ns, while in a conventional synchrotron the energy can be varied cycle by cycle, with short pulses generally separated by 1-2 s dead-time (see section 1.1.3.2).

The passive beam delivery approach generally applies to cyclotron produced beams, and its principle is sketched in Figure 1.9. The beam extracted from the accelerator is fixed in size and energy, and is first broadened by scattering devices. Afterwards, a range modulator (generally a rotating wheel) is used to spread out the monoenergetic Bragg peak with the aim of covering the whole target volume.  The wheel periodically inserts material of varying thickness into the beam line, resulting in a range modulation at the desired frequency. The obtained SOBP can be shifted as a whole thanks to the addition of range shifters of fixed thickness. After the energy (range) adaptation, the beam is shaped according to the PTV definition with collimators (often multi-leaf) and compensators, which are specific to each patient.

Passive beam shaping

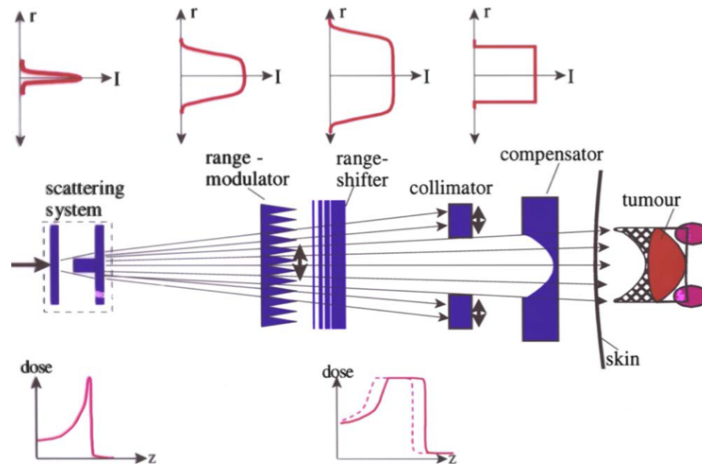


Figure 1.9: Schematic view of a fully passive beam delivery system. In Schardt et al. 2010.

The passive beam delivery technique presents two main disadvantages with respect to the active delivery described in the following. First, the structure of the created SOBP is fixed  so and the depth-dose can only be tailored to the distal end of the target volume and not to the proximal end, given the fact that the SOBP can only  be shifted towards the entrance region. This feature automatically leads to a considerable dose is given to normal tissues outside the target volume, in particular in the proximal part. Second, the amount of material inserted in the beam line causes nuclear interactions which lead to the creation of secondary high-LET fragments (mainly neutrons), affecting the dose delivered to the entrance region.

When the beam is produced with a synchrotron,  the possibility to switch the energy from pulse to pulse makes feasible an active target scanning and beam range adaptation. The active beam delivery systems exploit the electrical charge of the accelerated particles to deflect the beam laterally through magnets and perform a scan of the defined treatment field. A schematic view of an example of active delivery system is provided in Figure 1.10. The target volume is divided into iso-energetic layers which are irradiated sequentially by deflecting the beam with dipoles in order to fully cover a grid of pre-defined voxels.

Active beam scanning

Even if this approach is demanding from the accelerator performance point of view, it brings

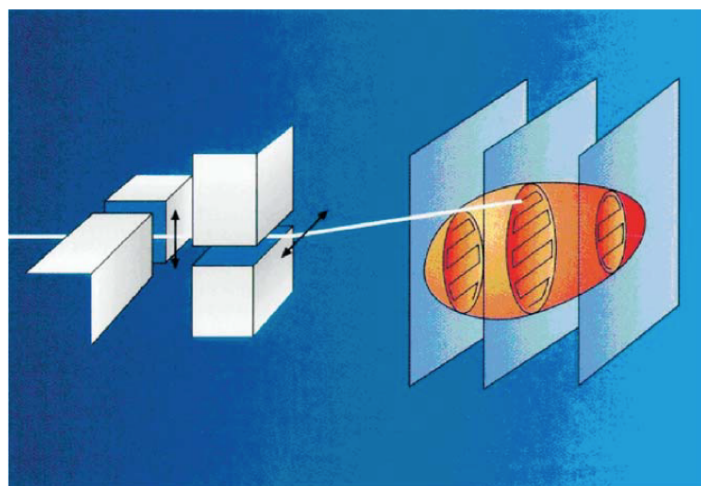
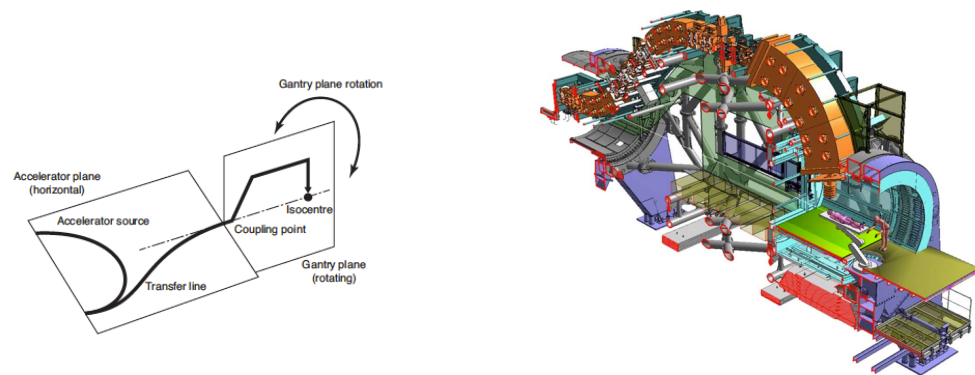


Figure 1.10: Schematic view of a fully active beam delivery system. In particular, here the GSI Helmholtz Centre for Heavy Ion Research, Germany (GSI) raster scanning system is depicted. In Schulz-Ertner et al. 2006.

several advantages with respect to a passive one: there is no need for patient specific equipment like collimators and compensators, and any volume can be in principle covered with a conformal dose; the dose can be adapted on a single voxel basis; the material in the beam line is minimized so that the production of secondary particles is strongly reduced. With such a delivery system, the term Intensity-Modulated Particle Therapy (IMPT) has been introduced in analogy to the Intensity-Modulated RadioTherapy (IMRT) techniques applied in standard photon radiotherapy. The first so-called “spot-scanning” system was introduced at National Institute of Radiological Sciences, Japan (NIRS), already in the early 80’s (Kanai et al. 1983). This first experience was soon followed by a pilot project of spot-scanning at Paul Scherrer Institut, Villigen, Switzerland (PSI) (Pedroni et al. 1995) and by the realization of a fully 3D scanning beam system at GSI, where the “raster-scan” technique is implemented (Haberer et al. 1993) (with the beam moved from one voxel to the next one with no interruptions, and all points in an iso-energy slice connected together in a dense grid). Nowadays, various companies are offering commercial scanning beam system solutions, so that a rapid spread of this convenient technique is foreseen for the next years.

Rotating-gantries We described till here static beam configurations, with a fixed irradiation position. In the clinical routine, in order to further improve the target volume-to-healthy tissue dose ratio, various beam penetration angles can be foreseen, similarly to standard photon therapy (event if a reduced number of different angles is required). In addition to this, deep-seated tumors close to OsAR can require specific irradiation angles to be treated with the desired safety margins. In order to achieve this goal, two approaches are possible: rotate the patient or rotate the beam line. Even if the patient rotation solution has been explored in the past, several reasons are in favor of a fixed supine position, with only horizontal rotations allowed: the supine position is in compliance with the pre-treatment imaging (Computed Tomography (CT) scan) used for treatment planning (see section 1.1.4); a patient rotation necessarily leads to organ motion which is undesired; the supine position is more reproducible in the different treatment fractions. As a consequence, rotating gantries have been developed to allow for the beam line displacement. The electron linacs employed in conventional radiotherapy are

generally mounted on gantries which can rotate 360 degrees around the patient couch to select the optimum beam direction. Likewise, in hadrontherapy, rotating gantries solutions have been designed for both protons and heavier ions. In contrast to the compact gantries used in standard radiotherapy, the high beam magnetic rigidity (defined as the product of the bending radius and the required magnetic field strength) is a constraint on the size of these structures for proton therapy, and, much more, for heavier ion therapy. In general, the beam is first deflected away from the extraction axis, and then bent back to the patient direction with several dipoles. Moreover, quadrupoles are used to optimize the beam focusing before the treatment room. A scheme of a standard gantry design is given in Figure 1.11a. As already mentioned in section 1.1.3.1, the first gantry for protons was installed at the Loma Linda University Medical Center in 1990, followed in 1996 by the first one in Europe at PSI in 1996, which also included an upstream scanning system (Pedroni et al. 1995). At present most of proton therapy centers are equipped with at least one rotating gantry, generally with passive beam delivery systems. The huge dimensions imposed by the carbon ion beam rigidity (three times bigger rigidity for 5000 MeV carbon ions with respect to 200 MeV protons) limited the implementation of such a technology in carbon therapy centers, while different technical solutions have been explored. As an example, at Heavy Ion Medical Accelerator in Chiba, Japan (HIMAC), in a single treatment room the beam can be delivered to the patient via an horizontal and a vertical line, for the sequential treatment from different angles. The first rotating gantry system for heavy ions was installed at HIT and is now in operation: the diameter is of 13 m, for a total weight of about 700 tons (see Figure 1.11b).



(a) Schematic design of a rotating gantry installed in a particle therapy center.
In Owen et al. 2014.

(b) Scheme of the HIT ion rotating gantry. In Schardt et al. 2010.

Figure 1.11: Schemes of a standard gantry design (left) and of the carbon-ion rotating gantry installed at HIT (right).

Intense research efforts are dedicated to improve the gantry technology, mainly directed towards the implementation of more compact systems equipped with superconducting magnets. A first superconducting carbon ion gantry has been recently installed at NIRS, and is approximately half size with respect to the German one (Iwata et al. 2013).

1.1.4 Treatment planning

Given the available accelerator and beam delivery system, the best possible treatment features are elaborated by the treatment planning process, which combines the clinical information

about the patient with the physical and biological aspects of particle therapy. The treatment planning is always patient and disease-specific, and is based on imaging techniques aiming to provide the physicians with the data necessary to delineate the target volume and the surrounding OsAR. The minimal approach is represented by a pre-treatment x-ray CT scan, providing quantitative information about the anatomical structures via photon attenuation images. As briefly outlined in the previous paragraph, it is important to record the pre-treatment images in the same conditions (patient position, fixation structures, etc.) later applied in the treatment itself. Complementary imaging devices, such as MRI and PET (Levy 2007), are often used in combination with CT to improve the target definition quality, mainly in case of proximity with OsAR. In addition to the target delineation, the physicians are also in charge of the therapy prescription, which includes the total dose to be delivered to the PTV, the dose limits for the surrounding tissues, and the fraction planning. All the listed information are the input for the Treatment-Planning System (TPS), which makes the connection between the prescribed dose distribution and the beam acceleration and delivery devices. The physicists and clinicians use the TPS to define all the treatment beam-specific features such that the clinical prescription is satisfied at the maximum extent. The software output details the beam entrance ports to be used (in terms of gantry positions, if a gantry is available), the beam ranges and intensities, the irradiation scheme in terms of dose-per-voxel, and, more generally, the expected dose distribution in the patient, which allows to quantify the Tumor Control Probability (TCP) and the probability of complications to the normal tissues. As the whole planning process is based on x-ray CT scans, providing photon beam attenuation images, a relationship between the CT values and ion RSP is needed. The CT values are expressed in HU, defined as

Treatment-
Planning
System

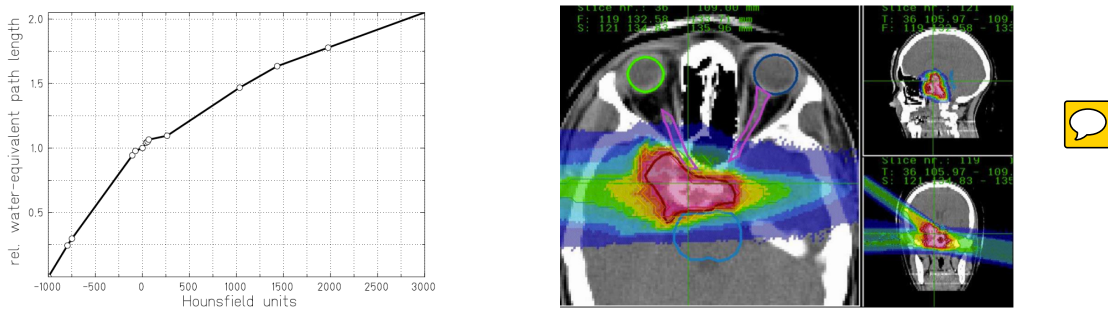
From
Hounsfield
Units (HU)
to Relative
Stopping
Power (RSP)

$$\text{CT value}(\vec{x}) = 1000 \times \frac{\mu(\vec{x}) - \mu_w}{\mu_w} \quad (1.9)$$

where \vec{x} is the considered location, $\mu(\vec{x})$ the x-ray absorption coefficient in tissue, μ_w the one in water as reference. Water is always used as reference medium, in particular through the concept of Water-Equivalent Path Length (WEPL). There is not a functional relationship between the two quantities, and systematic studies have been carried out at PSI for protons (Schaffner et al. 1998; Schneider et al. 1996). For carbon ions, similar investigations have been performed at NIRS (Kanematsu et al. 2003; Matsufuji et al. 1998) and GSI (Jakel et al. 2001; Rietzel et al. 2007), and experimental verification has been obtained via measurements on animal tissues. In Figure 1.12a the data of a look-up table for the conversion of HU into carbon ion WEPL are plotted in the HU range of relevant biological tissues.

The conversion factors are tabulated and implemented in the main TPSs, but several studies are still ongoing in order to optimize the calibration accuracy (as an example, see Inaniwa et al. 2018). As highlighted in several research work, this is one of the main source of uncertainty affecting proton and carbon ion range prediction and, so, treatment precision. Possible investigated solutions to reduce systematic uncertainties in the RSP determination related to the Hounsfield unit conversion are represented by proton Computed Tomography (pCT) and dual energy x-ray CT (Yang et al. 2010). Further details will be given in section 1.1.5. In addition to the beam range determination, the TPS software must also deal with biological dose calculations. Indeed, as highlighted in section 1.1.2, charged particles differ from photons in their radiobiological properties and effects. Notwithstanding the 10-20% RBE variations verified for protons with varying LET along the path in the patient tissues, a practical constant value of 1.1 is generally used in clinics (ICRU 2007; Paganetti et al. 2002). This value corre-

Biological dose
modeling



(a) Hounsfield look-up table for carbon ion treatment planning, based on the data collected at GSI and reported in Jakel et al. 2001. In Rietzel et al. 2007.

(b) Biologically effective dose distribution for the treatment of a skull base tumor, optimized with the TPS TRIP (Kramer et al. 2000) at GSI. In Schardt et al. 2010.

Figure 1.12: The treatment planning system process is based on anatomical information about the patient, given by CT scans, and physician treatment prescription. The CT values must be converted to RSP and tabulated experimental data are used (left), while biological dose calculation models are applied to optimize the biological dose distribution to be delivered during the treatment (right).

sponds to the average RBE at mid SOBP overall dose levels. As mentioned in section 1.1.2, several studies are ongoing in the last years with the aim of optimizing the biological models and applying a variable proton RBE in clinics, and the topic is still open to discussion in the expert community [??](#). A different approach must be applied to heavy ions (carbon ions in particular), given the much stronger dependence of their RBE on the various parameters listed in section 1.1.2. Focusing on carbon ions, treatment plans are generally optimized using the so-called RBE-weighted dose, calculated according to verified models based on experimental data. Two main models are nowadays implemented in clinical practice. On one side, the Japanese centers use a model developed at NIRS, based on in vitro cell killing experiments on human salivary glands and neutron irradiation experience gathered at HIMAC, as well as on the application of the Linear-Quadratic (LQ) model (Matsufuji et al. 2007). Recently, a modified Microdosimetric Kinetic Model (MKM) has been introduced in order to optimize the plans to active scanning with ion beams (Inaniwa et al. 2015). On the other side, a specific biophysical model has been developed in Germany at GSI, called Local Effect Model (LEM), and it is now used in the clinical centers in Germany, Italy and China. Its main idea is to transfer known cell-survival data for photons to ions, assuming that the difference in biological efficiency arises only from a different pattern of local dose deposition along the primary beam (Jäkel et al. 2001; Kramer et al. 2000). The two models have been verified to give comparable results, in agreement with the measured RBE, with in-vitro experiments on mice cells (Uzawa et al. 2009), while different predictions are obtained when different treatment schemes on different tissues are studied (Fossati et al. 2012; Steinsträter et al. 2012). The definition of a common effective dose prediction method is ongoing: this will allow for comparative studies of clinical results and for an improved collaboration of the few ion treatment centers operating all over the world. These biological models are mainly applied for the planning of active scanning treatments, for which the target volume is previously divided into slices: the dose is then optimized for iso-range slices. In contrast, for passive beam delivery systems, the plan optimization is generally reduced to the study and production of the patient-specific beam modulators. In the future, biology-guided forms of particle therapy can

Treatment of moving organs

be foreseen; the RBE variations, instead of being an issue for which corrections are needed to the treatment planning, could be used to the treatment effectiveness advantage. Focusing on the possible direction of improvements in the future of treatment planning, the research efforts are concentrated in the last years also on another fundamental topic: the treatment of moving organs. It is clear that the well-defined ion range and narrow dose peak makes them potentially more sensitive towards inter- and intra-fractional organ motion, as highlighted in Bert et al. 2008; Engelsman et al. 2013; Phillips et al. 1992 and Thörnqvist et al. 2013, as an example. Concerning the organ displacement between following fractions, it can be corrected by more frequent imaging scans, ideally a new one before every treatment fraction, in order to adapt the treatment planning to weight variations, target size modifications and similar anatomical effects. The organ movement caused by the respiratory cycle requires more complex strategies to be taken into account for the treatment plan and delivery. The respiratory motion patterns are generally complex and not regular, involving translational and rotational displacements. Several strategies to mitigate the effect of organ motion are being investigated, some of them directly coming from the experience gathered in IMRT. As well summarized in Schardt et al. 2010, among these strategies it is worth to mention rescanning of repainting techniques, based on the average effect of several irradiations with reduced beam fluence on the same iso-range slices; gating techniques, which aims to correlate the irradiation active time to a continuous monitoring of the respiration cycle; tracking, which requires a 3D compensation of the target motion in real-time, particularly adapted for scanning techniques.



Some of the cited techniques, or combinations of them, are being tested and are now at the validation stage, but there still wide room for improvements towards the application of 4D treatment planning (Bert et al. 2017; Graeff et al. 2013). Further information about this topic can be found in a recent review by Kubiak (Kubiak 2016).

Range predictions, biological modeling and organ motion are only some of the sources of uncertainties affecting the planning and delivery of ion therapy treatment, detailed in section 1.1.5; for this reason, safety margins

Safety margins

are applied in clinics for the definition of the irradiation target volume. In the actual clinical routine, the PTV is a geometrical extension of the so-called Clinical Target Volume (CTV) and is delineated in order to account for treatment uncertainties. Safety margins are also applied in standard x-ray therapy (McKenzie et al. 2000), where under- or over-shooting errors have limited effects with respect to ion beam therapy. As highlighted in Albertini et al. 2011, the application of safety margins is useful to improve the treatment plan robustness in case low dose gradients are applied, while the effect results marginal for highly modulated IMPT. At present, in order to account for the overall effects of all source of uncertainties in the range prediction (MCS, beam energy straggling, imaging tools accuracy and calibration, biological effects, patient positioning and organ motions), margins up to $3.5\% + 3 \text{ mm}$ can be applied around the CTV (Paganetti 2012a).



In the following paragraph, the uncertainties related to ion therapy treatment are discussed in details, with particular care devoted to possible clinical solutions.

1.1.5 Ion beam therapy uncertainties and treatment monitoring

is affected by uncertainties due to both the target and the projectile feature knowledge: in particular, target composition, mass density and linear stopping power, as well as the beam energy distribution, result in a considerable spread in the beam effective range with respect to the predicted one.



1.1.5.1 Positron Emission Tomography

PET is at present the only method clinically implemented for ion range verification (Bauer et al. 2013; Enghardt et al. 2004; Hishikawa et al. 2002; Parodi et al. 2007). PET techniques are based on the same principle as the ones employed in nuclear medicine diagnostics (see section 1.2): in particular, for the application in ion beam range monitoring, PET machines aim to detect the two back-to-back 511 keV photons produced by the annihilation of positrons (created by the emitter fragments of nuclear reactions) with patient electrons, resulting in a delayed radiation which should be detected with time coincidences, allowing for an intrinsic background reduction. Nevertheless, the monitoring with positron emitters secondary signal must deal with a limited count rate compared to medical imaging PET, with the lifetime of emitters providing a delayed information that implies the signal integration over a whole treatment fraction (not a single spot or group of spots), with physiological washout effects depending on the emitters lifetime.

IN-BEAM, IN-ROOM, OFF-LINE PET

Even if the only available and functional range monitoring system in a clinical center is based on this technique (Enghardt et al. 2004), several clinical experience with commercial or adapted PET system already shown intrinsic limitations mainly connected to the ring geometry (not directly applicable to the treatment monitoring due to the presence of the beam) or in general to geometrical constraints limiting the field of view and the resulting system global efficiency and spatial accuracy (the limited detection angle generates artifacts in the final image) (Parodi 2016). The research is ongoing and new results are expected for the next years thanks to the introductions of new systems with adapted geometries  the improvements in acquisition and reconstruction techniques and to the clinical introduction of time-of-flight systems, intrinsically able to improve the detector spatial resolution via interaction time information, and depth-of-interaction reconstruction, which will allow for a more precise spatial reconstruction for reduced angular artifacts effects. 

1.1.5.2 Prompt-gamma detection



1.1.5.3 Interaction vertex imaging

1.1.5.4 Other techniques

1.2 Nuclear medicine

1.2.1 PET and SPECT

1.2.2 State of the art of PET and SPECT

2

Prompt gamma detection and imaging

Contents

2.1 Photons	28
2.1.1 Photon interactions in matter	28
2.1.2 Photon detection	28
2.2 Prompt gammas	28
2.2.1 Ion range monitoring with prompt gamma radiation	28
2.3 Gamma cameras	28
2.3.1 Applications in medicine	28
2.3.2 Ion beam range monitoring	28
2.3.3 Nuclear medicine	28
2.4 Gamma cameras state of the art	28

2.1 Photons

2.1.1 Photon interactions in matter

$$h\nu' = \frac{h\nu}{1 + \frac{h\nu}{m_0c^2}(1 - \cos(\theta))} \quad (2.1)$$

2.1.2 Photon detection

2.2 Prompt gammas

2.2.1 Ion range monitoring with prompt gamma radiation

2.3 Gamma cameras

2.3.1 Applications in medicine

2.3.2 Ion beam range monitoring

2.3.3 Nuclear medicine

LINE CONE RECONSTRUCTION (Cree et al. 1994), (Basko et al. 1998), (Parra 2000), (Hirashawa et al. 2003), (Maxim et al. 2009)

ITERATIVE RECONSTRUCTION (Schöne et al. 2010), (Zoglauer et al. 2011), (Gillam et al. 2011), (Lojacono et al. 2013), (Mackin et al. 2012)

2.4 Gamma cameras state of the art

3

CLaRyS prototypes

The characterization method and the results presented in section 3.2.2 of this chapter have been submitted for publication on JINST.

Contents

3.1 CLaRyS gamma camera components	30
3.1.1 Scatterer	31
3.1.2 Collimator	36
3.1.3 Absorber	36
3.1.4 Beam tagging hodoscope	41
3.1.5 Camera acquisition system	47
3.1.6 Camera acquisition, monitoring and slow control software	50
3.1.7 Camera integration and mechanical support	51
3.1.8 Data analysis and image reconstruction	52
3.2 Camera component characterization and development status	55
3.2.1 Scatterer silicon layer characterization	55
3.2.2 Absorber Bismuth Germanium Oxide - $\text{Bi}_{12}\text{GeO}_{20}$ (BGO) blocks characterization	57
3.2.3 Hodoscope Photo-Multipliers (PMs) characterization	73
3.2.4 Hodoscope fiber test with electron source	78
3.3 Summary and perspectives	81
3.3.1 Silicon scatterer	82
3.3.2 BGO absorber	83
3.3.3 Scintillating fiber hodoscope	84
3.3.4 Acquisition and software	85
3.4 Conclusions	86

Following the highlighted limits of ion beam therapy (see chapter 1), a collaboration of five French research institutions was established in 2010 with the aim of exploring different experimental solutions for the ion range online monitoring. The research group originally involved the Institut de Physique Nucléaire de Lyon, France (IPNL), the Centre de Physique des Particules de Marseille, France (CPPM), the Laboratoire de Physique Subatomique et Corpusculaire, Grenoble, France (LPSC), the Laboratoire de Physique de Clermont, France (LPC) and the Centre de Recherche en Acquisition et Traitement de l'Image pour la Santé, Lyon, France (CREATIS). The collaboration focuses on the investigation of methods and detection solutions for the online monitoring of ion beam range during ion beam therapy treatment, and is so called Contrôle en Ligne de l'hadronthérapie par Rayonnements Secondaires (CLaRyS).

The main goal of the created collaboration is the parallel development of three gamma detection systems to be employed for ion range online monitoring purpose in the ion beam therapy field: a Positron Emission Tomography (PET) detector called Détecteur Pixélisé de Grand Acceptance (DPGA), a multi-collimated gamma camera and a Compton camera.

The design and development of the PET system is managed by the LPC group, which left the collaboration in 2017, and this detection system is not treated in this thesis work.

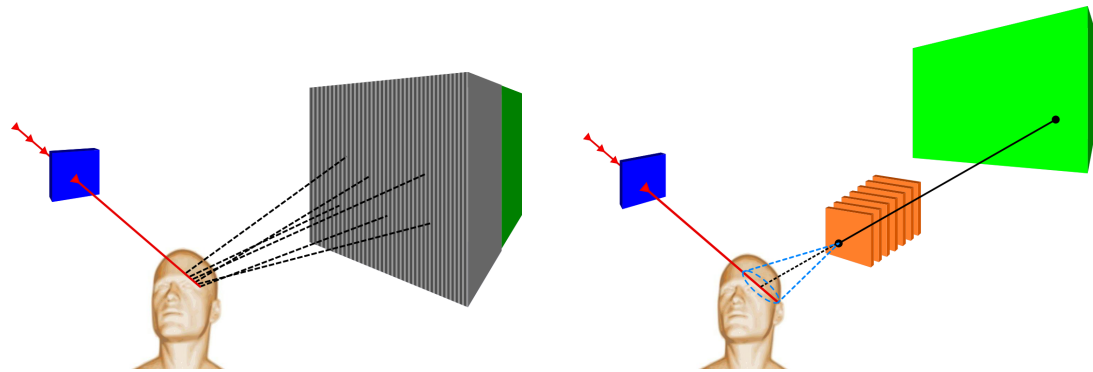
In this chapter the two gamma cameras (multi-collimated and Compton) prototypes are described in details, and the present status of the instrumental development is presented. A complete overview of the detector development carried out in the last years is presented for the sake of completeness, and my personal contributions are listed and detailed in the final section 3.4. In the following, an entire chapter (chapter 6) is dedicated to the tests of the detectors performed on ion beams.

3.1 CLaRyS gamma camera components

The two gamma cameras under development by the CLaRyS collaboration are devoted to the detection of prompt-gamma rays emitted during ion beam treatments (see section ??). The design of the two cameras has been optimized by different Monte Carlo simulation studies for what concerns both the detector components and the geometrical setup.

As already mentioned, a Compton camera is usually composed of two detector sections, a scatterer and an absorber: the CLaRyS prototype respects the standard design. In the scatterer, described in section 3.1.1, the prompt-gamma incoming ray is deflected by Compton interaction and the interaction position and energy deposited are stored. The scattered photon reaches then the absorber section, where its energy is ideally totally deposited and stored, again with the interaction position. This configuration is used to provide what is usually defined as “electronic collimation”, but a mechanical collimation is still an option for photon detection and localization. The scatterer section can be replaced by a mechanical collimator, described in section 3.1.2, which selects the parallel incoming photons then absorbed by the same absorber detector (a geometrical setup adaptation is possible to optimize the detection performance and will be discussed in the following). The mechanically collimated system is called multi-collimated camera, due to the collimator multi-slit structure.

As underlined in section ??, the prompt-gamma measurements are affected by several sources



(a) Scheme of the multi-collimated camera with the beam tagging hodoscope.

(b) Scheme of the Compton camera with the beam tagging hodoscope.

Figure 3.1: Schematic view of the two CLaRyS gamma camera prototypes: the multi-collimated camera (a) and the Compton camera (b), both coupled to the beam tagging hodoscope. The ion beam is represented by the red line, and some beam bunches have been highlighted. The detection principle is also sketched for the two detectors: the tungsten collimator select the parallel incoming photons for the multi-slit collimated camera (a), while the Compton cone is reconstructed with the two interactions in scatterer and absorber in the Compton camera (b).

of background: in particular, the signals detected by the two cameras can come from secondary particles other than prompt-gammas, like photons from positron annihilation, neutrons and protons (for beam of ions heavier than protons). One of the possible solution for background rejection is the use of Time-Of-Flight (TOF) information (see section ??), requiring a further detection section dedicated to the beam tagging. A beam tagging hodoscope is being developed in parallel and can be coupled to both the gamma cameras for TOF measurements; its description is presented in section 3.1.4.

A schematic view of the two prototypes is given in Figure 3.1.

3.1.1 Scatterer

The scatterer stack is one of the components of the Compton camera prototype. Dedicated to the photon Compton scattering, its design has been studied to fulfill the camera requirements.

The Compton events reconstruction strongly relies on the measurement of the energy deposited by the photon in its Compton interaction, mandatory to properly calculate the Compton scattering angle, which is then the aperture of the resulting Compton cone. The camera accuracy is then strictly dependent on the scatterer energy resolution. At the same time, the camera efficiency is dominated by the balance between Compton interaction and photoelectric absorption probability in the scatterer detector.

Given the need for at least two interactions for a proper event reconstruction (a Compton scattering in the scatterer section and an ideally complete absorption in the absorber section, described in 3.1.3), the material choice and the geometrical configuration play a fundamental role in the camera operation. The setup must be tuned in order to define the best trade-off

between Compton and photoelectric interaction probability and to optimize, as mentioned, the detector energy resolution.

Given the fact that the Compton interaction probability linearly increases with the material atomic number (Z), while the photoelectric absorption depends on Z^n with n varying between 4 and 5 according to the photon primary energy (Knoll 2000), it is clear that a low Z material is preferred. Considering now the detector energy resolution, it must be noticed that the main parameter affecting the deposited energy detection is the so called “Doppler spread”. The Compton angle reconstruction formula in equation ?? neglects the initial recoil electron state, which is considered free or unbound. The Compton energy transfer continuum results affected by the binding energy of the electron, with a relatively increasing effects for decreasing incident photon energy. This effect adds uncertainty on the reconstructed deposited energy, and so in the Compton angle calculation. Given its direct dependence on the recoil electron binding energy, the “Doppler spread” is reduced for low Z materials. For a given material, the effect is larger for higher scattering angles and it decreases with increasing energy of the incident photon. Following the described theoretical considerations, silicon detectors are the most coherent choice. This choice has been verified in simulation, where a silicon scatterer has been compared to competitor materials; the results are included in the Monte Carlo study presented in chapter 5.

Dedicated Monte Carlo simulation studies have been performed in order to define the most suitable geometrical configuration for the Compton camera, including the scatterer stack (Richard 2012). As a trade-off between detection efficiency and total cost, 10 layers were included in the original scatterer design. Concerning the layer size, about $10 \times 10 \text{ cm}^2$ of active area in the transverse plane have been identified as the most convenient choice, also considering the absorber size (see section 3.1.3) and the distances between the detection sections required by the TOF measurements and imposed by the detector rate acceptance in clinical conditions (see appendix A). Moving to the layer thickness, its choice is governed by the definition of the camera operation. The CLaRyS Compton camera does not aim to track the Compton recoil electron, which must be then absorbed inside the same scatterer layer where the Compton interaction took place. This requirement is necessary to well reconstruct the Compton interaction angle, which needs the whole transferred energy as parameter; in addition to this, a recoil electron escaping the involved detection layer can interact in a different layer causing false coincidences which affect the camera efficiency and imaging accuracy. In order to minimize the recoil electron escape probability, relatively thick detectors are needed.

The technological choice of the collaboration was oriented to silicon Double-sided Silicon Strip Detectors (DSSDs), provided by the Norwegian company SINTEF. A schematic view of the detector principle is given in Figure 3.2a. The silicon crystal is doped with negative (n) and positive (p) charge carriers on the two opposite sides, creating diodes which are then reverse biased. A polarization voltage is applied to the two opposite sides of the crystal, and a depletion region with no free charges is created. An ionizing particle interacting in the depletion region generates electron-hole pairs in number proportional to the deposited energy. The generated charges drift towards anode (electrons) and cathode (holes) and are converted into electrical signals. The read-out is ensured by the implanted strips, which transfer the charges outside the detection region.

Each layer has an active volume of $96 \times 96 \times 2 \text{ mm}^3$, segmented with 64 strips per detection

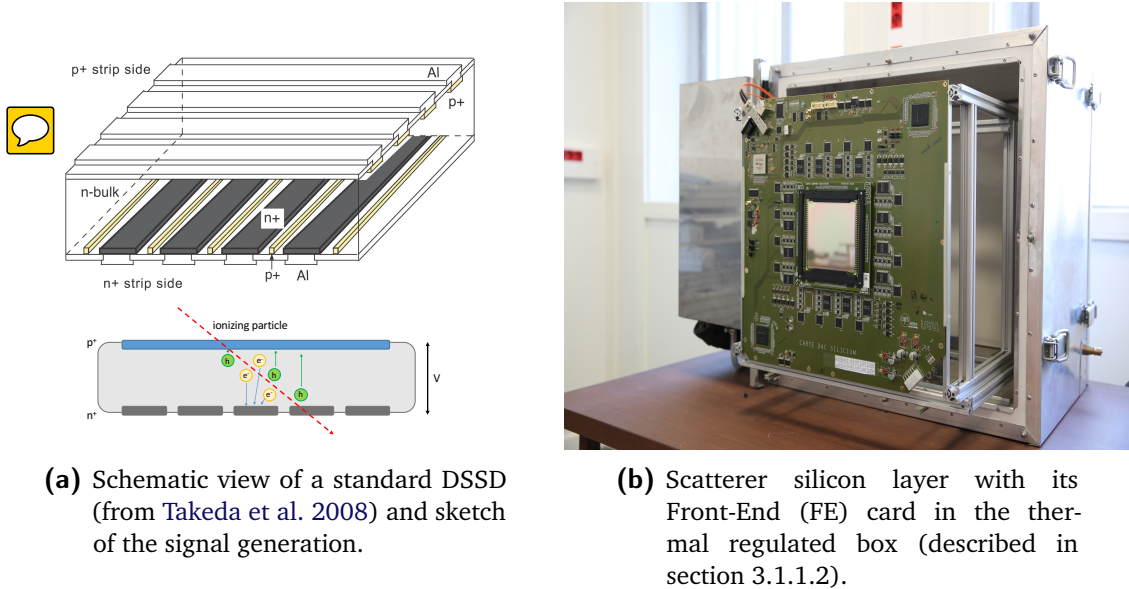


Figure 3.2: Overview of the scatterer layers, with its working principle (a) and a picture of the detector connected to the Front-End (FE) card in the thermal regulated box (b).

plane. The strip pitch is 1⁴¹ mm, for a strip width of 1.31 mm. The applied polarization voltage is nominally -750 and it is uniformly shared the whole surface to obtain a homogeneous depletion region. A guard ring, composed of 2¹ strips surrounding the read-out ones on the p side, ensures the desired voltage gradient The more peripheral strip of the guard ring on the p side is connected to the high voltage while the n side has a single strip for the guard ring in peripheral position and connected to the ground. The p and n read-out strips are then connected to the Front-End (FE) electronics via bonding cables.

The FE electronics card has been developed by the Institut de Physique Nucléaire de Lyon, France (IPNL) electronics group and is described in details in section 3.1.1.1. The silicon detector is directly plugged on the card, and the mechanical support for the scatterer stack has been studied according to the card size, as shown in Figure 3.2b.

Among the 10 received DSSDs, only 7 fulfilled the requirements imposed by the Compton camera application, mainly in terms of noise level (leakage current); 3 layer have been rejected, so that the final prototype scatterer is composed of 7 silicon planes.

The 7 selected layers have been characterized with a temporary acquisition system in terms of leakage current at different temperatures. The results of these measurements can be found in [Lev 2015](#). The measurements allowed to verify the producer specifications in terms of polarization voltage to be applied for a complete detector depletion, as well as to identify the noisy strips and create a complete characterization database. In addition to this, they highlighted the need to cool the detectors down with respect to the room temperature (25°C) in order to reduce the leakage current to acceptable levels, and so reducing the total noise level, affecting the detector performance In order to accomplish the cooling task and respect, at the same time, the clinical restriction a thermal regulated box based on cold air pump has been designed and produced. It operates as the scatterer stack mechanical support, and it is described in section 3.1.1.2.

3.1.1.1 Scatterer Front-End card

As mentioned in the previous paragraph, the main requirement for the scatterer detector modules is a very good energy resolution. The desired working performance can be quantified as follows:

- 1 keV Full Width at Half Maximum (FWHM) energy resolution;
- 1.41 mm spatial resolution (corresponding to the strip pitch);
- 15 ns FWHM time resolution.

The scatterer FE card has been developed by the IPNL electronics group in order to achieve this performance. It is composed of two well separated sections, analog and digital, which must be kept separated in the card layout in order to minimize the contribution of the digital noise on the treatment of the analog signals. Moreover, in order to reduce the electronic noise, the analog section must be placed as close as possible to the detector, to minimize the signal path length.

At first, a dedicated Application-Specific Integrated Circuit (ASIC) has been designed and developed to treat the signals directly coming from the DSSD ([Dahoumane et al. 2014](#)). Each ASIC processes 8 detectors channels, so that 8 ASIC per plane are required for the read-out of a complete silicon layer. This section represents the core of the analog stage. The ASIC has been designed and tested to achieve the desired performance in terms of Equivalent Noise Charge (ENC), which must be lower than 118 electrons Root Mean Square (RMS) in order to obtain the 1 keV FWHM energy resolution, signal dynamics and accepted detection rate. The analog raw signal first passes through a Charge Sensitive Amplifier (CSA), which returns an analog amplified signal. This pulse can be further amplified with a Slow Shaper (SHS) based on a Capacitor Resistor - Resistor Capacitor (CR-RC) filter, which filters and shapes the signal in about 1 μ s, or via a fast amplifier (with 15 ns shaping time). The first mode is used for a refined charge (deposited energy) measurement and can be employed for detector tests and characterization, while the second is the standard working one which allows for fast energy and time measurements. The amplified signal finally passes through a discriminator, which gives a digital output. Analog (from CSA or SHS) and digital signals are then sent to the digital stage of the card for the measurement of time, position and energy.

The digital stage is mainly composed of one Analog-to-Digital Converter (ADC) module per ASIC and two Field Programmable Gate Arrays (FPGAs). The analog signal from the ASIC is processed by the ADC, which is a 12-bit module with 8 channels, with a sampling rate of 100 Mega Sample Per Second (Msps). Each ADC returns 16 Low-Voltage Differential Signaling (LVDS) pairs (2 per channel), which are sent to the FPGAs together with two clock signals (two LVDS pairs) and the 8 digital outputs of the ASIC. So, 44 input channels of the FPGA are used for the acquisition of 8 read-out channels (one ASIC). Two FPGAs Altera Cyclone III ([Altera 2012](#)) are installed on the card to handle the signals coming from the whole detector (128 channels, 64 per detection plane): both of them are equipped with a Time-to-Digital Converter (TDC) for the time measurement.

A third FPGA (Altera StratixII GX ([Altera 2009](#))) is finally installed on the card to handle the

processed data collection and the communication with the acquisition system, described in section 3.1.5, via a 3 Gbit/s link.

The ASIC has been developed in three versions, and the cards have been optimized during the development process and produced in its final version (shown in Figure 3.3a) in the  Spring 2017. The 7 cards are now available and the development of the FPGA firmware is ongoing.

More details about the card layout, components and operating principle, as well as a description of the tests performed during the development can be found in [Chen 2017](#) and [Dahoumane et al. 2012](#).

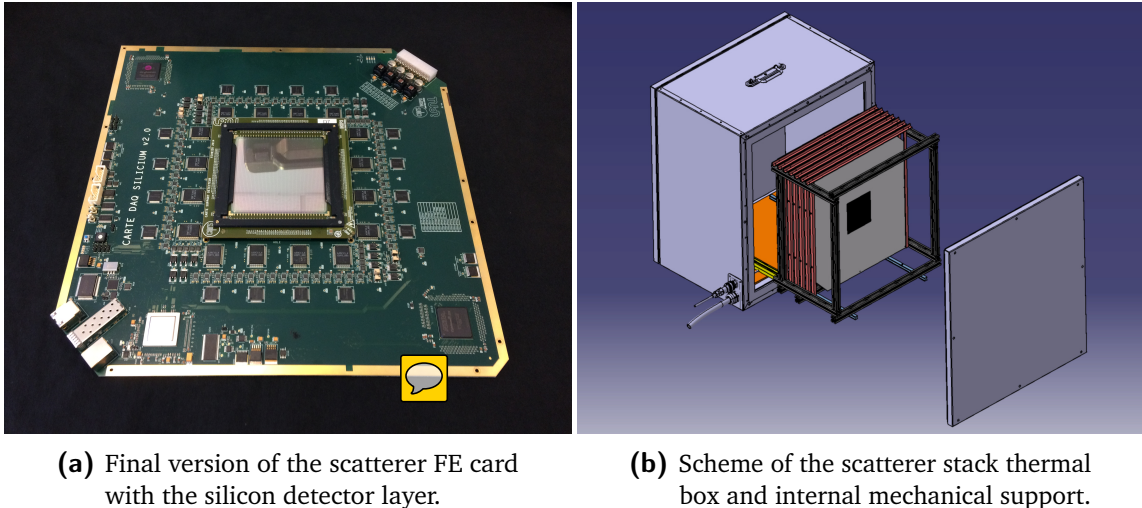
3.1.1.2 Scatterer thermal regulated box

The results of the leakage current tests performed on the silicon detectors showed the need of cooling the detector down to achieve the required performance in terms of noise, which affects the spatial, time and energy resolutions. The leakage current has been studied in temperature cycles in the range -40 - +40 °C, and an overall consistent behavior has been observed both on N and P strips of the detector. The leakage current slightly increases in the range -40 - 0 °C, with values in the range 0 - 8 nA for the analyzed strips, and then drastically increases beyond 0 °C, with peaks of more than 80 nA at +40 °C. The complete description of the performed measurements and the detailed results can be found in [Ley 2015](#).

A cooling system is needed for the silicon detectors operations: it must be able to keep the temperature constant and below, at least, 0 °C, preferably around -20 °C where the leakage current is more stable in case of small temperature variations. The clinical environment limitations must be considered to design such a cooling system (portability, gas, noise level), as well as the material budget and the mechanical integration with the other camera components.

The implemented solution consists in the thermal regulated box shown in Figure 3.2b, together with one of the silicon layers. The size of the box is $490 \times 490 \times 300$ mm³, and the structure is composed of 2 mm of aluminum and three insulation layers of 10 mm of silica aerogel Spaceloft® ([Aspen Aerogels 2011](#)), for an equivalent thickness of 2 mm of silicon (0.7% of interaction probability for 1 MeV photons). The cooling is performed via an electric air pump, which is able to keep the temperature inside the box at -20 °C with a 400 W heat evacuation power. The heat power produced by the 7 silicon FE cards in operation must be verified, but the estimate confirms the effectiveness of the thermal box nominal performance. Once card and detector will be fully operational, a test will be performed to check the temperature stability inside the box 

The FE cards and the silicon layers are fixed inside the box via a mechanical support designed and produced by the IPNL mechanics group. The support, which ensures a millimeter position accuracy, is fixed on metal rails which allow to easily handle each detector layer. A scheme of the thermal box and the internal support is shown in Figure 3.3b.



(a) Final version of the scatterer FE card with the silicon detector layer.

(b) Scheme of the scatterer stack thermal box and internal mechanical support.

Figure 3.3: Scatterer silicon layers equipment: final version of the FE card (a) and scheme of the detector integration in the thermal regulated box (b).

3.1.2 Collimator

The multi-collimated camera is equipped with a multi-slit collimator, with tungsten slabs of $1.5 \times 120 \times 170 \text{ mm}^3$. Its design has been extensively studied in Monte Carlo simulations (Pinto et al. 2014), and it can be easily adapted to different geometrical configurations of the absorber detector and to various monitoring requirements. In particular, the distance between neighboring slabs can be modified, as well as the number of total slabs, in order to find the best trade-off between detection efficiency and spatial resolution; this depends on the distance patient-collimator, on the required extension of the field of view and on the desired monitoring time. Two identical collimators of $30 \times 14 \times 17 \text{ cm}^3$ have been produced, in order to be able to set several absorber configurations in the transverse direction (extended version along the beam axis or in the perpendicular direction). In Figure 3.4a a picture of the tungsten collimator is presented, while in Figure 3.4b we show a schematic view of a possible multi-collimated camera configuration.

3.1.3 Absorber

The Compton and multi-collimated camera absorber was initially conceived as a very large surface plane composed of 96 BGO blocks recovered from a dismantled PET system HR+ by SIEMENS, documented in (Adam et al. 1997; Brix et al. 1997).

BGO is one of the most used scintillators for gamma detection applications, thanks to a fair energy resolution and an optimal gamma detection efficiency, given the high effective atomic number (75) and high density (7.12 g/cm^3) (Elftmann et al. 2015) which maximize the photo-electric effect. Moreover, the absence of internal radioactivity which characterizes other scintillator materials employed in the same field (i.e. Lutetium-Yttrium Oxyorthosilicate - $\text{Lu}_{2(1-x)}\text{Y}_{2x}\text{SiO}_5$ (LYSO), Cerium-doped Lutetium Oxyorthosilicate - $\text{Lu}_{2(1-x)}\text{Ce}_{2x}\text{SiO}_4$ (LSO)), makes it suitable for low noise detectors, required by a Compton camera to reduce the amount of random coincidences, one of the main sources of background for the application in ion beam

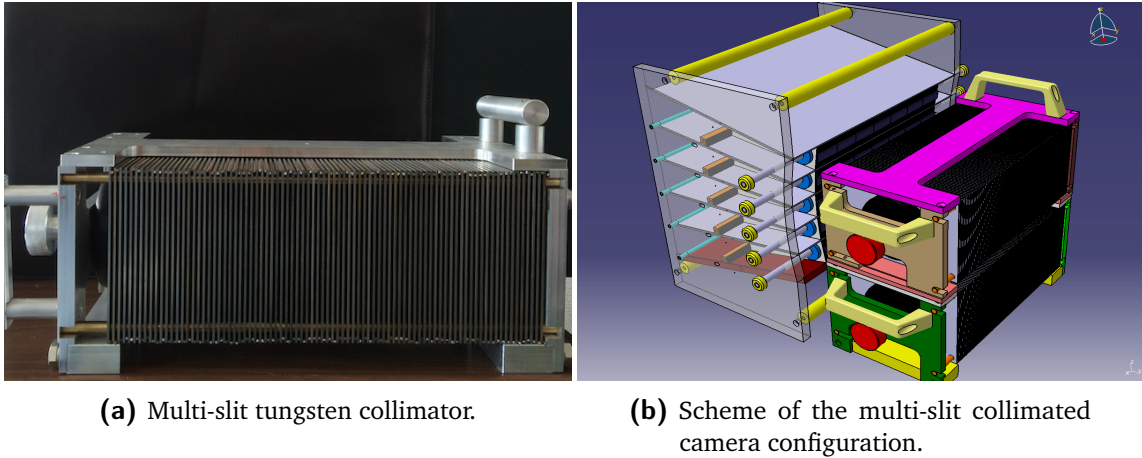


Figure 3.4: Tungsten collimator and its setup in the multi-slit collimated camera. Two identical collimators are available, with $1.5 \times 120 \times 170 \text{ mm}^3$ tungsten slabs and a pitch of 8 mm. The two tungsten multi-slit collimators are placed in front of a 6×5 Bismuth Germanium Oxide - $\text{Bi}_{12}\text{GeO}_{20}$ (BGO) block absorber setup in its mechanical support (see section 3.1.3). Both the single collimator setup (size and pitch) and the two collimators configuration can be easily modified to adapt the system to peculiar applications.

therapy monitoring (Ortega et al. 2015). As highlighted in (Hueso-González et al. 2015), LYSO and LSO show overall better performances with respect to BGO for what concerns energy, time and spatial resolution, due to an about 4 times higher light yield, but the gap is reduced for the detection of gamma rays in the prompt-gamma energy range (especially beyond 1 MeV). The limited cost of BGO with respect to LSO and the comparable performances in the prompt-gamma energy range make it an optimal solution for prompt-gamma camera prototypes.

Each BGO block composing the gamma camera absorber has a surface of $3.5 \times 3.8 \text{ cm}^2$, with a thickness of 3.0 cm. The mono-block BGO crystal is streaked in a 8×8 pseudo-pixel matrix; a reflecting material is inserted between the pseudo-pixels to improve the light collection and optimize the spatial information accuracy via pixel separation. The read-out is achieved via four Photo-Multiplier (PM) tubes per block, composing a quartet, coupled to the block back surface. Thanks to the internal streaked structure of the block, the scintillation light is shared among the four PMs depending on the pseudo-pixel where the interaction takes place (in case of multiple interactions more than one pseudo-pixel can be involved). The streaks have a different thickness according to their position in the block: they fully cover the block thickness on the block borders and they progressively shorten towards the block center, with a mono-block structure in the central block section on the entrance face. The reconstruction of the position of interaction is done via Anger logic, i.e. with a center of gravity calculation.

The whole set of recovered blocks was supposed to undergo a “reconditioning” process, including the PM removal, the crystal back surface polishing with diamond-based abrasive tool, the single PMs gain characterization and grouping in quartets with similar gains, the final re-coupling of the PMs and block shielding.

A set of “reconditioned” blocks have been tested with the method described in section 3.2 and their performance have been compared to a set of original blocks. An overall degradation of the detection performance has been verified on all the tested “reconditioned” blocks, which

showed lower amplitude output signals probably link to a reduction of the collected scintillation light. Various correction methods have been tested, with unsatisfactory results. According to the outcome of these tests, summarized in [Sandjong et al. 2017](#), the collaboration finally opted to adapt the camera design for the use of original, “non-reconditioned” BGO blocks.

Thirty original blocks are now available to compose the absorber  detector. In addition to the already presented features, it must be noticed that the lateral surfaces of the original blocks, as well as the half of the PM length, are covered with a reflecting material which ensures the complete collection of the scintillation light. This is probably a component which was not well reproduced during the reconditioning process. The whole structure is then protected by a 1 mm thick aluminum foil, which also isolates from external light contamination.

Figure 3.5a shows one BGO block before the coupling to the PM quartet: the streaked structure is clearly visible, as well as the white reflecting material separating the pseudo-pixels and the one surrounding the block lateral sides. As mentioned, the same material also covers part of the photo-multiplier tubes, as shown in picture 3.5b, where the four PMs are glued to the block back surface. The described aluminum cover is visible in Figure 3.5c, while in Figure 3.5d a scheme of a block together with the related PM quartet is given. The spatial reconstruction logic is also reported in the same figure.

3.1.3.1 Absorber Front-End and read-out cards

General design

A custom front-end card has been designed and produced by the LPC research group Application et Valorisation des Interactions Rayonnements-Matière (AVIRM) and is used for the read-out of each BGO block. The card is equipped with four voltage modulators which divide the provided high voltage on the four PM tubes. The voltage sent to each PM can be tuned via screw-potentiometers on these modules. A ± 5 V low voltage is applied to the cards as supply for the differential amplifier modules, one per PM. Differential output channels are used to send the PM signals to the read-out card, called Analog Sampling Module (ASM) board, via flat cables. A picture of the FE card is given in Figure 3.6a. To be noticed that four analog output channels  has been added on some cards in order to allow laboratory tests with a signal treatment based on standard electronics modules, as described in section 3.2. These outputs retrieve the signal before the differential amplification stage, so that the low voltage supply is not needed for this read-out configuration.

The PM signals amplified by the FE card (differential outputs) are received by the ASM boards. Developed by the LPC AVIRM group, it is based on the VERSABUS Module Eurocard (VME) standard and designed for the application in the DPGA PET system, equipped with LYSO monocrystals, grouped in quartets and read-out by the same FE card described above. The adaptation to the gamma camera application, so that for the BGO modules signal treatment, involves only the firmware part. Each board has 24 differential inputs and it is so able to read the signals from 6 BGO blocks; a total of 5 boards are then needed for the complete read-out of the gamma camera absorber (30 blocks). The incoming signals are treated by three intermediate cards equipped with a Domino Ring Sampler (DRS)4 chip ([Ritt 2009](#)), designed and developed at the Paul Scherrer Institut, Villigen, Switzerland (PSI), with  8 sampling channels at a maximum frequency of 5 Giga Sample Per Second (Gsp/s) (200 ps for 1024 samples, and an

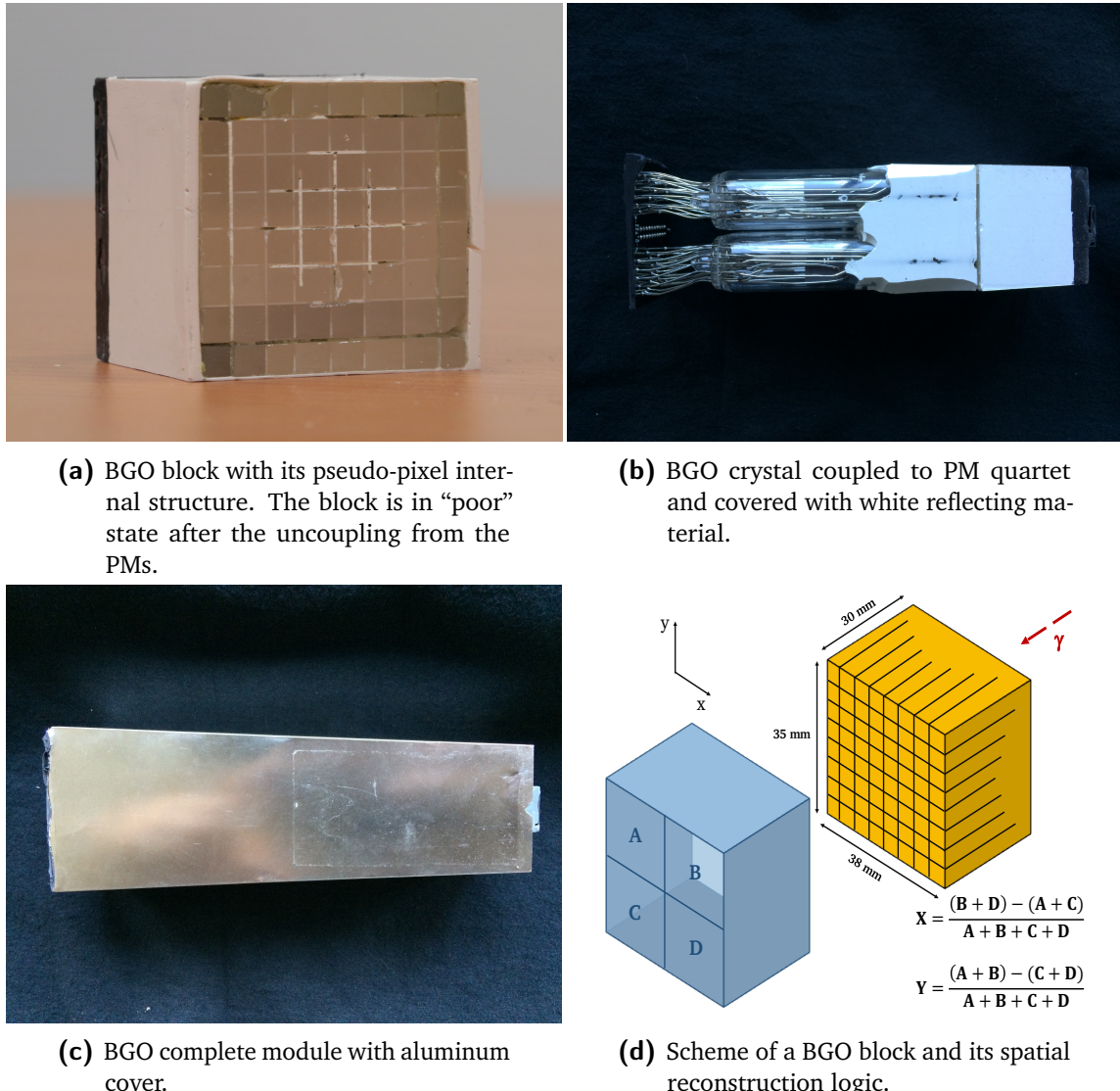
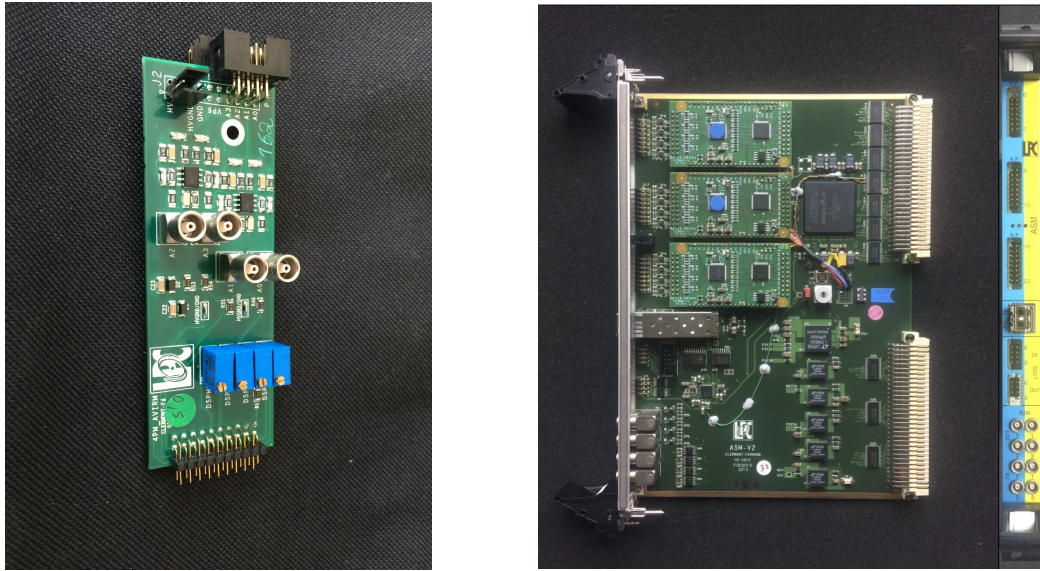


Figure 3.5: Components of an absorber module and its working principle.



(a) FE card of the absorber BGO detectors.
4 analog outputs have been added for test purpose.

(b) ASM board of the absorber BGO detectors. Each board performs the read-out of 6 blocks.

Figure 3.6: Absorber read-out electronics: FE card (a) and ASM board (b).

ADC 12 bit-20 MHz module. The sampling frequency of the DRS4 can be modified to fit with the specific application: in particular, the BGO blocks produce wider signals with respect to the LYSO crystals of the DPG4. The Altera Cyclone IV GX (Altera 2015) receives and handles the digital outputs of the three intermediate cards and is in charge of sending the data to the acquisition system via a 3 Gbit/s optical link. The FPGA also governs the generation of the pre-trigger signal which is sent to an auxiliary board called Trigger et HORloge (THOR) in order to start the acquisition of the gamma cameras, as detailed in section 3.1.5.

Absorber acquisition with development card

During the development of the final camera acquisition system based on the Micro Advanced Telecommunications Computing Architecture (μ -TCA) equipment, which required a dedicated firmware development and testing process, a temporary acquisition system has been set for the absorber BGO blocks, mainly dedicated to the test and characterization of the ASM boards. It is based on a development commercial electronics card, provided by Terasic (Altera University Program), equipped with an FPGA Altera Cyclone V (Terasic 2015). The card can be programmed for the needed tasks, and it is directly connected to an acquisition PC via Ethernet cable. Three High-Speed Mezzanine Card (HSMC) connectors allow for the connection to an expansion board SFP-HSMC (Terasic 2009), again by Terasic (Altera University Program), provided with a second FPGA and with optical fiber input/output connectors for the interface to the ASM boards. A single optical input is configured for this acquisition setup, with the firmware developed by the AVIRM group in LPC and adapted at the IPNL; one single ASM card can be connected to the board, so that a maximum of 6 BGO blocks can be read-out at the same time. A picture of the development card connected to the mezzanine is given in Figure 3.7a. Figure 3.7b shows an example of the user interface and data visualization of the C++ based acquisition software developed and provided by the AVIRM group.

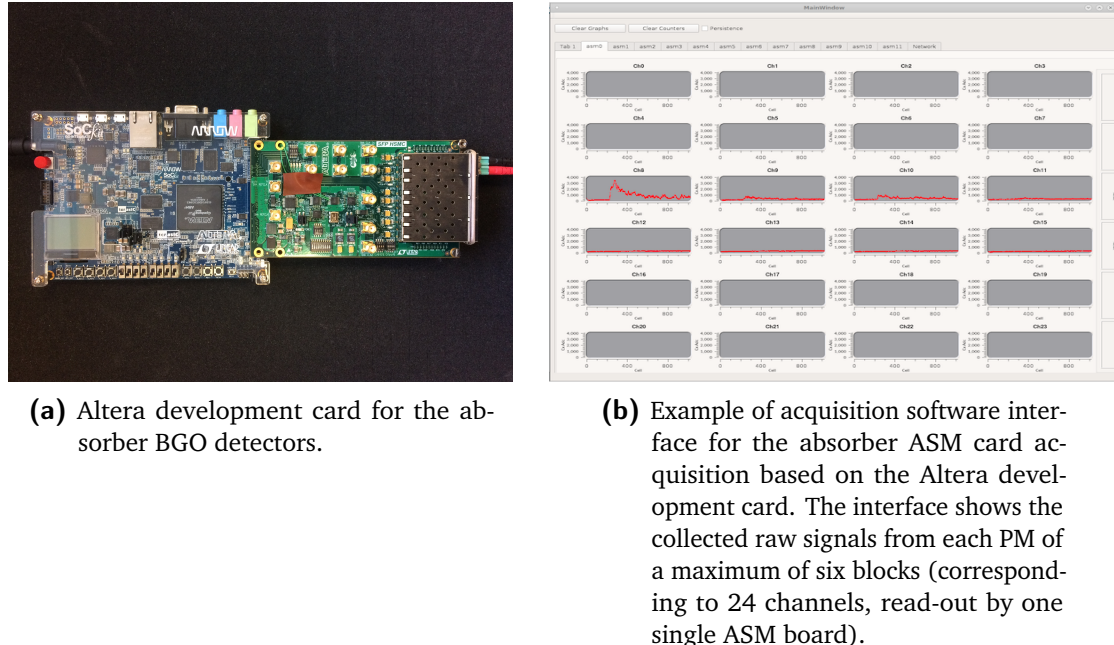


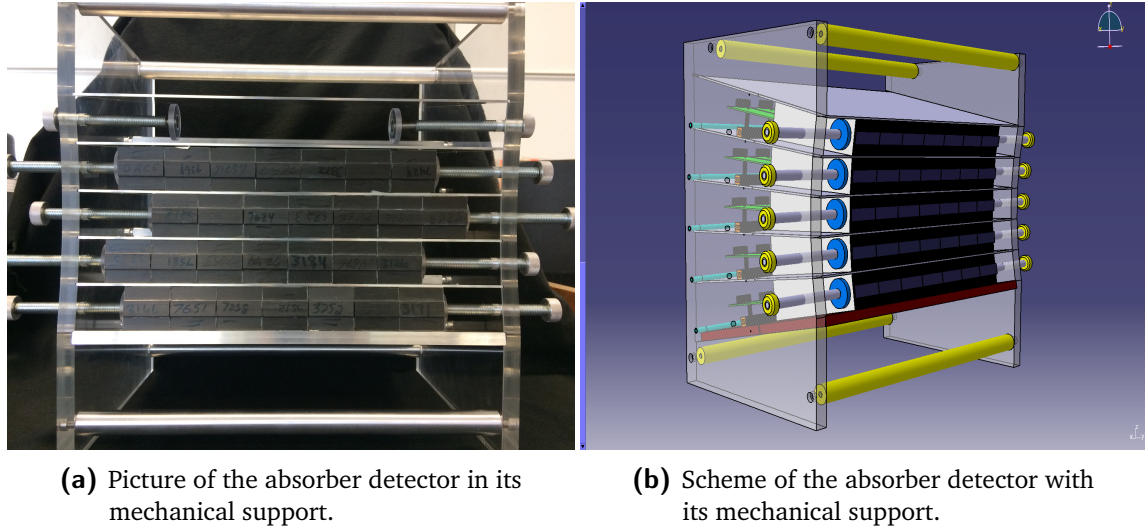
Figure 3.7: Details of the temporary absorber acquisition based on the Altera development card.

3.1.3.2 Absorber mechanical support

A first mechanical structure for the absorber detector was initially conceived by the LPC group in order to hold up to 100 modules, foreseen by the original camera design. The reduction of the number of available blocks caused by the “reconditioning” process failure made it necessary an adaptation of such a support. The new design has been carried out by the mechanics group of the IPNL in order to be compact and flexible in terms of detection modules setup. Figure 3.8 displays both a picture and a scheme of the absorber configuration with its mechanical support. The two lateral sides are built with Poly Methyl Metacrylate (PMMA) boards connected by metal bars, and the BGO blocks can be arranged in up to 5 rows of variable size, ranging from 3 to 7 blocks. Each block row is supported by a thin metal foil, designed to reduce at minimum the blocks separation and to respect the original ring geometry deriving from the SIEMENS PET system. The blocks composing a row are then laterally pressed via two screws on the two sides of the structure, which can also be used to adapt the rows relative position horizontally. On the back side, a metal bar is added to avoid undesired movements, and the FE cards are fixed with plastic pillars. The realized support results to be versatile, compact and adapted to the prototype tests for both the Compton camera (where a squared setup is preferred) and the multi-collimated one (where the collimator geometry must be fit by the absorber geometrical configuration).

3.1.4 Beam tagging hodoscope

A beam tagging hodoscope is being developed in parallel to the two gamma cameras, mainly for background rejection and reconstruction optimization purposes. As already mentioned, the detection of prompt-gammas (with mechanical or “electronic” collimation), is affected by the presence of other secondary particles produced during the ion beam irradiation, mainly



(a) Picture of the absorber detector in its mechanical support.

(b) Scheme of the absorber detector with its mechanical support.

Figure 3.8: Absorber front view with the BGO block lines arranged in the mechanical support (a). Scheme of the BGO absorber with its mechanical support (b).

neutrons. This background source can be efficiently identified and removed applying TOF selection windows to the data acquisition. The TOF measurements can be performed using the accelerator radio-frequency signal as reference for cyclotron accelerators, while a direct beam detection results to be more accurate for synchrotron based treatments. An auxiliary detector is then needed before the beam interaction in the patient.

The CLaRyS hodoscope prototype is designed to provide space and time information about the incoming primary beam, particle by particle or bunch by bunch, depending on the beam intensity and detector efficiency and rate acceptance which must be characterized. In addition to the already explained use of the time information, a space primary particle tagging can be used to improve the reconstruction accuracy and constraint the possible reconstructed emission vertex in case of analytic reconstruction approach for both the multi-collimated and Compton cameras (see chapter 2).

The detector under development is based on squared 1 mm^2 polystyrene scintillating fibers BCF-12, 140 mm in length, provided by Saint Gobain ([Saint Gobain 2017](#)). A picture of the hodoscope on its mechanical support (detailed in the following) is presented in Figure 3.9. The fibers are arranged into two perpendicular planes for a two-dimensional spatial information: each plane is composed of 128 fibers, for a total active area (for 2D measurements in coincidence) of $128 \times 128 \text{ mm}^2$. The active detector surface is completely covered with black tape, which shields from external light. The scintillation light produced in the fibers by an ionizing particle depositing energy is transported to the read-out system via FORETEC optical fibers (1.55 cm diameter, 1 m length), which are connected to the scintillating fibers thanks to a custom mechanical support and to a proper gluing process (see Figure 3.10a). Each scintillating fiber is read-out on both sides to optimize the detector efficiency and to improve the time resolution, which does not depend on the interaction position along the fiber with this configuration; the total number of read-out channels is then 512. The signal read-out is ensured by 8 multi-anode PMs Hamamatsu H8500 ([Hamamatsu 2006](#)) shown in Figure 3.10c. The optical fibers are connected to the PM anode surfaces through a plastic custom mask, shown in Figure 3.10d. The PMs are equipped with custom black boxes which operate as mechani-

cal support and external light protection (see Figure 3.10a). In order to provide further light isolation, the whole PM boxes are covered with black tape.

The optical fibers are connected to the 8 PMs with a logic aiming to increase the maximum counting rate. 4 PMs are dedicated to the read-out of the horizontal fibers, and 4 to the vertical ones, and the neighboring fibers are connected to different PMs. An active area of $4 \times 4 \text{ mm}^2$ on the two planes is then read-out by all the 8 PMs. Moreover, the two sides of the same scintillating fiber are connected on the same PM. This fiber connection logic also improves the detector robustness; in case of problem on one PM, only 1 mm each 4 mm is lost on a single plane, so that the detection of the beam is still possible on the whole active area.

Each PM is connected to a single custom FE card. The hodoscope FE cards have been developed by the IPNL electronics group: their design is described in section 3.1.4.1. 8 FE cards are then used for the read-out, and the collected data are sent to the acquisition system described in section 3.1.5.

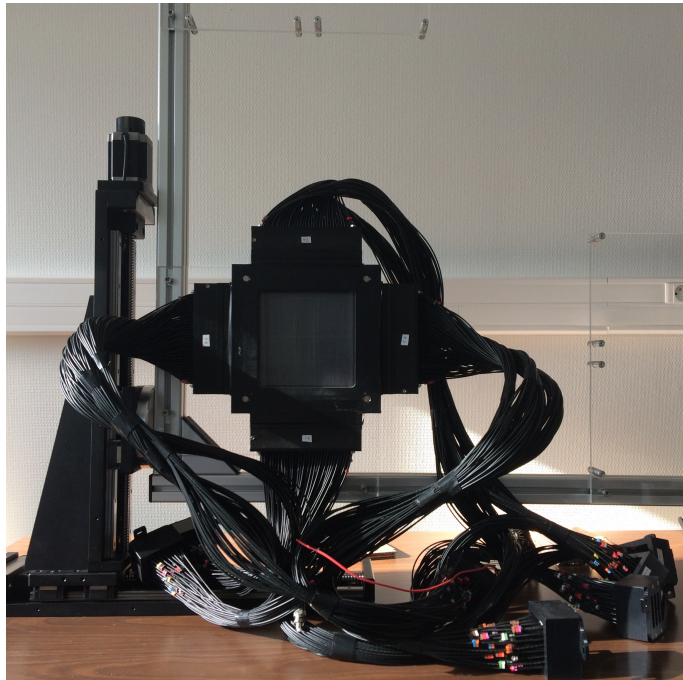


Figure 3.9: 128×128 scintillating fiber hodoscope on its 2-dimensional moving support.



3.1.4.1 Hodoscope Front-End card

The hodoscope is designed to tag in space and time the incoming beam ions, so that the signal read-out must be optimized to provide accurate time measurements and a high detection rate acceptance, with reduced dead time and detection efficiency close to 100%. In particular, the design requirements include a maximum counting rate acceptance of 10^8 Hz per detection plane, with a time resolution of 1 ns (Krimmer et al. 2014). The hodoscope FE card shown in Figure 3.11a has been developed by the IPNL electronics group to fulfill the listed requirements. The Hamamatsu PM is connected to the 64-channel connector (4 connectors of 16 channels each) and two custom ASICs are dedicated to the data first treatment (32 channels each).

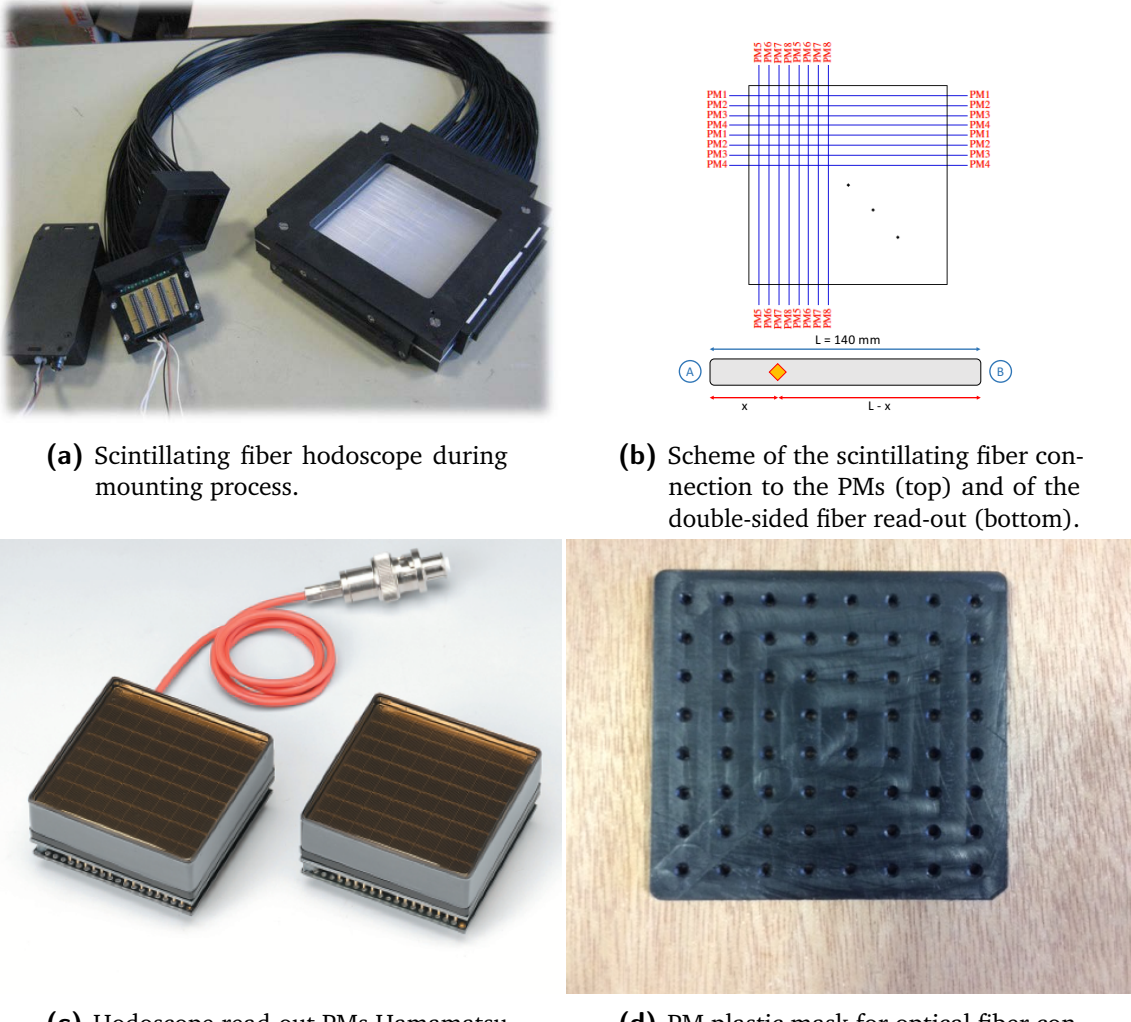


Figure 3.10: Details of the scintillating fiber hodoscope setup.

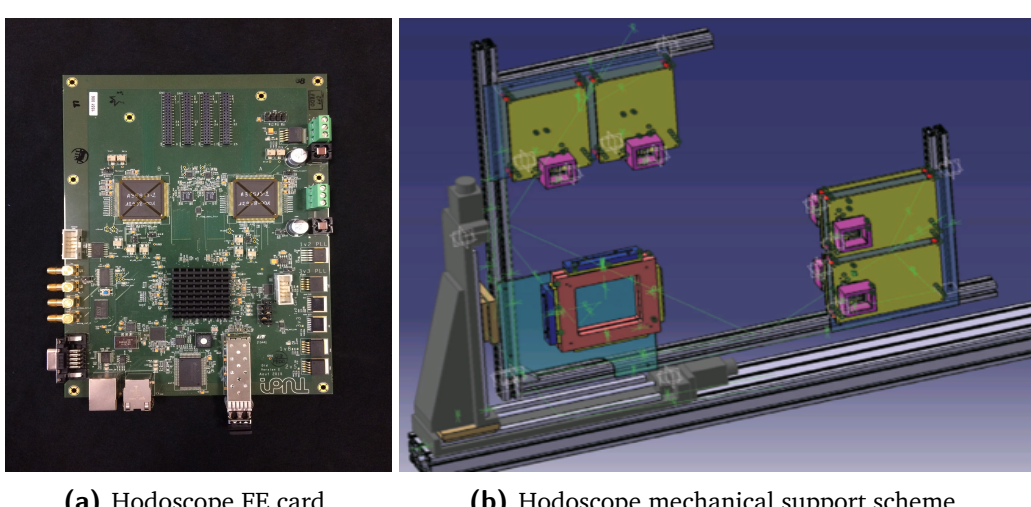


Figure 3.11: HODOPIC board (a) and scheme of the beam-tagging hodoscope two-dimensional moving sup (b).

A first version of the FE ASIC has been developed in 2012 by the group Micro-électronique RHône AUvergne (MICRHAU) for the read-out of 8 channels (designed for the 32×32 fiber hodoscope prototype described in section 3.1.4.3). The input part is composed of a current conveyor, and the output one has two sections: a current discriminator and a charge pre-amplifier for the charge measurements in test mode (Deng et al. 2012, 2013). In addition, the ASIC gain can be tuned channel by channel, so that the response of each PM output channel can be fine tuned with respect to the others.

The second version of the ASIC includes all the features of the first version, with the addition of a TDC based on a 160 MHz clock for a more accurate time tagging of the detected events. Moreover, a Delay Locked Loop (DLL) is installed to divide the main clock in 32 intervals: for each event, the DLL state is stored in a 32 bit register and then encoded in a 5-bit Gray decoder. As a result, the TDC has a 6.25 ns dynamics, with a sampling step of 195 ps and a time resolution of 58.8 ps RMS, for a maximum accepted rate of 10^8 Hz (Deng 2012).

The third and final ASIC version, called HODOPIC, is adapted to the big size hodoscope (512 read-out channels), with the extension to 32 channels and with the TDC implemented on the second version. An external ADC is used for the charge measurement in test mode for a single channel, selected via slow control. All the ASIC outputs are sent to a FPGA installed on the card for the actual time measurement and data decoding. The FPGA finally handles the data transmission to the acquisition system, depending on the card version.

A first card has been developed to test the first ASIC version with the 32×32 fiber hodoscope. It is based on a FPGA Altera Cyclone III (Altera 2012) and on 9 ASICs, with a LabVIEW acquisition. A single card is enough for the read-out of the complete small hodoscope prototype. This first setup has been tested on beam at Grand Accelerateur National d'Ions Lourds, Caen, France (GANIL) and Heidelberg Ion Therapy Center, Germany (HIT), and a sub-ns time resolution has been verified, together with the expected 1 mm spatial resolution on the two fiber planes and an efficiency of more than 90% at a 10^6 acquisition rate.

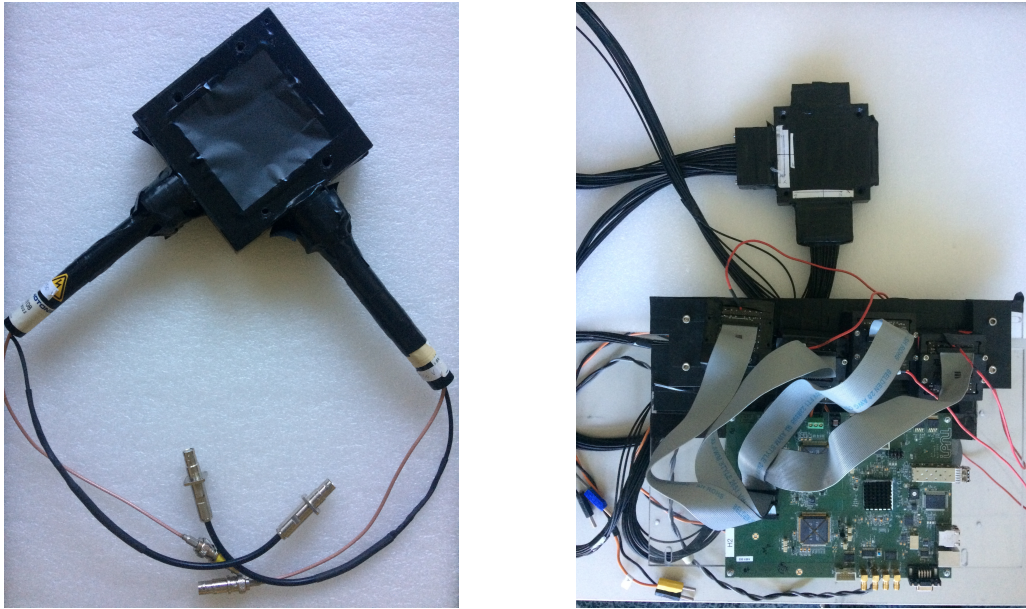
The second prototype of the card, shown in Figure 3.11a, has been adapted to the 512-channel hodoscope described in the previous section and to the gamma camera acquisition system described in 3.1.5: each card has two HODOPIC ASICs, 32 channels each, so that it is designed for the read-out of a single 64-anode PM. 8 cards are then needed for the read-out of the whole hodoscope. This version is based on a FPGA Altera StratixII GX (Altera 2009), and the connection to the acquisition is ensured by a 3 Gbit/s optical link. 4 digital input-output channels are installed for test and validation purpose, together with an Ethernet port.

Further details about the different card versions and the applied validation tests can be found in Chen 2017.

The hodoscope card firmware has been developed in 2017 and tested in simplified versions on beam, as detailed in chapter 6.

3.1.4.2 Hodoscope mechanical support

The beam tagging hodoscope is set between the beam nozzle and the patient and requires a dedicated mechanical support. In order to profit of the large active area and to be able to



(a) Hodoscope small prototype, 1×1 scintillating fibers.

(b) Hodoscope small prototype, 32×32 scintillating fibers, connected to the HODOPIC FE board.

Figure 3.12: Hodoscope small prototypes.

remotely control the hodoscope position in the beam transverse plane, the detector is mounted on a 2-dimensional moving table (see the picture in Figure 3.9), which also supports the FE cards. Detector and FE cards are then integral and translate together. A scheme of the moving table is given in Figure 3.11b.

The 2-axis table is provided by Beijing Winner Optical Instruments; it is composed of two motorized linear stages, connected via a right angle bracket. The two stages have a moving range of 30 cm each and the stepper motors have a step resolution of 20 μm . The employed motor controller is a Newport XPS-Q8 ([Newport 2017](#)), equipped with 8 channels for the simultaneous control of a maximum of 8 motors. The movements are steered with an online interface or with a LabVIEW-based program, which will be integrated in the final setup of the slow control software under development with the cameras.

3.1.4.3 Small hodoscope prototypes

Before the production of the large active surface hodoscope prototype described in section 3.1.4, two smaller prototypes have been produced and tested in order to assess the potential of such a kind of detector for the required application. The first and simplest version consisted of one single scintillating fiber per plane, and the readout was performed with two PM tubes directly coupled to the scintillating fibers, without optical fibers. A picture of this prototype is given in Figure 3.12a. This simple version of the detector has been used as a demonstrator of the basic detection principle.

A second small size version of the final detector has been produced with almost the same features as the large area prototype but with simplified read-out logic. It is equipped with

two perpendicular planes of 32 1 mm² scintillating fibers each (Saint Gobain BCF-10 ([Saint Gobain 2017](#))), with a length of 4 cm and a total active area for a 2D read-out of 32×32 mm². As in the big hodoscope, the scintillating fibers are coupled to FORETEC optical fibers which transfer the scintillation light to 4 Hamamatsu H8500 PMs. 16 channels per PM are used, so that 2 PMs are dedicated to the horizontal fibers and 2 to the vertical ones, and the signal read-out is performed on a single side of the scintillating fiber. The total number of read-out channels is 64, a single FE card is sufficient for the whole detector. In Figure 3.12b the 32×32-fiber hodoscope prototype is shown together with its FE card; 4 connection cables (16 channels each) are used to couple the PMs to the FE card.

The 32×32-fiber hodoscope prototype has been tested in 2014 on proton and carbon ion beams (at the GANIL - 75 MeV/u ¹³C, HIT - protons and carbon ions at various energy, Institut de Physique Nucléaire d'Orsay, France (IPNO) - 25 MeV protons) with the first version of the FE card (see section 3.1.4.1): an efficiency of more than 90% has been retrieved, with a time resolution of 1 ns FWHM (timing measurements performed with respect to the accelerator high frequency signal). Some more details about this beam tests results are given in chapter 6. The final version of the FE card has been also tested with this detector, and the test description and results are presented in chapter 6.

3.1.5 Camera acquisition system

The TOF gamma cameras developed by the CLaRyS collaboration are composed of various detection sections: beam tagging hodoscope and BGO absorber for the multi-slit collimated camera, with the addition of the silicon scatterer stack for the Compton camera. The acquisition system must be able to handle the data flux from the different components, for a total of 20 FE cards (7 for the silicon scatterer, 8 for the hodoscope and 5 for the absorber), select the events according to the chosen trigger logic and create and send the data packets with the right format to the acquisition PC.

The system is based on the μ-TCA standard; originally conceived as an adaptation of the Advanced Telecommunications Computing Architecture (ATCA) systems used in the telecommunication field for high-flux data transfers, it is employed for relatively simpler tasks and adopted in the particle physics domain since less than ten years ([Abellan et al. 2013](#); [Cachemiche et al. 2012](#)). A standard μ-TCA crate equipped with a μ-TCA Carrier HUB (MCH) (shown in Figure 3.13a) is used as general purpose support for the Advanced Mezzanine Card (AMC), which is the section adapted for each specific application. An AMC40 has been developed for high energy physics applications, in particular for the Large Hadron Collider beauty (LHCb) experiment at Conseil Européen pour la Recherche Nucléaire, Geneva, Switzerland (CERN), and has been adapted for the gamma camera acquisition system by the CPPM research group (see Figure 3.13b). This card includes a FPGA Altera Stratix V ([Altera 2016](#)), 24 optical inputs at 4.8 Gbit/s and 12 at 9.6 Gbit/s, a 1 Gbit/s Ethernet output for the connection to the acquisition PC. In addition to the μ-TCA based components, two intermediate cards in VME format complete the acquisition system. The so-called THOR cards (see Figure 3.13c), developed in VME format at LPC in parallel to the ASM card, are used to generate and share the clock signal (40 MHz) common to the whole electronics cards for synchronization purpose (first card) and to govern the pre-trigger and trigger signals (second card) as explained in the following lines.

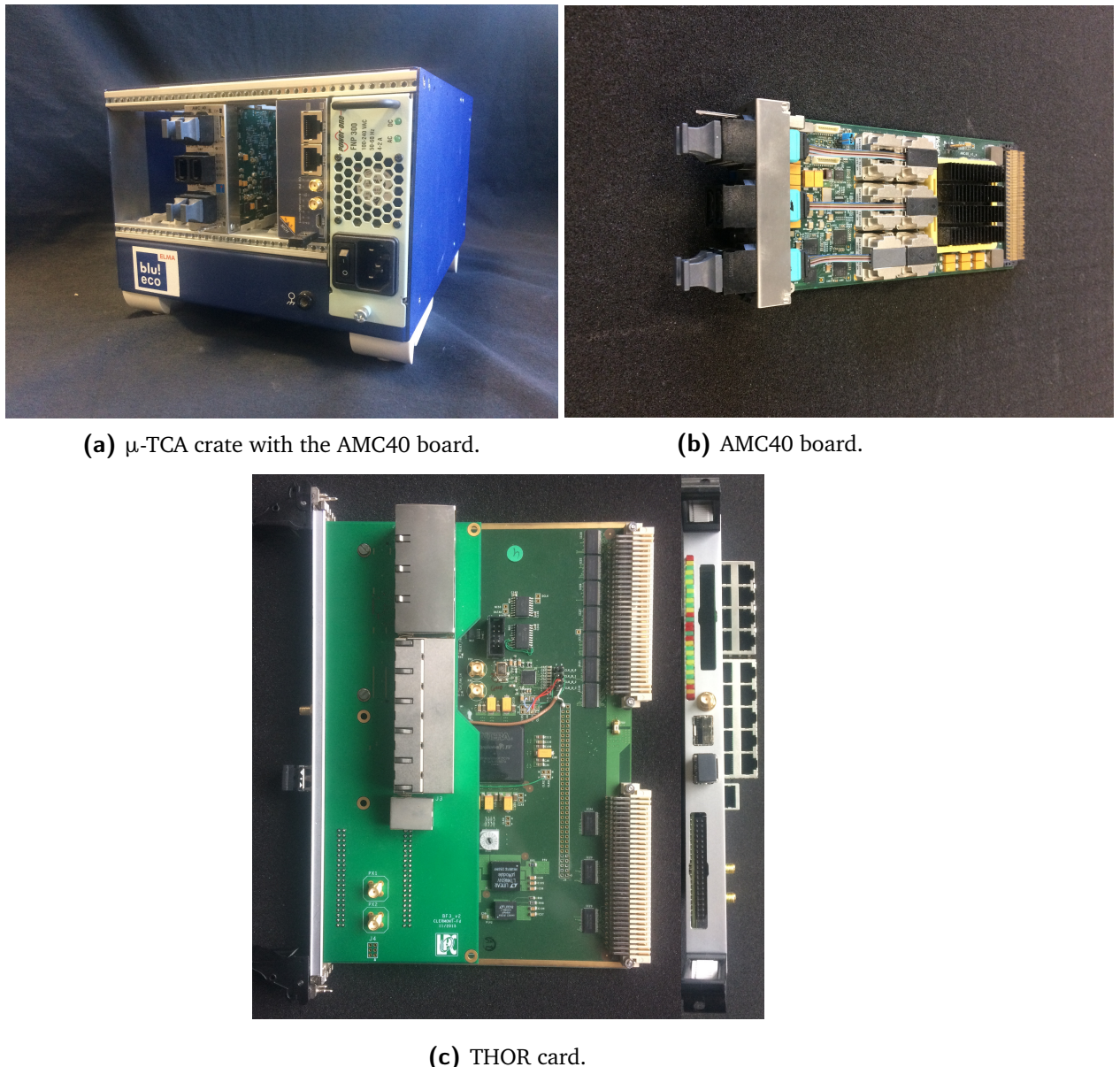


Figure 3.13: Acquisition system components: μ-TCA crate (a), AMC40 board (b) and THOR card (c).

For both cameras, the acquisition starts in case the absorber section detects an interaction: the ASM involved card deals with the creation of a pre-trigger signal, which corresponds to the digital output signal and contains a time stamp (see the ASM card description in section 3.1.3.1). The pre-trigger is sent to the THOR card which governs its sending to the AMC40 card. To be noticed that the ASM card should be in principle able to handle both pre-trigger and data packets, but for this first prototype, the THOR card allows to avoid conflicts in the ASM card signal handling. The acquisition process is easier and safer with the THOR card interaction.

In the multi-slit collimated camera, the pre-trigger signal directly operates as a trigger validating the data collection from absorber and hodoscope. In the Compton camera, the AMC40 receives the pre-trigger from the THOR card and sends it to the scatterer FE cards, which explore their buffer looking for events in the coincidence time window; if a coincidence is found, a trigger signal is generated by the scatterer FE card and sent to the acquisition system, which then starts the data read-out from all the detectors. A simplified graphical overview of the complete acquisition system and logic is given in Figure 3.14.

The AMC40 card makes use of a buffer for each FE card of the three detector sections, where the collected data are stored until the creation of packets of the selected size to be sent to the acquisition PC. The data transfer is achieved via a 1 Gbit/s Ethernet link, and the chosen standard is the User Datagram Protocol (UDP). The data format has been fixed at the camera conception stage and slightly modified following the electronics developments; it is deeply described in the appendix A, which also reports the expected data flow obtained in previous simulation studies.

In addition to the already explained functions, the μ -TCA is also in charge of handling the slow control signals for the configuration of the detector FE cards. The chosen format is in this case the Transmission Control Protocol (TCP), which is more reliable and ensures a feedback in case of communication failure. The possible slow control signals are detailed in appendix A.

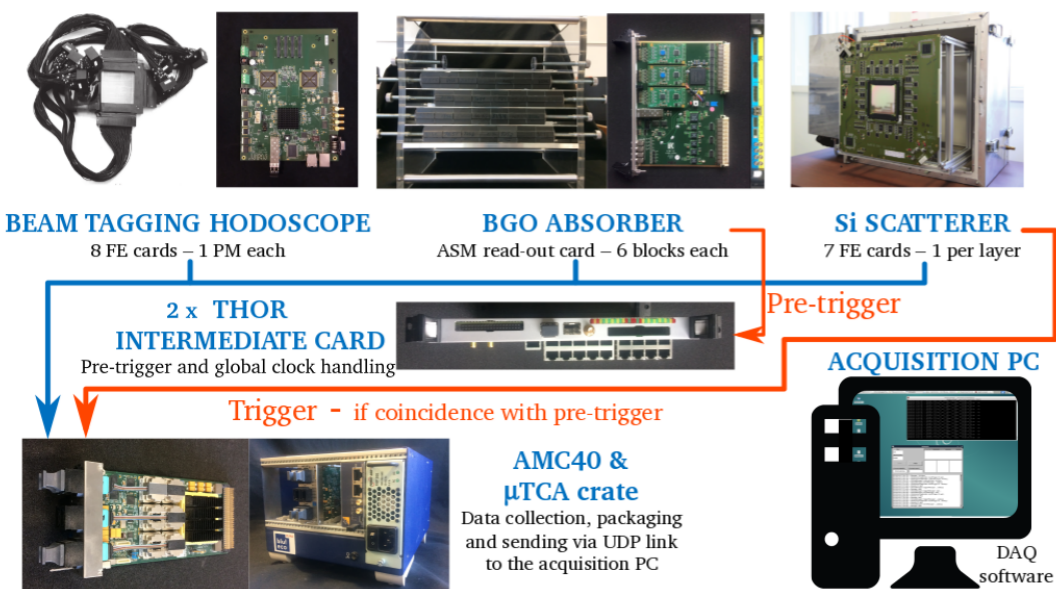


Figure 3.14: Schematic view of the Compton camera acquisition system. For the multi-collimated camera, the trigger and pre-trigger signals are the same.

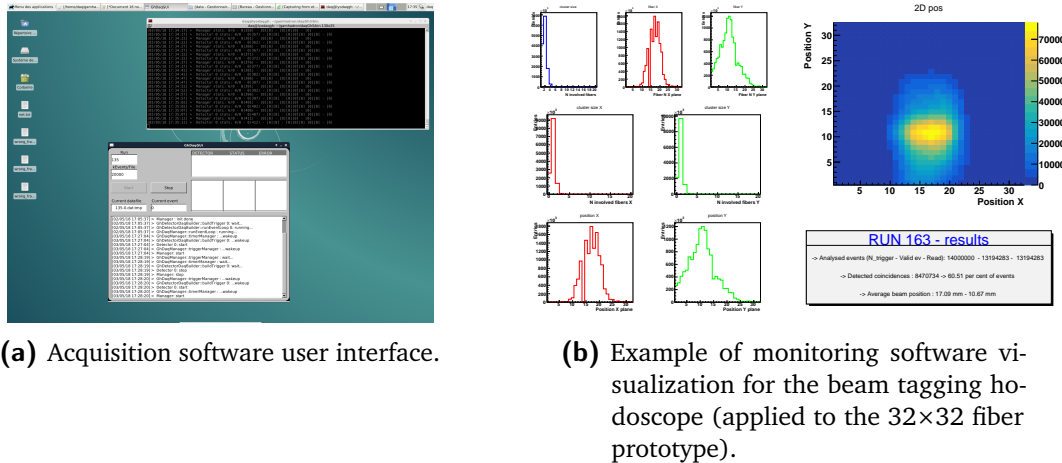


Figure 3.15: Software tools: user interface of the acquisition C++ software (a) and example of the ROOT (Brun et al. 1997) monitoring software visualization for the beam tagging hodoscope 32×32 fiber prototype.

3.1.6 Camera acquisition, monitoring and slow control software

The UDP data packets sent by the μ -TCA acquisition system via Ethernet link are received by the acquisition PC thanks to a C++ based acquisition software, developed at the IPNL. The software decodes the data packets and builds the events by grouping the data from the two (for the multi-slit collimated camera) or three (for the Compton camera) detection sections according to the time stamp. During the decoding process, the software also verify the received data format and can highlight problems in the data encoding by the μ -TCA; this feature is used during the test phase to check the functionality of the AMC40 firmware. The reconstructed events are then stored in binary files with the structure presented in appendix A. The data file size can be selected by fixing the number of events stored per run in the acquisition run, knowing that each event can be composed by **11** slightly different number of bits, according to the amount of detector modules involved. The file collection corresponding to the same run will be then grouped at the analysis stage. The number of events per file must be tuned taking care of the available Random Access Memory (RAM) (32 Gb), where the data are temporarily stored before the writing process on the hard-disk. In Figure 3.15a the minimal graphical interface developed for the acquisition software is shown.

A monitoring software has been developed in order to have a direct real-time feedback on the camera data acquisition. The software can show some information about the ongoing data collection, and it is at present designed to work on a single detector section (hodoscope, scatterer or absorber). It is based on ROOT (Brun et al. 1997) with the following working logic: during the acquisition, it continuously searches for new data files in the storage folder, and analyses in the desired way a selected number of events per file, directly from the binary format. An example of the visualized output for an hodoscope monitoring is shown in Figure 3.15b. This picture corresponds to an acquisition performed during a beam test at the Centre Antoine Lacassagne, Nice, France (CAL), where the 32×32 fiber hodoscope have been tested, together with the monitoring software. More details about the beam test are given in chapter 6.

As mentioned, the present version of the software is not yet adapted to the monitoring of

the whole camera, even if it can handle at least two detectors with minor modifications. In addition to this, it is not automatically synchronized with the acquisition software, and not optimized in terms of needed calculation time. In the next future the planned upgrade will slightly modify the working logic by directly connecting the monitoring to the acquisition: the acquisition software will automatically send a selected fraction of events to the monitoring output during the acquisition, so that the search for data files would not be anymore necessary. This will drastically reduce the monitoring dead time and calculation time, achieving an actual online control.

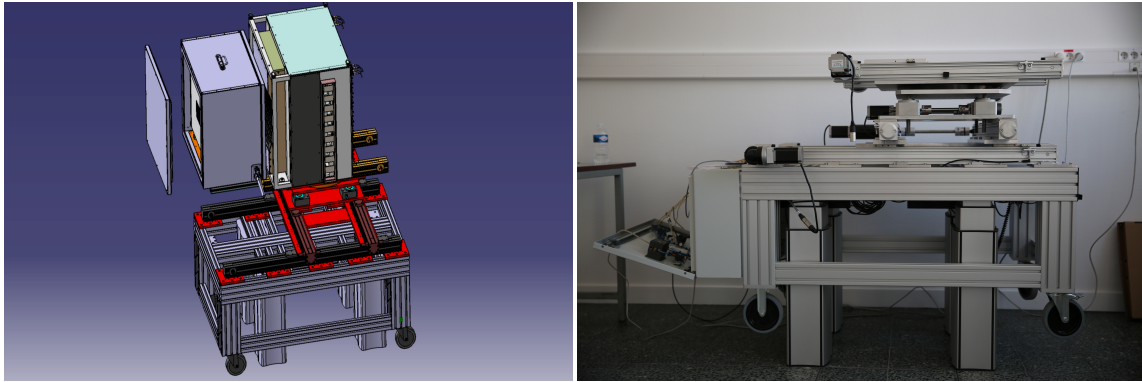
Acquisition and monitoring software has been tested thanks to a data simulator developed in C++, which is able to create data UDP packets with the correct format and send them on the same Ethernet port used for the data collection, simulating a server-client communication.

As mentioned in section 3.1.5, the μ -TCA handles both the data collection and transfer and the slow-control of the whole system, where with slow-control we intend the configuration of all the electronics cards (discriminator thresholds, channel gains, ASIC reset signals, working mode, etc.) and the read-out of the feedback signals. The development of the slow-control software is ongoing at the IPNL: it is designed in LabVIEW and includes all the needed controls in a single user interface. A dedicated PC is foreseen for this task, connected to the μ -TCA via TCP protocol. The slow-control software will also govern the high and low voltage suppliers for the detectors and acquisition electronics boards, the scatterer thermal box temperature setup and control, the steering of the 2D positioning table dedicated to the hodoscope, and the steering of the camera moving table, described in the next section. All the listed instruments will be connected to a patch panel, and a local network will be created for the camera equipment.

3.1.7 Camera integration and mechanical support

In order to setup the two camera configurations (multi-slit and Compton), the described components, together with the related mechanical supports, must be integrated in an integral system, with the exception of the beam tagging hodoscope which has its own dedicated mechanical support, being placed between the beam nozzle and the target. A general mechanical structure is then needed to support the camera; it is required to be movable, as compact as possible but at the same time robust and large enough to support absorber and scatterer (or collimator), for a total maximum weight of about 100 kg. In addition to this, it should be possible to remotely control the position of the various camera components in order to adapt their position in 3D with respect to the beam line and to the target.

The realized solution is shown in Figure 3.16b. It is composed of two sections: a positioning table on wheels, designed and provided by Rose & Krieger, equipped with 4 telescopic feet, and a 4-axis moving table installed on it, developed by Kinetic System. The wheels allow to first position the camera, and the 4 telescopic feet are used to regulate with 1 mm precision the whole system height, in the range 630 mm - 1280 mm from the ground, to be adapted to the specific beam line. The feet are expected to be able to support a maximum weight of 150 kg. The telescopic feet are not connected to the slow-control but are controlled by a remote controller on the table itself. On the top surface of the table, $1200 \times 750 \text{ mm}^2$, the 4-axis moving table is fixed and allows to adapt the camera position in 3D (distance camera-target, height, direction parallel to the beam line) with a $100 \mu\text{m}$ resolution and a range of 40 cm. In addition to this, a fourth axis allows to adjust the distance between the two detector



(a) Schematic view of the Compton camera integration on the positioning table.

(b) Gamma camera position table.

Figure 3.16: Details of the gamma camera integration and mechanical support.

components in the direction perpendicular to the beam line, in a range of 30 cm (to be noticed that this range is reduced by the size of the scatterer thermal box). The four axes are connected to the positioning table patch panel, which is directly controlled by the slow-control program in LabVIEW. Finally, a further manual control allows to rotate the whole system with respect to the table axis, in a range of ± 10 degrees.

In Figure 3.16a we present the mechanical scheme of the complete positioning table, with the Compton camera installed on it.

In Figure 3.17 we show a view of the three detectors composing the Compton camera, with one scatterer layer installed in the thermal box and the absorber mounted on the positioning table, and the beam tagging hodoscope on the right side on its dedicated mechanical support.

3.1.8 Data analysis and image reconstruction

All the data collected at the detector characterization stage (in standalone working mode) are analyzed via ROOT (Brun et al. 1997) and Python custom developed codes. Further details are given in section 3.2, where the performed characterization measurement on the three detector section are described. Concerning the data analysis for the complete systems (multi-collimated and Compton camera), automatic ROOT-C++ based programs will be developed in order to achieve an online data treatment for both tests and clinical application purposes. The raw collected data samples must be adapted to the image reconstruction codes, needed to retrieve the final image for both camera configurations.

The multi-collimated camera is designed to provide 1-D information about the prompt-gamma emission distribution along the beam direction: the required data treatment is then relatively simple, and based on the chosen geometrical configuration of collimator and absorber. The detected events are spatially assigned to the BGO block pseudo-pixel where the gamma interaction took place, by means of center of gravity calculation with the four signals provided by the involved block and then with an automatic algorithm developed for test purposes and detailed in section 3.2.2.3. Knowing the block position within the whole absorber setup, the



Figure 3.17: Compton camera with beam tagging hodoscope on the developed mechanical supports.

prompt-gamma emission profile can be reconstructed assuming a photon path perpendicular to the absorber entrance face. This simple approach can be refined thanks to the spatial information given by the beam tagging hodoscope. The detected beam position can constrain the reconstructed emission position to a point, so that a 3-D emission profile can be obtained. This solution is being explored but a final, working reconstruction code is still not available.

Concerning the Compton camera, the image reconstruction requires the detection of coincidences in the scatterer and absorber sections: position and deposited energy information in the two detectors allow for the reconstruction of the emission cone via Compton kinematics, as explained in details in chapter 2. The photon emission profile (prompt-gammas for the ion beam therapy application, gamma emitted by the radio-tracer for the nuclear medicine approach) is then obtained via the overlap of several reconstructed cones. As described in chapter 2, analytic and iterative algorithms have been proposed and developed to reconstruct the final image given by a Compton camera, which intrinsically transport a 3-D information. In particular, the image reconstruction of the CLaRyS Compton camera relies on a line-cone analytic algorithm based on back-projection and on the code developed by the CREATIS group for the iterative method (Hilaire et al. 2014; Lojacono et al. 2013; Maxim 2014).

The analytic line-cone reconstruction is only applicable in ion beam therapy monitoring and is based on the intersection of each reconstructed emission cone with the beam direction information given by the beam tagging hodoscope. This method assumes that the prompt-gammas are generated along the beam path, considered as a straight line, and limits to two points the possible emission position for each detected events. The overlap of several events will then allow for the emission distribution definition in 3-D. The Compton camera performance have been tested for the application in ion beam therapy monitoring, and this reconstruction code has been employed to treat the simulated data: the results are given in chapter 4, where we usually refer to this reconstruction method as “line-cone”.

The iterative algorithm is called List Mode-Maximum Likelihood Expectation Maximization (LM-MLEM) and is able to include in the calculations the space and energy resolution of the involved detectors, leading to the reconstruction of a 3-D image. It requires the definition of a reconstruction volume, which is divided in a given number of voxels, and the list of coincidence events. Starting from the simple event back-projection, it defines the probability that a given photon detected in the Compton camera has been emitted from the voxels in the defined volume. For every iteration, this probability is re-computed taking into account the results of the previous iteration, converging to the most likely emission distribution. The number of iterations is fixed by the user and must be a trade-off between reconstruction accuracy and calculation time. This method has been used with ion beam therapy monitoring simulated data and compared to the line-cone method (see chapter 4), as well as for the reconstruction of point-like sources simulated for the application of the camera in nuclear medicine, presented in chapter 5. To be noticed that, concerning the reconstruction of prompt-gamma emission distribution in ion beam therapy application, the spatial information about the beam given by the beam tagging hodoscope is still not included in the employed version of the code. An upgrade is under study and is at present at the preliminary test stage.

3.2 Camera component characterization and development status

As detailed in the previous sections, the CLaRyS TOF gamma cameras are equipped with various detector components with very different features. Each part must be separately studied in order to characterize its behavior and allow the final camera integration and operation.

I mostly worked on the beam tagging hodoscope and on the BGO absorber, and in the next paragraphs the performed measurements are described in details. Concerning the scatterer stack, the results achieved before the beginning of my PhD thesis are briefly described for the sake of completeness.

The results presented in this section also introduce the following one (3.3), where all the development steps still needed for a clinical implementation of the cameras are explained.

3.2.1 Scatterer silicon layer characterization

The 7 DSSDs selected for the application in the Compton camera system among the 10 provided by the producer have been characterized in terms of leakage current. The measurements have been performed by colleagues before the beginning of my PhD thesis. The extended description of the employed test-bench, the performed tests and the results is presented in Ley 2015.

The leakage current is an evaluation of the systematic uncertainty expected on each read-out channel, corresponding to a background current detected without an energy deposit in the depletion region. The 7 layers have been tested at the complete depletion voltage of -750 V with a test-bench developed at the IPNL specifically for these measurements. It is composed of a custom electronics card which is used to supply the detector with the depletion voltage and to the current read-out via the connection to a nano-ampere meter (Nuclear Instrumentation Module (NIM) module with 0.1 nA resolution). Moreover, temperature variations in the range -40°C - +40°C have been realized with an automatic system, with the detectors and read-out card placed in a temperature programmable chamber Weiss WTL 64 (WeissTechnik 2017). The temperature variations, the channel selection and the data acquisition are handled by a Raspberry Pi. The temperature step has been fixed to 5°C. Finally, temperature cycles have been carried out in order to study the detector response to rapid temperature variations and the time required to stabilize the leakage current at the working temperature, with temperature steps between -20°C (working temperature) and +25°C (room temperature).

The leakage currents measured at room temperature (+25°C) are homogeneous on all the strips, with some local exceptions. The average detected value is about 20 nA. Concerning the measurements at -40°C, the average value for the n strips is close to 0 nA, while a current of 3-4 nA is still detected on the p strips. On each layer, a maximum of 3 strips show higher leakage current values; this is acceptable for the final application in the Compton camera. Moving from -40°C to +40°C, the leakage currents respect, on average, the expected trend defined by equation 3.1 (Spieler 1998).

$$I_p(T) \propto T^2 \times e^{-\frac{E}{2k_B T}} \quad (3.1)$$

where $I_p(T)$ is the leakage current as a function of the temperature, T is the temperature in Kelvin, E the silicon energy gap energy in eV, k_B the Boltzmann constant (8.617×10^5 eV K $^{-1}$).

The leakage current is generally stable or is slightly increasing for temperatures below 0°C, with values always below 10 nA. Beyond 0°C, it rapidly increases reaching some tens of nA at 40°C, depending on the specific strip. This observation justify the need of the described thermal regulated box, which is able to maintain a constant temperature of -20°C during the detector operation, placing them in a minimum and stable leakage current regime.

The application of quick temperature variation steps between -20°C and +25°C allowed to estimate the time required by the detector to re-establish the working regime with minimal leakage current. When moving from -20°C to +25°C, the leakage current increases rapidly up to the values already detected during the slow temperature variations, with a transition time of the order of less than ten minutes. Approximately the same time is required to stabilize the leakage current after the cooling down to -20°C.

In addition to the described leakage current measurements carried out with the 7 cm^2 DSSDs, a small silicon layer prototype (8×8 strips) has been tested with the first version of the FE card ASIC. The first version of the card allowed for the read-out of 8 channels, so that the p strips have been characterized with this read-out system, while the n strip data have been collected with NIM modules. The data treatment has been performed thanks to VME modules.

The detector has been exposed to Sodium-22 (^{22}Na) and Cobalt-57 (^{57}Co) radioactive sources: the ^{22}Na source, producing two back-to-back 511 keV gammas as a result of the β^+ annihilation, has been used for timing measurements in coincidence with a Lanthanum Bromide (LaBr_3) crystal, while the 122 keV photons of the ^{57}Co source are used to characterize the energy response by photoelectric absorption.

The detected time resolution has been estimated to be in the range 13-23 ns FWHM for the p strips, and between 30 and 80 ns FWHM for the n strips (knowing that the “hole” drift time is about 3-4 times more than the electron one). The energy resolution is between 10 and 20 % FWHM for the tested strips. This test also allowed to verify the first version of the card and move forward with the development of the second and third version at present available for the final detector.

Thanks to the summarized measurements, a calibration database is available for the 7 silicon layers, which showed overall stable and acceptable performance. The final version of the card must be tested in order to check these results, validate the board behavior and move to the first detector tests on beam. All the details concerning the next development steps are presented in section 3.3.1.

3.2.2 Absorber BGO blocks characterization

The BGO modules composing the Compton and multi-collimated camera absorber have been recovered from a SIEMENS PET system: they have been originally optimized for the detection of 511 keV photons from positron annihilation, and they have to be tested for the new gamma detection system, which must be able to deal with photons in the prompt-gamma energy range, i.e. from some hundreds of keV to a few MeV.

Each block must be characterized in terms of spatial and energy response, and the read-out PMs have to be calibrated to obtain a uniform response on the whole block surface (see section 3.1.3 for the detector description). The employed method relies on the work presented in Rogers et al. 1994 and Tornai et al. 1994 and on the calibration process described in Golnik 2015 and Hueso-González et al. 2015, and has been extended with more refined features.

The measurements are performed with the irradiation by gamma sources, emitting photons at defined energies: in particular, we used 511 keV and 1275 keV photons from a ^{22}Na source, and the two photons emitted by a Cobalt-60 (^{60}Co) source, at energies of 1173 keV and 1332 keV.

The employed ^{22}Na source is a cylindrical source with an active diameter of 4 mm, and an activity of about 400 kBq: it has been placed at a distance of about 5 cm from the block entrance surface, with the center of the source facing the center of the block transverse surface. The ^{60}Co source has been installed in a lead cylindrical container (12 cm radius and 35 cm height), equipped with three different apertures: point-like ($2 \times 2 \text{ mm}^2$), linear ($2 \times 50 \text{ mm}^2$) and squared ($50 \times 50 \text{ mm}^2$). The design of the lead container has been studied in simulation to ensure the proper radiation protection, and produced according to the specifications defined by the IPNL mechanics group. The activity of the ^{60}Co source is about 1.7 MBq, and the square shape has been used to obtain an homogeneous irradiation of the BGO block, with the block set with the center of the entrance surface corresponding to the source position, at a distance of 12 cm.

The signals produced by the four PMs of each block are collected via four analog outputs on the FE card (see picture 3.6a). The four retrieved signals per event are treated via standard NIM modules in order to be adapted to the acquisition systems and measurement purposes.

Two different acquisition systems have been used for this characterization work. First, the PXIe described in section 3.2.3 with its two flash ADC read-out modules, 8 channels each, is used for the spatial and energy characterization and calibration of the tested blocks. A scheme of the acquisition setup for this part of the calibration is given in figure 3.18. The raw signals coming from the four PMs are amplified and shaped via NIM modules (quad shaping bipolar amplifiers), which were fine-tuned via a pulse generator in order to adapt the amplification factor of each channel (an amplification factor of about 50 has been applied to the raw signals). The amplified signals are then split in order to be treated for trigger purpose. The trigger for the acquisition is based on the sum of the four signals, and a fixed threshold is applied for background rejection. The employed discriminator provides the logical trigger signal, which is sent to the trigger input of the ADC modules on the PXI. The four amplified signals, conveniently delayed, are sent as inputs to the ADC modules on the PXI, together with the sum signal which is used for experimental verification of the acquisition setup. A LabVIEW-based acquisition software, developed for this particular application at the IPNL,

provides real time event visualization together with a partial, on-line spatial reconstruction of the events, and stores them in text files for further analysis. A second threshold can be set at the software level in case particular selections are needed during the acquisition, otherwise the event selection is performed at the analysis stage.

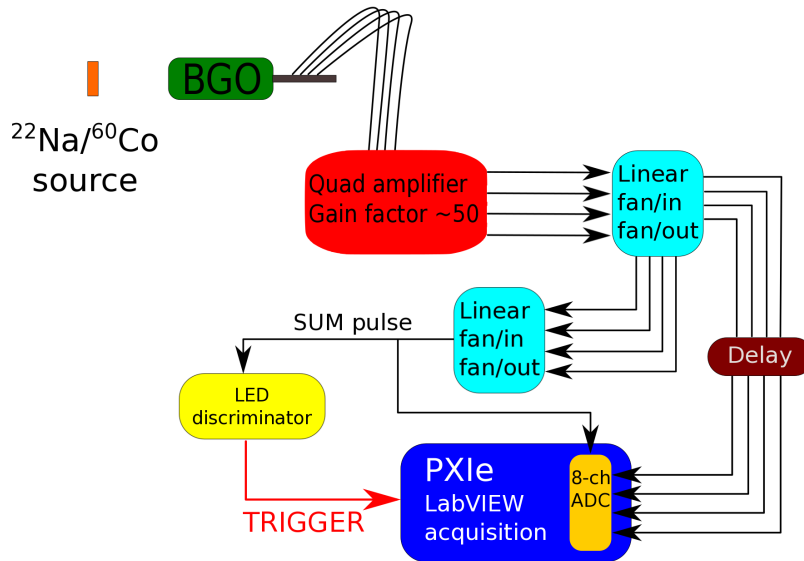


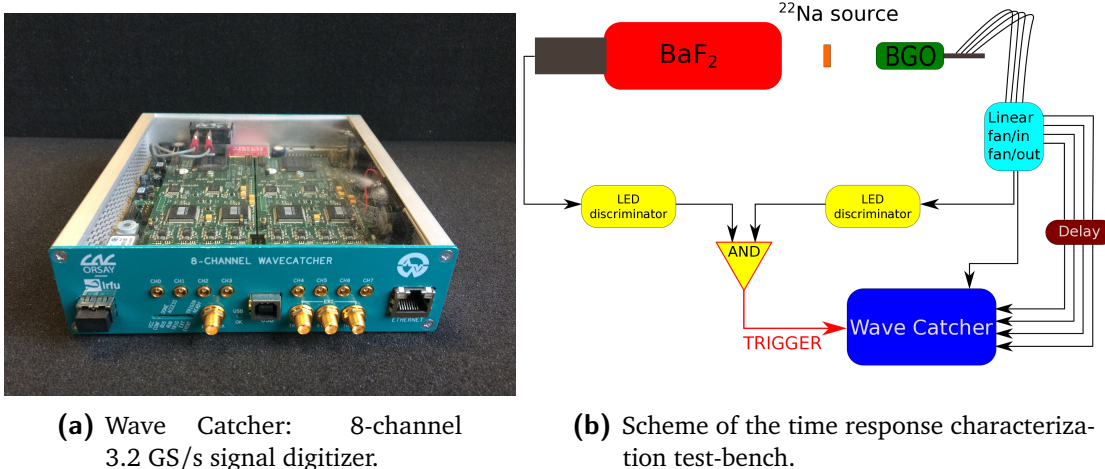
Figure 3.18: Scheme of the spatial and energy characterization test-bench.

Concerning the timing characterization measurements, an eight-channel signal digitizer at 3.2 GS/s has been employed for high time resolution acquisitions. The so-called WaveCatcher, shown in Figure 3.19a, has been developed by the Laboratoire de l'Accélérateur Linéaire, Paris, France (LAL) in Orsay and the Institut de Recherche sur les lois Fondamentales de l'Univers, Paris, France (IRFU) in CEA-Saclay, and its features are detailed in Breton et al. 2014. The digitizer is connected to the acquisition PC via Universal Serial Bus (USB) port, and the data read-out and storage are performed thanks to a custom acquisition software. The measurements are based on the coincidence detection of back-to-back 511 keV photons emitted by a ^{22}Na radioactive source, in order to be able to compare the time response of the tested BGO block to a reference fast timing scintillator. An external trigger is then provided to the WaveCatcher by treating the BGO block and reference scintillator signals with logic coincidence NIM modules, after proper discrimination. Further details are given in section 3.2.2.4, while a scheme of the acquisition setup is given in Figure 3.19b.

3.2.2.1 Space and energy calibration and characterization

The space and energy calibration process is mainly divided into three stages:

- PM gain equalization (^{22}Na): the block is irradiated with the ^{22}Na source and the raw ADC distributions for the four PMs are retrieved. The upper-energy falloff in the raw ADC spectra are taken as reference to equalize the distributions. Four energy calibration factors are extracted and used to the data correction; this correction corresponds to the PM gain equalization.



(a) Wave Catcher: 8-channel 3.2 GS/s signal digitizer.

(b) Scheme of the time response characterization test-bench.

Figure 3.19: Details about the BGO block time response characterization.

- Pixel identification (^{60}Co): once the calibration factors are extracted thanks to the ^{22}Na irradiation data, the block is exposed to the ^{60}Co source. The collected data are analyzed as in the previous step and calibrated according to the already calculated correction factors. The energy spectrum, the mono-dimensional spatial projections and the flood map are produced. The custom algorithm briefly described in the following section 3.2.2.3 has been developed to identify the pseudo-pixel positions on the flood map. It is applied to the ^{60}Co irradiation data and the pseudo-pixel position map is stored.
- Pixel energy calibration: the ^{22}Na irradiation data are re-analyzed in this last calibration step in order to assign each interaction to a single pseudo-pixel according to the pixel position map obtained with the ^{60}Co data. Then, the energy spectrum of each pixel can be produced and the two identified peaks (corresponding to the two photon energies emitted by the ^{22}Na source - 511 keV and 1275 keV) can be used to equalize the pseudo-pixel response. The sum of all the pixels spectra produces the block energy spectrum. At this stage, the ADC channel values are calibrated to obtain the absorbed energy values in keV.

It is worth to notice that the ^{60}Co irradiation is useful for the pixel identification given the high energy and narrow energy range of the emitted photons. The equalization factors obtained with the ^{22}Na source irradiation have been verified to be consistent with the ^{60}Co irradiation data, as expected. The whole method results to be robust.

3.2.2.2 Qualitative test of spatial reconstruction accuracy

Specific acquisitions have been devoted to the test of the block spatial accuracy potential. The detector is expected to be able to locate the collected interaction on the pseudo-pixel grid, but the possible sub-pixel accuracy can be tested with a collimated source scan of the block surface. The ^{60}Co source has been employed for this purpose, with the linear aperture. The block has been placed on a moving table with no distance between its entrance surface and the collimator aperture. The whole surface has been irradiated with horizontal and vertical movements of 1 mm and 2 mm per step. The collected data have been calibrated with the

factors obtained with the homogeneous ^{22}Na irradiation, as explained in the previous section. We present and qualitatively discuss the results in section 3.2.2.6.

PUT ALSO POINT-LIKE SCAN ???? 

3.2.2.3 Pixel identification and energy calibration algorithm

Subsequent to that gain equalization process, an automatic iterative algorithm has been developed to identify the block pseudo-pixel positions. Integrated mono-dimensional spatial projections are computed along rows and columns of the calibrated flood map in order to derive the peak and valley positions in the distributions with the ROOT (Brun et al. 1997) methods included in the TSpectrum class and simple analytical calculations. With the resulting valley positions, a first rectangular grid of pseudo-pixels is initialized. The projection of each identified pseudo-pixel row (respectively column) is re-analyzed using the same integrated 1-D spatial projections along columns (respectively rows) looking for peaks and valleys as before. A refined grid is then produced, distorted from the initial rectangular one, and this process is iterated until a complete 8×8 pseudo-pixel grid is obtained.

Once the pseudo-pixels grid is fixed, the maximum (center of gravity of counts) of each pseudo-pixel region is automatically identified and its position defines the pseudo-pixel center relative position in the map.

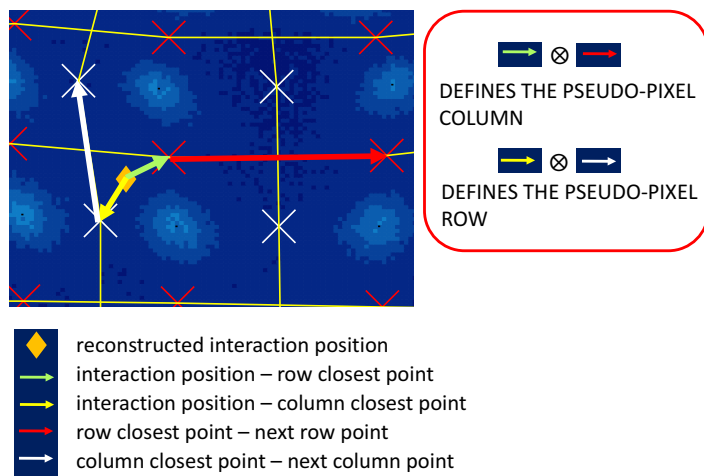


Figure 3.20: Logic for the event assignment to a single pixel. The dual pseudo-pixel grid is displayed: in white the mid points on the pseudo-pixel edges along rows, in red along columns. The sign of the outer products detailed in the red box are used to define the column and row (so that the pseudo-pixel) where to assign the reconstructed event.

The event data are then assigned to the pseudo-pixels with the application of the following process, illustrated in Figure 3.20. The dual pseudo-pixel grid is created rows- and columns-wise to get the mid points on the pseudo-pixel edges. The even data assignment is then done by calculating the minimal distance between a column and a row average point with respect to the reconstructed event and then calculating two outer products, between the vector connecting

the reconstructed point and closest column (row) average point and the vector connecting this average point to the previous or next one on the same column (row). The sign of the products defines the column (row) where to assign the interaction. Knowing the relative position of the interaction point with respect to the two minimal distance points on row and column, the correct pseudo-pixel is identified. A more simple approach could have been used, using the search of the minimal distance between the reconstructed event position and the pseudo-pixels centers, but it proved to be more liable to some assignment discrepancies due to the grid distortions.

3.2.2.4 Time response characterization method

The test-bench for the time response characterization has been set as shown in Figure 3.19b. A Barium Fluoride (BaF_2) mono-block scintillator, read-out by a single photo-multiplier tube, has been used as reference detector. Its excellent time resolution makes it suitable for relative timing measurements in comparison to the BGO blocks. The reference scintillator and the BGO block under test have been set at arbitrary distances from the ^{22}Na source with the aim of detecting in coincidence the two 511 keV back-to-back photons resulting from the positron annihilation. The four raw signals coming out from the BGO block are summed with a NIM linear fan-in/fan-out module, and the resulting signal is sent to a leading edge discriminator and converted to a logic signal according to a fixed threshold. The single signal emerging from the reference detector passes through a selected threshold and is converted to logic signal. The two digital pulses, 100 ns width, are then sent to a coincidence module to create the trigger input for the WaveCatcher acquisition system described in section 3.2.2. The four BGO output raw signals, the reference scintillator raw output signal and the sum of the four raw BGO signals are sent to the WaveCatcher for digitization. An example of the collected raw signals from the reference block is shown in figure 3.21: the 4 output signals of each single PMT are shown together with the resulting sum signal. The four signals exhibit a noisy feature that could be observed using the fast sampling acquisition, with a 80-100 MHz oscillatory behavior. At the present stage we did not infer the sources of this noise, that would be canceled by appropriate lower frequency filtering.

For each coincidence event, the six collected signals are analyzed with focus on the signal rising edge. The time corresponding to the amplitude maximum and to 20%, 30%, 50% and 80% of the maximum is retrieved for constant fraction discrimination tests. In addition to this, a fixed threshold is used for fixed value discrimination.

Different comparison methods have been tested in order to identify the more robust one for the definition of the time resolution of the blocks. The noisy structure of the single BGO raw signals (see figure 3.21) leads to very variable results depending on the defined threshold, and the more stable results are given by the comparison of the sum of the four BGO signals and the reference scintillator with the arrival time identified by a fixed tuned threshold. With this method, the arrival time of each signal can be defined and the time difference distribution of the two signals can be produced.

The same analysis has been applied to a data set obtained with two identical BaF_2 detectors exposed to the ^{22}Na source in coincidence. This data set allowed for the definition of the reference scintillator time resolution.

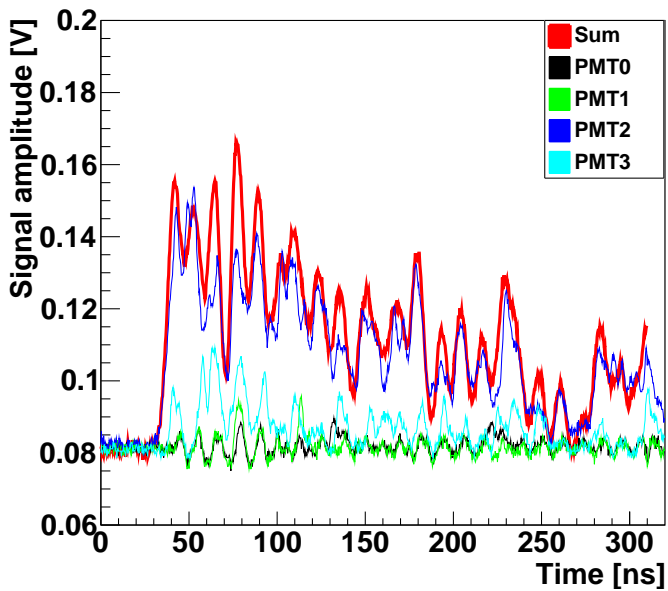


Figure 3.21: Reference BGO block raw signals collected with the Wave Catcher acquisition system. The four outputs of the single PMTs are shown together with the sum signal.

The resulting BGO time resolution is defined as the FWHM of arrival time difference distribution between BGO block and reference scintillator, with the subtraction of the reference scintillator contribution via uncertainties composition calculation.

3.2.2.5 Results: PM gain equalization

Figures 3.22, 3.23, 3.24, 3.25 show the effect of the PM gain equalization on the data collected with the reference BGO block irradiated with the ^{22}Na source. Figures 3.22a and 3.22b show the raw and equalized ADC profiles of the four read-out photo-multipliers (the peaks above 3000 ADC counts in Figure 3.22a correspond to the saturation of the NIM linear fan-in/fan-out module used to handle the data read-out; these values are rejected during the equalization stage). Figures 3.23a and 3.23b show the projection on the two axes of the position of interaction reconstructed via Anger logic, before (left) and after (right) the PM gain equalization. Figures 3.24a and 3.24b show the ADC event spectrum, obtained by the sum of the ADC values of the four PMs, before (left) and after (right) the PM gain equalization. Figures 3.25a and 3.25b show the two dimensional event position map (this will be called “flood map” in the following), before (left) and after (right) the PM gain equalization; the interaction position is reconstructed via Anger logic (see Figure 3.5d for details).

As shown by Figures 3.22 to 3.25, the PM gain equalization performed in this first calibration step is mandatory to optimize the spatial and energy response of the tested block. Figure 3.23b highlights the better definition of the pseudo-pixels ensured by the gain equalization: the peak-to-valley ratio is increased, in particular for the most external pixels. The spatial response improvement is also reflected in a better energy response, as shown in Figure 3.24b, where the two energy peaks of the ^{22}Na source are more narrow with respect to the ones obtained with the raw data. The obtained energy response is still not satisfactory, and the next steps

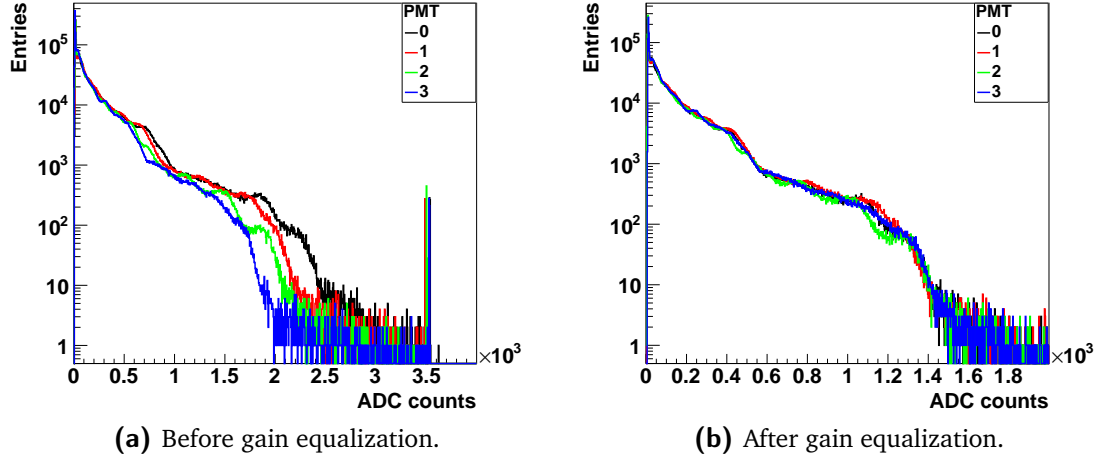


Figure 3.22: PM signal amplitude spectra before (a) and after (b) the PM gain equalization.

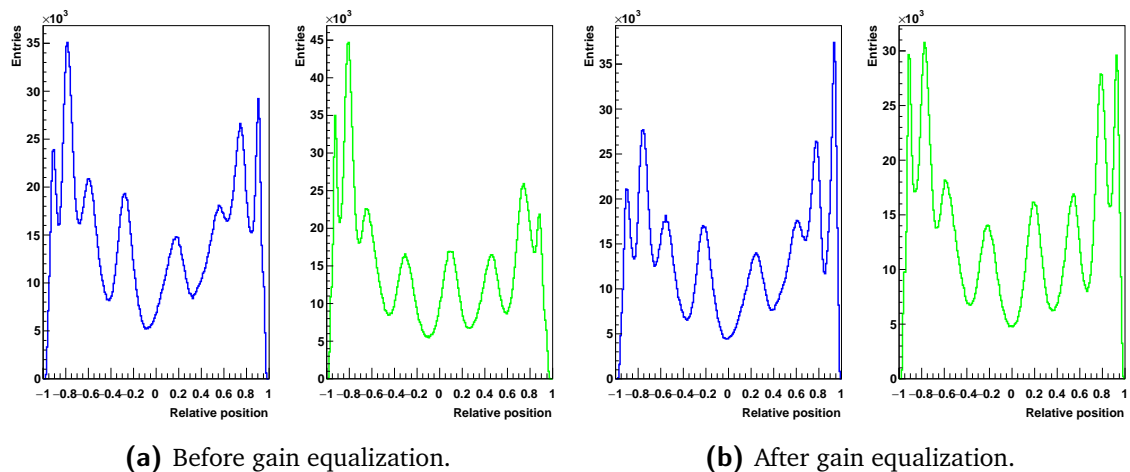


Figure 3.23: 1D integrated position distribution on the two transverse dimensions before (a) and after (b) the PM gain equalization. Blue curves: horizontal dimension. Green curves: vertical dimension.

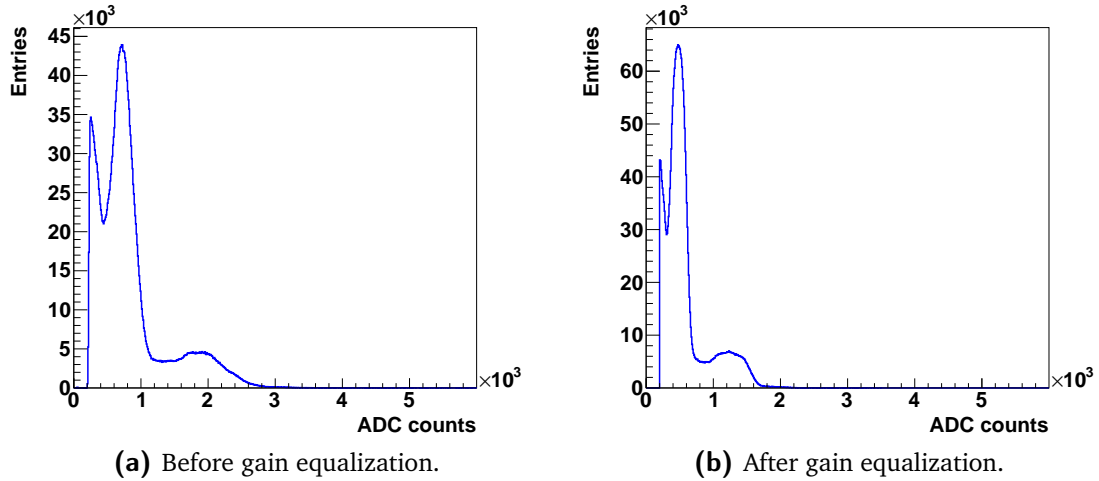


Figure 3.24: Block energy spectrum before (a) and after (b) the PM gain equalization.

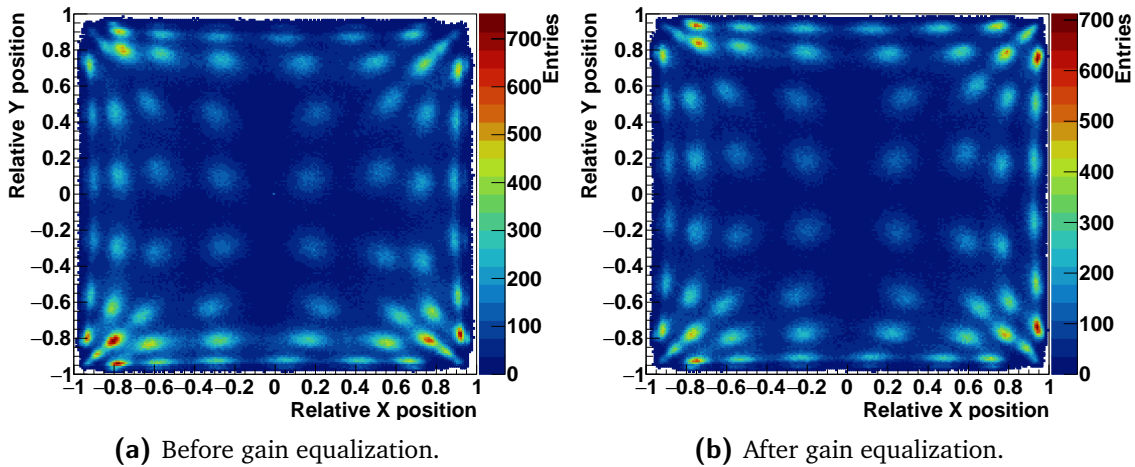


Figure 3.25: 2D reconstructed position map before (a) and after (b) the PM gain equalization.

of the calibration process are dedicated to the improvement of this result. The flood map in Figure 3.25b shows how the gain equalization and the offset tuning allow to arrange the position map over the whole block surface; the borders are better defined and the pseudo-pixels on the block limits (especially on the corner) are better separated.

3.2.2.6 Results: block spatial precision

Figure 3.26 shows four consecutive steps of the ^{60}Co source collimated irradiation, with a 2-mm step movement from left to right and the linear aperture ($2 \times 50 \text{ mm}^2$) set in vertical position. A qualitative analysis is enough to appreciate the block spatial precision limitation. The presented four points of the scan irradiated a total of three pseudo-pixel columns, moving from the left geometrical border of one column to the center of the next one. As shown by Figure 3.26b and 3.26d, as the collimator aperture position is in front of the center of a pixel column, the whole pseudo-pixel surface is reconstructed: no difference is observed with

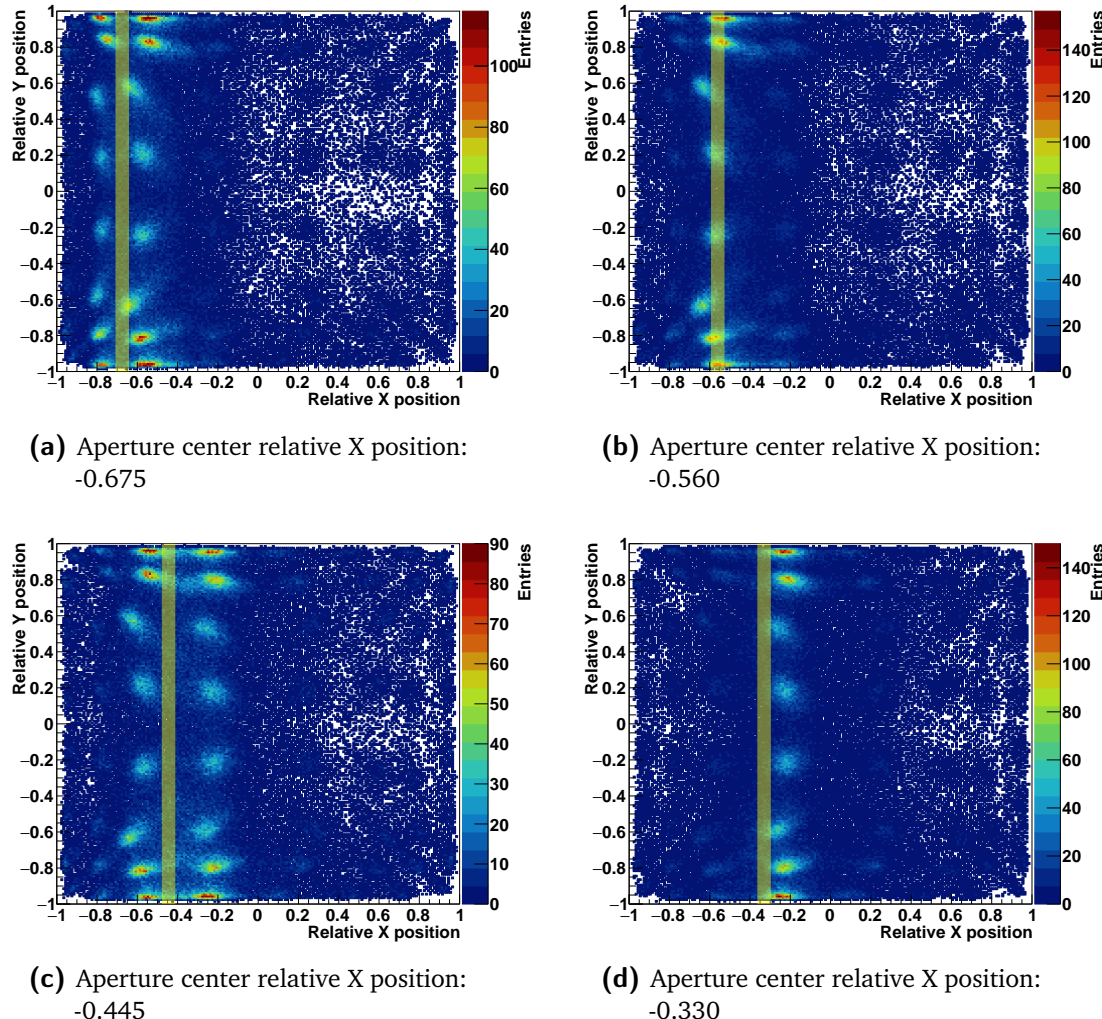


Figure 3.26: 2D reconstructed position maps during a 2-mm step scan performed with the ^{60}Co source with the line aperture from the left to the right size of the block surface. 4 reference measurements points, the position of the aperture is shown by the semi-transparent yellow band.

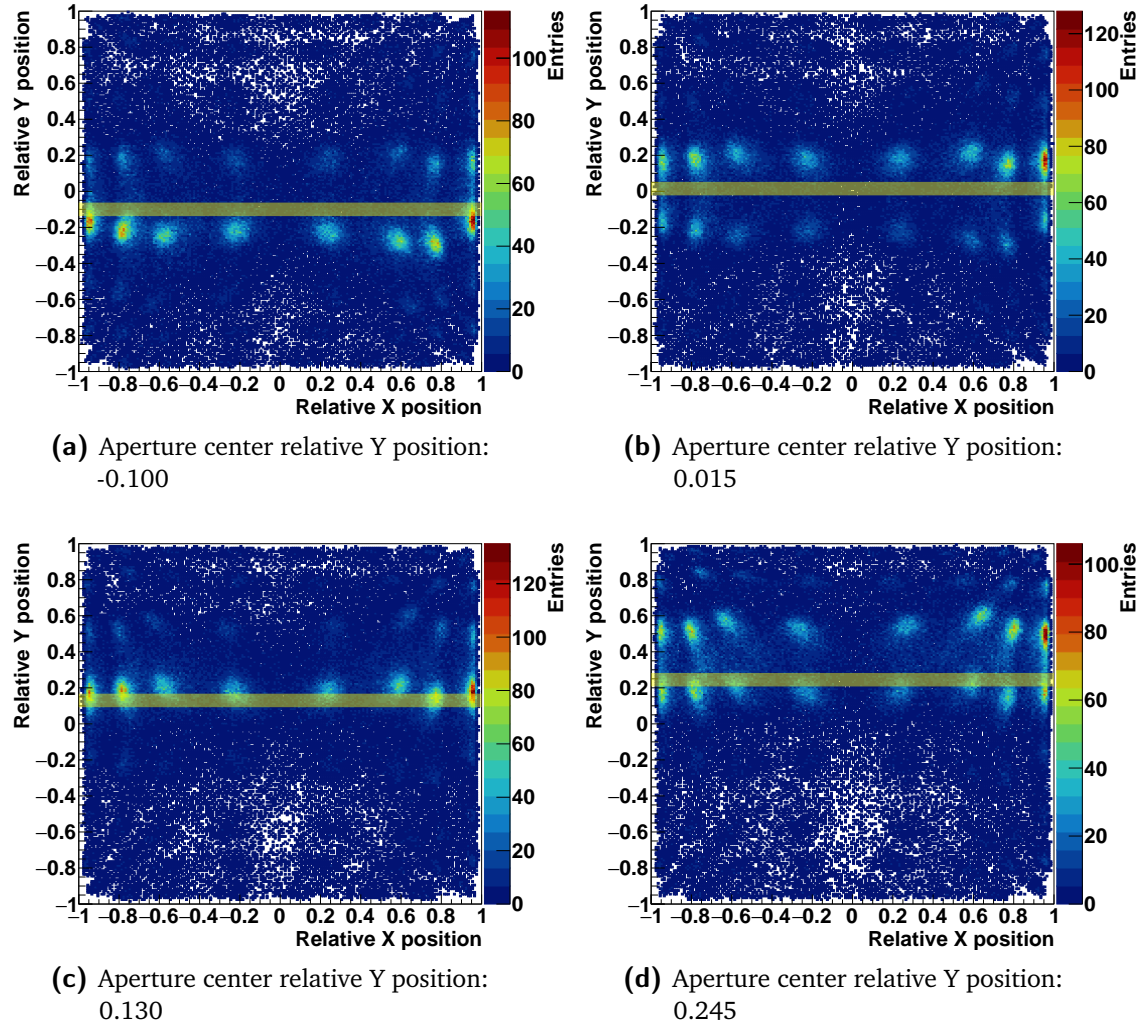


Figure 3.27: 2D reconstructed position maps during a 2-mm step scan performed with the ^{60}Co source with the line aperture from the bottom to the top side of the block surface. 4 reference measurements points, the position of the aperture is shown by the semi-transparent yellow band.

respect to the same column in Figure 3.25b, obtained with the homogeneous irradiation. In case the aperture faces the border between two pixel columns (Figure 3.26a and 3.26c), the events are shared between the two. This could show a possibility of sub-pixel resolution for integrated measurements, which is anyway not reproducible on a single event basis. The same behavior has been verified with a vertical scan (shown from Figure 3.27a to Figure 3.27d); the collimator and table configurations has been **keep** unchanged, while the block has been turned of 90°.

In order to further confirm these results, a scan with reduced step size (1 mm) has been performed with the same collimator aperture, and no modifications have been detected in the spatial distribution of events for the steps centered on the same pseudo-pixel column. As before, when the collimator aperture faces the limit between two pseudo-pixels columns, the events are equally distributed on the two. 9 measurement positions for this 1 mm scan are shown from Figure 3.28a to Figure 3.28i.

All these **set** of data verify that the spatial reconstruction accuracy of the employed blocks is limited to the pseudo-pixel size, and a sub-pixel resolution is not achievable on a single event basis.



3.2.2.7 Pixel identification

The results of the pixel identification algorithm described in section 3.2.2.3 are shown in Figure 3.29. Figure 3.29a shows the identified average values of the pseudo-pixels positions on the two transverse dimensions. As already detailed in the description section, starting from these average positions, the single pseudo-pixels positions in rows and columns are extracted and the “valleys” between neighboring pseudo-pixels are used to define the grid shown in Figure 3.29b together with the pseudo-pixel center position map.

3.2.2.8 Pixel energy calibration

Once the pseudo-pixel positions and the related grid are defined, each interaction can be assigned to a single pixel. The energy spectrum of each pixel is then separately studied in order to equalize the energy response on a pixel basis.

The assignation method described in section 3.2.2.3 makes use of the dual pseudo-pixel position map shown in Figure 3.30. The position assignment scheme to pseudo-pixels is shown in Figure 3.31: a color has been given to each reconstructed point according to the pseudo-pixel region where it has been assigned by the described method. The method robustness is verified by the comparison of this map to the grid in figure 3.29b and 3.30.

In Figure 3.32 the results of the pseudo-pixel energy calibration are shown. Figure 3.32a (left) shows the overlap of the energy spectra for 60 pseudo-pixels before the energy calibration and equalization. The 4 pseudo-pixels on the corners show a very different energy response and are not included in this picture. This is probably due to a no **complete** light collection. The different response of each pixel to the two energy peaks is clearly visible. For each spectrum the low energy peak is assigned to 511 keV, w**th** the high energy one to 1275 keV. In this way,

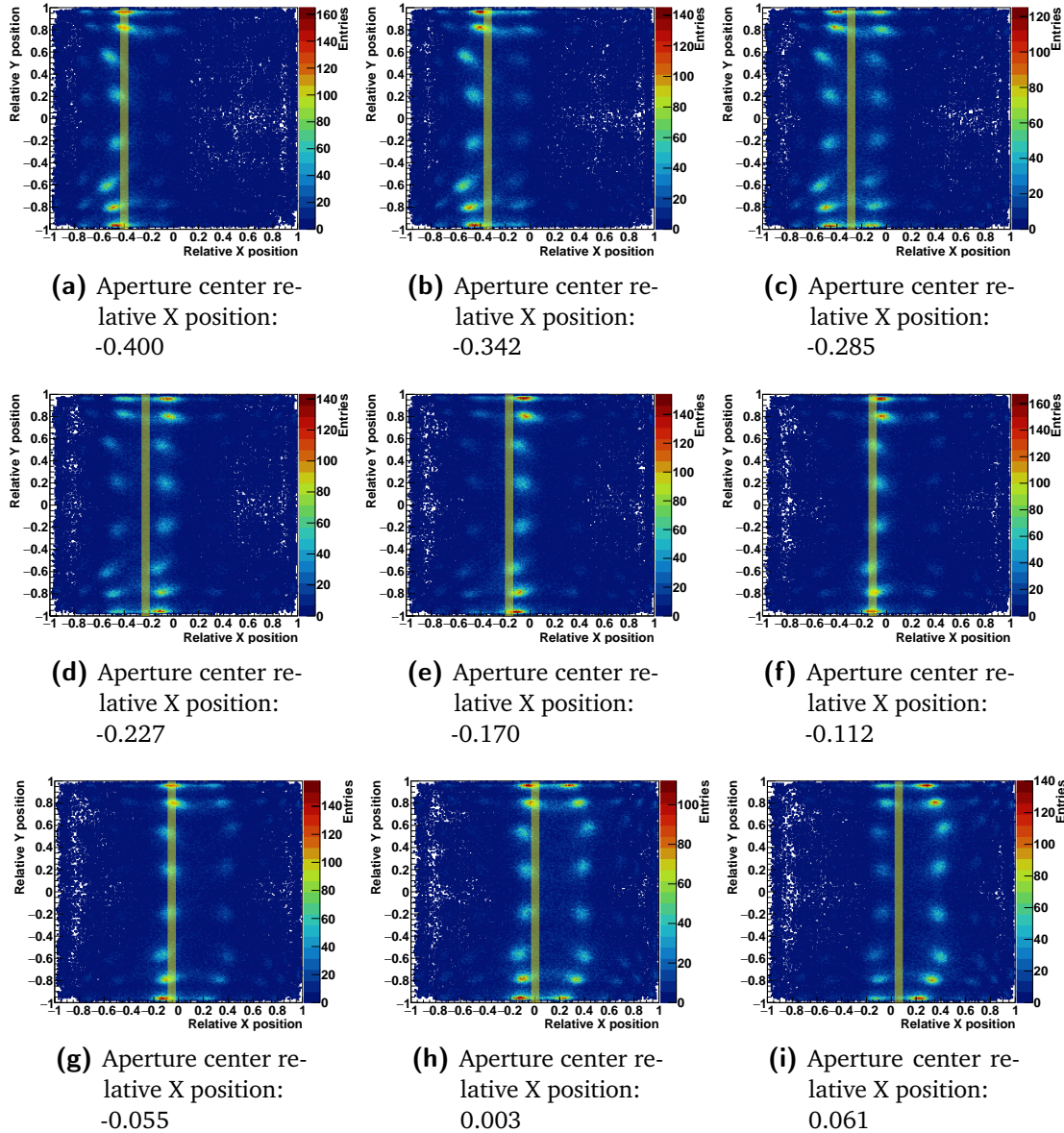


Figure 3.28: 2D reconstructed position maps during a 1-mm step scan performed with the ^{60}Co source with the line aperture. 9 reference measurements points, the position of the aperture is shown by the semi-transparent yellow band.

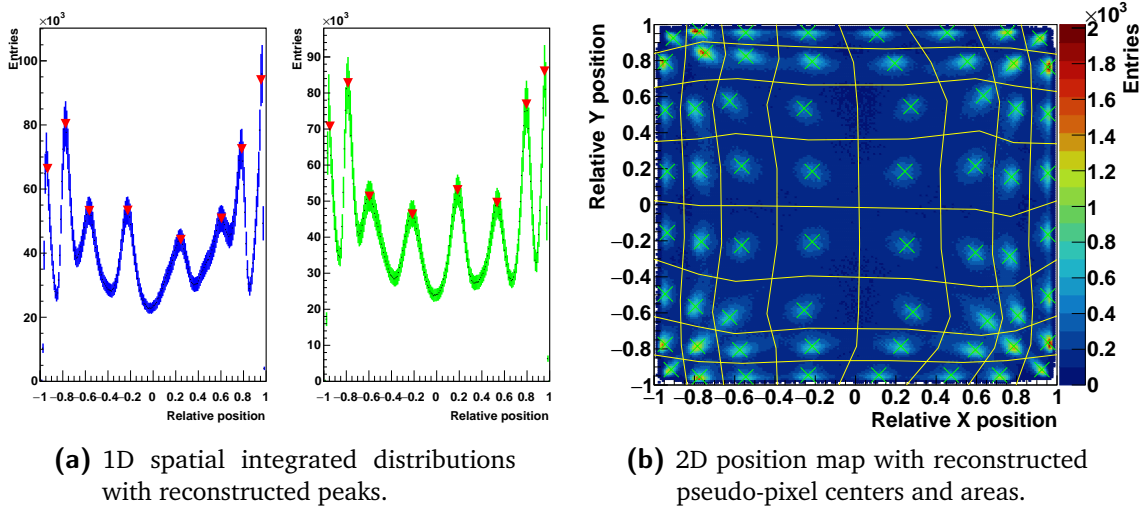


Figure 3.29: 1D integrated position distributions on the two transverse dimensions with the retrieved position of the pseudo-pixel average center (a). Reconstructed 2D map with the identified pseudo-pixels positions and surfaces.

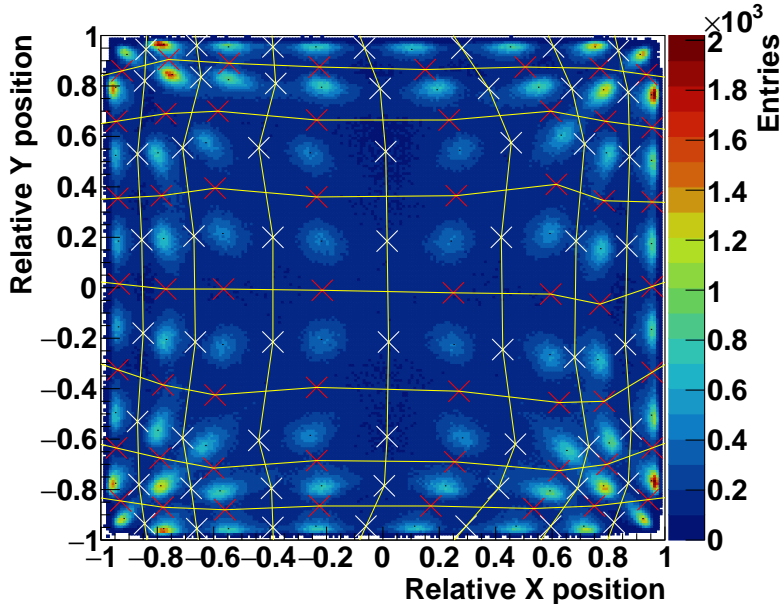


Figure 3.30: Auxiliary position map used for the assignment of the reconstructed events to a single pixel. The highlighted points represent the “valleys” between neighboring pixels on their separation borders.

the spectra are linearly calibrated and equalized, as shown in Figure 3.32a (right). For the 4 corner pseudo-pixels, the calibration is based only on the 1275 keV peak, while the 511 keV reference peak is substituted by the null ADC value.

Once the single pixel energy responses are equalized and calibrated, the whole block energy spectrum can be derived with the sum of **the** all pixels. In Figure 3.32b (left) the ADC spectrum is shown before the equalization process, while in Figure 3.32b (right) the calibrated energy spectrum is presented. In Figure 3.32b (left) the energy spectra related to three refer-

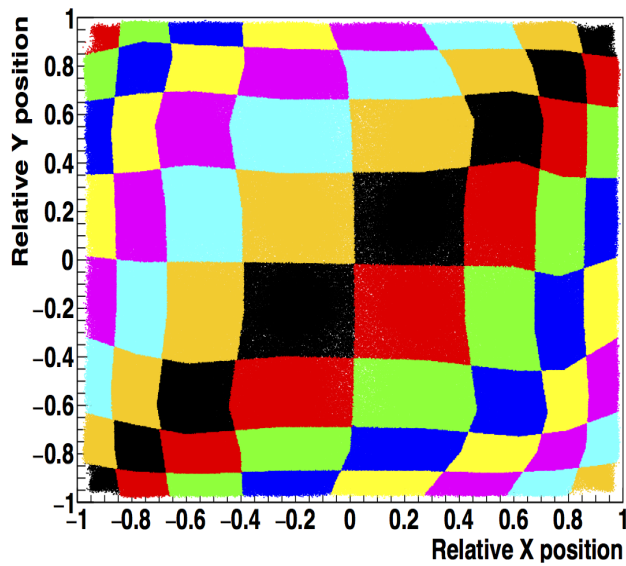


Figure 3.31: 2D map of the reconstructed event assignations to pseudo-pixels.

ence position on the block surface are reported: this makes possible to appreciate the different contributions to the non-calibrated spectrum and the behavior of different block sections. The block peripheral pixels show an overall lower light collection and a lower efficiency in detecting high energy photons (reduced peak integral with respect to the center and mid-center pseudo-pixels). Concerning the central pixels, the slight in-homogeneity is probably due to the streaked structure which guides less than on the borders the scintillation photons.

The two spectra are represented in logarithmic scale in order to better appreciate the calibration effect: it allows for the optimization of the energy response on the two spectroscopic lines of the ^{22}Na source. At this stage, the energy resolutions of the block can be defined as the FWHM of the two energy peaks.

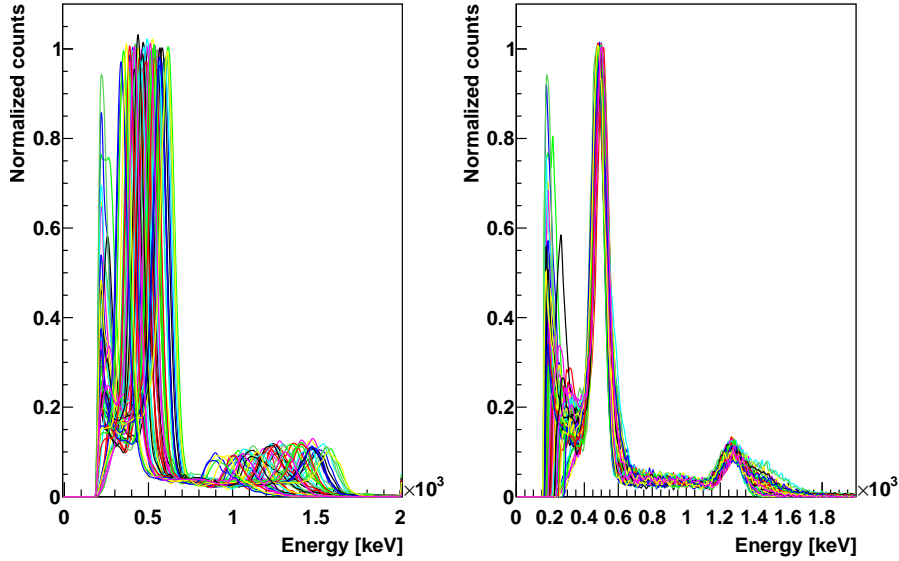
In Table 3.1, the energy resolutions derived after the calibration process are compared to the raw ones, obtained by the non-calibrated data.

Table 3.1: Comparison of the results obtained with the two pixel-assignment methods.

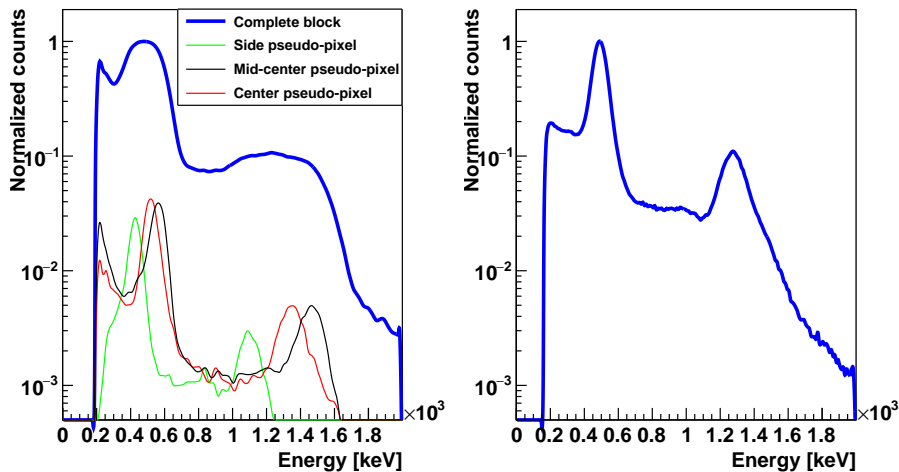
	Energy resolution @ 511 keV FWHM [%]	Energy resolution @ 1275 keV FWHM [%]
Before equalization	46.12	39.43
After equalization	23.03	18.04

The results reported in Table 3.1 show the need for the implemented calibration process, which allows to optimize the BGO block spatial and energy response.

Thanks to the assignment of each reconstructed event to a single pseudo-pixel, the relative efficiency can be evaluated on a single pseudo-pixel basis. The two color maps in Figure 3.33 show the number of events collected by the 64 pseudo-pixels during the ^{22}Na source homoge-



(a) Single pixel energy spectrum before (left) and after (right) equalization.



(b) Block energy spectrum before (left) and after (right) pixel response equalization.

Figure 3.32: Single pseudo-pixels (a) and whole block (b) energy spectra with the ^{22}Na source before (left) and after (right) the calibration process. The whole block spectra are reported in logarithmic scale. Three non calibrated spectra of pixels in reference positions (border, mid-center and center area) on the block are also reported with the non calibrated spectrum (a normalization factor has been applied for visualization purpose).

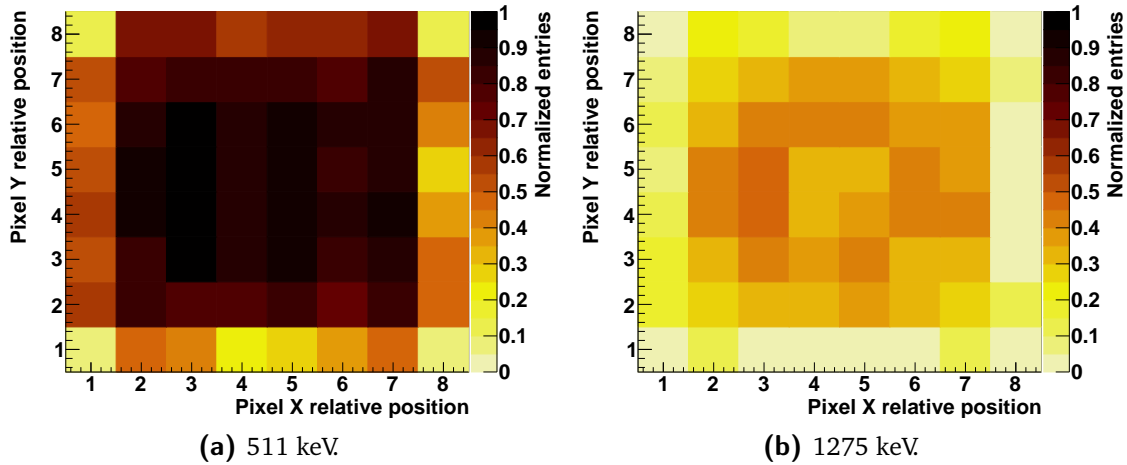


Figure 3.33: Relative number of entries for each pseudo-pixel as a function of the pixel relative position, represented by the row and column numbers (0 to 8 from left to right and bottom to top of the block surface). Figure(a) shows the entries in a selected energy window around 511 keV, Figure(b) in an energy window around 1275 keV. All the entries are normalized to the maximum collected number of entries, corresponding to 511 keV events in the central section of the block.

neous irradiation, with an energy selection performed on the two photons emitted by the source (511 keV events in Figure 3.33a and 1275 keV events in Figure 3.33b). The entries are normalized to the maximum number of entries in a pseudo-pixel, detected for a 511 keV energy selection.

Figures 3.33a and 3.33b show that the expected homogeneous distribution of events over the whole block surface is confirmed for the central pseudo-pixels of central lines (1 and 7), while the block borders present a factor 2-3 lower detection efficiency. In particular, the pseudo-pixels on the 4 corners (line 0 and 7, pseudo-pixels 0 and 7), have an efficiency of a factor between 5 and 6 lower with respect to the center of the block surface. This effect is partially due to geometrical factors, given the fact that the side pseudo-pixels are slightly smaller with respect to the central one (as also shown by the reconstructed 2D map in Figure 3.29b). In addition to this, the light collection is probably less performing in case of photons interacting on the block borders, causing the loss of events. By comparing the two maps, an overall reduced efficiency for the detection of photons beyond 1 MeV is verified. This is expected given the factor ~ 2 difference in the photopeak efficiency of BGO at 511 keV and 1275 keV (Saint Gobain 2016). Moreover, the reduced efficiency in the central block area for 1275 keV photons can be related to the photo-multiplier tubes round geometry, which determines a dead space in the center of the block back surface (Uribe et al. 2003). The effect of the dead area is diminished by the light sharing effect at low energy, but it becomes considerable in case of deep-penetrating higher-energy photons. In order to fully understand the relative and absolute efficiency of each block section, an irradiation with a collimated source scanning the whole active area is foreseen. This will allow one to precisely define the detection rate variations on the block active area.



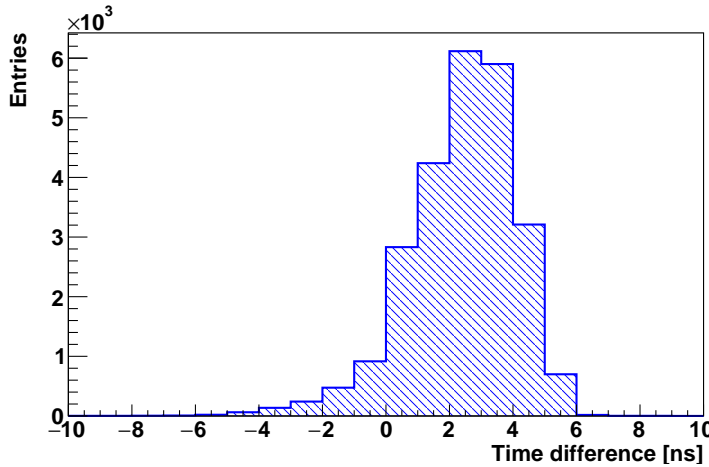


Figure 3.34: Distribution of arrival time differences between reference scintillator (a BaF₂ monoblock detector with 1 ns resolution) and BGO block.

3.2.2.9 Time characterization

Figure 3.34 shows the distribution of arrival time differences between the reference BaF₂ detector and the tested BGO block. The time resolution is defined as the FWHM of this distribution.

3.2.2.10 Results for the 30 blocks

In Table 3.2 the results obtained for the calibration and characterization of a set of 10 blocks are listed. The characterized blocks show very uniform results, with an average energy resolution of 25% FWHM at 511 keV and 20% FWHM at 1275 keV and an average time resolution of 4.42 ns FWHM tested with coincidences of 511 keV photons. Both the energy and time resolution are expected to be improved for the detection of photons in the prompt-gamma energy range, in particular above 1 MeV.

The last five blocks in the list of Table 3.2 showed detection problems, due to very low signal level on the read-out PMs or a poor spatial reconstruction accuracy with one missing pseudo-pixel on the two-dimensional map, probably due to crystal aging. The blocks with PMs issues will not be employed in the final absorber configuration, while the other two will be probably placed in the peripheral area in order to keep a wide active detection surface.

3.2.3 Hodoscope PMs characterization

The beam tagging hodoscope read-out is performed via 8 multi-anode PMs, Hamamatsu H8500 (Hamamatsu 2006), shown in Figure 3.10c. In order to guarantee a uniform response of the whole detector active area, composed of 256 scintillating fibers, the PMs must be previously characterized in terms of gain with a light source of fixed and known wave-length and intensity. The source selected for the measurements is a blue Light Emitting Diode (LED)

Table 3.2: Calibration and characterization results for 19 tested BGO blocks.

BGO block ID	Energy resolution @ 511 keV FWHM [%]	Energy resolution @ 1275 keV FWHM [%]	Time resolution FWHM [ns]
Ref. block			
7627	23	18	4.0
3166	27	24	4.4
3171	23	18	4.4
3184	24	20	4.3
3232	24	20	3.6
3280	24	19	4.3
3322	25	20	4.2
3972	25	21	5.2
4368	25	20	5.3
5243	25	19	3.9
7130	24	21	4.9
7218	25	21	2.1 
7240	25	20	6.7
7258	26	19	4.9
7369	23	19	4.3
7424	25	21	4.9
7581	26	23	4.1
7586	26	24	4.4
7601	24	19	4.1
7612	23	19	4.1
7624	22	19	3.9
7651	24	20	3.9
7657	24	19	2.7
14676	25	19	5.1
31210	25	21	4.8
3252	problem with PM 0		
3375	1 pseudo-pixel missing		
6823	1 pseudo-pixel missing		
7644	problem with PM 2		
7653	1 pseudo-pixel missing		
21097	problem with PM 2		
Complete set	25 ± 1	20 ± 2	4.5 ± 0.9

(Hewlett-Packard HLMP-CB), installed on the test-bench shown in Figure 3.35a and described in the following. The test-bench has been developed by the LPC AVIRM group (see [Gaglione 2013](#)) and adapted at the IPNL to a different acquisition system.

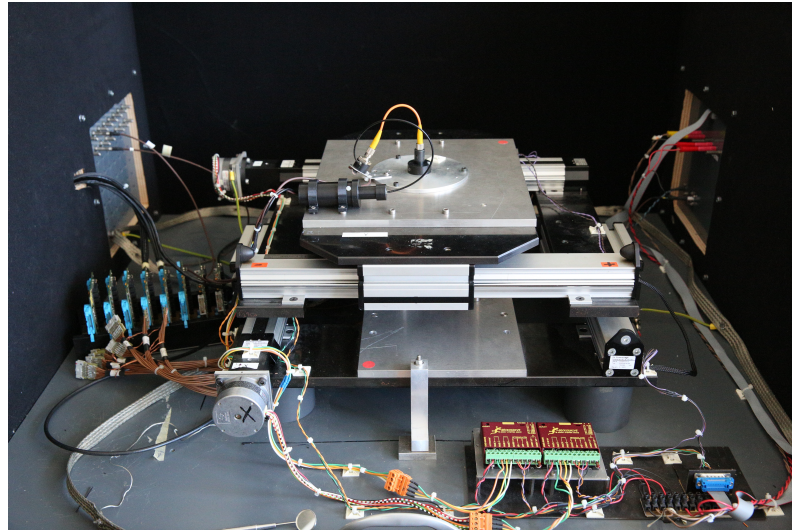
The goal of the characterization measurements is to trace a gain map of the whole PM surface, with the aim of storing calibration data to be used to both tune the PM working parameters (supply voltage and threshold) and correct the collected data. This is achieved by scanning the PM photo-cathode surface with the LED. The LED is so mounted on a motorized double-axis table, controlled by two G203V stepper modules provided by GeckoDrive Motor Controls ([GeckoDrive 2010](#)). The two axes have a total range of 20 cm each, and the step resolution achieved by the controllers is 20 μm . A metal support is set on the table in order to fix the LED. It produces light pulses synchronized with a pulse generator, which is also used as trigger signal for the acquisition system, as detailed later. The light pulse produced by the LED is split into two pulses with a 45°C mirror: one pulse is sent to the H8500 PM to be tested via optical fiber, in order to obtain a light beam perpendicular to the cathode surface (FWHM beam width estimated in 0.5 mm), the second one is detected by an Hamamatsu R5600 PM ([Hamamatsu 1995](#)), used as reference for the correction of temperature fluctuations. The PM under tests is fixed below the optical fiber output with a plastic support, not connected to the moving table. The whole described system is contained in a black box for external light shielding.

The output signals from the H8500 PM are initially amplified by custom pre-amplification cards: 8 cards are available and have been characterized in terms of amplification gain. Once amplified, the signals of the H8500 PM, together with the output of the reference PM, are sent to the acquisition system composed of a National Instrument PXI Express 1082 ([National Instruments 2010](#)) equipped with two 8-channel flash ADC modules (NI PXI-5105) and a two-channel ultra-fast digitizer (NI PXI-5154). The flash ADC modules have a maximum sampling rate of 60 MHz and are used for the read-out of the H8500 PM signals, while the ultra-fast digitizer, able to sample at a frequency up to 1 GHz, is used for the reference PM.

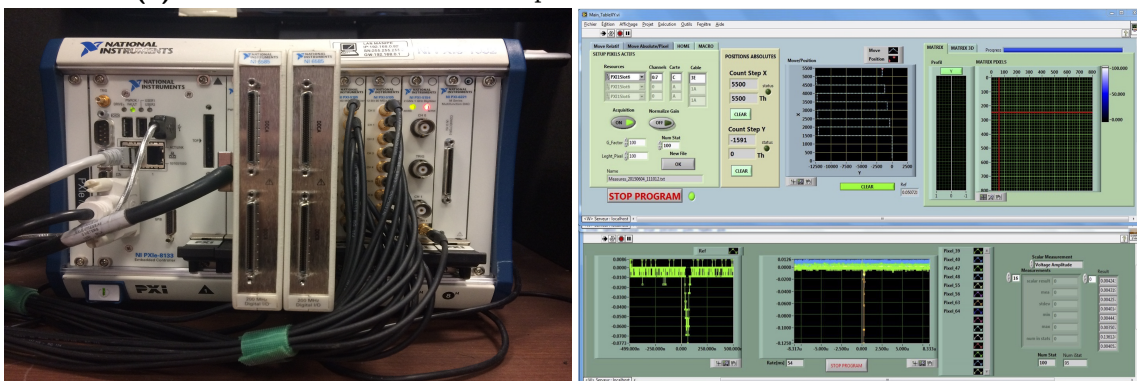
The acquisition and control software is developed with LabVIEW (2009) installed on the PXI; a picture of the software user interface is shown in Figure 3.35c. The PXI receives the signals from the two PMs and is also connected to the table stepper modules, so that the LabVIEW software can handle and synchronize data acquisition and table movements. The table movements can be automatized via LabVIEW macros, where step size, number and direction are stored and then used for the acquisition. The acquisition trigger, as mentioned, is given by the pulse generator which also controls the light pulses of the LED; in this way, a fixed number of pulses per table position can be recorded, and the measurement process is completely automatic. During the acquisition, the LabVIEW software automatically corrects the collected data according to the reference PM signal amplitude and to the pre-amplification card gain.

Given the limited number of flash ADC channels, only 16 PM pixels can be characterized per acquisition; four acquisitions are needed to scan the complete PM surface.

Each performed acquisition is set to scan a matrix of 4×4 PM pixels, and safety margins are arranged on the PM sides in order to ensure a complete surface irradiation. As shown in the schematic view of the PM in Figure 3.36a, the total PM size is $52 \times 52 \text{ mm}^2$, for an active area of about $49 \times 49 \text{ mm}^2$. The active area of the pixels on the borders is slightly wider than the central ones. In order to optimize the measurement process, a preliminary analysis has been done for the definition of the needed step length, and the details are reported in [Coudurier](#)



(a) Overview of the test-bench setup for the Hamamatsu PM characterization.



(b) National Instruments PXIe acquisition system.

(c) Example of LabVIEW software interface for the Hamamatsu PMs characterization.

Figure 3.35: Test-bench and tools for the characterization measurements performed on the Hamamatsu PMs of the beam tagging hodoscope.

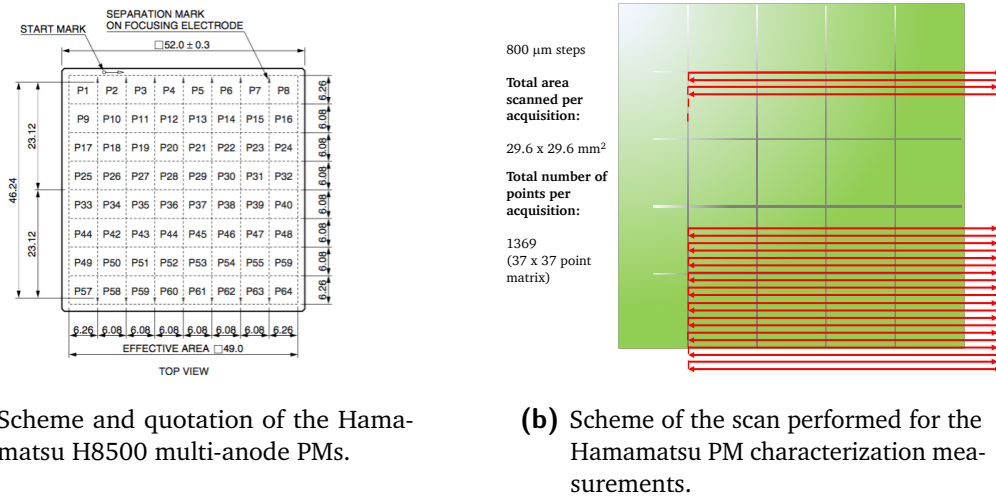


Figure 3.36: Details of the hodoscope PMs and of the performed characterization measurements.

2015. A trade-off between measurement accuracy, required time and stored data file size has been found with a step of 800 μm , so that each pixel is scanned with approximately 64 measurement points and the transition between neighboring pixels can be appreciated. A schematic of a table reference movement is presented in Figure 3.36b. To be noticed that for each irradiated point, 100 LED pulses are sent to the detector and the average amplitude value is calculated and collected.

The 8 Hamamatsu PMs have been completely scanned without the optical fiber mask used in the hodoscope and shown in Figure 3.10d, and the results are shown here for one reference PM. Some tests have been also performed with the fiber mask, in order to test the PM response mainly in terms of expected cross-talk between neighboring pixels. A complete result database has been created for calibration purpose.

Figure 3.37a shows the two-dimensional maps of a reference PM response for a complete irradiation, obtained with four separated acquisitions without the plastic fiber mask. Figure 3.37b shows the response of the same PM with the plastic fiber mask fixed on its surface. The reported signal amplitude has been normalized to the reference PM Hamamatsu R5600 for temperature oscillation correction.

In Figure 3.38 the two-dimensional response map for the 8 PMs are shown. In order to obtain a visual uniformity, the amplitude values have been normalized to the maximum value of each PM. We can observe response dis-uniformity on each PM surface, estimated in a factor ranging between 2 and 3. The retrieved response of each pixel will be useful for the calibration of the hodoscope final acquisition chain, in particular for what concerns the electronics FE settings (threshold and gain of each channel). In addition to this, these calibration measurements will allow for a proper data correction at the analysis stage.

The irradiation performed with the fiber plastic mask are also used to study the signal cross-talk between neighboring pixels, which is expected to be negligible according to the provider specifications, given for similar measurements and shown in Figure 3.39a. The analysis results for one of the studied PMs are shown in Figure 3.39b as reference.

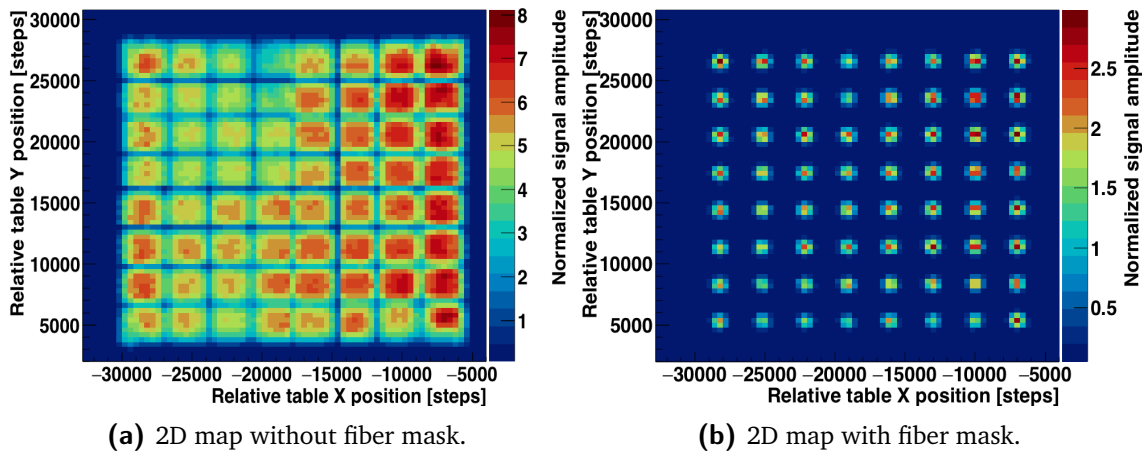


Figure 3.37: Two-dimensional response maps of one of the Hamamatsu PMs for the scintillating fiber hodoscope readout, obtained with the irradiation with a blue LED. The signal amplitude is normalized to the reference PM response.

The retrieved cross-talk is more important with respect to the provider specifications (to be noticed that the measurement conditions are slightly different), but always below 3% for the tested anodes. This cross-talk level is negligible and can be easily suppressed by a proper threshold setting.

3.2.4 Hodoscope fiber test with electron source

After the complete characterization of the Hamamatsu multi-anode PMs, they have been installed in the black boxes connected to the optical fibers of the hodoscope prototype, and the complete detection chain have been qualitatively tested to check the scintillating fiber light transmission to the optical fibers and to the read-out PMs. The observations have been performed by directly checking the pre-amplified PM output signal (with the same custom cards mentioned in the previous section) on an oscilloscope. A mechanical intervention has been necessary to fix some of the optical fibers not properly pasted to the plastic mask on the PM surface. In addition to this, a layer of black silicone has been added on the plastic mask surface to improve the light isolation on the only side where it is impossible to place the isolating black tape.

hodoscope prototype has been then tested with a beta source (^{90}Sr) for verification, and the obtained signal distributions (retrieved as before with an oscilloscope acquisition after signal pre-amplification) have been compared to simulation study performed by an internship Master 1 student (Vallois 2016). He tested simulation the irradiation of the whole hodoscope surface with an equivalent ^{90}Sr source to retrieve the deposited energy distribution on the scintillating fibers. This distribution can be compared to the collected signals amplitude distribution obtained with the experimental tests, in order to calibrate the relationship signal amplitude-deposited energy. The distance between the source and the fiber was set to 3 mm in the simulation code, to reproduce the gap created by the plastic box of the real source, which was directly on the fiber for the experimental measurements. In Figure 3.40 the results

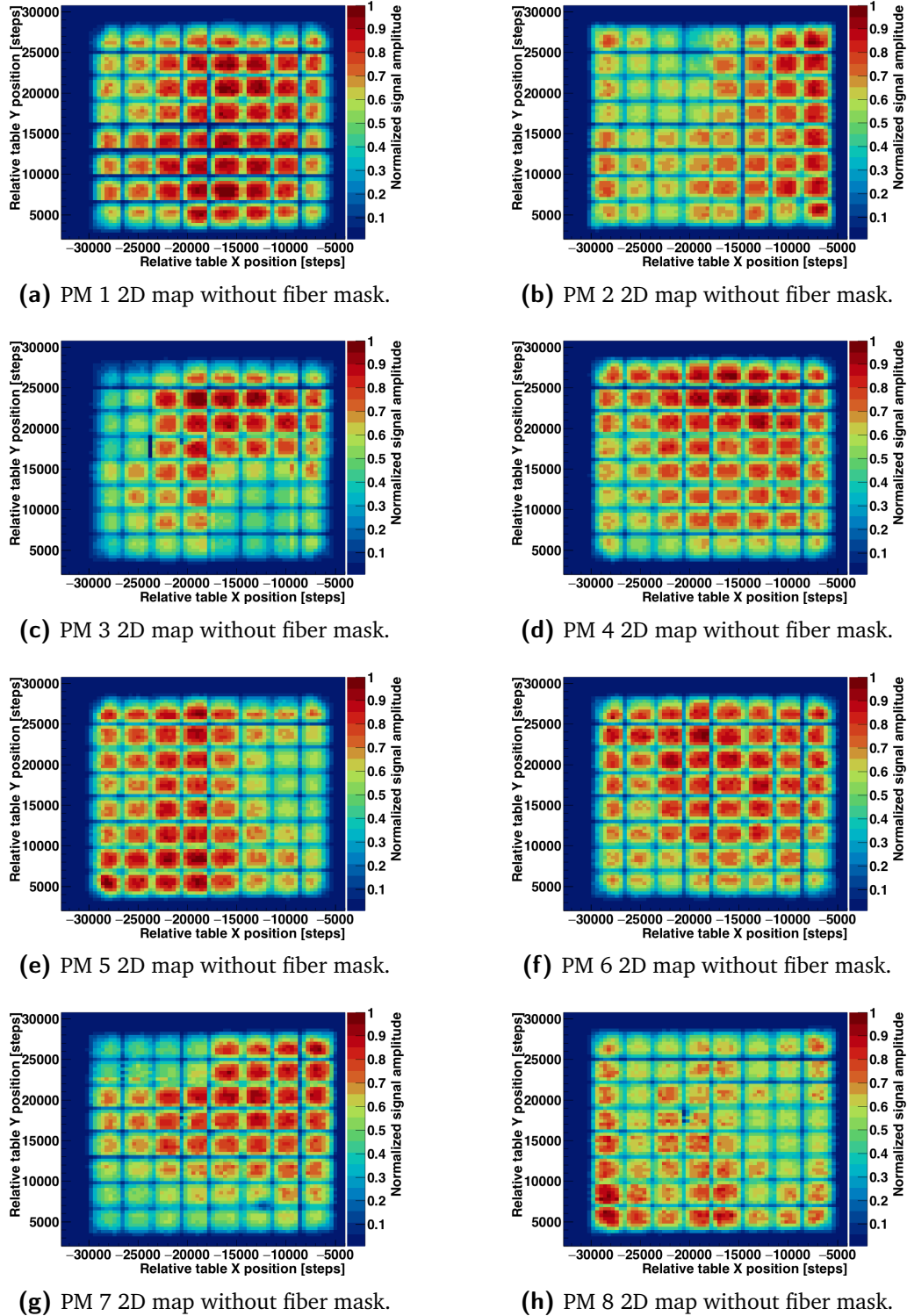
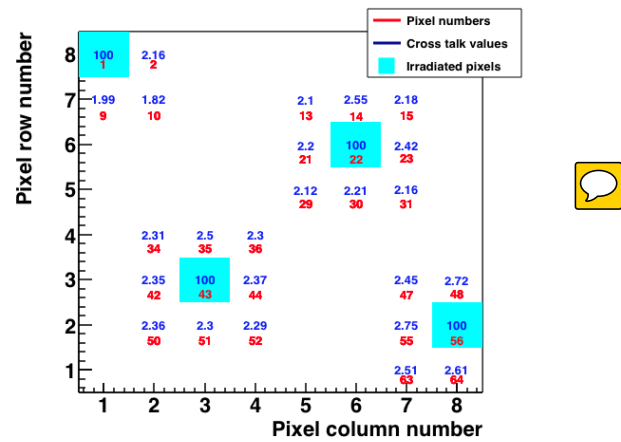


Figure 3.38: Two-dimensional response maps of the Hamamatsu PMs for the scintillating fiber hodoscope readout, obtained with the irradiation with a blue LED. The signal amplitude is normalized to the reference PM response and then to each PM maximum detected amplitude.

● Measured by using a fiber

FIBER SIZE: 1.0 mm Dia. (Kuraray; Clear Fiber NA=0.72)
LIGHT SOURCE: W-LAMP (W/BLUE FILTER)

	P1	P2	P3	P4	P5	P6	P7	P8	
P1	100	1.3	—	—	—	—	—	—	P8
P9	1.4	0.3	—	—	—	—	—	—	P16
P17	—	—	0.1	0.8	0.2	—	0.2	1.2	P24
P25	—	—	0.5	100	0.7	—	0.7	100	P32
P33	—	—	0.1	0.9	0.2	—	0.2	1.2	P40
P41	—	—	—	—	—	—	—	—	P48
P49	—	—	—	0.3	1.3	0.3	—	—	P56
P57	—	—	—	2.0	100	2.0	—	—	P64
P57	P58	P59	P60	P61	P62	P63	P64		



- (a) Signal cross-talk provided by Hamamatsu for the PM H8500 (Hamamatsu 2006). The measurements have been performed with a 1 mm diameter optical fiber; the irradiated anode is in the light blue box, and the cross-talk on the neighboring ones is expressed in %.

- (b) Signal cross-talk on a reference PM measured with a blue LED irradiation through the plastic fiber mask. The irradiated anode is in the light blue box, and the cross-talk on the neighboring ones is expressed in %.

Figure 3.39: Cross-talk study on neighboring PM pixels. The experimental results obtained with the irradiation with a blue LED through the plastic fiber mask on a reference PM (right) are compared to the specifications provided by the producer, measured in similar conditions (left). The cross-talk is expressed in % with respect to the irradiated anode, which is represented by the light-blue cell with 100% of the signal.

for a reference fiber are shown. The distribution entries have been normalized to the total number of events for visualization purpose.

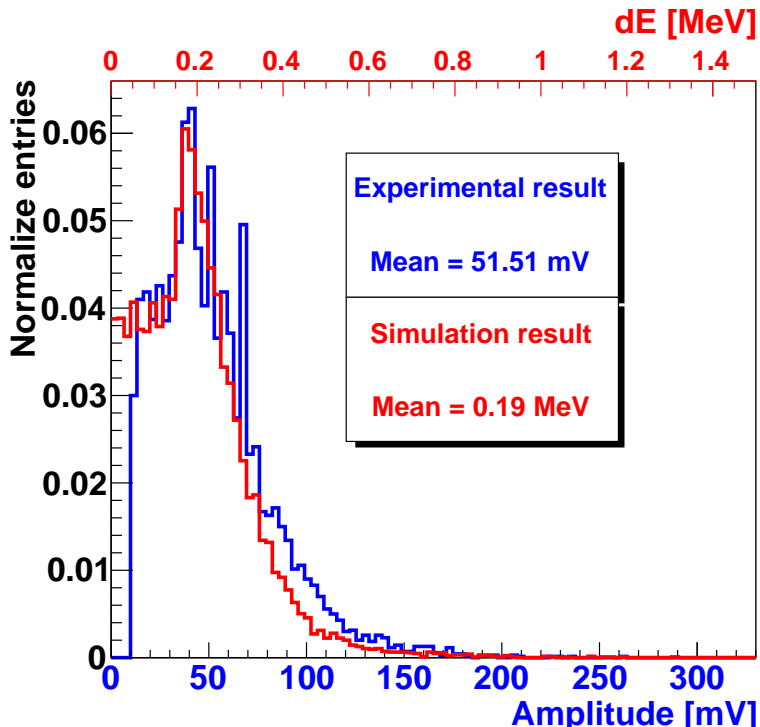


Figure 3.40: Comparison of the simulated distribution of energy deposited by electrons from the ^{90}Sr source on a single hodoscope fiber to the experimental signal amplitude distribution from a scintillating fiber irradiated with the ^{90}Sr source.

The comparison presented in Figure 3.40 can be useful as estimate of the expected signal for a given energy deposited by a ionizing particle (about 50 mV for about 200 keV of energy deposited). Knowing the applied amplification factor (given by the per-amplification card characterization) and the relative gain of each PM pixel, the expected raw signal integral can be estimated.

A complete characterization of the hodoscope acquisition chain will be necessary on proton and carbon beams in order to verify the beam primaries energy deposit on the scintillating fibers and tune the working parameters. In particular, the increased energy deposit expected for proton and carbons with respect to electrons should allow for a reduction of the high voltage applied to the PM. With reduced voltage, the detection rate capability would be improved. All these assumption will be tested on beam in the next future.

ADD HERE THE RESULTS OF THE SUMMER ABOUT THE ASIC GAIN AND THRESHOLD CHARACTERIZATION, AND COMMENT LINKING TO CHAPTER 6 FOR THE BEAM TESTS.

3.3 Summary and perspectives

The CLaRyS collaboration is developing in parallel two gamma cameras for ion beam therapy monitoring and nuclear medicine applications. At present, the detector components are be-

ing tested separately for characterization purposes at the IPNL. I presented in this chapter a complete description of the detector components with the related FE electronics, mechanical support, acquisition system and software tools, together with the all the characterization measurements I performed on the various detector sections. In the following, in addition to a short summary of the present status of the instrumental development of each camera component, I list the main task to be accomplished for the final integration a complete operation of the whole camera.

3.3.1 Silicon scatterer

Among the 10 DSSD layer provided by the seller, only 7 respected the design requirements and have been selected for the use in the Compton camera prototype. The 7 selected layer have been characterized in terms of leakage current with an acquisition system specifically developed for this purpose. Temperature cycles have been performed in order to precisely define the cooling performance needed to obtain the required noise level. These measurements allow to fix the working temperature to -20°C and lead to the conception and production of a thermal regulated box, working with cold air and so adapted to the clinical use. A modular mechanical support has been fixed inside the camera to sustain the silicon layers with their FE cards. The FE card has been designed and tested at the IPNL, and includes a custom ASIC which have been optimized with three different developed versions. The final version of the whole board have been produced in 7 copies in 2017 and they are now available for the next test stages.

The development of the FE board firmware is at present ongoing at the IPNL, and the first tests of data collection with a temporary acquisition system and injected charges have been performed. A further verification and optimization of the code will be carried out in the next future, and the silicon layers will be tested with their FE cards by the end 2018 with the μ -TCA acquisition system. The present AMC40 firmware performance has never been tested with the scatterer detectors before; some modifications can then be foreseen to optimize the data taking process, for what concerns both the stand-alone test mode and the operation within the complete system.

Moving to the thermal regulated box, its cooling performance has been tested without the detectors, so that a test with the power consumption of the seven operational detectors and boards has still to be performed. Additionally, the box has to be adapted to arrange the incoming and outgoing cables (power supply and data). Outside the box, a patch-panel will be also realized in order to properly set all the needed connections. The patch panel will be conceived to be integral to the box and adapted to the camera moving table, where the box will be installed for the final camera integration.

Once the acquisition will be fully operational, laboratory measurements with gamma sources are foreseen to characterize the detector response. Low energy gammas will be employed to test the DSSD energy resolution with full gamma absorption on a single strip basis, on p and n sides, while higher energy gamma irradiation is foreseen to study realistic detection conditions and verify efficiency, time and spatial performance (time resolution, average cluster size as a function of the energy). Once a full characterization of each channel of the 7 layer will be achieved, tests on beam with prompt-gammas are planned in stand-alone operation and, finally, with the complete Compton camera.



3.3.2 BGO absorber

As mentioned in the detector description section, the original camera design included 96 BGO blocks recovered from a dismantled SIEMENS PET system. The reconditioning process aimed to re-polish the crystal surfaces, tests the PMs with a light source and group them in quartets with compatible gains. As reported, the reconditioned block prototypes tested didn't show the expected improved performance, but on the contrary an overall signal degradation has been observed, probably due to a worsened light collection. Several configurations have been tested with non satisfactory results, so that the present camera is set up with 30 original blocks, which have been deeply studied and characterized at the IPNL, as detailed in section 3.2.2. The calibration and characterization method developed for the BGO block can be applied to similar detectors and represents an extension of previous studies (Golnik 2015; Hueso-González et al. 2015; Rogers et al. 1994; Tornai et al. 1994). Some of the features developed for the characterization tests, as the automatic research of the pseudo-pixel position and the pseudo-pixel assignation algorithm, will be used in the final camera at the data analysis stage, with simple adaptation to the camera acquisition system and data format. The complete set of characterization measurements described in this chapter have been performed with commercial acquisition systems and the required raw data treatment was performed with commercial NIM modules. The ASM red-out boards are at present under test at the IPNL, and their firmware must be optimized for the μ -TCA acquisition. Once ready, the complete acquisition chain will be tested, including the pre-trigger logic with the THOR board, the μ -TCA data collection and communication to the acquisition PC.

With a fully operational absorber, test with prompt-gammas (and so on proton and carbon beams) will be performed to test the block behavior in the prompt-gamma energy range, where an overall performance improvement is foreseen (in terms of space, time and energy resolution). Some tests performed at the GANIL in 2014, with an original block and an acquisition similar to the one employed for the characterization tests, showed promising results: in particular, a 2 ns FWHM time resolution was achieved with prompt-gammas (see Ley 2015). These results have to be verified with all the camera BGO blocks. Moreover, a first prototype of multi-slit collimated camera will be tested on beam with the final acquisition, and the coupling to the hodoscope is foreseen to perform the first TOF measurements. In addition to this, with proton and carbon beams the absorber geometry (in terms of block arrangement in the mechanical support) will be tested to obtain the optimal configuration with the minimization of dead areas between the blocks. To be noticed that different geometrical setup can be foreseen for Compton and multi-collimated camera, and for the peculiar desired measurement (detection of the all ion range, test of prompt-gamma distribution in the plane parallel to the beam line, etc.).

Concerning the mechanical support, it is finalized and already prepared for the integration on the moving table. As for the scatterer, a patch panel will be realized to arrange all the cables which have to be connected between FE and ASM cards. The 5 needed ASM cards will be placed in a dedicated VME crate, which will be integral to the table. Its setup will be fixed in order to minimize the interference with the table movements.

MODIFY HERE ACCORDING TO THE SEPTEMBER TEST! LINK TO CHAPTER 6

3.3.2.1 Absorber upgrade

One of the already identified main limitations of the Compton camera for the application in ion beam therapy monitoring at clinical beam intensity is the relevant background due to random coincidences. As already mentioned, the random coincidences can be created by secondary particles different from prompt-gammas, or, less likely, by two prompt-gammas in the same time window. The TOF solution has been verified to be efficient in reducing the first kind of random coincidences, and the background subtraction performance ensured by this method strongly relies on the detector time resolution. An improvement in the camera component time resolution would allow for a reduction of the coincidence window, further increasing the amount of rejected random coincidences.

A possible upgrade  the absorber detector has already been considered for a second version of the Compton camera prototype, and involves a commercial detector provided by Damavan Imaging, called Temporal Delta Compton. It is based on a scintillation LuYbO₃ or Cerium Bromide (CeBr_3) crystals coupled to very fast Philips DPC3200 Tile sensors  with a Single Photon Time Resolution (SPTR) of the order of 100 ps (Brunner et al. 2016). This excellent time resolution allows for a direct measurement of the scintillation light shower development within the crystal, resulting in the possibility to retrieve a 3D spatial information in parallel to a time resolution in the hundred of ps scale. This solution will be further discussed in the future and can be applied for a second prototype of the Compton camera.

3.3.3 Scintillating fiber hodoscope

Three prototype  of scintillating fiber hodoscope are available at the IPNL: 1×1 fiber, 32×32 fibers and the large size version with two planes of 128 fibers. The 1×1 fiber has been studied at the beginning of the development process as proof of concept, and the employed technology has been transferred to the two final prototypes with the required improvements. The increased size of the 128×128 fiber one lead to the addition of the two-sided  fiber read-out, for efficiency optimization and improved timing performance. All the other features are common to the two, including the installed multi-anode PMs (Hamamatsu H8500) and the related FE card. The advantage of the 32×32 hodoscope is the possibility to perform a complete read-out of the active surface with a single FE card, so that no synchronization features are required in the card and acquisition firmwares. This is the main reason why the first beam test performed on the hodoscope have been carried out with the small version (see chapter 6 for the description and the results of the beam tests). The FE card firmware is at present at the optimization stage, and the performed test allowed to define the needed improvements, mainly connected to the time measurements capabilities. In addition to this  the synchronization of the 8 cards used for the read-out of the 128×128 fiber prototype  must still be achieved. The first acquisition tests performed during the proton beam exposure allowed to validate the acquisition software and the μ-TCA firmware in a simple version, but additional trigger features must still be added to integrate the hodoscope in the final camera configuration. Concerning the detector performance, the optimization of the working parameters (gain and threshold of each read-out channel) required the development of an automatic measurement system, which will be employed on beam to perform similar characterization in presence of proton induced signals. Finally, the mechanical support is fully operational: the motor steering must be integrated in the slow-control software.

The overall development is at the final stage, and the integration of the hodoscope in a first multi-slit collimated camera configuration is foreseen, as mentioned, in order to perform preliminary test of TOF background rejection capabilities. 

MODIFY HERE ACCORDING TO THE SUMMER RESULTS AND SEPTEMBER TEST

3.3.3.1 Hodoscope upgrade

As already explained concerning the absorber possible upgrade, the main direction for an improved camera prototype is the optimization of the detector timing capability. The LPSC group in Grenoble is developing high time resolution diamond detectors, which can be considered for a new version of the beam tagging hodoscope. The so-called MoniDiam project aims to develop a diamond based hodoscope prototype with the related fast electronics to enable a time resolution of a few tens of ps. In addition to this, the diamond based detectors are intrinsically affected by a very low noise level and allow to overcome the radiation hardness limitation imposed by the present scintillating fiber prototype, together with further extending the rate capabilities to an expected 100 MHz acquisition rate. Some tests of small diamond detector prototypes have already been performed with pulsed beams at the European Synchrotron Radiation Facility, Grenoble, France (ESRF) in Grenoble and with 95 MeV/u carbon beam at the GANIL, with promising results: a polycrystalline detector, $5 \times 5 \times 0.3$ mm³, exposed to the 95 MeV/u GANIL carbon beam, showed a time resolution of 37 ps RMS coupled to an energy resolution of the order of 7% RMS for 25 MeV of deposited energy (see Gallin-Martel et al. 2016). Similar measurements performed with diamond crystal with different sizes showed compatible results, with a time resolution between 20 and 90 ps RMS and an energy resolution between 7 and 9 % RMS (Gallin-Martel, M.-L. et al. 2018). A large area prototype of 15×15 cm² is expected to be tested in 2019 and is a good candidate for a improved versions of the Compton and multi-collimated cameras.

3.3.4 Acquisition and software

The acquisition μ -TCA based system development is managed by the CPPM research group, and frequent tests has been performed at the IPNL to verify and integrated its functionality to the read-out detector cards. As reported in the description, it should be able to receive and treat the trigger signal generated by the absorber for the multi-collimated camera or by the silicon scatterer for Compton one, collect the data flow from all the detectors, group them into UDP packets with the proper format and send them to the acquisition PC. The main tasks (data collection, packet creation and communication to the PC) have been already verified on beam for a single detector and a single FE board, so that now the trigger treatment capabilities and the ability to handle all the detectors components have to be developed in the AMC40 firmware and tested with the final system. Moreover, the μ -TCA must also be able to transfer the slow control signals sent by the LabVIEW software to the selected read-out cards; this feature is still at the debug stage.

Concerning the acquisition software, it has already been tested and validated with a data simulator, with a maximum achieved acquisition rate of about 300 Mb/s, sufficient to manage the

data from the complete camera (see appendix A). It will be tested step by step with the increasing number of FE boards involved in the measurements. In parallel, the monitoring software is now available and operational for each single detection section, but an optimize version allowing for an on-line visualization of the whole camera acquisition must still be studied. Finally, the slow control software development is ongoing; all the required working parameters can already be controlled by different pieces of software, which must be integrated in a complete user interface and tested with the μ -TCA for what concerns the FE cards configuration. All the parameters related to the moving table motors (for camera and hodoscope), detector and card low and high voltage, have already been tested and do not require the μ -TCA intervention.

3.4 Conclusions

During the three years of my PhD thesis, the instrumental development of the single detector components, as well as of the two cameras, saw an important advancement, thanks to the synchronized effort of the whole collaboration. In this chapter, the advancements achieved in the last years have been described in details, including, in addition to my personal contributions, results obtained before the beginning of my PhD thesis or in parallel by CLaRyS collaborators.

I personally characterized the hodoscope PMs as described in section 3.2.3, following the preliminary internship work of a master student (Coudurier 2015) and using an instrumental setup already created by a previous PhD student (Gaglione 2013). During the first months of my work, I adapted the acquisition system in order to perform automatic scans of the hodoscope PM surfaces, I acquired data for the whole set of available PMs and I performed the complete data analysis to produce the results presented in the description section. In parallel, I studied in simulation the design of the lead collimator produced to host the ^{60}Co high activity source described in section 3.2.2. The source was originally foreseen to be employed for the characterization of the scatterer silicon layers, so that I optimized the design of the three apertures (point-like, linear and squared) in order to obtain the desired irradiation of the DSSDs layer surfaces. The collimator structure is designed, in collaboration with the radiation protection IPNL expert, to allow the source usage in a “public” area, so that the geometrical configuration is imposed by these constraints. The collimator production has been performed by an external company, and I directly participated in the source positioning inside the collimator, as well as to the radiation tests in its final location. Since the beginning 2016, I focused my efforts on the hodoscope, starting from the 128×128 fiber prototype mounting (I installed the characterized PMs) and testing with a simple acquisition, in order to verify the optical fiber and scintillating fiber connection. I identified the defective channels and participated in the fixing process with the mechanics IPNL group. After that, with the help of a master student, I performed a first characterization of the complete read-out chain for each channel, and compared the results of the irradiation with a beta source to simulation, for a preliminary detector calibration (see section 3.2.4 and Vallois 2016). In the following months I mainly focused on the simulation works presented in chapters 4 and 5, participating in parallel to the electronics development advancements. In particular, I collaborated with the IPNL electronics group to the characterization of the scatterer FE card in terms of electronic noise, by analyzing and discussing the collected data. Since the beginning of 2017, my attention was directed to the absorber components. As described in section 3.1.3, the whole set of original recovered block should have been “reconditioned” in order to be adapted and

optimized to the new application in the CLaRyS gamma camera, and I directly worked on the test and characterization of the first reconditioned blocks received by the LPC group. With the help of a master student working for its internship, we developed an acquisition system based on the BGO block acquisition card, commercial NIM modules and the PXI described in section 3.2.3, and we tested several blocks reconditioned with different methods, in comparison to a reference original block. The test results are reported in [Sandjong et al. 2017](#) and were not satisfactory, so that we decided to move to the application of original, “non-reconditioned” blocks, with a reduced size absorber configuration. The acquisition system we developed to characterize the reconditioned blocks have been used to test the original ones, which I completely characterized starting from September 2017. During the characterization process, I optimized, with the participation of a master student, the test method and developed the analysis and performance optimization process described in section 3.2.2 and published in [Fontana2018](#). Concerning the mechanical supports, I participated in the design and realization of the reduced-size camera absorber support, in the final configuration of the hodoscope moving table, with particular focus on the setup of the patch panel for the cable connections, and to the first cooling tests involving the thermal regulated chamber to be employed with the scatterer layers. Moreover, I worked with IPNL colleagues to develop the LabVIEW based remote controlled of the camera moving table described in section 3.1.7 and shown in Figure 3.16b, which is still under test. Moving to my contribution to the camera software, I personally developed all the analysis code used to produce the results presented in this chapter, with the exception of the scatterer layer tests. Furthermore, I developed the camera monitoring software described in section 3.1.6, and I always participated in the optimization of the acquisition software, coded by the IPNL computing group, as well as in the design of the different acquisition card firmwares. Finally, I tested the hodoscope on beam during three tests campaigns, described in details in chapter 6.

The project is now reaching the final stage, where all the performed laboratory test and development studies will be transferred to the multi-collimated and, even most, to the Compton camera, which is foreseen to be tested on beam before t

4

Compton camera application for ion beam therapy monitoring

5

Compton camera application in nuclear medicine

Most of the results presented in this chapter have been published in (Fontana et al. 2017a) and (Fontana et al. 2017b).

Contents

5.1 Introduction	92
5.2 Material and methods	93
5.2.1 Radioactive sources	93
5.2.2 Compton camera simulation and data analysis	93
5.2.3 Anger camera simulation and data analysis	98
5.2.4 Figures of merit for the comparison study	104
5.3 Results: Compton camera study for SPECT application	104
5.3.1 Influence of Compton camera scatterer detector energy resolution . .	105
5.3.2 Compton camera coincidence study	106
5.3.3 Compton camera desing study	107
5.4 Results: Benchmark of Compton camera and Anger camera performance	108
5.5 Summary and discussion	110

5.1 Introduction

Single Photon Emission Computed Tomography (SPECT) is one of the most widespread techniques for nuclear medicine diagnostics examinations. In most of the clinical cases, a radio-tracer is injected in the patient and the emitted γ -rays are collected by scintillating detectors coupled to physical collimation systems. This process leads to the reconstruction of a planar transmission image. Such a kind of imaging tool relies on the first idea proposed by Hal Anger ([Anger 1958, 1964](#)), and it is now commercially available in different variants with peculiar features and applications. A complete system is often composed of at least two rotating detection heads, allowing a tomographic data acquisition and the reconstruction of a three-dimensional image of the radio-tracer distribution (see chapter 1 for further details).

The main consequence of the collimation system is a forced trade-off between sensitivity and spatial resolution: The spatial resolution is completely determined by the collimator geometry, and it can only be increased by reducing the collimator hole size, at the expense of a reduction in the detector sensitivity since fewer photons survive the mechanical selection. Moreover, the collimator thickness and septa limit the primary energy acceptance, and the performance of Anger cameras generally downgrades as the energy increases.

In order to overcome this mechanical collimator limitation, it is natural to move towards an “electronic collimation”, where the emitted photons are tracked and the emission point is reconstructed via Compton kinematics, and so to the application of Compton cameras in this field ([Everett et al. 1977; Singh 1983](#)).

L. Han and colleagues ([Han et al. 2008](#)) have performed a simulation work comparing a standard Anger camera and a Compton camera prototype for a fixed source energy of 364 keV (Iodine-131 (^{131}I) gamma ray emission). The expected enhanced detection efficiency associated to the Compton camera with respect to the Anger system was estimated to a factor 20 at the tested energy, while the spatial resolution was compared for equal imaging time.

Starting from the results of Han and colleagues, we tested in simulation the performance of the CLaRyS Compton camera prototype (see chapter 3) for the application in SPECT. The aim of this simulation work consists in extending the aforementioned study to a wide energy range, with simplified analysis methods. The CLaRyS prototype is compared to the Infinia Anger camera delivered by General Electrics Healthcare ([GE Healthcare 2006](#)). The detector performances are compared in terms of efficiency and spatial response with the exposure to mono-energetic point-like radioactive sources at different energies, ranging from 245 keV to 2.614 MeV. The noise components related to the target (patient), such as photon attenuation, photon diffusion, patient movements, are common for both detectors and not considered in this context.

It should be noticed that the Compton detection principle requires coincidences between the two detector sections (scatterer and absorber), so that the random coincidence rate plays a fundamental role in the complete system performance, like in Positron Emission Tomography (PET) machines. The effect of these random coincidences will therefore be investigated. Moreover, a reliable Compton scattering cone reconstruction requires a precise energy resolution for the scatterer section of the detector. The influence of this parameter will be studied. Finally, the Doppler broadening effect will be quantified to give the physical limits of the Compton

imaging technique knowing that silicon corresponds to the lowest Z material available for gamma detection with precise energy resolution. A comparison with a different possible scatterer material is also performed for verification.

All the obtained results are discussed with direct reference to (Han et al. 2008), focusing on the possible advantages offered by the use of a Compton camera (in particular the CLaRyS prototype), which intrinsically introduce the possibility to update the clinical standards in terms of source kinds, energies and activities, examination duration, patient dose, imaging techniques.

5.2 Material and methods

In this section, the sources of gamma rays simulated for the study are presented and discussed and the two simulated systems are described in detail, as well as the proposed analysis techniques. In addition to this, some comments are given about the criteria chosen to represent a relevant comparison between the two investigated detectors.

5.2.1 Radioactive sources

Both simulated systems have been exposed to monochromatic point-like gamma sources in air. The performance of the two cameras has been studied in terms of spatial resolution and detection efficiency as a function of the gamma source energy, related to actual radioemitters, already used in clinical practice or suggested for this kind of application in previous works (Nurdan et al. 2015). The explored energy range was chosen having in mind the possible clinical usage of Compton systems like the one developed by the CLaRyS collaboration, to extend the present field of application of SPECT imaging.

In Table 5.1, the characteristics of the considered radioactive sources are given. Most of the sources do not emit gamma rays at a single energy, but only the ones selected for this study are presented in the table, together with the related branching ratio.

5.2.2 Compton camera simulation and data analysis

5.2.2.1 Simulation settings

The simulation code for the Compton camera was developed with GEometry And Tracking 4 (GEANT4) v.9.6 and the camera design is based on the specifications of the prototype at present under development by the CLaRyS collaboration, detailed in chapter 3. It should be noticed that the real size of the detector components slightly differs from the ones reproduced in simulation, which have been used in the code for simplicity. The geometric setting of the camera has initially been optimized for the application in ion therapy monitoring via prompt-gamma emission (see chapter 4) and has been adapted for SPECT for this study in order to maximize the similarities between the two systems (Compton and Anger camera) in terms

Table 5.1: Radioactive sources used in the comparison study. Decay mode list: EC for electron capture, $\beta-$ for electron emission, $\beta+$ for positron emission, IT for isomeric transition. Half-life expressed in days (d), hours (h) or minutes (m). Data extracted using the National Nuclear Data Center On-Line Data Service from the Evaluated Nuclear Structure Data File database, file revised as of (2017-05-17) (Bhat 1992).

Isotope	Gamma energy [keV]	Branching ratio [%]	Decay mode	Half-life
Indium 111	245	94.1	EC	2.8 d
Iodine 131	364	81.5	$\beta-$	8 d
Yttrium 91m	555	95.0	IT	50 m
Bismuth 212	727	6.7	$\beta-$	60 m
Iodine 132	773	75.6	$\beta-$	2.3 h
Iron 59	1099 - 1292	56.5 - 43.2	$\beta-$	45 d
Zinc 65	1116	50.0	EC / $\beta+$	244 d
Calcium 47	1297	67.0	$\beta-$	4.5 d
Magnesium 28	1342	54.0	$\beta-$	21 h
Sodium 24	1368	100.0	$\beta-$	25 h
Potassium 42	1524	18.1	$\beta-$	12 h
Thallium 208	2614	99.8	$\beta-$	3 m

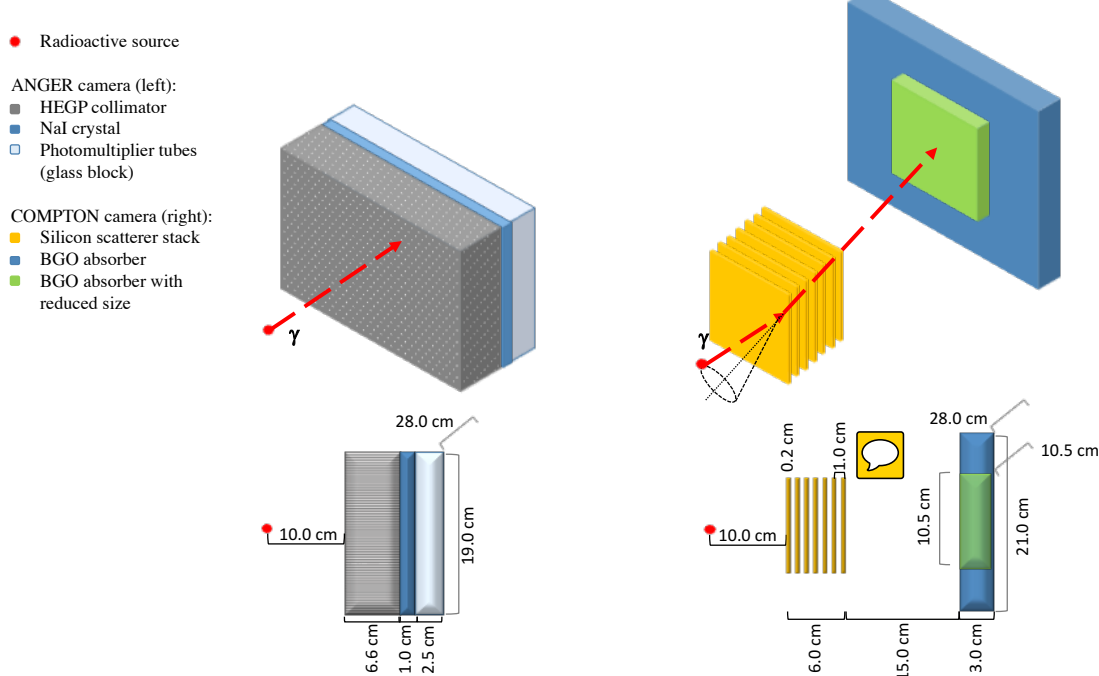


Figure 5.1: Sketch of the simulated geometry of the two systems: Anger camera (left) and Compton camera (right), in 3 dimensions (top line) and side projection (bottom line).

of detector acceptance, as detailed in the following. A SPECT specific optimization would depend on the choice of the particular gamma energy and it has not been studied yet.

The distance between the last silicon plane (center) and the center of the absorber is set to 15 cm (see Figure 5.1). Moreover, the absorber size has been adapted to be as close as possible to the Anger camera detector, maintaining the real Bismuth Germanium Oxide - Bi₁₂GeO₂₀ (BGO) block size. As a result, a matrix of 8×6 blocks has been arranged, for a total surface of 28×21 cm². In the work of Han and colleagues ([Han et al. 2008](#)) a Philips camera was described in GATE as Anger system and the same NaI absorber detector was adapted for the simulation of the Compton system with the introduction of silicon pad detectors as scatterer part. The two geometries compared in this study are slightly different but the common absorber size strategy has been maintained.

The values for energy and spatial resolution of the silicon and BGO detectors used in the simulation were derived from the first tests performed on the detector prototypes (see chapter 3). For the silicon planes, the energy resolution is obtained from the Equivalent Noise Charge (ENC):

$$\sigma_E = W_{Si} \sqrt{ENC^2 + F_{Si} \frac{E_{dep}}{W_{Si}}}, \quad (5.1)$$

where $F_{Si} = 0.115$ is the silicon Fano factor, E_{dep} is the energy released in the detector (in eV) and W_{Si} is the energy required to create an electron-hole pair in silicon (3.6 eV). The ENC strongly affects the detector performance and it will be analyzed in the following.

The spatial resolution was set according to the geometric parameters considering that the employed Double-sided Silicon Strip Detectors (DSSDs) have a total of 64 strips per side, with a pitch of 1.4 mm. The position of each interaction is set in the center of the strip where it is recorded in both detection planes. Charge sharing on neighbor strips can in principle allow for sub-pitch resolution, but according to preliminary characterization measurements the probability of such a kind of events is less than 10%, and will be so neglected. The interaction depth is set as the center of the involved detector slab. The time resolution has been set to 20.0 ns Full Width at Half Maximum (FWHM) based on characterization measurements performed at the Grand Accelerateur National d'Ions Lourds, Caen, France (GANIL) accelerator in France and in the lab at Institut de Physique Nucléaire de Lyon, France (IPNL) (see chapter 3 and [Ley 2015](#)).

The energy and timing resolution in the BGO blocks are set to 21% FWHM and 3.0 ns FWHM respectively, also based on characterization measurements performed with a cesium-137 source (662 keV gamma ray emission) and at the GANIL with prototype blocks. Concerning the spatial resolution, it has been verified that a sub-pixel resolution is not achievable on a single event basis, it is therefore fixed to the size of a single pixel (see chapter 3). Each block surface is streaked with an 8×8 pixel matrix, 4.4 mm side, not reproduced in the simulation code. Each interaction is assigned to the center of the pixel where it is localized at the analysis stage, while the interaction depth is set at the center of the involved block.

5.2.2.2 Data collection and analysis

The radioactive source is placed at 10 cm distance from the first silicon detector, in the center of the scatterer stack transverse surface, and the number of simulated primaries is set to 10^7 gammas per energy step. To speed up the simulation, the primary gammas are emitted in a direction within the acceptance cone defined by the first Compton camera silicon plane. All results are then normalized to the full solid angle.

All the events with at least one interaction in a silicon plane or at least one interaction in a BGO block are stored during the simulation process in two data sets, one per detector section. A small fraction of events presents interactions in more than one scatterer plane (< 1% at 245 keV) and/or in more than one BGO block (~8% at 245 keV). This kind of events leads to ambiguities in the cone reconstruction, because the cone vertex and axis are not univocally defined, and it is not treatable via List Mode-Maximum Likelihood Expectation Maximization (LM-MLEM) reconstruction. Alternative reconstruction algorithms (such as the one included in the Medium-Energy Gamma-ray Astronomy library (MEGAlib) (Zoglauer et al. 2006)) are able to estimate the most likely scenario for multiple interactions, at the expense of larger uncertainties and longer calculation time. The multiple interaction events, representing approximately 8% of the total at 245 keV, are then refused in this study for simplicity. This choice reduces the detection efficiency, so that the value obtained here could be seen as the lower limit for this kind of detection system. Once the two lists of events are built, the time coincidences are defined according to the source activity, the detector geometry and the single detection section time resolution. Finally, the emission points are reconstructed with a LM-MLEM algorithm developed by the Centre de Recherche en Acquisition et Traitement de l’Image pour la Santé, Lyon, France (CREATIS) institute in Lyon (Lojacono et al. 2013). The iterative algorithm reconstructs the Compton cones from the position and energy deposited in the scatterer stack and in the absorber blocks. A reconstruction volume must be defined, as well as a voxel 3 dimensional matrix in this volume. For this study the reconstruction volume has been fixed to $5 \times 5 \times 5 \text{ cm}^3$ around the source, with a matrix of $51 \times 51 \times 51$ voxels, and 15 algorithm iterations: this number is a compromise between reconstruction performance and calculation time.

5.2.2.3 Compton camera study for SPECT application

As already mentioned in the introduction, a critical parameter in the Compton camera performances is the scatterer detector energy resolution. The goal of the instrumental development is to obtain an energy resolution as close to 1 keV (σ_E) as possible. The silicon detectors composing the stack have been tested at various temperatures in order to understand the behavior of the electronic noise and of the leakage current, and the read-out electronics is being developed with the aim to reduce the electronic noise (see chapter 3). The first laboratory tests showed an energy resolution at 25°C of approximately 10-15 keV FWHM with a first read-out card prototype. The new card has been tested with simulated signals and gives a noise level closer to the expectations. No data are yet available to determine the detector energy resolution at different temperatures and with the final card version. In the simulation two different resolutions have been considered in order to verify the influence of this parameter on the final reconstructed image. The two chosen values are $\sigma_E = 2 \text{ keV}$ and $\sigma_E = 4 \text{ keV}$, corresponding to about 5 keV and 9.5 keV FWHM, respectively, both calculated at 200 keV of released energy

using equation 5.1. The influence of Doppler broadening has also been studied by disabling the Doppler effect in the simulation with the energy resolution set to $\sigma_E = 2 \text{ keV}$. Finally, a different possible scatterer material, Cadmium Telluride (CdTe), has been tested at the same resolution in order to verify the expected advantage given by the choice of silicon.

A coincidence study is mandatory to define the source activity to be used in the simulations dedicated to the benchmark with the Anger camera. Timing information is not included in the simulation code and a time structure must be assigned to the simulated primaries at the data analysis stage. A reference time is chosen randomly from an uniform distribution between 0 s and the data acquisition time and assigned to a primary photon. The data acquisition time (T_{DAQ}) is calculated as the expected time needed for the emission of the desired number of primaries ($N_{\text{primaries}}$) according to the source activity A_{source} :

$$T_{\text{DAQ}} = \frac{N_{\text{primaries}}}{A_{\text{source}}}.$$
 (5.2)

The source activity is not fixed at the simulation stage but only during data analysis afterwards. It can therefore be easily modified to perform a study of the camera performance with different kinds of sources. The scatterer and absorber interaction times are calculated with respect to the reference primary emission and included in the related data sets for the analysis.

Two sets of data are produced as output of this analysis, one for the scatterer and one for the absorber. Each element in the two sets corresponds to an interaction in the detector and includes the 3 dimensional position, energy released, time with respect to the total data acquisition time and primary reference index provided by the simulation. The elements in the two data lists are ordered for increasing time. The detectors time resolution specified in section 5.2.2 and a time window set to 20 ns, corresponding to a 3σ acceptance, are then used for the coincidence definition for different source activities. The time of each element in the absorber data set is compared to the time of the elements in the scatterer data set. A coincidence is defined when the scatterer event time is within the time window centered in the absorber event time. Each element is used one time and the analysis continues until the end of the absorber data list. If the two elements (one from the scatterer data set and one from the absorber one) forming a coincidence have the same reference index, they correspond to interactions of the same primary photons and the coincidence is then a true one. If the reference index is different for the two elements, the coincidence is random. The number of true and random coincidences has been studied as a function of the source activity in a range of clinical interest between 1 MBq and 500 MBq, for a fixed energy value of 555 keV. The variation of the influence of random coincidences as a function of the energy was also investigated at a fixed source activity of 200 MBq.

The scatterer energy resolution and the source activity have been fixed for the benchmark study. The choice of their values is discussed in section 5.3.

Finally, with the same scatterer energy resolution and the source activity, the design of the Compton camera has been tested for this specific application, in particular for what concerns the number of employed scatterer planes. In addition to the original design configuration with seven DSSDs, additional sets of simulations have been performed at four reference primary gamma energy reducing the number of layers in each set, in order to assess the camera opti-

mal configuration as a function of the gamma energy. The results are shown in section 5.3.3 and are expressed according to the figures of merit used for the benchmark study (see section 5.2.4).

5.2.3 Anger camera simulation and data analysis

5.2.3.1 Simulation settings

The Anger camera system is simulated with GEANT4 Application for Tomographic Emission (GATE) v.7.1 and it is based on the General Electrics Healthcare Infinia SPECT system ([GE Healthcare 2006](#)), a commercial clinical camera with parallel hole collimator and Sodium Iodide doped with Thallium (NaI(Tl)) scintillator. A single detection head is simulated in order to obtain a direct performance comparison to the Compton system.

The chosen configuration includes a High Energy General Purpose (HEGP) lead collimator, 6.6 cm thick, with a surface of $28 \times 19 \text{ cm}^2$ (see Figure 5.1). The parallel hole grid is composed of hexagonal shaped holes, 0.2 cm radius, arranged in a quincunx structure, with a septal thickness of 1.8 mm. This collimator is optimized for energies below 364 keV, corresponding to the main gamma emission energy of ^{131}I . The NaI(Tl) crystal is simulated as a single block of $28 \times 19 \times 1 \text{ cm}^3$, in contact with the collimator back surface and read out by photo-multiplier tubes. The photo-multiplier grid is represented with a glass block of 2.5 cm thickness behind the crystal, with the same transverse surface (see Figure 5.1). The spatial and energy resolutions have been set according to the manufacturer specifications. Unless otherwise stated, their values correspond to one standard deviation. A lower detection energy threshold has been set to 80 keV.

The source is placed at 10 cm distance from the collimator surface (the distance chosen in the Infinia data sheet), as for the Compton camera with respect to the first silicon layer, and its transverse position corresponds to the center of the central collimator hole. For each source energy, 10^8 primary photons are simulated in 4π . An event corresponds to single or multiple interaction of a photon (or secondary particle produced by the photon interaction in the collimator) in the NaI(Tl) crystal. All the detected interactions are computed and the gamma interaction position is calculated during the simulation as the center of gravity of the positions of all the hits (energy transfers of secondary electrons), with the deposited energy as weight for the calculation. The deposited energy corresponds to the sum of the energies released during each hit. A set of interaction points and energy deposited is then stored.



5.2.3.2 Data analysis

Four source primary energies have been chosen as references of the studied energy range and are used in the following to show the analysis method and the study results. The low energy range is represented by the Indium-111 (^{111}In) emission at 245 keV, the first energy above the Anger camera construction limit has been set to 555 keV Yttrium-91m (^{91m}Y), while Iron-59 (^{59}Fe) at 1099 keV and Potassium-42 (^{42}K) at 1524 keV have been chosen to represent the medium and high energy range respectively.

Figure 5.2 presents the raw radial event distributions for the four reference energies. Each distribution bin content is normalized according to the surface of the circular region corresponding to each radius. The first distribution bin always corresponds to the radius of the central collimator hole, with the partial inclusion of the surrounding septa. This choice is determined by the detector and collimator geometry and by the source position. It is possible to list three different kinds of events contributing to the radial distributions:

1. photons passing through the collimator holes without interactions,
2. photons traversing the collimator septa without interactions,
3. photons interacting in the collimator septa.

Only the first listed contribution transports true spatial information about the source location, and these photons generate the signal. All other kinds of events contribute to the background, which rapidly increases with the primary photon energy.

A background rejection is performed in order to extract the distribution corresponding to the signal. The complex background contribution cannot be determined analytically, we therefore approximated the background profile as a linear fit to the tail of the radial distribution. The fit limits have been defined as follows:

- the lower limit is calculated as the radial distance where the photon flux on the NaI(Tl) detector is reduced to a fraction $\frac{1}{e}$ by absorption effect in the collimator septa;
- the upper limit has been fixed to the half of the collimator smaller lateral side (95 mm), in order to avoid any kind of geometric effect due the binning choice or the normalization surface selection. The bin size creates artifacts in the radial distribution corresponding to the collimator limits, because three different geometries are involved: the circular surface covered by each distribution bin, the hexagonal shape of the collimator holes and the rectangular collimator geometry.

The estimated background profile is subtracted from the raw distribution and the result is used as reference of the image signal (Figure 5.2).

Three validation tests have been performed in order to check this analysis method.

First, according to the geometry of the collimator and to the mass attenuation coefficient of NaI(Tl) ([Hubbell et al. 1987](#)), we evaluated the expected number of entries in the first distribution bin (before normalization), corresponding to the central collimator hole in front of the source. The calculation is performed with the attenuation law of photons in 1 cm of NaI(Tl). A dedicated set of simulations has been performed equivalent to the ones for the Anger camera described in section 5.2.3.1, but using an ideal detector and a reduced number of photons of 10^7 . No uncertainties are applied on the position of photon interactions to avoid resolution effects and the background is estimated via a linear fit as described above. The obtained entries in the first distribution bin after the fit selection are compared to the ones obtained with the theoretical calculation. In Figure 5.3 the results are shown as a function of the source energy.

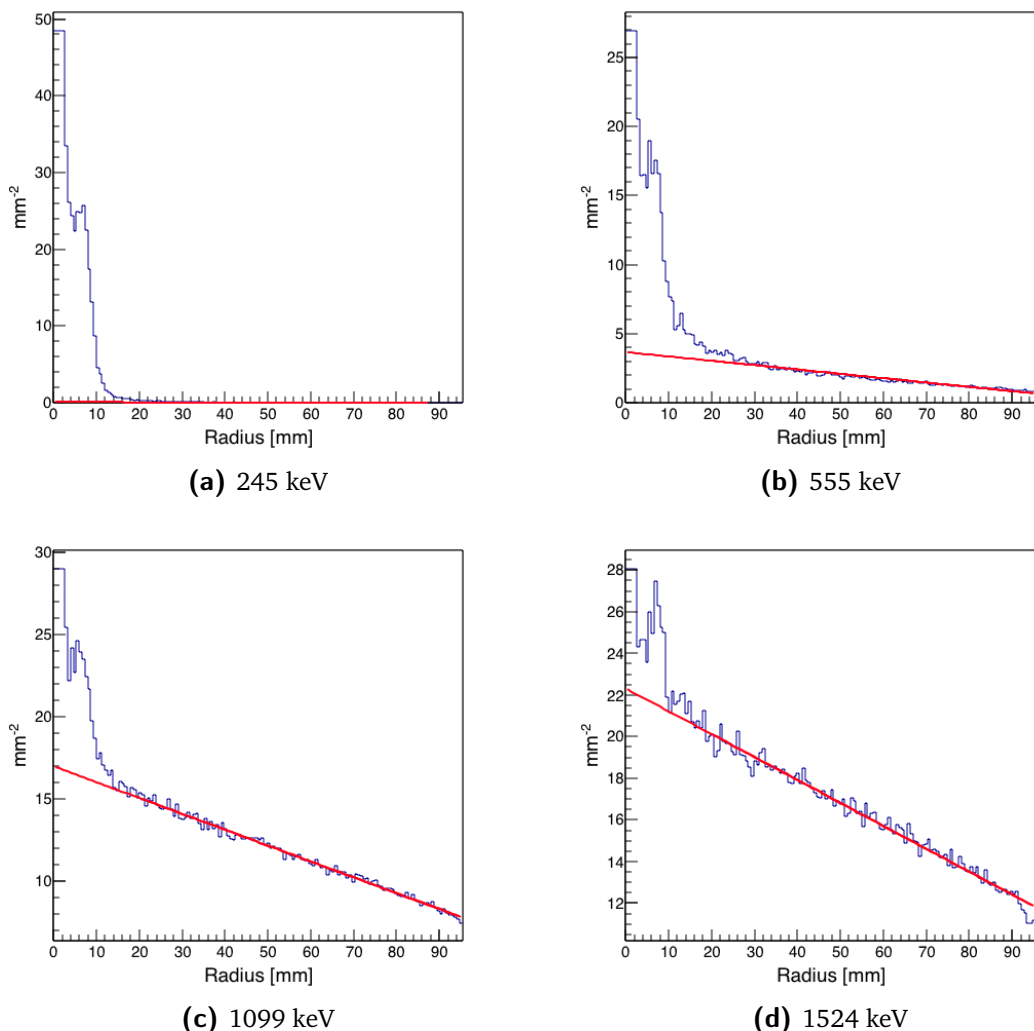


Figure 5.2: Radial event distribution normalized by the circular surface corresponding to each bin for 4 representative source energies, with the linear fit performed for background rejection. The total number of simulated primaries for each data set is 10^8 .

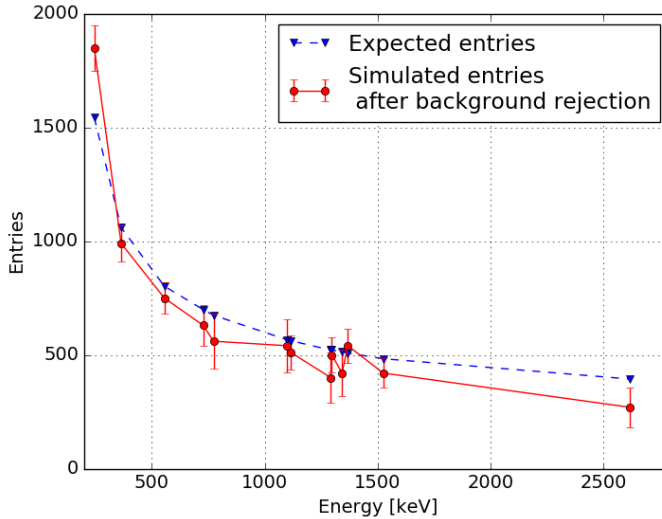


Figure 5.3: Comparison between expected entries in the central collimator hole (blue dashed curve) calculated according to pure geometrical factors and detector interaction cross section and simulated detected entries after background subtraction (red solid curve) with null spatial resolution (ideal detector) to avoid resolution effects and lower energy threshold set to 80 keV.

There is a good agreement between the values calculated with the attenuation law and the simulation data selected with the fit-based background subtraction, and the detected variations from the ideal trend are within the statistical fluctuations. A slight overall effect of under-detection is observed (about 10% on average), while the single value at 245 keV shows an opposite behavior (with a difference of less than 20%). This is related to the chosen fit function.

As a second validation, an additional set of simulations has been performed with the same settings as defined in section 5.2.3.1 but with an infinitely dense collimator. This configuration removes the background contribution given by the photons deflected via Compton interaction on the collimator septa. The raw radial distributions obtained with this set of simulation is compared to the radial distribution “derived” by the simulations with nominal settings after the application of the fit-based background subtraction. The results are shown in Figure 5.4.

It can be noticed that the distribution overall trend is reproduced by the fit-based background subtraction method, the main source of difference being probably the contribution of the scattering in the hole grid surrounding the central one.

The third validation test consisted in a set of simulation with a full lead collimator, with no holes. This configuration allows to estimate the distribution of events traversing the collimator with no interaction, with the aim of demonstrating the efficiency of the selection method to remove their contribution to the final image. Figure 5.5 shows the comparison between the raw distributions (no event selection is applied) obtained with the standard configuration and with the full collimator. The amount of photons able to traverse the lead block at low energy (245 and 555 keV) is totally negligible, while at higher energies this kind of events creates an offset which follows the raw event distribution. Anyway, by observing the selection functions obtained by the linear fit in Figure 5.2, the efficiency of the background employed rejection method in removing this contribution results clear.

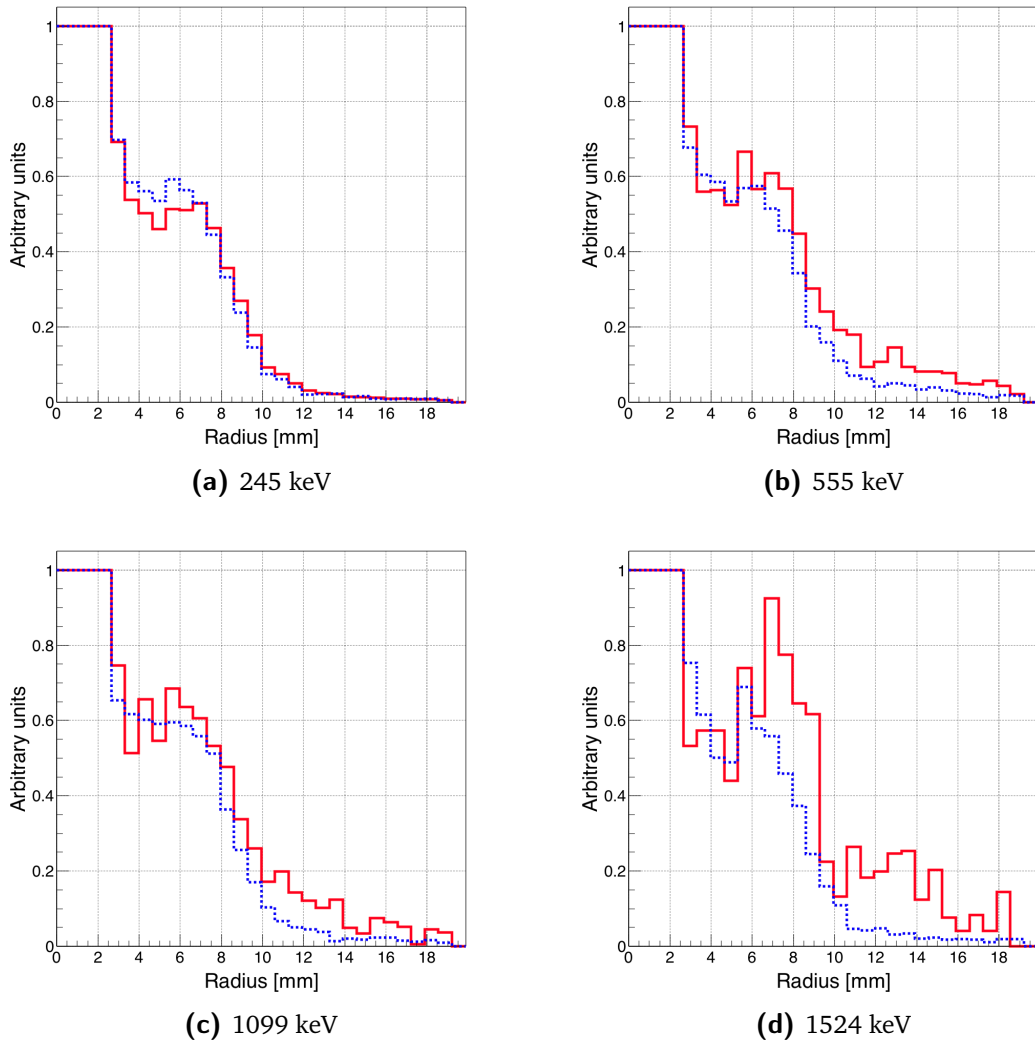


Figure 5.4: Normalized radial distribution with background rejection (red solid lines) compared to normalized radial distribution for infinite density collimator (blue dashed lines).

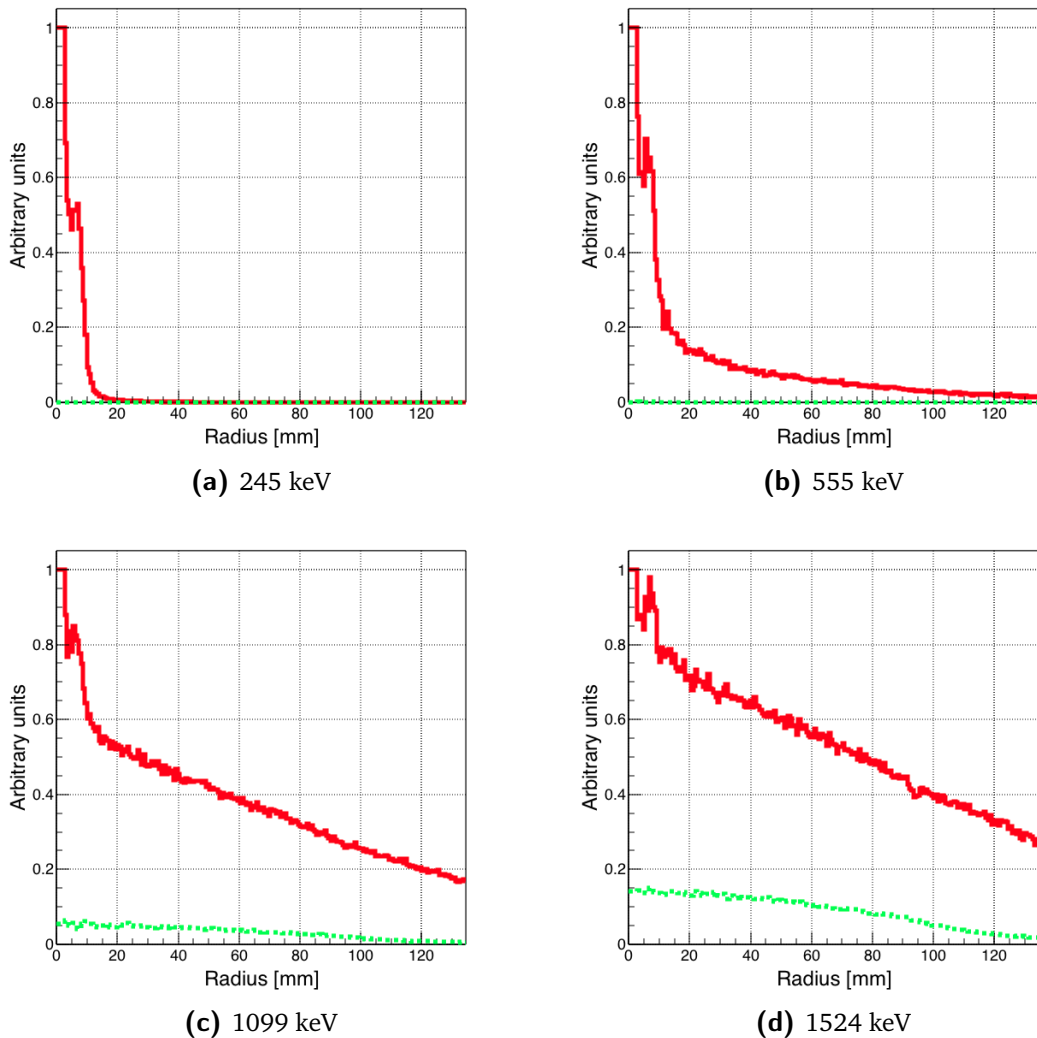


Figure 5.5: Normalized radial distribution with no event selection (red solid lines) compared to normalized radial distribution for full collimator (green dashed lines). Both curves are normalized to the maximum of the raw radial distribution.

The linear fit appears to be a robust way to select the signal transporting spatial information from the source and is applied with no modification for the entire energy range, giving to the analysis method the desired consistency.

5.2.4 Figures of merit for the comparison study

The two cameras are studied and compared according to three figures of merit which refer to their main detection parameters: spatial resolution, detection efficiency, and signal-to-background ratio. The definition of these three values must be adapted to the two detectors, keeping in mind their differences: on one side the Anger camera provides a transmission image through a mechanical collimator, with no need for a reconstruction process and with a single detector component; on the other side, the Compton camera relies on event time-coincidences and needs a reconstruction algorithm to obtain the final spatial distribution.

In this study, the imaging process of a point source was simulated. The three figures of merit are therefore evaluated based on the radial event distribution, in order to profit of the radial symmetry of the simulated system.

For the Compton camera, the standard deviation of the radial distribution is used to express the detector spatial resolution, the detection efficiency is defined as the ratio between reconstructed events (via LM-MLEM algorithm) and total simulated primaries, and the signal-to-background ratio corresponds to the ratio between the number of reconstructed events and the total number of coincidences selected before the reconstruction with the coincidence analysis.

For the Anger camera, it is difficult to define the spatial resolution, as shown in (Cecchin et al. 2015). Here, we use the standard deviation of the signal radial distribution in order to be consistent with the Compton camera definition already proposed (the “signal” substantive means entries after background rejection). The detection efficiency is defined as the ratio between the number of signal events and the total number of simulated primaries. Finally, the signal-to-background ratio is evaluated as the ratio between the signal events (the entries in the radial distribution after the fit-based background rejection) and the total number of events recorded by the detector (the entries in the raw radial distribution).

5.3 Results: Compton camera study for SPECT application

The results of the characterization of the CLaRyS Compton camera prototype for the application in SPECT are presented in the following sections, dedicated to the study of the scatterer detector energy resolution and of the Doppler broadening effect, and to the analysis of the rate of random coincidences, respectively.

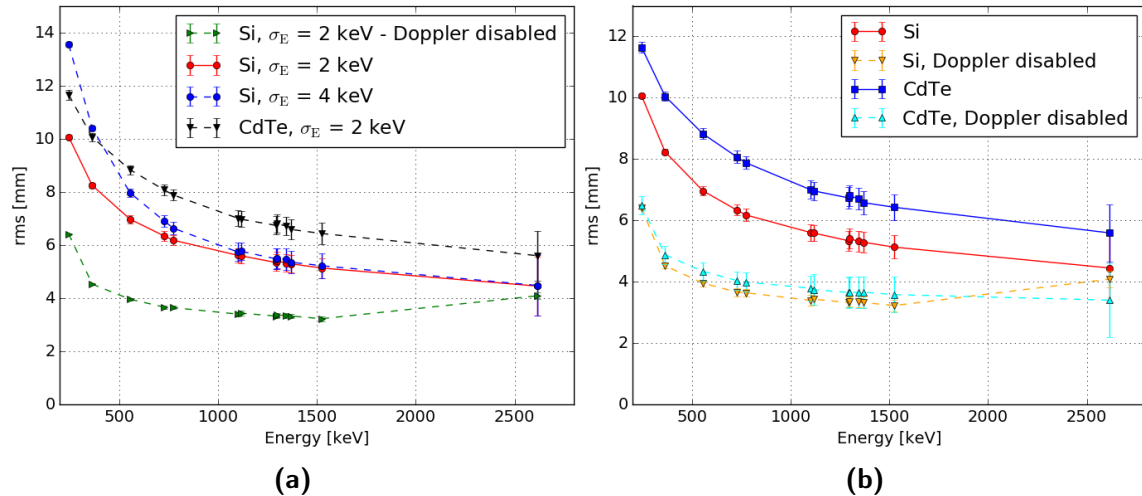


Figure 5.6:  Constructed radial distribution standard deviation as a function of the source energy. Two energy resolution values are set to the silicon detectors ($\sigma_E = 2 \text{ keV}$ - red dots solid line - and $\sigma_E = 4 \text{ keV}$ - blue dots dashed line), the Doppler broadening effect has been removed (green horizontal triangles dashed line) and the scatterer material has been changed with CdTe solid state detectors (black vertical triangles dashed line), for a fixed energy resolution of $\sigma_E = 2 \text{ keV}$.

5.3.1 Influence of Compton camera scatterer-detector energy resolution

Figure 5.6 shows the standard deviation of the radial distribution obtained after the LM-MLEM reconstruction (see section 5.2.2.2) as a function of the source energy for the two different analyzed noise levels ($\text{ENC} = 500 \text{ e}^-$, corresponding to $\sigma_E = 2 \text{ keV}$, and $\text{ENC} = 1100 \text{ e}^-$, corresponding to $\sigma_E = 4 \text{ keV}$). The maximum detected difference is about 35%, but the influence of the silicon detectors' energy resolution rapidly reduces at increasing energy. In the same figure, the results for the simulation without the Doppler broadening for the lowest energy resolution are shown. It is clear that this parameter has a strong influence for the Compton camera spatial resolution, at least for energies below 2.5 MeV. This result justifies the choice of silicon as scatterer material, because it is the lowest Z available detector and therefore minimizes the Doppler contribution. This is underlined by the black curve corresponding to a CdTe detector, i.e. a higher Z material than silicon. For this last study, the electronic noise level has been set for CdTe in order to have the same intrinsic resolution as for silicon ($\sigma_E = 2 \text{ keV}$ obtained with equation 5.1).

For the benchmark with the Anger camera, the ENC value of the Compton camera scatterer components has been fixed to 500 e^- , which corresponds to the expected average level of noise affecting the silicon detectors between -20°C (identified as the ideal working temperature) and 0°C (the silicon detectors are cooled down with a thermal-regulated box, see chapter 3 for a detailed description) and with the final acquisition card (about $2 \text{ keV } \sigma_E$). This value has to be experimentally verified.

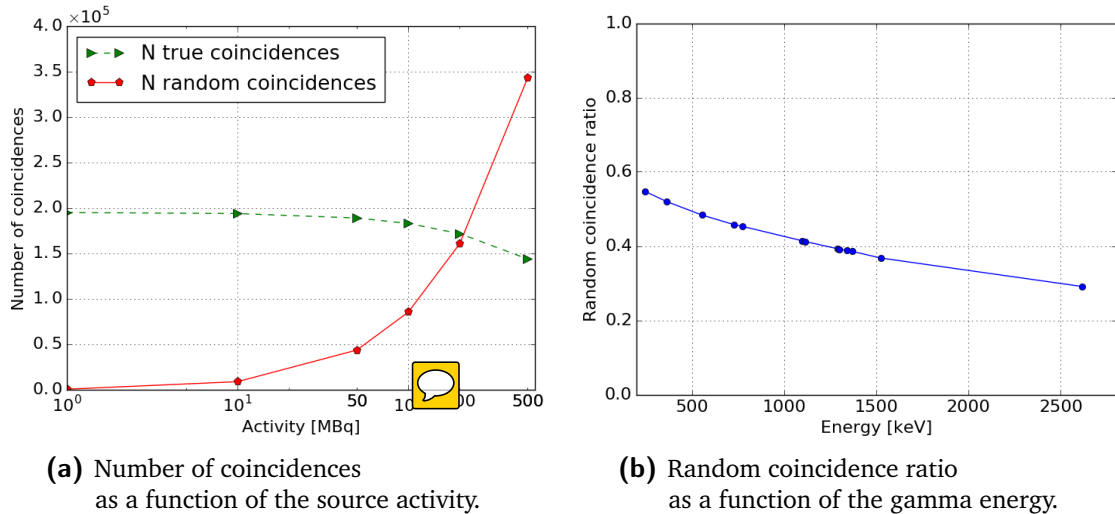


Figure 5.7: (a): number of true (green) and random (red) coincidences as a function of the source activity in the range 1-500 MBq, for the reference energy of 555 keV. (b): Percentage of random coincidences as a function of the source energy, with a fixed source activity of 200 MBq. Compton camera parameters: time resolution FWHM of 20 ns for silicon detectors, 3 ns for BGO and a coincidence window of 40 ns. The source branching ratio has been set to 100% for all sources for simplicity in the comparison of results.

5.3.2 Compton camera coincidence study

Figure 5.7 (left) shows the numbers of true and random coincidences as a function of the source activity, ranging between 1 and 500 MBq in order to explore the whole range potentially employed in real examinations. The energy is set to 555 keV.

At 200 MBq source activity, the same amount of true and random coincidences is observed at 555 keV gamma energy. With activities above this value, the ratio between true and random coincidences is less than one. In principle the reconstruction LM-MLEM program can partially reject this kind of events and if we consider the expected important increase in detection efficiency guaranteed by the “electronic collimation”, it results clearly that it is not worth to employ high activity sources (or that a smaller camera can be considered at the expense of the examination time). 

For the further analysis and the final detector comparison, the source activity has been then set to 200 MBq, and the number of random coincidences is studied as a function of the source energy. Figure 5.7 (right) shows the ratio of detected random coincidences over the total number of reconstructed coincidences (see Section 5.2.2.2) as a function of energy for a fixed activity of 200 MBq. The ratio decreases for increasing energies, because the product of independent interaction probabilities in two detectors decreases faster than the true coincidence one. Therefore, an increasing reconstruction efficiency with LM-MLEM is verified (see Section 5.4).

5.3.3 Compton camera desing study

The reconstructed events efficiency for four reference primary gamma energies is shown in figure 5.8a for five different scatterer configurations: starting from the original design with seven silicon layers, one layer has been removed for each simulation set, until a minimal scatterer stack composed of only three layers. Figure 5.8b shows the results of the same sets of simulations for what concerns the reconstructed event radial distribution Root Mean Square (RMS).

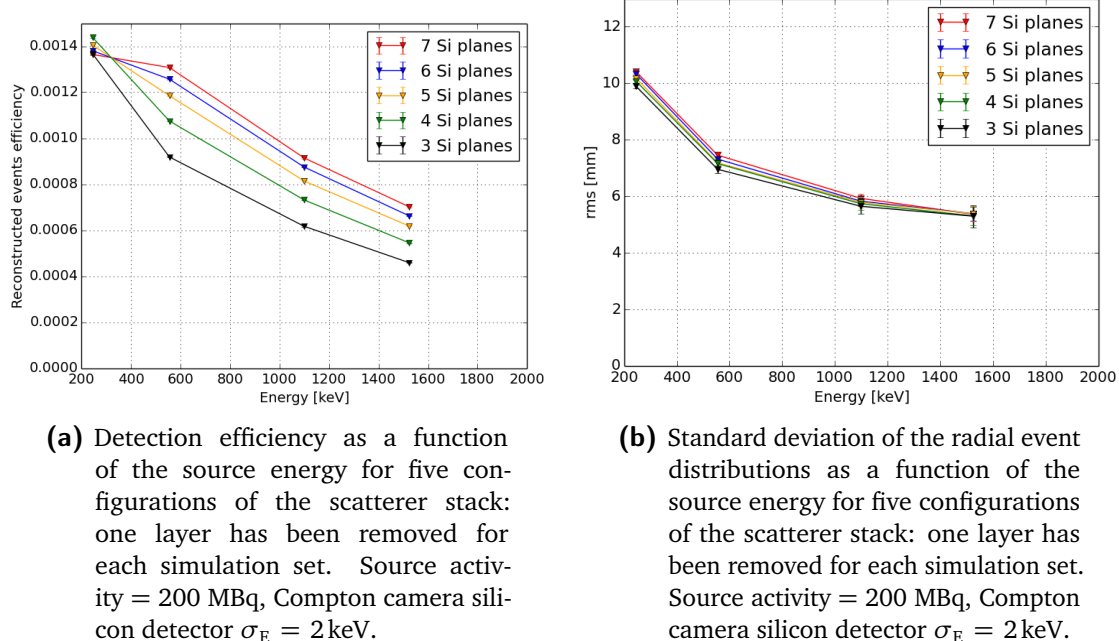


Figure 5.8: Results of the Compton camera design study: reconstructed events efficiency (left) and standard deviation of the radial event distribution (right) as a function of the primary gamma energies for four reference energies and five scatterer stack configurations, with seven, six, five, four and three layers.

Concerning the reconstructed events efficiency, an overall efficiency drop is observed for the scatterer configurations with more than four layers at 245 keV photon energy: this probably reveals an effect of total gamma absorption in the scatterer detector section, in parallel to an increased number of events deflected with large Compton angles which escape the absorber field of view. This effect is not confirmed at increasing gamma energy, already at 555 keV. In this energy range, the expected reduction of the overall efficiency for reduced number of scatterer layers (due to the diminished Compton effect probability) is verified. The radial distribution standard deviation shows minimal variations for the different tested configurations.

At very low gamma energy a scatterer configuration with four silicon scatterer planes appears to be the optimal solution. This is the energy range for which the Compton camera advantages with respect to the commercial Anger cameras are expected to be less remarkable, as explained and verified in the next sessions. At increasing energy, relevant to profit the Compton camera advantageous features, the original CLaRyS camera design is verified to be the best configuration; this setup has been implemented for the benchmark study.

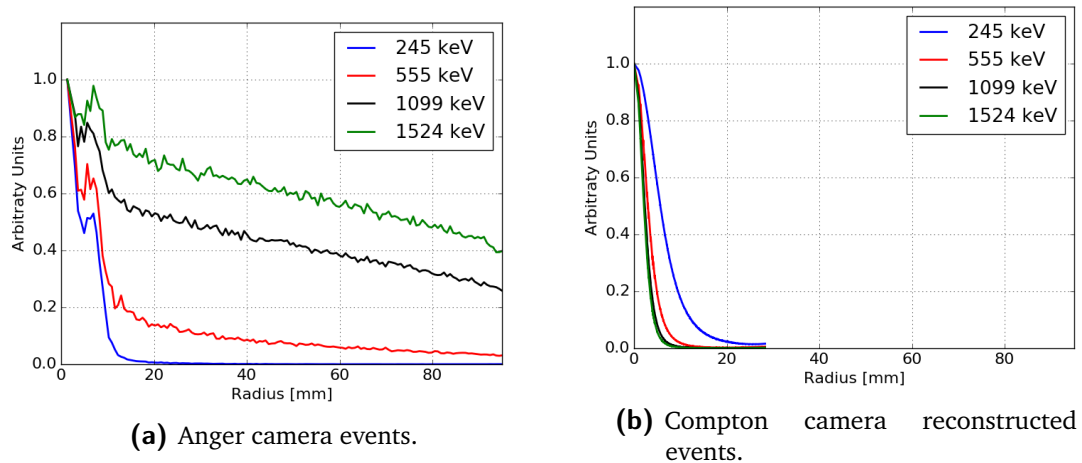


Figure 5.9: Overlap of the normalized radial distributions for 4 selected source energies.

5.4 Results: Benchmark of Compton camera and Anger camera performance

The analysis methods presented in section 5.2.2.2 and section 5.2.3.2 for the Compton and Anger camera, respectively, have been applied to the simulated data sets of the two cameras at all energies.

The radial distributions for Anger and Compton camera at the different reference source energies and a source activity of 200 MBq are shown in Figure 5.9. The same reference energies selected in section 5.2.3.2 are included here. The radial range is limited to the smaller collimator lateral size (95 mm), according to the fit limits imposed on the Anger camera data (see Section 5.2.3.2). The curves are normalized to 1 for an easier visual comparison.

In Figures 5.10, 5.11, and 5.12, the detection efficiency, the radial distribution standard deviation and the signal-over-noise ratio are respectively shown as a function of the source energy for the two sets of data. Uncertainties (one standard deviation) are reported for all the values and included in the data points when not visible.

From Figure 5.10 one can point out the advantage provided by the absence of a physical collimation system in terms of detector efficiency. It should be noticed that two different scales are applied to Figure 5.10 in order to show the two plots on the same figure and appreciate the variations with respect to the energy. The detection efficiency of the Compton camera is always more than a factor 20 higher than the one of the Anger camera. Although the images of the Anger and Compton cameras are based on different kinds of spatial information (a line and a cone, respectively), the Compton camera efficiency should allow a substantial reduction of the injected source activity and/or of the acquisition time. The efficiency of both cameras constantly decreases with increasing energy, because of the decreasing photon interaction probability. The only exception is found at the lowest considered energy of 245 keV in the Compton camera, due to an increased probability of photon absorption in the scatterer and, in parallel, a larger fraction of events with wide Compton scattering angles at low gamma energy.

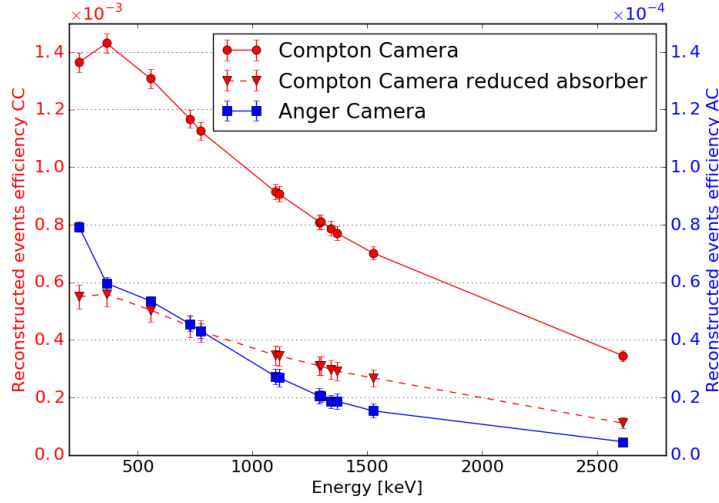


Figure 5.10: Detection efficiency as a function of the source energy. Source activity = 200 MBq, Compton camera silicon detector $\sigma_E = 2\text{ keV}$.

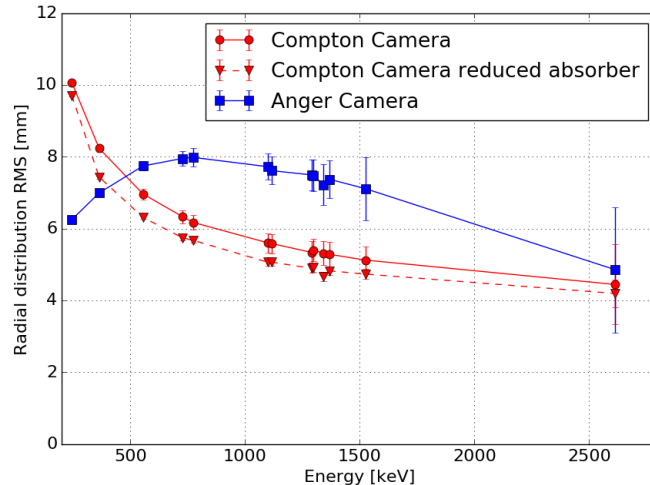


Figure 5.11: Standard deviation of the radial event distributions as a function of the source energy. Source activity = 200 MBq, Compton camera silicon detector $\sigma_E = 2\text{ keV}$.

The standard deviation of the radial distribution, shown in Figure 5.11, confirms the optimization of the chosen collimator for the Anger camera for low energies (below 364 keV). With the ad-hoc background subtraction operated here, which is not realistic for an extended source, the Anger camera outperforms the Compton one in terms of spatial resolution at low energies (by > 3 mm at 245 keV and about 1.3 mm at 364 keV). However, above 500 keV, the Compton camera can provide a better spatial resolution with a difference ranging between a fraction of millimeter up to about 2 mm. For energies above 1.5 MeV, the two curves of standard deviation for the two cameras reach similar values (< 0.5 mm difference at 2614 keV), but Figure 5.12 shows how the background rejection for the Anger camera and the MLEM reconstruction for the Compton system (see Sections 5.2.3.2 and 5.2.2.2) affect this result. Above 364 keV, the selection for the background rejection of the Anger camera data drastically reduces the number of events contributing to the final image (the ratio between selected and detected events approaches zero). With an extreme selection, at very high energy the only events contributing

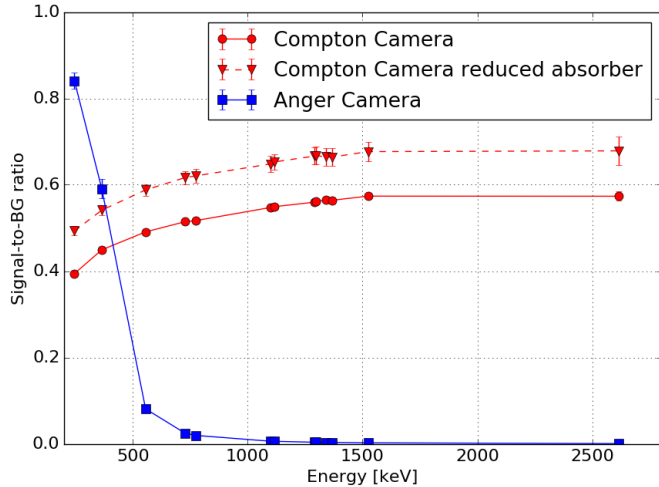


Figure 5.12: Signal-to-background ratio as a function of the source energy. Source activity = 200 MBq, Compton camera silicon detector $\sigma_E = 2\text{ keV}$.

to the final image are the events traversing the central hole of the collimator, resulting in an enhanced spatial resolution (see Figure 5.4d). The signal-to-background ratio of the Compton camera confirms the expectations concerning the reconstruction algorithm performance: if compared to Figure 5.7 (right), the curve in Figure 5.12 shows how the rejected events correspond approximately to the amount of random coincidences.

5.5 Summary and discussion

The Compton camera under development by the CLaRyS collaboration is now at the characterization stage. Originally designed and optimized for the application in ion beam therapy monitoring for the detection of prompt-gamma rays in a wide energy range (between some hundreds of keV until about 10 MeV), it is here studied as SPECT detector in comparison to a commercial system based on the Anger gamma camera design.

The expected significant enhancement in terms of detection efficiency, for comparable imaging performance in terms of spatial accuracy, has been already proven in simulation in (Han et al. 2008) with a silicon-sodium iodide based Compton camera prototype at a single primary energy of 364 keV. A factor 20 efficiency gain has been reported.

First of all, the present simulation study aimed to extend these results by testing the two detectors at increasing primary gamma energies, ranging from 245 keV to 2614 keV. A common analysis method has been defined in order to obtain comparable results, always keeping as reference the final image. The results were directly compared in terms of detection efficiency, spatial resolution (standard deviation of the radial event distribution) and event selection (background rejection for the Anger camera and LM-MLEM algorithm selection for the Compton camera) via the definition of three figures of merit.

A preliminary study has been performed on the simulated Compton camera data in order to

fix the main parameters of the camera simulations, namely the energy resolution of the silicon scatterer detectors and the source activity determining the coincidence rate. Two ENC values have been studied, resulting in a maximum difference in spatial resolution of 35% at the lowest energies, rapidly decreasing at increasing primary energy. A value of $\text{ENC} = 500 \text{ e}^-$ has been chosen as the closest to the instrumental development expectations and first tests. The influence of the Doppler broadening on the spatial resolution has been also estimated in a factor $\sim 1/3$ at 500 keV, then reduced up to ~ 0 at 2.5 MeV of primary gamma energy, with fixed energy resolution ($\sigma_E = 2 \text{ keV}$ - $\text{ENC} = 500 \text{ e}^-$) in the silicon detectors. Moving to the coincidence rate analysis, at the reference energy of 555 keV and with detector time resolution set according to first characterization results, the simulated data have been analyzed by reproducing a source activity in the range 1-500 MBq. The result shows the expected increase in the random coincidence rate at increasing source activity, with a ratio between true and random coincidences close to one at 200 MBq. This value has been chosen as clinical reference for the comparison analysis. In addition to this, the geometrical configuration of the scatterer stack has been studied in order to check alternative setups with reduced number of DSSDs; this study confirmed the choice of seven planes, implemented for the benchmark analysis.

The results discussed in section 5.4 confirm the conclusion of Han et al. about the advantage given by the usage of a Compton system and show how the gain factor in the detector efficiency is maintained at increasing energy. Concerning the detector spatial resolution, the Compton camera outperforms the Anger system at energies above about 500 keV. The Anger camera spatial resolution can be boosted by aggressive background subtraction in the considered case (point-like source image), at the expense of a drastic signal suppression. However, this approach is not reproducible and exploitable in actual clinical conditions and the obtained results are not comparable to the Compton camera performance at the same energy.

The results of this work clearly show the potential of the Compton camera for the application in nuclear medicine examination, opening new possibilities for the clinical implementation. The studied detector has originally been designed and optimized for another application, and it has only been adapted for SPECT here, but not yet optimized in terms of detector geometry (size, position, and inter-detector distances). For an optimized detector, performance is therefore expected to be improved with respect to the presented results. In future development, the reconstruction LM-MLEM algorithm should be adapted to this application and the reconstruction parameters should be studied to further enhance the final performance, in particular for what concerns random coincidence rejection.

Anyway, these first evidences already allow one to investigate the possible modifications introduced by the clinical set of Compton detection systems. The enhanced detection efficiency in parallel with comparable spatial performances paves the way to the diffused usage of less active sources, or alternatively allows a substantial reduction of examination time: as a result, the dose delivered to the patient would be reduced. On the other side, the possible introduction of sources with higher primary emission energy will reduce the effect of photon attenuation in the patient (not studied in this simulation work), improving by definition the spatial information and further reducing the effective dose delivered to the patient. Simple analytic calculations can show how a photon attenuation of about 66% is foreseen for 364 keV photons in 10 cm of water, while the effect is reduced, for example, to 49 % at photon energy of 1099 keV (Hubbell et al. 1987). Higher energies can be employed also with Anger cameras, at the expense of introducing thicker collimators with reduced holes size, with the result of a reduced efficiency with respect to the analyzed HEGP collimator. Furthermore, a possible

implementation of Compton cameras is also foreseen for targeted radionuclide therapy, where the radionuclides used in clinics often have gamma radiation emission at relatively high energy. This signal is difficult to be detected and treated with conventional SPECT cameras, while the Compton detection technique could make it quantitatively exploitable in clinical practice, for both pre- and per- treatment images.

Even though Compton cameras intrinsically lead to 3 dimensional images with a single detector head, the spatial resolution associated to the direction normal to the detector planes has to be more deeply studied, but this feature is an additional point in favor of the introduction of Compton systems in the clinical environment, moving beyond the tomographic concept and towards more compact detector solutions. Several studies are ongoing in order to improve the image reconstruction algorithms and, so, the 3 dimensional imaging performance ([Kuchment et al. 2016](#)). Different detection approaches can also, in principle, lead to improved image quality in 3 dimensions, such as the Compton electron tracking ([Kabuki et al. 2007](#); [Sonoda et al. 2015](#)). Moreover, a further enhancement in image reconstruction should be given by the measurement of the photon depth of interaction: the photon is assumed to interact in the center of the detector components for our prototype, while perpendicularly segmented detectors can ensure an improved resolution in the third dimension and a resulting enhanced reconstruction accuracy, also involving better 3 dimensional imaging capabilities.

The advantages of the Compton detection principle are here shown thanks to a first detector prototype, but there is still wide room for improvement.

Once the CLaRyS Compton camera will be completed and characterized, tests in clinical environment are foreseen in the field of medical imaging. The actual potential of such a kind of detector will be then quantified with experimental data.

6

Beam tests

Contents

6.1	Hodoscope: december 2017	114
6.2	Hodoscope: may 2018	114
6.3	Collimated camera: august 2018	114
6.4	Collimated camera: september 2018	114

6.1 Hodoscope: december 2017

6.2 Hodoscope: may 2018

6.3 Collimated camera: august 2018

6.4 Collimated camera: september 2018

7

Conclusions and discussion

Appendices

A

Compton camera data format

A.1 Introduction



This document aims to formalize and fix the Compton camera data format. The structure of the data sent by each detector section (scatterer, absorber and beam hodoscope) to the acquisition card is detailed, as well as the structure of the events sent to the acquisition PC.

A.2 General features

A.2.1 Common information

The detector Front-End (FE) cards are connected to the Micro Advanced Telecommunications Computing Architecture (μ -TCA) via optical links, with a speed of 3.0 Gbit/s. The transfer frequency is 150 MHz.

All the FE card Time-to-Digital Converters (TDCs) share the same synchronized clock, at a 40 MHz frequency, which is sent to the cards through an external link.

Every data packet sent to the μ -TCA by the Front End cards starts with the following information:

- N° Front End (8 bits);
- N° Trigger (24 bits);
- N° Mode (8 bits);
- N° of element in the packet (8 bits).

A.2.1.1 Front End number

The FE number is the identification code of each FE card. A mechanical switch on the card defines the ID which is sent in the data packet header.

In Table A.1 the FE number IDs are listed with the corresponding cards.

Table A.1: Front End number associated to each Front End card.

FE number	FE card
0	All detectors
1	Silicon 1
2	Silicon 2
3	Silicon 3
4	Silicon 4
5	Silicon 5
6	Silicon 6
7	Silicon 7
8	Silicon 8
9	Silicon 9
10	Silicon 10
11	ASM 1
12	ASM 2
13	ASM 3
14	ASM 4
15	ASM 5
16	ASM 6
17	ASM 7
18	ASM 8
19	ASM 9
20	ASM 10
21	ASM 11
22	ASM 12
23	ASM 13
24	ASM 14
25	ASM 15
26	ASM 16
27	Hodoscope 1
28	Hodoscope 2
29	Hodoscope 3
30	Hodoscope 4
31	Hodoscope 5
32	Hodoscope 6
33	Hodoscope 7
34	Hodoscope 8
99	μ -TCA

A.2.1.2 Pre-trigger and trigger

The trigger number identifies each event, where an event is generated every time a coincidence is detected between a Bismuth Germanium Oxide - $\text{Bi}_{12}\text{GeO}_{20}$ (BGO) block and a silicon layer. Once an interaction is detected in a BGO block, the associated Analog Sampling Module (ASM) card generates a pre-trigger signal which is sent to the Trigger et HORloge (THOR) card. This intermediate card shares the pre-trigger signal with the silicon FE cards; if an interaction with a compatible time stamp is found in one of the silicon layer, a trigger signal is generated and sent to all the silicon FE card, as well as to the ASM and hodoscope cards via the THOR card. The trigger signal validates the event, and each FE card sends the collected data to the μ -TCA system. The trigger number allows for a complete event reconstruction by the event builder on the acquisition PC. In Figure ?? the trigger generation process is sketched.

To be noticed that each FE cards sends the collected data independently from the others.

Trigger and pre-trigger encoding

Pre-trigger and trigger signals are used by all the detectors to select the collected data to be sent to the acquisition system. The data selection and transfer must be as fast as possible in order to minimize the trigger latency and camera dead time. In order to reduce the transmission time, pre-trigger and trigger signals have been encoded on 24 bits.

This same trigger number is sent at the beginning of each data packet and is used by the event builder to associate the interactions collected by the three detector sections. With a 24-bit encoding, the trigger number is reset every $1 \text{ ns} \times 2^{24} = 16,78 \text{ ms}$. This time window is short for the event builder, so that for the physical data it is extended to 32 bits for all the FE cards in order to have a reset every $1 \text{ ns} \times 2^{32} = 4,2 \text{ s}$, which is enough for the reconstruction of the events.

A.2.1.3 Mode number

The Compton camera detector components can work in different mode, according to the application requirements. At least two working modes are possible for every detector section: an “optimal” mode, corresponding to the final camera configuration; a “test” mode, allowing for the collection of more raw information. Every operating mode presents a peculiar data format, so that the data packets size is not fixed. In order to fix the acquisition tuning, the mode number is defined before its beginning.

The operating mode are identified as following:

- N° Mode = 1 : 1st mode for silicon
- N° Mode = 2 : 2nd mode for silicon
- N° Mode = 3 : 3rd mode for silicon

A Compton camera data format

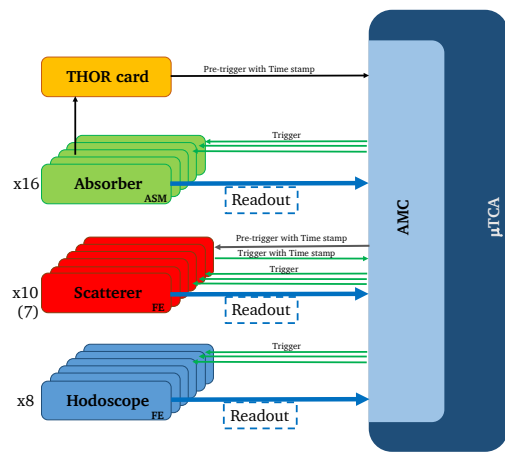
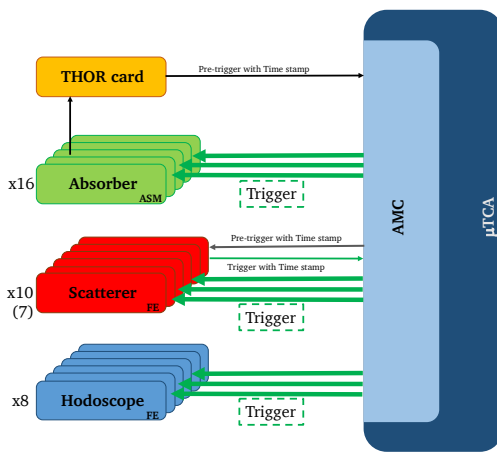
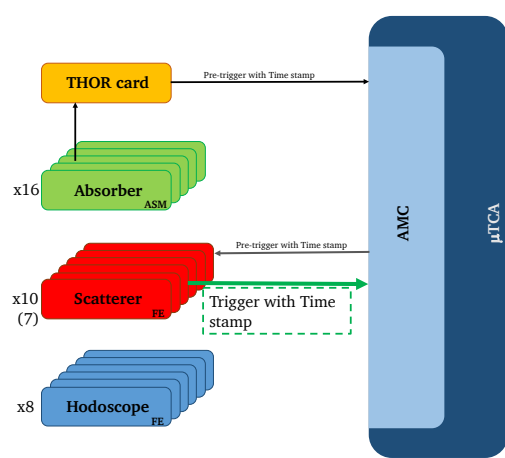
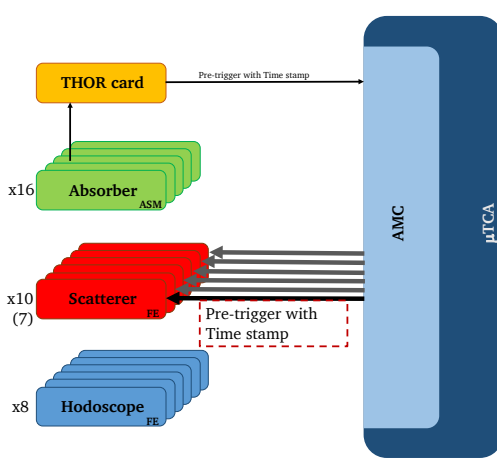
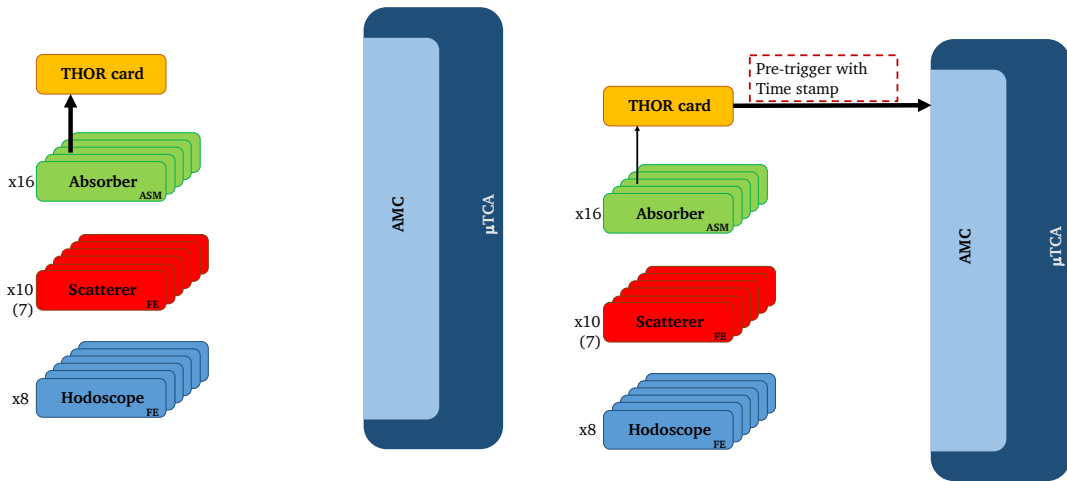


Figure A.1: Data acquisition logic: pre-trigger and trigger generation and readout process.

- N° Mode = 4 : 4th mode for silicon
- N° Mode = 5 : 1st mode for BGO
- N° Mode = 6 : 2nd mode for BGO
- N° Mode = 7 : 1st mode for hodoscope
- N° Mode = 8 : 2nd mode for hodoscope.

A.3 Physical data format

A.3.1 Scatterer detector data format

Four different data formats, corresponding to four working modes, have been defined for the silicon scatterer operation (Figure A.2). For mode 1 and 2, the collected total charge is directly evaluated on the FE card via the slow shaper output and one Application-Specific Integrated Circuit (ASIC), while for mode 3 and 4 the ASIC pre-amplifier output directly sends a sampling of the raw signal. In this last case, the number of samples can be tuned and each sample corresponds to 10 ns. The complete sampling is stored in a dedicated buffer.

Modes 1 and 3

In mode 1 and 3, for each detector strip involved in the interaction, the strip ID, total collected charge and time are stored. The interaction position will be calculated via a center of gravity algorithm at the analysis stage. The raw information about the number of involved strips is useful for the evaluation of the signal dispersion in the detector.

Modes 2 and 4

In mode 2 and 4, the interaction is calculated on the FE card and the number of involved strip is then not stored.

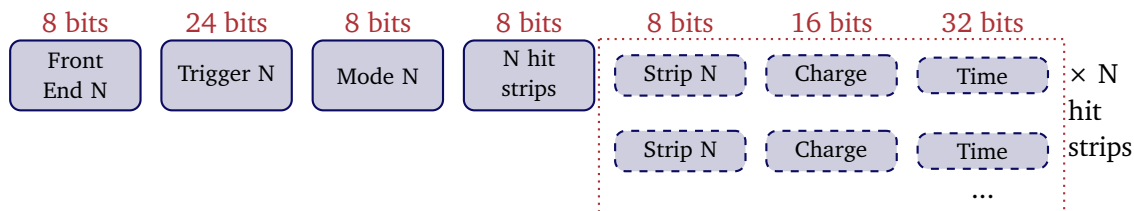
A.3.2 Absorber detector data format

The BGO block readout is performed via the ASM cards. Each card is equipped with 24 input ports (signal Photo-Multiplier (PM)), corresponding to 6 BGO blocks. Two possible working modes have been defined for the BGO absorber: the collected total charge and time are evaluated on the card, or the PM raw signals are sampled and the sampling is sent to the acquisition (Figure A.3). Charge and time are then calculated at the analysis stage. This second operating mode can be useful in the test phase but it determines a low acquisition rate, so that it can be used only at low beam intensity.

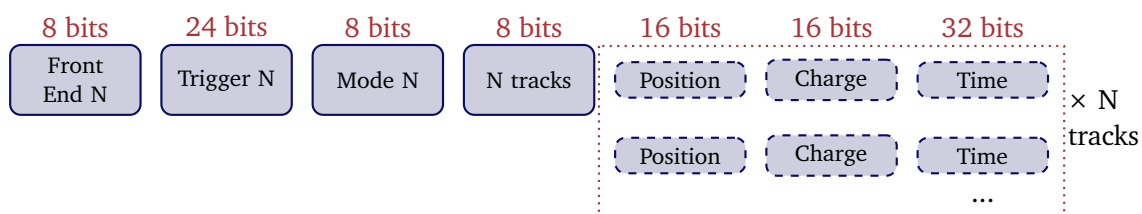
The complete sampling is stored in a dedicated buffer.

A Compton camera data format

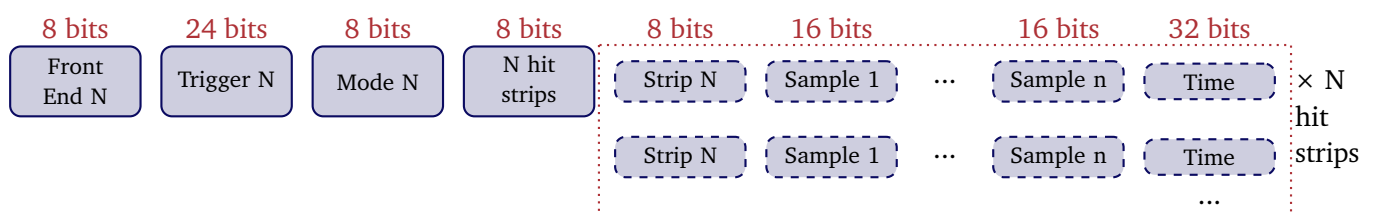
Mode 1



Mode 2



Mode 3



Mode 4

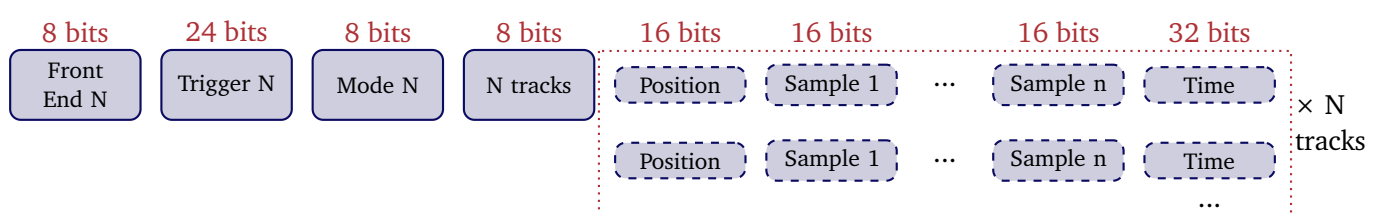
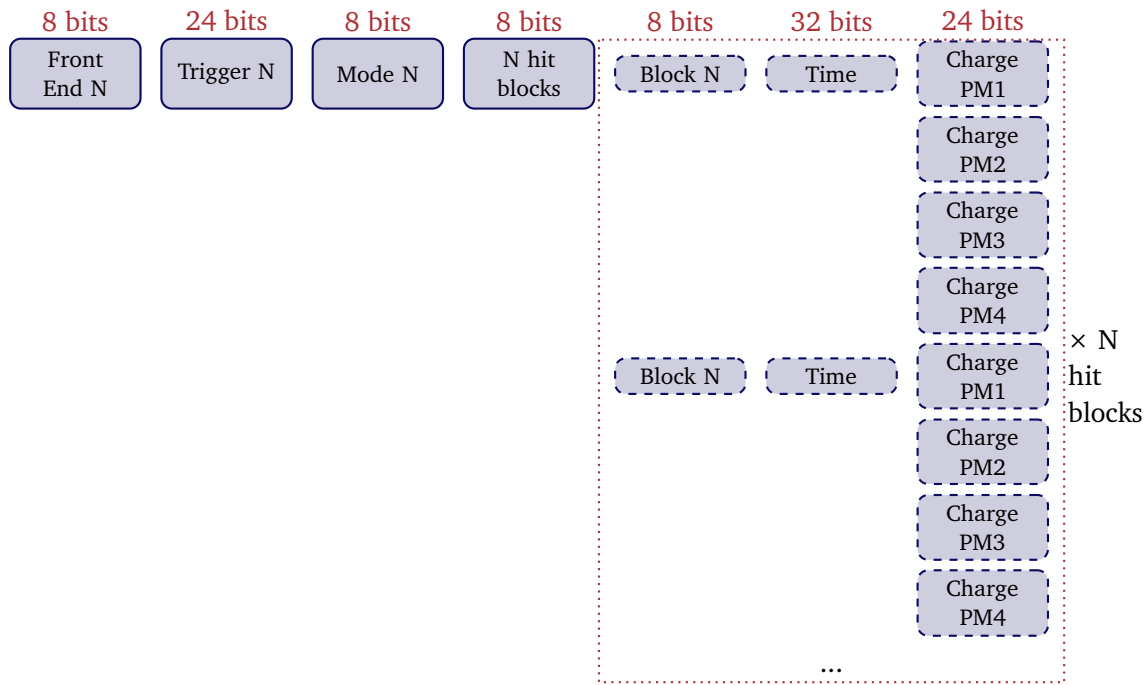


Figure A.2: Scatterer detector data format.

Mode 1



Mode 2

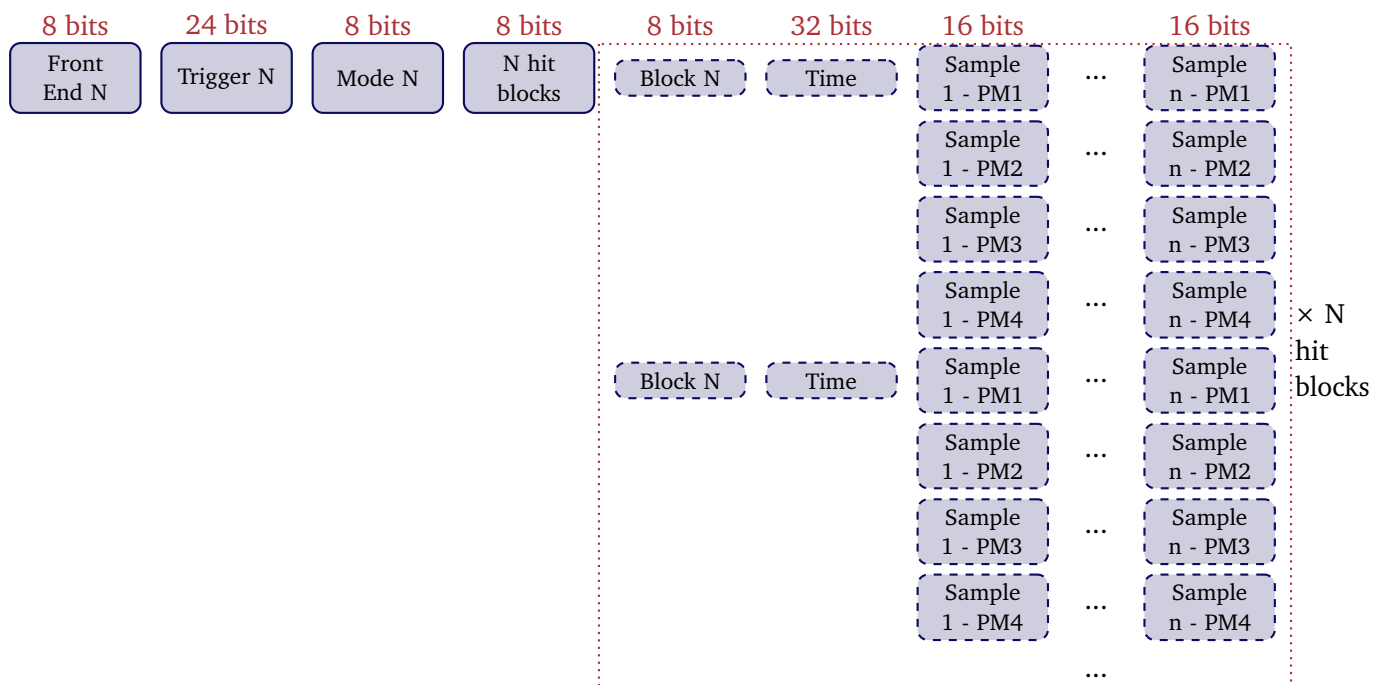


Figure A.3: Absorber detector data format.

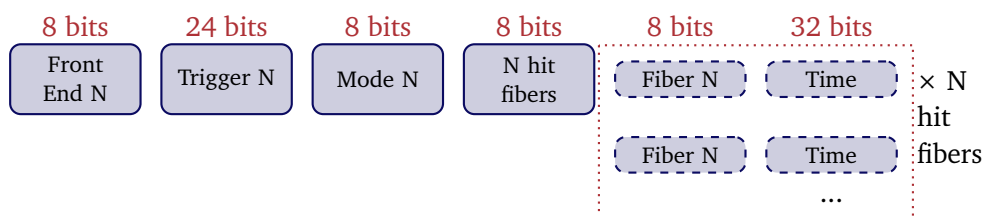
A.3.3 Beam hodoscope data format

The beam tagging hodoscope is composed of two perpendicular planes of 128 scintillating fibers each. Each fiber is read-out on the two sides, for a total of 512 read-out channels. The output signals are send via optical fibers to 8 64-channel PMs H8500 by Hamamatsu. 8 FE cards have been developed for the signal collection, one per PM, and are equipped with two custom ASICs (32 channels each) and one Field Programmable Gate Array (FPGA).

Concerning the “optimal” mode (1st operating mode for the hodoscope), the only collected information are the ID of the involved fibers and the interaction time. The ASICs allow for a minimum time resolution of 10 ns; this means that if two particles interacts in the hodoscope within a 10 ns window, they will be considered as part of a single event.

In test mode, the total collected charge can be calculated. This feature is useful to evaluate the detector aging effect due to radiation exposure. The charge measurement is anyway limited to a single channel per ASIC, so to two channels per PM. The ASIC channel able to measure the charge is identified as “N° Fiber charge 1” and “N° Fiber charge 2”.

Mode 1



Mode 2

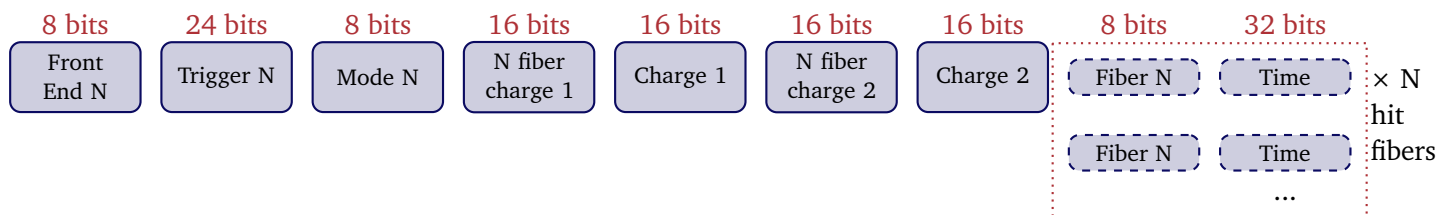


Figure A.4: Beam hodoscope data format.

A.4 Slow control, trigger and monitoring data format

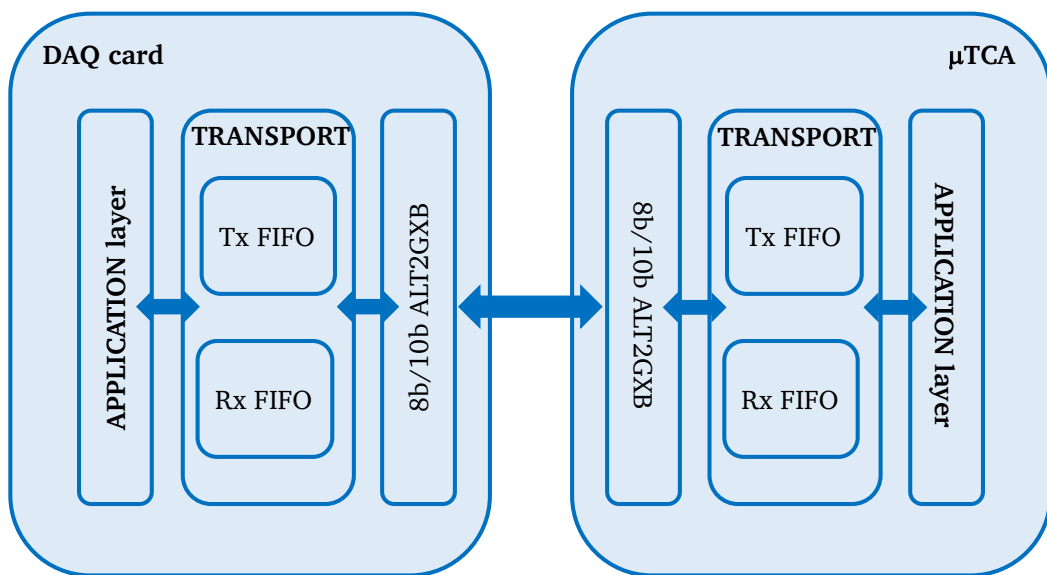
A.4.1 Communication architecture

The Endpoint architecture is composed of three layers:

- application layer

- mac (or transport) layer/processor packet
- physical layer

Figure A.5: Architecture of communication between DAQ cards and μ-TCA.



A.4.2 Transport protocol and processor packets

A.4.2.1 Definitions

It is worth to define some useful terms for the following part of the document:

- byte : 8 bits
- word : 16 bits
- K : control byte
- D : data byte
- cargo : data group
- terminator : packet end

- CRC : cyclic redundancy code

The CRC allows one to detect the transmission errors and the data transfer issues. A specific algorithm must be used, as CRC-16 : $X^{16} + X^{15} + X^2 + 1$. In the present protocol, a “parity pattern of 16 bits” have been used.

The transport layer ensures a proper packets exchange between two terminals via the data encapsulation. The data come from the application layer and are then sent to the physical layer.

A.4.2.2 Data encoding

For the transport layer, the data structure is created via the addition of a packet header, corresponding to a parity bit, of a 16 bit parity pattern and a bit for the end of the packet. The data are 8 bits/10 bits encoded. This standard 8 bits/10 bits encoding ensures sufficient data transitions for clock recovery.

A.4.2.3 Packets format

All the data packets have the same structure. A K byte (control symbol) is followed by the cargo to be sent. The end of the packets changes according to the cargo parity.
If the cargo contains an even number of bytes, the packet ends with K.28.6.

Table A.2: Packet with an even byte number cargo.

Item	Packet beginning	Cargo	Packet end
1	One K byte	0 - N D-bytes	K.28.6

If the cargo contains an odd number of bytes, the packet ends without any control symbol.

Table A.3: Packet with an odd byte number cargo.

Item	Packet beginning	Cargo	Packet end
1	One K byte	0 - N D-bytes	Beginning of a new packet

Remark :

- SYN packet is a special kind of packet starting with K.28.6 and ending with K.28.5. It is only composed of these two bytes (16 bits). It allows the receiver to find the beginning

and the end of the transmitted bytes with the aim to reconstruct the events in parallel. The synchronization speed is 44 Hz (defined by Carlos Abellan).

- In order to optimize the throughput, the control symbol at the beginning of the packet can probably be removed (further study needed).

A.4.2.4 Possible control symbols

In Table A.4, all the possible control symbols are listed (defined by Carlos Abellan).

Table A.4: Control symbol definition.

Item	Name	Control code	Comment
1	K.28.0	0x1C	Acknowledgement
2	K.28.1	0x3C	Ask for writing registers
3	K.28.2	0x5C	Ask for reading registers
4	K.28.3	0x7C	Special command
5	K.28.4	0x9C	Monitoring
6	K.28.5	0xBC	Default synchronization
7	K.28.6	0xDC	IDLE (default) and packet end
8	K.28.7	0xFC	Pre-trigger
9	K.23.7	0xF7	Trigger
10	K.27.7	0xFB	
11	K.29.7	0xFD	
12	K.30.7	0xFE	Physical data

A.4.3 Transport layer

A.4.3.1 Control packet

This kind of packet is used to check the link and for the control/command operations.

- For the link check, two kinds of packets are used: synchronization packet and IDLE packet.
- For the control/command operations, here are some examples: register configuration, FPGA dynamical programming, monitoring, etc.

Control symbol for control :

Acknowledgement packet (Front End cards → μ-TCA)

Table A.5: Control symbol definition.

Item	Name	Control code	Comment
1	K.28.0	0x1C	Acknowledgement
2	K.28.1	0x3C	Ask for writing registers
3	K.28.2	0x5C	Ask for reading registers
4	K.28.3	0x7C	Special command
5	K.28.4	0x9C	Monitoring
6	K.28.5	0xBC	Synchronization
7	K.28.6	0xDC	IDLE (default) and end of packet

This packet is sent by the FE cards and interpreted as an acknowledgement by the μ -TCA. If a part is missing, it is set to zero.

- If 0 = validation
- If 1 = problem detected

Table A.6: Definition of the acknowledgement packet.

Word	1 st byte	2 nd byte							
		7b	6b	5b	4b	3b	2b	1b	0b
1	K.28.0	0	Pb Front End num- ber	Pb with packet begin- ning	Pb with packet end	Pb with CRC	Pb with number of re- ceived words	Pb with parity bit of parity bit of bit of byte 2	parity bit of the ac- knowl- edge- ment packet
2									Front End number

A.4.3.2 Configuration packets

Writing register process (μ -TCA → Front End cards)

The process starts with a packet sent by the μ -TCA asking for the register writing. The receiver (FE card) sends back an acknowledgement packet to finish the process. In Table A.7 the format of this writing register packet is reported.

Reading register process (μ -TCA → Front End cards)

The process starts with a packet sent by the μ -TCA asking for the register reading. The receiver

Table A.7: Writing register packet.

Word	1 st byte	2 nd byte	Comment
1	K.28.1	Front End number + 1 parity bit	N/A
2	2 bytes with the number of words to be written		The length is word-based: max $2^{16} - 1 = 65535$ words
3	Register address		Address where the writing process starts
4..N+3	Data to be written		0000 0000
N+4	CRC composed of the “xor” of all bits in the same position, from word 2 to word (N+3)		

(FE card) sends back the “measure packet” if the command is correct, an acknowledgement packet if it is not.

At the beginning of the slow control, the physical addresses on the FE cards are read at the address 0.

In Table A.8 the format of this reading register packet is reported.

Table A.8: Reading register packet.

Word	1 st byte	2 nd byte	Comment
1	K.28.2	Front End number + 1 parity bit	N/A
2	2 bytes with the number of words to be read		The length is word-based: max $2^{16} - 1 = 65535$ words
3	Address of 1 st data to be read		Address where the reading process starts
4	CRC composed of the “xor” of all bits in the same position, from word 2 to word 3		/

A.4.3.3 Monitoring process (Front End cards → μ-TCA)

In case of issues, for example when the temperature of a card go beyond a fixed threshold, the DAQ card sends a “monitoring” packet to the μ-TCA. There is not a corresponding acknowledgement from the μ-TCA.

A Compton camera data format

Table A.9: Two special registers(μ -TCA → Front End cards)

Register address	Details	Comment
0	Front End number	No writing rights: register in read-only mode. Hard coded on DAQ card.
1	It defines the working modes	Optimal mode, test mode, collimated camera mode, Compton camera mode, individual detector section test. It is possible to write in the register.
2	It defines the detector to test (in single detector test mode)	Scatterer, absorber, hodoscope.
3	BGO number of sampling	For test mode with the BGO blocks signal sampling.
4	Silicon number of sampling	For test mode with the silicon layers signal sampling.

Table A.10: Measurement packet (Front End cards → μ -TCA)

Word	1 st byte	2 nd byte	Comment
1	K.28.1	Front End number + 1 parity bit	
2	2 bytes for the number of data words to send		The length is word-based: max $2^{16} - 1 = 65535$ words
3	Register address		Address where the writing process starts
4..N+3	Read data		0000 0000
N+4	CRC composed of the “xor” of all bits in the same position, from word 2 to word (N+3)		/

Table A.11: Monitoring packet.

Word	1 st byte	2 nd byte	Comment
1	K.28.4.	Front End number + 1 parity bit	Message in Table A.12.
2	15 bits for the message + 1 parity bit		Message in Table A.12.

Table A.12: Monitoring messages.

Item	Message	Bit[15]	...	Bit[7]	Bit[6]	Bit[5]	Bit[4]	Bit[3]	Bit[2]	Bit[1]	Comment
		Message type						Further information			
1	FPGA recon-figuration error	0	0	0	0	0	1	0	0	0	N/A
2	Tempe- rature alarm	0	0	0	0	1	0	x	x	x	Bit “x” is 1 if the corresponding detector goes beyond the threshold (0 elsewhere)
3	Busy	0	0	0	1	0	0	0	0	0	Front End is not able to send data
...											

A.4.3.4 Special command process (μ -TCA \rightarrow Front End cards)

This process is designed to allow the μ -TCA to send special commands to the FE cards.

Table A.13: Special command packets

Word	1 st byte	2 nd byte
1	K.28.3	Front End number + 1 parity bit
2	15 bits for the special command + 1 parity bit	

A register database (containing the operating mode identification) must be fixed and shared between all the detectors.

A.4.4 Data packets (Front End card \rightarrow μ -TCA)

In the section the packets concerning trigger, pre-trigger and physical data are described. No acknowledgement is demanded for this kind of packets.

Pre-trigger format

This packet is sent to the μ -TCA by the THOR card. The μ -TCA then shares it with all the

Table A.14: Special commands examples

Item	Command name	Bit[15..1] of 2 nd word	Comment
1	System reset	"0000 0000 0001 001"	Acknowledgement packet missing
2	Counter reset	"0000 0000 0001 000"	Acknowledgement packet needed
3	Start run	"0000 0000 0000 100"	Acknowledgement packet needed
4	Stop run	"0000 0000 0000 101"	Acknowledgement packet needed
5	Dynamical FPGA configuration	"0000 0000 0000 010"	Acknowledgement packet needed
6	Veto	"0000 0000 0000 011"	Example: μ -TCA cannot receive the data. Acknowledgement packet needed

Table A.15: Control symbol for pre-trigger, trigger and physical data.

Item	Name	Control code	Comment
1	K.28.7	0xFC	The pre-trigger is generated by the THOR card and sent to the μ -TCA who shares it with the silicon layers cards.
2	K.23.7	0xF7	The trigger is generated by a single silicon layer card and sent to the μ -TCA who shares it with all the FE cards.
5	K.30.7	0xFE	The FE cards send the data.

silicon FE cards.

Table A.16: Pre-trigger packet

Item	1 st byte	2 nd - 4 th bytes
1	K.28.7	24 bits for the trigger number

Trigger format

This packet is sent back to the μ -TCA if a silicon FE card finds an interaction in coincidence after the reception of the pre-trigger packet. The trigger is always sent before the physical data packets. The μ -TCA then sends the trigger packet to all the FE cards (scatterer, absorber, hodoscope).

Table A.17: Trigger packet

Item	1 st byte	2 nd - 4 th bytes
1	K.23.7	24 bits for the trigger number

Physical data packet format

This packet sends the “useful” data to the μ -TCA. The data format (cargo) is defined in chapter 3.

Table A.18: Physical data packet

Item	1 st byte	Cargo	End of packet
1	K.30.7.	From 0 to Nbr-1 words of D characters	K.28.6 or the beginning of a new packet.

A.5 UDP packets format

Once the μ -TCA receives the data from the FE cards, a physical event is generated and stored in dedicated buffers. The buffers are then sent to the acquisition PC via UDP packets. Each detector section has its own UDP socket, and three receiving ports are used for the three data fluxes: 60001 for the hodoscope, 60002 for the absorber, 60003 for the scatterer. The content of the data buffers are sent in order to avoid to divide events in different packets, so that each UDP packet is completely independent from the others and contains complete events. The maximum size of a packet is set to 1500 (UDP data = 1472), or to 9000 for the so called “jumbo frames”, used for high speed acquisitions.

Each UDP packet has a custom defined header, composed of:

- 32 bits: packet number, starting from 0;

- 16 bits: number of data structures in the packet;

The data structures are then in a list one after the other with the already described format.

A.6 Data throughput expected in clinical conditions

A.6.1 Clinical intensities

In clinical standards, the beam maximum intensity is:

- protons : 10^{10} protons/s
- carbon ions : 5×10^7 C ions/s

The Compton camera must be designed in order to be able to handle the whole range of clinical intensities. The design reference is then the maximum intensity, about 2×10^{10} protons/s) delivered by the cyclotron C230 by IBA. The number of proton  delivered per second is higher than the maximum considered rate (10^{10} protons/s).

As shown by the simulation results, the Compton camera can not be used for an online monitoring at the maximum beam intensity for both proton and carbon ion beams. The main limitation comes from the amount of random coincidences detected by the camera for high intensity beams. One possible solution is to deliver a lower intensity beam for the range monitoring before the beginning of the treatment. The results shown here relate  to a reduced intensity, corresponding to the one selected via the simulation studies.

A.6.1.1 Review: detector and target sizes

Detectors sizes:

- Silicon scatterer : 7 silicon layers, $9.6 \times 9.6 \times 0.2 \text{ cm}^3$ (first layer 20 cm far from the beam line)
- BGO absorber: BGO block $3.5 \times 3.8 \times 3.0 \text{ cm}^3$ (67.5 cm far from the beam line - center of the block)

Poly Methyl Metacrylate (PMMA) target size: cylindrical shape, diameter 15 cm, 20 cm length along the beam direction.

A.6.2 Coincidence rate

In Table A.19 the coincidence and single (pre-trigger) rates expected for the different detector section are listed according to the beam kind and intensity. This values correspond the Compton camera, while for the collimated camera a reduced rate is expected for the absorber due to the presence of the physical collimator.

Table A.19: Coincidence and single rate as a function of the beam intensity. The BGO single rate corresponds to the pre-trigger rate.

	Clinical intensity		Reduced intensity		Collimated camera	
	Protons	Carbon ions	Protons	Carbon ions	Protons	Carbon ions
Intensity(ions/s)	2×10^{10}	5×10^7	1×10^8	5×10^6	2×10^{10}	5×10^7
Coincidence rate per incident ion	9×10^{-4}	8×10^{-4}	9×10^{-4}	8×10^{-4}	/	/
Coincidence rate (Hz)	$1,8 \times 10^7$	4×10^4	9×10^4	4×10^3	/	/
Single rate BGO (Hz) - 96 blocks	$7,8 \times 10^7$	$1,4 \times 10^6$	$3,9 \times 10^5$	$1,4 \times 10^5$	/	/
Single rate BGO (Hz) - 1 block	$8,1 \times 10^5$	$1,5 \times 10^4$	4×10^3	$1,5 \times 10^3$	/	/
Single rate BGO (Hz) - 1 ASM card (6 blocks)	$6,5 \times 10^6$	$1,2 \times 10^5$	$3,2 \times 10^4$	$1,2 \times 10^4$	/	/

The application of the Compton camera at clinical intensity seems not feasible. The camera distance with respect to the beam line should be increased to lower the rate to 1×10^5 Hz (which means to put the 1st silicon layer 1 m far from the beam line). For a carbon ion beam at 5×10^7 Hz, the estimated coincidence rate is 4×10^4 Hz, with 1.4×10^6 single rate on the absorber (measurements of coincidence rate on the HIT accelerator adapted to a real camera size with a 40 ns coincidence window, Krimmer ANIMMA 2013). The data flow between the μ -TCA and the acquisition PC corresponds to the coincidence rate, due to the fact that only coincidence events are stored.

A.6.3 Data flow (Front End cards → μ -TCA)

The data format previously described has been used to evaluate the data flow between each FE card and the μ -TCA. The calculation is performed according to the “optimal” mode of each detector. For the BGO, we only consider events where the 4 PMs are involved. For the silicon layers, two cases are considered:

- Case 1 : one single layer with 6 involved strips;
- Case 2 : all the 7 layers involved with 6 hit strips per layer.

A Compton camera data format

Concerning the hodoscope, we considered an event with one hit fiber readout on the two sides.

The 8bits/10bits encoding is included in the calculation.

Table A.20: Data flux between FE cards and μ -TCA.

	Clinical intensity	Reduced intensity		
	Protons	Carbon ions	Protons	Carbon ions
Intensity (ions/s)	2×10^{10}	5×10^7	1×10^8	5×10^6
Pre-trigger flux (Mbits/s)	$2,5 \times 10^3$	47,6	13,3	4,76
Trigger flux (Mbits/s)	612	1,4	3,1	0,1
BGO data flux (Mbits/s) - 96 blocks	$1,7 \times 10^5$	373	873	37,3
BGO data flux (Mbits/s)- 1 block	$1,7 \times 10^3$	3,88	8,73	0,3
BGO data flux (Mbits/s) - 1 carte ASM	$1,4 \times 10^4$	31,1	69,9	3,1
Silicon data flux (Mbits/s) - case 1	$2,3 \times 10^5$	522	$1,2 \times 10^3$	52,2
Silicon data flux (Mbits/s) - case 2	$1,6 \times 10^6$	$3,7 \times 10^3$	$8,2 \times 10^3$	366
Hodoscope data flux (Mbits/s)	$8,1 \times 10^4$	180	404	18

A.6.4 Acquisition data flow (μ -TCA \rightarrow Acquisition PC)

The data flow from the μ -TCA to the acquisition PC is detailed here. The UDP encoding is included in the calculation.

Table A.21: Data flow between μ -TCA and acquisition PC.

	Clinical intensity	Reduced intensity		
	Protons	Carbon ions	Protons	Carbon ions
Intensity (ions/s)	2×10^{10}	5×10^7	1×10^8	5×10^6
Coincidence rate per incident ion	9×10^{-4}	8×10^{-4}	9×10^{-4}	8×10^{-4}
Coincidence rate (Hz)	$1,8 \times 10^7$	4×10^4	9×10^4	4×10^3
Data flow (Mbits/s) - case 1	$2,2 \times 10^4$	46,7	112	5,0
Data flow (Mbits/s) - case 2	6×10^4	133	300	13,3

A.6.5 Conclusions

As already mentioned, the Compton camera application is not feasible at clinical beam intensities 

In order to have an online monitoring of the beam range, a reduced intensity must be foreseen. The main limitation is the rate of random coincidences detected at high intensity, while from the technological point of view no limitations are highlighted by this study. In the collimated camera configuration, where no coincidences are required and the random coincidences limitation is removed, we can then expect to be able to work at real clinical intensity.

Table 7.22: Acquisition format of the Compton camera data.

COMPTON CAMERA ACQUISITION DATA FORMAT				
	Description	Size (bytes)	Size (bits)	Details
Beginning of file (10 bytes)	File start ID	2	16	FOFO (hex) fixed ID
	Run number	4	32	Automatically increasing in DAQ software - it can be manually fixed
	Total number of events	4	32	Fixed at the beginning of the acquisition, it defines the file size
Event header (11 bytes) x total number of events	Event start ID	2	16	ABCD (hex) fixed ID
	Event number	4	32	Automatically increasing in μ-TCA data format
	Trigger number	3	24	Automatically increasing in μ-TCA data format
	Number of hits in trigger	2	16	
Data header (7 bytes) x number of hits in trigger	Hit start ID	1	8	EB (hex) fixed ID
	FE number	1	8	see Table A.1
	Trigger number	3	24	repeated from Event Header
	Mode number	1	8	see figure A.4 (7 or 8 for the hodoscope - 7 = optimal, 8 = test)
	Number of involved fibers	1	8	
Hit structure scatterer (7 bytes - mode 1, 9 bytes - mode 2, mode 3 and 4 with signal sampling) x number of involved strips (mode 1 and 3) or tracks (mode 2 and 4)	Strip number	1	8	mode 1 and 3
	Position	2	16	mode 2 and 4
	Time	4	32	all modes
	Charge	2	16	mode 1 and 2
	Signal samples	2	16	mode 3 and 4 - size per sample - n samples, with n selected in acquisition code
Hit structure absorber (17 bytes - mode 5, mode 6 with signal sampling) x number of involved blocks	Block number	1	8	both modes
	Time	4	32	both modes
	Charge PM 1-4	3	24	mode 5 - size per PM - 4 PMs per block
	Signal samples	2	16	mode 6 - size per sample per PM - n samples, with n selected in acquisition code, 4 PMs per block
Hit structure hodoscope (5 bytes - mode 7, 7 bytes - mode 8) x number of involved fibers	Fiber number	1	8	ranges from 0 to 128
	Time	4	32	in both modes 7 and 8
	Charge	2	16	only for mode 8
End of file (10 bytes)	File end ID	2	16	F1F1 (hex) fixed ID
	Number of events in file	4	32	for verification and debugging
	Number of octets in file	4	32	for verification and debugging

List of abbreviations

¹¹¹In Indium-111 98



¹³¹I Iodine-131 92, 98

¹³¹In Indium-131 4

²²Na Sodium-22 ix, 56–62, 70, 71

⁴²K Potassium-42 98

⁵⁷Co Cobalt-57 56

⁵⁹Fe Iron-59 98

⁶⁰Co Cobalt-60 ix, 57, 59, 64–66, 68, 86

^{91m}Y Yttrium-91m 98

μ-TCA Micro Advanced Telecommunications Computing Architecture v, viii, xi, xiii, 40, 47–51, 82–86, 119–122, 127, 129–135, 137, 138, 140

A.D.A.M. Advanced Oncotherapy 17

ADC Analog-to-Digital Converter 34, 40, 45, 57–59, 62, 69, 75

AMC Advanced Mezzanine Card viii, 47–50, 82, 85

ASIC Application-Specific Integrated Circuit 34, 35, 43, 45, 51, 56, 82, 123, 126

ASM Analog Sampling Module viii, 38, 40, 41, 47, 49, 83, 120–123, 137, 138

ATCA Advanced Telecommunications Computing Architecture 47

AVIRM Application et Valorisation des Interactions Rayonnements-Matière 38, 40, 75

BaF₂ Barium Fluoride ix, 61, 73

BGO Bismuth Germanium Oxide - Bi₁₂GeO₂₀ i, iv, viii, ix, xi, xiii, 29, 36–42, 47, 52, 55, 57–59, 61, 62, 70, 72–74, 83, 87, 95, 96, 106, 121, 123, 132, 136–138

BNCT Boron Neutron Capture Therapy 15

CAL Centre Antoine Lacassagne, Nice, France 50

List of abbreviations

- CdTe** Cadmium Telluride x, 97, 105
- CeBr₃** Cerium Bromide 84
- CERN** Conseil Européen pour la Recherche Nucléaire, Geneva, Switzerland 17, 47
- CLaRyS** Contrôle en Ligne de l'hadronthérapie par Rayonnements Secondaires i, ii, 30, 32, 42, 47, 54, 55, 81, 86, 87, 92, 93, 104, 107, 110, 112
- CNAO** Centro Nazionale di Adroterapia Oncologica, Italy vii, 16, 17
- CPPM** Centre de Physique des Particules de Marseille, France 30, 47, 85
- CR-RC** Capacitor Resistor - Resistor Capacitor 34
- CREATIS** Centre de Recherche en Acquisition et Traitement de l'Image pour la Santé, Lyon, France 30, 54, 96
- CSA** Charge Sensitive Amplifier 34
- CSDA** Continuous Slowing Down Approach 6, 9
- CT** Computed Tomography i, vii, 20, 22, 23
- CTV** Clinical Target Volume 24
- DLL** Delay Locked Loop 45
- DPGA** DéTECTeur Pixélisé de Grande Acceptance 30, 38, 40
- DRS** Domino Ring Sampler 38, 40
- DSSD** Double-sided Silicon Strip Detector i, 32–34, 55, 56, 82, 86, 95, 97, 111
- DWA** Dielectric Wall Accelerator 17
- EM** Electromagnetic 6, 8, 10
- ENC** Equivalent Noise Charge 34, 95, 105, 111
- ESRF** European Synchrotron Radiation Facility, Grenoble, France 85
- FE** Front-End viii, xiii, 33–36, 38, 40, 41, 43–47, 49, 56, 57, 77, 82–86, 119–123, 126, 130, 131, 133–135, 137, 138, 140
- FFAG** Fixed Field Alternating Gradient 16

FPGA Field Programmable Gate Array 34, 35, 40, 45, 47, 126, 129, 133, 134

FWHM Full Width at Half Maximum xi, 34, 47, 56, 62, 70, 73–75, 83, 95, 96, 106

GANIL Grand Accelerateur National d’Ions Lourds, Caen, France 45, 47, 83, 85, 95

GATE GEANT4 Application for Tomographic Emission 98

GEANT4 GEometry And Tracking 4 93

GSI GSI Helmholtz Centre for Heavy Ion Research, Germany vii, 20, 22, 23

Gsps Giga Sample Per Second 38

HEGP High Energy General Purpose 98, 111

HIMAC Heavy Ion Medical Accelerator in Chiba, Japan 21, 23

HIT Heidelberg Ion Therapy Center, Germany vii, 5, 16, 17, 21, 45, 47

HSMC High-Speed Mezzanine Card 40

HU Hounsfield Units 22

IBA Ion Beam Applications, Belgium vii, 16, 17

IMPT Intensity-Modulated Particle Therapy 20, 24

IMRT Intensity-Modulated RadioTherapy 20, 24

INFN Istituto Nazionale di Fisica Nucleare, Italy 17

IPNL Institut de Physique Nucléaire de Lyon, France 30, 33–35, 40, 41, 43, 50, 51, 55, 57, 75, 82–87, 95

IPNO Institut de Physique Nucléaire d’Orsay, France 47

IRFU Institut de Recherche sur les lois Fondamentales de l’Univers, Paris, France 58

LaBr₃ Lanthanum Bromide 56

LAL Laboratoire de l’Accélérateur Linéaire, Paris, France 58

LED Light Emitting Diode x, 73, 75, 77–80

LEM Local Effect Model 23

List of abbreviations

- LET** Linear Energy Transfer 14, 19, 22
- LHCb** Large Hadron Collider beauty 47
- LIGHT** Linac for Image Guided HadronTherapy 17
- LLNL** Lawrence Livermore National Laboratory, USA 17
- LM-MLEM** List Mode-Maximum Likelihood Expectation Maximization 54, 96, 104–106, 110, 111
- LPC** Laboratoire de Physique de Clermont, France 30, 38, 40, 41, 47, 75, 87
- LPSC** Laboratoire de Physique Subatomique et Corpusculaire, Grenoble, France 30, 85
- LQ** Linear-Quadratic 23
- LSO** Cerium-doped Lutetium Oxyorthosilicate - Lu_{2(1-x)}Ce_{2x}SiO₄ 36, 37
- LVDS** Low-Voltage Differential Signaling 34
- LYSO** Lutetium-Yttrium OxyorthoSilicate - Lu_{2(1-x)}Y_{2x}SiO₅ 36–38, 40, 84
- MCH** μ-TCA Carrier HUB 47
- MCS** Multiple Coulomb Scattering 10, 24
- MEGAlib** Medium-Energy Gamma-ray Astronomy library 96
- MICRHANU** Micro-électronique RHône AUvergne 45
- MKM** Microdosimetric Kinetic Model 23
- MRI** Magnetic Resonance Imaging 4, 22
- Msps** Mega Sample Per Second 34
- NaI(Tl)** Sodium Iodide doped with Thallium 98, 99
- NIM** Nuclear Instrumentation Module 55–58, 61, 62, 83, 87
- NIRS** National Institute of Radiological Sciences, Japan 20–23
- OAR** Organ At Risk 6, 20, 22
- pCT** proton Computed Tomography 22

- PET** Positron Emission Tomography i, 4, 22, 25, 30, 36, 38, 41, 57, 83, 92
- PG** Prompt-Gamma i
- PM** Photo-Multiplier iv, ix, x, 29, 37–39, 41–47, 57, 58, 62–64, 73–81, 83, 84, 86, 123, 126, 137, 140
- PMMA** Poly Methyl Metacrylate 41, 136
- PSI** Paul Scherrer Institut, Villigen, Switzerland 20–22, 38
- PTV** Planned Target Volume 18, 19, 22, 24
- RAM** Random Access Memory 50
- RBE** Relative Biological Effectiveness 13, 14, 22–24
- RMS** Root Mean Square 34, 45, 85, 107
- RSP** Relative Stopping Power vii, 22, 23
- SHS** Slow Shaper 34
- SOBP** Sprea-Out Bragg Peak vii, 18, 19, 23
- SPECT** Single Photon Emission Computed Tomography i, 92, 93, 95, 98, 104, 110–112
- SPTR** Single Photon Time Resolution 84
- TCP** Tumor Control Probability 22
- TCP** Transmission Control Protocol 49, 51
- TDC** Time-to-Digital Converter 34, 45, 119
- THOR** Trigger et HORloge viii, 40, 47–49, 83, 121, 122, 133, 134
- TOF** Time-Of-Flight 31, 32, 42, 47, 55, 83–85
- TPS** Treatment-Planning System 22, 23
- UDP** User Datagram Protocol 49–51, 85
- USB** Universal Serial Bus 58
- VME** VERSABUS Module Eurocard 38, 47, 56, 83

List of abbreviations

WEPL Water-Equivalent Path Length 22

Bibliography

 Abellan, C., J.-. P Cachemiche, F. Réthoré, and C. Morel (June 2013). “A data acquisition system for medical imaging”. In: *2013 3rd International Conference on Advancements in Nuclear Instrumentation, Measurement Methods and their Applications (ANIMMA)*, pp. 1–7. DOI: 10.1109/ANIMMA.2013.6728028 (cit. on p. 47).

Adam, L. E., J. Zaers, H. Ostertag, H. Trojan, M. E. Bellemann, and G. Brix (June 1997). “Performance evaluation of the whole-body PET scanner ECAT EXACT HR + following the IEC standard”. In: *IEEE Transactions on Nuclear Science* 44.3, pp. 1172–1179. ISSN: 0018-9499. DOI: 10.1109/23.596983 (cit. on p. 36).

Albertini, F., E. B. Hug, and A. J. Lomax (2011). “Is it necessary to plan with safety margins for actively scanned proton therapy?” In: *Physics in Medicine & Biology* 56.14, p. 4399. URL: <http://stacks.iop.org/0031-9155/56/i=14/a=011> (cit. on p. 24).

Altera (2009). *Stratix II GX Device Handbook*. Volume 1. Altera Corporation (cit. on pp. 34, 45).

Altera (2012). *Cyclone III Device Handbook*. Volume 1. Altera Corporation (cit. on pp. 34, 45).

Altera (2015). *Stratix V Device Handbook*. Volume 3. Altera Corporation (cit. on p. 40).

Altera (2016). *Cyclone IV Device Handbook*. Volume 1. Altera Corporation (cit. on p. 47).

Amaldi, U. (2009). “Cyclinacs: Fast-Cycling Accelerators for Hadrontherapy”. In: *Nucl. Instrum. Meth. A*. arXiv: 0902.3533 [physics.med-ph] (cit. on p. 17).

Amaldi, U., P. Berra, K. Crandall, D. Toet, M. Weiss, R. Zennaro, E. Rosso, B. Szeless, M. Vretenar, C. Cicardi, C. De Martinis, D. Giove, D. Davino, M. R. Masullo, and V. Vaccaro (2004). “LIBO-a linac-booster for protontherapy: construction and tests of a prototype”. In: *Nuclear Instruments and Methods in Physics Research Section A: Accelerators, Spectrometers, Detectors and Associated Equipment* 521.2, pp. 512–529. ISSN: 0168-9002. DOI: <https://doi.org/10.1016/j.nima.2003.07.062>. URL: <http://www.sciencedirect.com/science/article/pii/S0168900203023994> (cit. on p. 17).

Amaldi, U., R. Bonomi, S. Braccini, M. Crescenti, A. Degiovanni, M. Garlasché, A. Garonna, G. Magrin, C. Mellace, P. Pearce, G. Pittà, P. Puggioni, E. Rosso, S. Verdú Andrés, R. Wegner, M. Weiss, and R. Zennaro (2010). “Accelerators for hadrontherapy: From Lawrence cyclotrons to linacs”. In: *Nuclear Instruments and Methods in Physics Research Section A: Accelerators, Spectrometers, Detectors and Associated Equipment* 620.2, pp. 563–577. DOI: <https://doi.org/10.1016/j.nima.2010.03.130>. URL: <http://www.sciencedirect.com/science/article/pii/S0168900210007357> (cit. on p. 17).

Amaldi, U., S. Braccini, and P. Puggioni (2009). “High Frequency Linacs for Hadrontherapy”. In: *Reviews of Accelerator Science and Technology* 02.01, pp. 111–131. DOI: 10.1142/S179362680900020X. eprint: <https://doi.org/10.1142/S179362680900020X>. URL: <https://doi.org/10.1142/S179362680900020X> (cit. on p. 17).

Bibliography

- Anger, H. O. (1958). "Scintillation Camera". In: *Review of Scientific Instruments* 29.1, pp. 27–33. DOI: 10.1063/1.1715998. eprint: <http://dx.doi.org/10.1063/1.1715998>. URL: <http://dx.doi.org/10.1063/1.1715998> (cit. on p. 92).
- Anger, H. O. (1964). "Scintillation Camera with Multichannel Collimators". In: *Journal of Nuclear Medicine* 5.7, pp. 515–531. eprint: <http://jnm.snmjournals.org/content/5/7/515.full.pdf+html>. URL: <http://jnm.snmjournals.org/content/5/7/515.short> (cit. on p. 92).
- Antoine, S., B. Autin, W. Beeckman, J. Collot, M. Condat, F. Forest, J. Fourrier, E. Froidefond, J. L. Lancelot, J. Mandrillon, P. Mandrillon, F. Méot, Y. Mori, D. Neuvéglise, C. Ohmori, J. Pasternak, and T. Planche (2009). "Principle design of a protontherapy, rapid-cycling, variable energy spiral FFAG". In: *Nuclear Instruments and Methods in Physics Research Section A: Accelerators, Spectrometers, Detectors and Associated Equipment* 602.2, pp. 293–305. DOI: <https://doi.org/10.1016/j.nima.2009.01.025>. URL: <http://www.sciencedirect.com/science/article/pii/S0168900209000059> (cit. on p. 17).
- Aspen Aerogels (2011). *Spaceloft® - High performance Insulation for building envelopes. Data Sheet*. Aspen Aerogels Inc. (cit. on p. 35).
- Barth, R. F., J. A. Coderre, M. G. H. Vicente, and T. E. Blue (2005). "Boron Neutron Capture Therapy of Cancer: Current Status and Future Prospects". In: *Clinical Cancer Research* 11.11, pp. 3987–4002. DOI: 10.1158/1078-0432.CCR-05-0035. eprint: <http://clincancerres.aacrjournals.org/content/11/11/3987.full.pdf>. URL: <http://clincancerres.aacrjournals.org/content/11/11/3987> (cit. on p. 15).
- Baskar, R., K. A. Lee, R. Yeo, and K.-W. Yeoh (2012). "Cancer and radiation therapy: current advances and future directions." eng. In: *Int J Med Sci* 9.3, pp. 193–199. DOI: 10.7150/ijms.3635 (cit. on p. 5).
- Basko, R., G. L. Zeng, and G. T. Gullberg (1998). "Application of spherical harmonics to image reconstruction for the Compton camera". In: *Physics in Medicine and Biology* 43.4, p. 887. URL: <http://stacks.iop.org/0031-9155/43/i=4/a=016> (cit. on p. 28).
- Bauer, J., D. Unholtz, F. Sommerer, C. Kurz, T. Haberer, K. Herfarth, T. Welzel, S. E. Combs, J. Debus, and K. Parodi (2013). "Implementation and initial clinical experience of offline PET/CT-based verification of scanned carbon ion treatment". In: *Radiotherapy and Oncology* 107.2, pp. 218–226. ISSN: 0167-8140. DOI: <https://doi.org/10.1016/j.radonc.2013.02.018>. URL: <http://www.sciencedirect.com/science/article/pii/S0167814013001606> (cit. on p. 25).
- Belkić, D. (May 2010). "Review of theories on ionization in fast ion-atom collisions with prospects for applications to hadron therapy". In: *Journal of Mathematical Chemistry* 47.4, pp. 1366–1419. DOI: 10.1007/s10910-010-9662-x. URL: <https://doi.org/10.1007/s10910-010-9662-x> (cit. on p. 13).
- Bentzen, S. M. (2006). "Preventing or reducing late side effects of radiation therapy: radiobiology meets molecular pathology." eng. In: *Nat Rev Cancer* 6.9, pp. 702–713. DOI: 10.1038/nrc1950 (cit. on p. 5).

- Bert, C., S. O. Grözinger, and E. Rietzel (2008). “Quantification of interplay effects of scanned particle beams and moving targets”. In: *Physics in Medicine & Biology* 53.9, p. 2253. URL: <http://stacks.iop.org/0031-9155/53/i=9/a=003> (cit. on p. 24).
- Bert, C. and K. Herfarth (2017). “Management of organ motion in scanned ion beam therapy”. In: *Radiation Oncology (London, England)* 12, p. 170. DOI: 10.1186/s13014-017-0911-z. URL: <http://www.ncbi.nlm.nih.gov/pmc/articles/PMC5674859/> (cit. on p. 24).
- Bethe, H. (1930). “Zur Theorie des Durchgangs schneller Korpuskularstrahlen durch Materie”. In: *Annalen der Physik* 397.3, pp. 325–400. DOI: 10.1002/andp.19303970303. eprint: <https://onlinelibrary.wiley.com/doi/pdf/10.1002/andp.19303970303>. URL: <https://onlinelibrary.wiley.com/doi/abs/10.1002/andp.19303970303> (cit. on p. 8).
- Bhat, M. R. (1992). *Evaluated Nuclear Structure Data File (ENSDF), Nuclear Data for Science and Technology*, page 817, edited by S. M. Qaim (SpringerVerlag, Berlin, Germany, 1992). URL: <https://www.nndc.bnl.gov/> (visited on 03/27/2017) (cit. on p. 94).
- Bichsel, H. (2013). “Chapter One - Stochastics of Energy Loss and Biological Effects of Heavy Ions in Radiation Therapy”. In: *Theory of Heavy Ion Collision Physics in Hadron Therapy*. Vol. 65. Advances in Quantum Chemistry. Academic Press, pp. 1–38. DOI: <https://doi.org/10.1016/B978-0-12-396455-7.00001-7>. URL: <http://www.sciencedirect.com/science/article/pii/B9780123964557000017> (cit. on p. 13).
- Blakely, E. A. and P. Y. Chang (2009). “Biology of charged particles.” eng. In: *Cancer J* 15.4, pp. 271–284. DOI: 10.1097/PPO.0b013e3181b666c5 (cit. on p. 5).
- Blakely, E. A., F. Q. Ngo, S. B. Curtis, and C. A. Tobias (1984). “Heavy-Ion Radiobiology: Cellular Studies”. In: *Advances in Radiation Biology*. Ed. by J. T. Lett. Vol. 11. Advances in Radiation Biology. Elsevier, pp. 295–389. DOI: <https://doi.org/10.1016/B978-0-12-035411-5.50013-7>. URL: <http://www.sciencedirect.com/science/article/pii/B9780120354115500137> (cit. on p. 14).
- Bloch, F. (1933). “Zur Bremsung rasch bewegter Teilchen beim Durchgang durch Materie”. In: *Annalen der Physik* 408.3, pp. 285–320. DOI: 10.1002/andp.19334080303. eprint: <https://onlinelibrary.wiley.com/doi/pdf/10.1002/andp.19334080303>. URL: <https://onlinelibrary.wiley.com/doi/abs/10.1002/andp.19334080303> (cit. on p. 8).
- Bohr, N. (1915). “On the decrease of velocity of swiftly moving electrified particles in passing through matter”. In: *The London, Edinburgh, and Dublin Philosophical Magazine and Journal of Science* 30.178, pp. 581–612. DOI: 10.1080/14786441008635432. eprint: <https://doi.org/10.1080/14786441008635432>. URL: <https://doi.org/10.1080/14786441008635432> (cit. on p. 9).
- Bothe, W. (Jan. 1921). “Das allgemeine Fehlergesetz, die Schwankungen der Feldstärke in einem Dielektrikum und die Zerstreuung der α -Strahlen”. In: *Zeitschrift für Physik* 5.1, pp. 63–69. DOI: 10.1007/BF01349687. URL: <https://doi.org/10.1007/BF01349687> (cit. on p. 10).
- Braccini, S. (2010). “Scientific and technological development of hadrontherapy”. In: *Astroparticle, Particle and Space Physics, Detectors and Medical Physics Applications*, pp. 598–609. DOI:

Bibliography

- 10.1142/9789814307529_0099. eprint: https://www.worldscientific.com/doi/pdf/10.1142/9789814307529_0099. URL: https://www.worldscientific.com/doi/abs/10.1142/9789814307529_0099 (cit. on p. 14).
- Bragg, W. H. M. A. and R. Kleeman (1904). “On the ionization curves of radium”. In: *The London, Edinburgh, and Dublin Philosophical Magazine and Journal of Science* 8.48, pp. 726–738. DOI: 10.1080/14786440409463246. eprint: <https://doi.org/10.1080/14786440409463246>. URL: <https://doi.org/10.1080/14786440409463246> (cit. on p. 6).
- Bragg, W. H. M. A. and R. Kleeman (1905). “On the α particles of radium, and their loss of range in passing through various atoms and molecules”. In: *The London, Edinburgh, and Dublin Philosophical Magazine and Journal of Science* 10.57, pp. 318–340. DOI: 10.1080/14786440509463378. eprint: <https://doi.org/10.1080/14786440509463378>. URL: <https://doi.org/10.1080/14786440509463378> (cit. on pp. 6, 9).
- Brahme, A. (2004). “Recent advances in light ion radiation therapy”. In: *International Journal of Radiation Oncology Biology Physics* 58.2, pp. 603–616. DOI: 10.1016/j.ijrobp.2003.09.034. URL: <http://dx.doi.org/10.1016/j.ijrobp.2003.09.034> (cit. on p. 5).
- Breton, D., E. Delagnes, J. Maalmi, and P. Rusquart (May 2014). “The WaveCatcher family of SCA-based 12-bit 3.2-GS/s fast digitizers”. In: *2014 19th IEEE-NPSS Real Time Conference*, pp. 1–8. DOI: 10.1109/RTC.2014.7097545 (cit. on p. 58).
- Brix, G., J. Zaers, L.-E. Adam, M. E. Bellemann, H. Ostertag, H. Trojan, U. Haberkorn, J. Doll, F. Oberdorfer, and W. Lorenz (1997). “Performance Evaluation of a Whole-Body PET Scanner Using the NEMA Protocol”. In: *Journal of Nuclear Medicine* 38.10, pp. 1614–1623. eprint: <http://jnm.snmjournals.org/content/38/10/1614.full.pdf+html>. URL: <http://jnm.snmjournals.org/content/38/10/1614.short> (cit. on p. 36).
- Brun, R. and F. Rademakers (1997). “ROOT: An object oriented data analysis framework”. In: *Nucl. Instrum. Meth.* A389, pp. 81–86. DOI: 10.1016/S0168-9002(97)00048-X (cit. on pp. 50, 52, 60).
- Brunner, S. E., L. Gruber, A. Hirtl, K. Suzuki, J. Marton, and D. R. Schaart (2016). “A comprehensive characterization of the time resolution of the Philips Digital Photon Counter”. In: *Journal of Instrumentation* 11.11, P11004. URL: <http://stacks.iop.org/1748-0221/11/i=11/a=P11004> (cit. on p. 84).
- Cachemiche, J.-P., P. Y. Duval, F. Hachon, R. Le Gac, and F. Réthoré (Sept. 2012). “xTCA developments in Marseille for the LHCb Readout”. In: *TWEPP 2012 Topical Workshop on Electronics for Particle Physics*. Oxford, United Kingdom. URL: <http://hal.in2p3.fr/in2p3-00757616> (cit. on p. 47).
- Cantor, D. (Apr. 1988). “Pioneers and early years. A history of British radiology”. In: *Medical History* 32.2, pp. 224–224. URL: <http://www.ncbi.nlm.nih.gov/pmc/articles/PMC1139872/> (cit. on p. 4).

- Caporaso, G. J.**, Y.-J. Chen, and S. E. Sampayan (2009). “The Dielectric Wall Accelerator”. In: *Reviews of Accelerator Science and Technology* 02.01, pp. 253–263. DOI: 10.1142/S1793626809000235. URL: <https://doi.org/10.1142/S1793626809000235> (cit. on p. 17).
- Catterall, M.**, C. Rogers, R. H. Thomlinson, and S. B. Field (1971). “An investigation into the clinical effects of fast neutrons”. In: *The British Journal of Radiology* 44.524. PMID: 4997649, pp. 603–611. DOI: 10.1259/0007-1285-44-524-603. eprint: <https://doi.org/10.1259/0007-1285-44-524-603>. URL: <https://doi.org/10.1259/0007-1285-44-524-603> (cit. on p. 15).
- Cecchin, D.**, D. Poggiali, L. Riccardin, P. Turco, F. Bui, and S. De Marchi (2015). “Analytical and experimental FWHM of a gamma camera: theoretical and practical issues.” In: *PeerJ* 3:e722 (cit. on p. 104).
- Chen, X.** (2017). “Développement de cartes Front-End avec leur firmware associé pour un hodoscope de faisceau et un diffuseur silicium utilisées pour le contrôle de dose en ligne en hadronthérapie.” Mémoire for CNAM engineer degree in Electronic Systems (cit. on pp. 35, 45).
- Coudurier, V.** (2015). “Caractérisation d’un hodoscope de faisceau pour l’hadronthérapie”. Master internship report (cit. on pp. 75, 86).
- Cree, M. J.** and P. J. Bones (June 1994). “Towards direct reconstruction from a gamma camera based on Compton scattering”. In: *IEEE Transactions on Medical Imaging* 13.2, pp. 398–407. DOI: 10.1109/42.293932 (cit. on p. 28).
- Dahoumane, M.**, D. Dauvergne, J. Krimmer, J.-L. Ley, É. Testa, and Y. Zoccarato (Nov. 2014). “A low noise and high dynamic range CMOS integrated Electronics associated with double sided Silicon Strip Detectors for a Compton camera gamma-ray detecting system”. In: *2014 IEEE Nuclear Science Symposium and Medical Imaging Conference (NSS/MIC)*, pp. 1–6. DOI: 10.1109/NSSMIC.2014.7431122 (cit. on p. 34).
- Dahoumane, M.**, D. Dauvergne, J. Krimmer, H. Mathez, C. Ray, É. Testa, A. H. Walenta, and Y. Zoccarato (Oct. 2012). “A low noise and high dynamic charge sensitive amplifier-shaper associated with Silicon Strip Detector for compton camera in hadrontherapy”. In: *2012 IEEE Nuclear Science Symposium and Medical Imaging Conference Record (NSS/MIC)*, pp. 1445–1451. DOI: 10.1109/NSSMIC.2012.6551351 (cit. on p. 35).
- Degiovanni, A.** and U. Amaldi (2015). “History of hadron therapy accelerators”. In: *Physica Medica* 31.4, pp. 322–332. ISSN: 1120-1797. DOI: <https://doi.org/10.1016/j.ejmp.2015.03.002>. URL: <http://www.sciencedirect.com/science/article/pii/S1120179715000629> (cit. on p. 14).
- Deng, S.-M.** (2012). “Etude de conception d’ASICs de lecture et d’étiquetage en temps associés à des photomultiplicateurs pour un hodoscope de faisceau en hadronthérapie”. PhD thesis. École Doctorale EEA (Électronique, Électrotechnique et Automatique), Université Claude Bernard - Lyon 1 (cit. on p. 45).
- Deng, S.-M.**, H. Mathez, D. Dauvergne, G.-N. Lu, and Y. Zoccarato (2012). “Front-end multi-channel PMT-associated readout chip for hodoscope application”. In: *Nuclear Instruments and*

- Methods in Physics Research Section A: Accelerators, Spectrometers, Detectors and Associated Equipment* 695. New Developments in Photodetection NDIP11, pp. 390–393. ISSN: 0168-9002. DOI: <https://doi.org/10.1016/j.nima.2011.11.042>. URL: <http://www.sciencedirect.com/science/article/pii/S0168900211020845> (cit. on p. 45).
- Deng, S.-M., H. Mathez, D. Dauvergne, Y. Zoccarato, and G.-N. Lu (Jan. 2013). “Very fast front end ASIC associated with multi-anode PMTs for a scintillating-fibre beam hodoscope”. In: *Journal of Instrumentation* 8, p. C01047. DOI: 10.1088/1748-0221/8/01/C01047. URL: <https://hal.archives-ouvertes.fr/hal-00990850> (cit. on p. 45).
- Despeignes, V. (1896). “Observations on a case of cancer of the stomach treated by Röntgen rays.” In: *Lyon Medical Journal* 82, p. 428 (cit. on p. 4).
- Duck, F. A. (June 2014). “The origins of medical physics”. In: *Physica Medica: European Journal of Medical Physics* 30.4, pp. 397–402. DOI: 10.1016/j.ejmp.2014.03.005. URL: <http://dx.doi.org/10.1016/j.ejmp.2014.03.005> (cit. on p. 4).
- Durante, M. and J. S. Loeffler (Dec. 2009). “Charged particles in radiation oncology”. In: *Nature Reviews Clinical Oncology* 7, p. 37. URL: <http://dx.doi.org/10.1038/nrclinonc.2009.183> (cit. on pp. 5, 14).
- Durante, M. and H. Paganetti (2016). “Nuclear physics in particle therapy: a review”. In: *Reports on Progress in Physics* 79.9, p. 096702. URL: <http://stacks.iop.org/0034-4885/79/i=9/a=096702> (cit. on pp. 5, 7, 10, 11, 13, 14, 18).
- Elftmann, R., J. Tammen, S. R. Kulkarni, C. Martin, S. Böttcher, and R. Wimmer-Schweingruber (2015). “Characterization of an LSO scintillator for space applications”. In: *Journal of Physics: Conference Series* 632.1, p. 012006. URL: <http://stacks.iop.org/1742-6596/632/i=1/a=012006> (cit. on p. 36).
- Engelsman, M., M. Schwarz, and L. Dong (2013). “Physics Controversies in Proton Therapy”. In: *Seminars in Radiation Oncology* 23.2. Controversies in Proton Therapy, pp. 88–96. ISSN: 1053-4296. DOI: <https://doi.org/10.1016/j.semradonc.2012.11.003>. URL: <http://www.sciencedirect.com/science/article/pii/S1053429612001063> (cit. on p. 24).
- Enghardt, W., P. Crespo, F. Fiedler, R. Hinz, K. Parodi, J. Pawelke, and F. Pönisch (2004). “Charged hadron tumour therapy monitoring by means of PET”. In: *Nuclear Instruments and Methods in Physics Research Section A: Accelerators, Spectrometers, Detectors and Associated Equipment* 525.1. Proceedings of the International Conference on Imaging Techniques in Subatomic Physics, Astrophysics, Medicine, Biology and Industry, pp. 284–288. ISSN: 0168-9002. DOI: <https://doi.org/10.1016/j.nima.2004.03.128>. URL: <http://www.sciencedirect.com/science/article/pii/S0168900204004218> (cit. on p. 25).
- Evans, T. C. (1951). “X-Ray Treatment-Its Origin, Birth and Early History. Emil H. Grubbe”. In: *The Quarterly Review of Biology* 26.2, pp. 223–223. DOI: 10.1086/398163. eprint: <https://doi.org/10.1086/398163>. URL: <https://doi.org/10.1086/398163> (cit. on p. 4).

- Everett, D. B., J. S. Fleming, R. W. Todd, and J. M. Nightingale (1977). "Gamma-radiation imaging system based on the Compton effect". In: *Proceedings of the Institution of Electrical Engineers* 124.11, p. 995. ISSN: 0020-3270. DOI: 10.1049/piee.1977.0203 (cit. on p. 92).
- Fontana, M., D. Dauvergne, J. M. Létang, J.-L. Ley, and É. Testa (2017a). "Compton camera study for high efficiency SPECT and benchmark with Anger system". In: *Physics in Medicine and Biology* 62.23, p. 8794. URL: <http://stacks.iop.org/0031-9155/62/i=23/a=8794> (cit. on p. 91).
- Fontana, M., D. Dauvergne, J.-L. Ley, J. M. Létang, V. Maxim, and É. Testa (2017b). "Versatile Compton camera for high energy gamma rays: Monte Carlo comparison with Anger camera for medical imaging". In: *2nd Jagiellonian Symposium on Fundamental and Applied Subatomic Physics*. Vol. 48. Krakow, Poland, pp. 1639–1645. DOI: 10.5506/APhysPolB.48.1639. URL: <https://hal.archives-ouvertes.fr/hal-01609541> (cit. on p. 91).
- Foray, N. (Nov. 2016). "Victor Despeignes, the Forgotten Pioneer of Radiation Oncology." eng. In: *Int J Radiat Oncol Biol Phys* 96.4, pp. 717–721. DOI: 10.1016/j.ijrobp.2016.07.019 (cit. on p. 4).
- Fossati, P., S. Molinelli, N. Matsufuji, M. Ciocca, A. Mirandola, A. Mairani, J. Mizoe, A. Hasegawa, R. Imai, T. Kamada, R. Orecchia, and H. Tsujii (2012). "Dose prescription in carbon ion radiotherapy: a planning study to compare NIRS and LEM approaches with a clinically-oriented strategy". In: *Physics in Medicine & Biology* 57.22, p. 7543. URL: <http://stacks.iop.org/0031-9155/57/i=22/a=7543> (cit. on p. 23).
- Friedrich, T., U. Scholz, T. Elsässer, M. Durante, and M. Scholz (2012). "Calculation of the biological effects of ion beams based on the microscopic spatial damage distribution pattern". In: *International Journal of Radiation Biology* 88.1-2, pp. 103–107. DOI: 10.3109/09553002.2011.611213. eprint: <https://doi.org/10.3109/09553002.2011.611213>. URL: <https://doi.org/10.3109/09553002.2011.611213> (cit. on p. 5).
- Gaglione, R. (2013). "Electronique d'acquisition d'une gamma-caméra." PhD thesis. École Doctorale Sciences pour l'ingénieur de Clermont-Ferrand (cit. on pp. 75, 86).
- Gallin-Martel, M.-L., Abbassi, L., Bes, A., Bosson, G., Collot, J., Crozes, T., Curtoni, S., Dauvergne, D., De Nolf, W., Fontana, M., Gallin-Martel, L., Hostachy, J.-Y., Krimmer, J., Lacoste, A., Marcatili, S., Morse, J., Motte, J.-F., Muraz, J.-F., Rarbi, F. E., Rossetto, O., Salomé, M., Testa, É., Vuia, R., and Yamouni, M. (2018). "A large area diamond-based beam tagging hodoscope for ion therapy monitoring". In: *EPJ Web Conf.* 170, p. 09005. DOI: 10.1051/epjconf/201817009005. URL: <https://doi.org/10.1051/epjconf/201817009005> (cit. on p. 85).
- Gallin-Martel, M.-L., A. Bes, A. Boukhémiri, G. Bosson, J. Collot, D. Dauvergne, M. Fontana, L. Gallin-Martel, A. Gorecki, J. Y. Hostachy, J. Krimmer, A. Lacoste, S. Marcatili, J. Morse, J. F. Muraz, F. E. Rarbi, O. Rossetto, M. Salomé, É. Testa, and M. Yamouni (2016). "Large area polycrystalline diamond detectors for online hadron therapy beam tagging applications". In: *2016 IEEE Nuclear Science Symposium, Medical Imaging Conference and Room-Temperature Semiconductor Detector Workshop (NSS/MIC/RTSD)*, pp. 1–5. DOI: 10.1109/NSSMIC.2016.8069398 (cit. on p. 85).

Bibliography

- GE Healthcare (June 2006). “Infinia”. In: Release 2.5 (cit. on pp. 92, 98).
- GeckoDrive (2010). *G203V stepper drive - data sheet*. REV7. GeckoDrive Motor Controls Inc. (cit. on p. 75).
- Giantsoudi, D., C. Grassberger, D. Craft, A. Niemierko, A. Trofimov, and H. Paganetti (2013). “Linear energy transfer-guided optimization in intensity modulated proton therapy: feasibility study and clinical potential.” eng. In: *Int J Radiat Oncol Biol Phys* 87.1, pp. 216–222. DOI: 10.1016/j.ijrobp.2013.05.013 (cit. on p. 14).
- Gillam, J. E., C. Lacasta, I. Torres-Espallardo, C. Candela Juan, G. Llosá, P. Solevi, J. Barrio, and M. Rafecas (2011). “A Compton imaging algorithm for on-line monitoring in hadron therapy”. In: vol. 7961, pp. 7961–8. doi: 10.1117/12.877678. URL: <https://doi.org/10.1117/12.877678> (cit. on p. 28).
- Giovannini, G., T. Bohlen, G. Cabal, J. Bauer, T. Tessonnier, K. Frey, J. Debus, A. Mairani, and K. Parodi (2016). “Variable RBE in proton therapy: comparison of different model predictions and their influence on clinical-like scenarios.” eng. In: *Radiat Oncol* 11, p. 68. DOI: 10.1186/s13014-016-0642-6 (cit. on p. 14).
- Golnik, C. (2015). “Treatment verification in proton therapy based on the detection of prompt gamma-rays.” PhD thesis. TU Dresden and Oncoray (cit. on pp. 57, 83).
- Gottschalk, B. (Dec. 2006). “Neutron dose in scattered and scanned proton beams: in regard to Eric J. Hall (Int J Radiat Oncol Biol Phys 2006;65:1-7).” eng. In: *Int J Radiat Oncol Biol Phys* 66.5, p. 1595. DOI: 10.1016/j.ijrobp.2006.08.014 (cit. on p. 13).
- Gottschalk, B., A. M. Koehler, R. J. Schneider, J. M. Sisterson, and M. S. Wagner (1993). “Multiple Coulomb scattering of 160 MeV protons”. In: *Nuclear Instruments and Methods in Physics Research Section B: Beam Interactions with Materials and Atoms* 74.4, pp. 467–490. ISSN: 0168-583X. DOI: [https://doi.org/10.1016/0168-583X\(93\)95944-Z](https://doi.org/10.1016/0168-583X(93)95944-Z). URL: <http://www.sciencedirect.com/science/article/pii/0168583X9395944Z> (cit. on p. 10).
- Gottshalk, B. and E. Pedroni (2008). “Treatment delivery systems”. In: *Proton and charged particle radiotherapy*. Vol. chap. 5. T. F. DeLaney, H. M. Kooy (Lippincott Williams, and Wilkins, Philadelphia), pp. 33–49 (cit. on p. 18).
- Graeff, C., R. Lüchtenborg, J. G. Eley, M. Durante, and C. Bert (2013). “A 4D-optimization concept for scanned ion beam therapy”. In: *Radiotherapy and Oncology* 109.3, pp. 419–424. DOI: 10.1016/j.radonc.2013.09.018. URL: <https://doi.org/10.1016/j.radonc.2013.09.018> (cit. on p. 24).
- Grassberger, C. and H. Paganetti (2011). “Elevated LET components in clinical proton beams”. In: *Physics in Medicine and Biology* 56.20, p. 6677. URL: <http://stacks.iop.org/0031-9155/56/i=20/a=011> (cit. on p. 12).
- Guan, F., L. Bronk, U. Titt, S. H. Lin, D. Mirkovic, M. D. Kerr, X. R. Zhu, J. Dinh, M. Sobieski, C. Stephan, C. R. Peeler, R. Taleei, R. Mohan, and D. R. Grosshans (May 2015). “Spatial mapping

- of the biologic effectiveness of scanned particle beams: towards biologically optimized particle therapy". In: *Scientific Reports* 5. URL: <http://dx.doi.org/10.1038/srep09850> (cit. on p. 14).
- Gunzert-Marx, K.**, H. Iwase, D. Schardt, and R. S. Simon (2008). "Secondary beam fragments produced by 200 MeV/u ^{12}C ions in water and their dose contributions in carbon ion radiotherapy". In: *New Journal of Physics* 10.7, p. 075003. URL: <http://stacks.iop.org/1367-2630/10/i=7/a=075003> (cit. on p. 12).
- Haberer, T., W. Becher, D. Schardt, and G. Kraft (1993). "Magnetic scanning system for heavy ion therapy". In: *Nuclear Instruments and Methods in Physics Research Section A: Accelerators, Spectrometers, Detectors and Associated Equipment* 330.1, pp. 296–305. ISSN: 0168-9002. DOI: [https://doi.org/10.1016/0168-9002\(93\)91335-K](https://doi.org/10.1016/0168-9002(93)91335-K). URL: <http://www.sciencedirect.com/science/article/pii/016890029391335K> (cit. on p. 20).
- Haettner, E., H. Iwase, M. Krämer, G. Kraft, and D. Schardt (2013). "Experimental study of nuclear fragmentation of 200 and 400 MeV/u C ions in water for applications in particle therapy". In: *Physics in Medicine and Biology* 58.23, p. 8265. URL: <http://stacks.iop.org/0031-9155/58/i=23/a=8265> (cit. on p. 12).
- Haettner, E., H. Iwase, and D. Schardt (2006). "Experimental fragmentation studies with ^{12}C therapy beams". In: *Radiation Protection Dosimetry* 122.1-4, pp. 485–487. DOI: 10.1093/rpd/ncl402. URL: <http://dx.doi.org/10.1093/rpd/ncl402> (cit. on p. 12).
- Halperin, E. C. (2006). "Particle therapy and treatment of cancer". In: *The Lancet Oncology* 7.8, pp. 676–685. DOI: 10.1016/S1470-2045(06)70795-1. URL: [http://dx.doi.org/10.1016/S1470-2045\(06\)70795-1](http://dx.doi.org/10.1016/S1470-2045(06)70795-1) (cit. on p. 5).
- Hamamatsu (1995). *Metal Package Photomultiplier Tube R5600 Series*. TPMH1066E08. Hamamatsu Photonics K. K. (cit. on p. 75).
- Hamamatsu (2006). *Flat Panel Type Multianode Photomultiplier Tube Assembly H8500, H8500B*. TPMH1282E09. Hamamatsu Photonics K. K. (cit. on pp. 42, 73, 80).
- Hamm, R. W., K. R. Crandall, and J. M. Potter (1991). "Preliminary design of a dedicated proton therapy linac". In: *Conference Record of the 1991 IEEE Particle Accelerator Conference*. DOI: 10.1109/PAC.1991.165037 (cit. on p. 17).
- Han, L., W. L. Rogers, S. S. Huh, and N. Clinthorne (2008). "Statistical performance evaluation and comparison of a Compton medical imaging system and a collimated Anger camera for higher energy photon imaging". In: *Physics in Medicine and Biology* 53.24, p. 7029. URL: <http://stacks.iop.org/0031-9155/53/i=24/a=002> (cit. on pp. 92, 93, 95, 110).
- Hilaire, E., C. Robert, X. Lojacono, D. Sarrut, I. Buvat, F. Peyrin, and V. Maxim (Feb. 2014). "Compton imaging in proton therapy: reconstructed image of the simulated prompt- γ distribution". In: *ICTR-PHE 2014*. Genève, Switzerland, S43. URL: <https://hal.archives-ouvertes.fr/hal-01052717> (cit. on p. 54).

Bibliography

- Hirasawa, M. and T. Tomitani (Apr. 21, 2003). “An analytical image reconstruction algorithm to compensate for scattering angle broadening in Compton cameras.” eng. In: *Phys Med Biol* 48.8, pp. 1009–1026 (cit. on p. 28).
- Hishikawa, Y., K. Kagawa, M. Murakami, H. Sakai, T. Akagi, and M. Abe (2002). “Usefulness of positron-emission tomographic images after proton therapy”. In: *International Journal of Radiation Oncology *Biology *Physics* 53.5, pp. 1388–1391. doi: 10.1016/S0360-3016(02)02887-0. URL: [http://dx.doi.org/10.1016/S0360-3016\(02\)02887-0](http://dx.doi.org/10.1016/S0360-3016(02)02887-0) (cit. on p. 25).
- Hubbell, J. H. and M. J. Berger (1987). *XCOM: Photon Cross Sections on a Personal Computer, Report NBSIR 87-3597* (1987), National Institute for Standards and Technology, U.S.A. URL: <http://physics.nist.gov/PhysRefData/XrayMassCoef/> (visited on 02/21/2017) (cit. on pp. 99, 111).
- Hueso-González, F., A. K. Biegun, P. Dendooven, W. Enghardt, F. Fiedler, C. Golnik, K. Heidel, T. Kormoll, J. Petzoldt, K. E. Römer, R. Schwengner, A. Wagner, and G. Pausch (2015). “Comparison of LSO and BGO block detectors for prompt gamma imaging in ion beam therapy”. In: *Journal of Instrumentation* 10.09, P09015. URL: <http://stacks.iop.org/1748-0221/10/i=09/a=P09015> (cit. on pp. 37, 57, 83).
- Hüfner, J., K. Schäfer, and B. Schürmann (Dec. 1975). “Abrasion-ablation in reactions between relativistic heavy ions”. In: *Phys. Rev. C* 12 (6), pp. 1888–1898. doi: 10.1103/PhysRevC.12.1888. URL: <https://link.aps.org/doi/10.1103/PhysRevC.12.1888> (cit. on p. 11).
- ICRU (1980). “ICRU Report 33 - Radiation Quantities and Units”. In: *Journal of the International Commission on Radiation Units and Measurements, Bethesda, MD* (cit. on p. 13).
- ICRU (1998). “ICRU Report 60 - Fundamental Quantities and Units for Ionising Radiation”. In: *Journal of the International Commission on Radiation Units and Measurements, Bethesda, MD* (cit. on p. 13).
- ICRU (2007). “ICRU Report 78 - Prescribing, recording, and reporting proton beam therapy”. In: *Journal of the International Commission on Radiation Units and Measurements, Bethesda, MD* (cit. on p. 22).
- Inaniwa, T., H. Tashima, and N. Kanematsu (Mar. 2018). “Optimum size of a calibration phantom for x-ray CT to convert the Hounsfield units to stopping power ratios in charged particle therapy treatment planning”. In: *Journal of Radiation Research* 59.2, pp. 216–224. doi: 10.1093/jrr/rrx059 (cit. on p. 22).
- Inaniwa, T., N. Kanematsu, N. Matsufuji, T. Kanai, T. Shirai, K. Noda, H. Tsuji, T. Kamada, and H. Tsujii (2015). “Reformulation of a clinical-dose system for carbon-ion radiotherapy treatment planning at the National Institute of Radiological Sciences, Japan”. In: *Physics in Medicine & Biology* 60.8, p. 3271. URL: <http://stacks.iop.org/0031-9155/60/i=8/a=3271> (cit. on p. 23).
- Iwata, Y., K. Noda, T. Murakami, T. Shirai, T. Furukawa, T. Fujita, S. Mori, K. Mizushima, K. Shouda, T. Fujimoto, T. Ogitsu, T. Obana, N. Amemiya, T. Orikasa, S. Takami, and S. Takayama (2013). “Development of a superconducting rotating-gantry for heavy-ion therapy”. In:

- Nuclear Instruments and Methods in Physics Research Section B: Beam Interactions with Materials and Atoms* 317. XVIth International Conference on ElectroMagnetic Isotope Separators and Techniques Related to their Applications, December 2-7, 2012 at Matsue, Japan, pp. 793–797. DOI: <https://doi.org/10.1016/j.nimb.2013.03.050>. URL: <http://www.sciencedirect.com/science/article/pii/S0168583X13003856> (cit. on p. 21).
- Jakel, O., C. Jacob, D. Schardt, C. P. Karger, and G. H. Hartmann (2001). “Relation between carbon ion ranges and x-ray CT numbers.” eng. In: *Med Phys* 28.4, pp. 701–703. DOI: 10.1118/1.1357455 (cit. on pp. 22, 23).
- Jäkel, O., M. Krämer, C. P. Karger, and J. Debus (2001). “Treatment planning for heavy ion radiotherapy: clinical implementation and application”. In: *Physics in Medicine & Biology* 46.4, p. 1101. URL: <http://stacks.iop.org/0031-9155/46/i=4/a=314> (cit. on p. 23).
- Jemal, A., M. M. Center, C. DeSantis, and E. M. Ward (2010). “Global Patterns of Cancer Incidence and Mortality Rates and Trends”. In: *Cancer Epidemiology and Prevention Biomarkers* 19.8, pp. 1893–1907. ISSN: 1055-9965. DOI: 10.1158/1055-9965.EPI-10-0437. eprint: <http://cebp.aacrjournals.org/content/19/8/1893.full.pdf>. URL: <http://cebp.aacrjournals.org/content/19/8/1893> (cit. on p. 4).
- Jones, B. (2015). “Towards Achieving the Full Clinical Potential of Proton Therapy by Inclusion of LET and RBE Models.” eng. In: *Cancers (Basel)* 7.1, pp. 460–480. DOI: 10.3390/cancers7010460 (cit. on p. 14).
- Kabuki, S., K. Hattori, R. Kohara, E. Kunieda, A. Kubo, H. Kubo, K. Miuchi, T. Nakahara, T. Nagayoshi, H. Nishimura, Y. Okada, R. Orito, H. Sekiya, T. Shirahata, A. Takada, T. Tanimori, and K. Ueno (2007). “Development of Electron Tracking Compton Camera using micro pixel gas chamber for medical imaging”. In: *Nuclear Instruments and Methods in Physics Research Section A: Accelerators, Spectrometers, Detectors and Associated Equipment* 580.2. Imaging 2006, pp. 1031–1035. ISSN: 0168-9002. DOI: <https://doi.org/10.1016/j.nima.2007.06.098>. URL: <http://www.sciencedirect.com/science/article/pii/S0168900207013186> (cit. on p. 112).
- Kanai, T., K. Kawachi, H. Matsuzawa, and T. Inada (1983). “Three-dimensional beam scanning for proton therapy”. In: *Nuclear Instruments and Methods in Physics Research* 214.2, pp. 491–496. ISSN: 0167-5087. DOI: [https://doi.org/10.1016/0167-5087\(83\)90621-X](https://doi.org/10.1016/0167-5087(83)90621-X). URL: <http://www.sciencedirect.com/science/article/pii/016750878390621X> (cit. on p. 20).
- Kanematsu, N., N. Matsufuji, R. Kohno, S. Minohara, and T. Kanai (2003). “A CT calibration method based on the polybinary tissue model for radiotherapy treatment planning”. In: *Physics in Medicine and Biology* 48.8, p. 1053. URL: <http://stacks.iop.org/0031-9155/48/i=8/a=307> (cit. on p. 22).
- Keevil, S. F. (2012). “Physics and medicine: a historical perspective”. In: *The Lancet* 379.9825, pp. 1517–1524. ISSN: 0140-6736. DOI: [https://doi.org/10.1016/S0140-6736\(11\)60282-1](https://doi.org/10.1016/S0140-6736(11)60282-1). URL: <http://www.sciencedirect.com/science/article/pii/S0140673611602821> (cit. on p. 4).

- Kereiakes, J. G. (1987). “The history and development of medical physics instrumentation: Nuclear medicine”. In: *Medical Physics* 14.1, pp. 146–155. doi: 10.1118/1.596105. eprint: <https://aapm.onlinelibrary.wiley.com/doi/pdf/10.1118/1.596105>. URL: <https://aapm.onlinelibrary.wiley.com/doi/abs/10.1118/1.596105> (cit. on p. 4).
- Knoll, G. F. (2000). *Radiation Detection and Measurement*. Third Edition. John Wiley & Sons Inc. (cit. on p. 32).
- Kramer, M., O. Jakel, T. Haberer, G. Kraft, D. Schardt, and U. Weber (2000). “Treatment planning for heavy-ion radiotherapy: physical beam model and dose optimization.” eng. In: *Phys Med Biol* 45.11, pp. 3299–3317 (cit. on p. 23).
- Krimmer, J., L. Caponetto, X. Chen, M. Chevallier, D. Dauvergne, M. De Rydt, S.-M. Deng, J.-L. Ley, H. Mathez, C. Ray, V. Reithinger, É. Testa, and Y. Zoccarato (Feb. 1, 2014). “111: Real-time monitoring of the ion range during hadrontherapy: An update on the beam tagging hodoscope”. In: *Radiotherapy and Oncology* 110, S54–S55. doi: 10.1016/S0167-8140(15)34132-3. URL: [http://dx.doi.org/10.1016/S0167-8140\(15\)34132-3](http://dx.doi.org/10.1016/S0167-8140(15)34132-3) (cit. on p. 43).
- Kubiak, T. (Oct. 2016). “Particle therapy of moving targets—the strategies for tumour motion monitoring and moving targets irradiation”. In: *The British Journal of Radiology* 89.1066, p. 20150275. doi: 10.1259/bjr.20150275. URL: <http://www.ncbi.nlm.nih.gov/pmc/articles/PMC5124789/> (cit. on p. 24).
- Kuchment, P. and F. Terzioglu (2016). “3D Image Reconstruction from Compton camera data”. In: arXiv: 1604.03805 [physics.data-an] (cit. on p. 112).
- Landau, L. (1944). “On the energy loss of fast particles by ionization”. In: *J. Phys.(USSR)* 8, pp. 201–205 (cit. on p. 9).
- Larsson, B. (1962). “On the application of a 185 MeV proton beam to experimental cancer therapy and neurosurgery: A biophysical study.” PhD thesis. Acta Universitatis Upsaliensis (cit. on p. 15).
- Lawrence, E. O. and M. S. Livingston (Apr. 1932). “The Production of High Speed Light Ions Without the Use of High Voltages”. In: *Phys. Rev.* 40 (1), pp. 19–35. doi: 10.1103/PhysRev.40.19. URL: <https://link.aps.org/doi/10.1103/PhysRev.40.19> (cit. on p. 15).
- Lennox, A. J. (1991). “Hospital-based proton linear accelerator for particle therapy and radioisotope production”. In: *Nuclear Instruments and Methods in Physics Research Section B: Beam Interactions with Materials and Atoms* 56-57, pp. 1197–1200. ISSN: 0168-583X. doi: [https://doi.org/10.1016/0168-583X\(91\)95130-6](https://doi.org/10.1016/0168-583X(91)95130-6). URL: <http://www.sciencedirect.com/science/article/pii/0168583X91951306> (cit. on p. 17).
- Levy, R. P. (2007). “PET-CT: Evolving role in hadron therapy”. In: *Nuclear Instruments and Methods in Physics Research Section B: Beam Interactions with Materials and Atoms* 261.1. The Application of Accelerators in Research and Industry, pp. 782–785. ISSN: 0168-583X. doi: <https://doi.org/10.1016/j.nimb.2007.04.039>. URL: <http://www.sciencedirect.com/science/article/pii/S0168583X07007975> (cit. on p. 22).

- Ley, J.-L. (2015). “Mise en oeuvre d'un démonstrateur de caméra Compton pour l'imagerie en médecine nucléaire et pour le contrôle en temps réel de l'hadronthérapie à l'aide des rayonnements gamma prompts.” PhD thesis. École Doctorale de Physique et d'Astrophysique de Lyon (cit. on pp. 33, 35, 55, 83, 95).
- Locher, G. L. (1936). “Biological effects and therapeutic possibilities of neutrons”. In: *Am. J. Roentgenol. Radium Ther.* 36.1, pp. 1–13 (cit. on p. 15).
- Lojacono, X., M.-H. Richard, J.-L. Ley, É. Testa, C. Ray, N. Freud, J. M. Létang, D. Dauvergne, V. Maxim, and R. Prost (2013). “Low Statistics Reconstruction of the Compton Camera Point Spread Function in 3D Prompt-gamma Imaging of Ion Beam Therapy”. In: *IEEE Transactions on Nuclear Science* 60.5, pp. 3355–3363. ISSN: 0018-9499. DOI: 10.1109/TNS.2013.2275200 (cit. on pp. 28, 54, 96).
- Lomax, A. J. (2009). “Charged Particle Therapy: The Physics of Interaction”. In: *The Cancer Journal* 15.4. URL: https://journals.lww.com/journalppo/Fulltext/2009/08000/Charged_Particle_Therapy__The_Physics_of.4.aspx (cit. on p. 13).
- Mackin, D., S. Peterson, S. Beddar, and J. Polf (June 7, 2012). “Evaluation of a stochastic reconstruction algorithm for use in Compton camera imaging and beam range verification from secondary gamma emission during proton therapy.” eng. In: *Phys Med Biol* 57.11, pp. 3537–3553. DOI: 10.1088/0031-9155/57/11/3537 (cit. on p. 28).
- Matsufuji, N., A. Fukumura, M. Komori, T. Kanai, and T. Kohno (2003). “Influence of fragment reaction of relativistic heavy charged particles on heavy-ion radiotherapy”. In: *Physics in Medicine and Biology* 48.11, p. 1605. URL: <http://stacks.iop.org/0031-9155/48/i=11/a=309> (cit. on p. 12).
- Matsufuji, N., H. Tomura, Y. Futami, H. Yamashita, A. Higashi, S. Minohara, M. Endo, and T. Kanai (1998). “Relationship between CT number and electron density, scatter angle and nuclear reaction for hadron-therapy treatment planning.” eng. In: *Phys Med Biol* 43.11, pp. 3261–3275 (cit. on p. 22).
- Matsufuji, N., T. Kanai, N. Kanematsu, T. Miyamoto, M. Baba, T. Kamada, H. Kato, S. Yamada, J.-E. Mizoe, and H. Tsujii (2007). “Specification of Carbon Ion Dose at the National Institute of Radiological Sciences (NIRS).” eng. In: *J Radiat Res* 48 Suppl A, A81–6 (cit. on p. 23).
- Maxim, V. (Jan. 2014). “Filtered Backprojection Reconstruction and Redundancy in Compton Camera Imaging”. In: *IEEE Transactions on Image Processing* 23.1, pp. 332–341. ISSN: 1057-7149. DOI: 10.1109/TIP.2013.2288143 (cit. on p. 54).
- Maxim, V., M. Frandes, and R. Prost (2009). “Analytical inversion of the Compton transform using the full set of available projections”. In: *Inverse Problems* 25.9, p. 095001. URL: <http://stacks.iop.org/0266-5611/25/i=9/a=095001> (cit. on p. 28).
- McKenzie, A. L., M. van Herk, and B. Mijnheer (2000). “The width of margins in radiotherapy treatment plans”. In: *Physics in Medicine & Biology* 45.11, p. 3331. URL: <http://stacks.iop.org/0031-9155/45/i=11/a=315> (cit. on p. 24).

Bibliography

- McMillan, E. M. (1945). "The synchrotron - a proposed high energy accelerator." In: *Phys. Rev.* 68.143 (cit. on p. 16).
- McNamara, A. L., J. Schuemann, and H. Paganetti (2015). "A phenomenological relative biological effectiveness (RBE) model for proton therapy based on all published in vitro cell survival data". In: *Physics in Medicine & Biology* 60.21, p. 8399. URL: <http://stacks.iop.org/0031-9155/60/i=21/a=8399> (cit. on p. 14).
- Moding, E. J., M. B. Kastan, and D. G. Kirsch (2013). "Strategies for optimizing the response of cancer and normal tissues to radiation." eng. In: *Nat Rev Drug Discov* 12.7, pp. 526–542. DOI: 10.1038/nrd4003 (cit. on p. 5).
- Molière, G. (Feb. 1948). "Theorie der Streuung schneller geladener Teilchen II. Mehrfach- und Vielfachstreuung". In: *Zeitschrift Naturforschung Teil A* 3, pp. 78–97. DOI: 10.1515/zna-1948-0203 (cit. on p. 10).
- National Instruments (2010). *PXI Express - NI PXIe-1082 User Manual*. 372752B-01. National Instruments (cit. on p. 75).
- Nedunchezian, K., N. Aswath, M. Thiruppathy, and S. Thirugnanamurthy (Dec. 2016). "Boron Neutron Capture Therapy - A Literature Review". In: *Journal of Clinical and Diagnostic Research : JCDR* 10.12, ZE01–ZE04. DOI: 10.7860/JCDR/2016/19890.9024 (cit. on p. 15).
- Newhauser, W. D. and M. Durante (May 2011). "Assessing the risk of second malignancies after modern radiotherapy". In: *Nature Reviews Cancer* 11, p. 438. URL: <http://dx.doi.org/10.1038/nrc3069> (cit. on p. 12).
- Newhauser, W. D., U. Titt, D. Dexheimer, X. Yan, and S. Nill (2002). "Neutron shielding verification measurements and simulations for a 235-MeV proton therapy center". In: *Nuclear Instruments and Methods in Physics Research Section A: Accelerators, Spectrometers, Detectors and Associated Equipment* 476.1. Int. Workshop on Neutron Field Spectrometry in Science, Technology and Radiation Protection, pp. 80–84. ISSN: 0168-9002. DOI: [https://doi.org/10.1016/S0168-9002\(01\)01400-0](https://doi.org/10.1016/S0168-9002(01)01400-0). URL: <http://www.sciencedirect.com/science/article/pii/S0168900201014000> (cit. on p. 12).
- Newhauser, W. D. and R. Zhang (2015). "The physics of proton therapy". In: *Physics in Medicine and Biology* 60.8, R155. URL: <http://stacks.iop.org/0031-9155/60/i=8/a=R155> (cit. on pp. 8, 11–13).
- Newport (2017). *XPS-Q8 Universal High-Performance Motion Controller/Driver*. v.1.4.x. Newport Corporation (cit. on p. 46).
- NuPECC (2014). "Nuclear Physics for Medicine". In: *Strasbourg: European Science Foundation*. URL: <http://www.nupecc.org> (cit. on p. 13).
- Nurdan, T. C., K. Nurdan, A. B. Brill, and A. H. Walenta (2015). "Design criteria for a high energy Compton Camera and possible application to targeted cancer therapy". In: *Journal of Instrumentation* 10.07, p. C07018. URL: <http://stacks.iop.org/1748-0221/10/i=07/a=C07018> (cit. on p. 93).

- Oliphant, M. O. (1943). "The acceleration of particles to very high energies". In: *Classified memo submitted to DSIR, United Kingdom, Sept. 1943* (cit. on p. 16).
- Ortega, P. G., I. Torres-Espallardo, F. Cerutti, A. Ferrari, J. E. Gillam, C. Lacasta, G. Llosá, J. F. Oliver, P. R. Sala, P. Solevi, and M. Rafecas (Mar. 7, 2015). "Noise evaluation of Compton camera imaging for proton therapy". eng. In: *Phys Med Biol* 60.5, pp. 1845–1863. DOI: 10.1088/0031-9155/60/5/1845 (cit. on p. 37).
- Owen, H., D. Holder, J. Alonso, and R. MacKay (2014). "Technologies for Delivery of Proton and Ion Beams for Radiotherapy". In: *Int. J. Mod. Phys.* A29, p. 1441002. DOI: 10.1142/S0217751X14410024. arXiv: 1310.0237 [physics.acc-ph] (cit. on p. 21).
- Paganetti, H. (June 2012a). "Range uncertainties in proton therapy and the role of Monte Carlo simulations". In: *Physics in Medicine and Biology* 57.11, R99–R117. DOI: 10.1088/0031-9155/57/11/R99. URL: <http://www.ncbi.nlm.nih.gov/pmc/articles/PMC3374500/> (cit. on p. 24).
- Paganetti, H. (2012b). *Proton Therapy Physics*. Boca Raton: CRC Press (cit. on pp. 7, 15).
- Paganetti, H. and P. Van Luijk (2013). "Biological Considerations When Comparing Proton Therapy With Photon Therapy". In: *Seminars in Radiation Oncology* 23.2, pp. 77–87. DOI: 10.1016/j.semradonc.2012.11.002. URL: <http://dx.doi.org/10.1016/j.semradonc.2012.11.002> (cit. on p. 13).
- Paganetti, H., A. Niemierko, M. Ancukiewicz, L. E. Gerweck, M. Goitein, J. S. Loeffler, and H. D. Suit (2002). "Relative biological effectiveness (RBE) values for proton beam therapy." eng. In: *Int J Radiat Oncol Biol Phys* 53.2, pp. 407–421 (cit. on p. 22).
- Parodi, K. (2016). "On- and off-line monitoring of ion beam treatment". In: *Nuclear Instruments and Methods in Physics Research Section A: Accelerators, Spectrometers, Detectors and Associated Equipment* 809. Advances in detectors and applications for medicine, pp. 113–119. DOI: <https://doi.org/10.1016/j.nima.2015.06.056>. URL: <http://www.sciencedirect.com/science/article/pii/S0168900215008062> (cit. on p. 25).
- Parodi, K., H. Paganetti, H. A. Shih, S. Michaud, J. S. Loeffler, T. F. DeLaney, N. J. Liebsch, J. E. Munzenrider, A. J. Fischman, A. Knopf, and T. Bortfeld (2007). "Patient Study of In Vivo Verification of Beam Delivery and Range, Using Positron Emission Tomography and Computed Tomography Imaging After Proton Therapy". In: *International Journal of Radiation Oncology Biology Physics* 68.3, pp. 920–934. DOI: 10.1016/j.ijrobp.2007.01.063. URL: <http://dx.doi.org/10.1016/j.ijrobp.2007.01.063> (cit. on p. 25).
- Parra, L. C. (Aug. 2000). "Reconstruction of cone-beam projections from Compton scattered data". In: *IEEE Transactions on Nuclear Science* 47.4, pp. 1543–1550. DOI: 10.1109/23.873014 (cit. on p. 28).
- Peach, K. J., J. H. Cobb, S. L. Sheehy, H. Witte, T. Yokoi, M. Aslaninejad, M. J. Easton, J. Pasternak, R. Barlow, H. L. Owen, S. C. Tygier, C. D. Beard, P. A. McIntosh, S. M. Pattalwar, S. L. Smith, S. I. Tzenov, N. Bliss, T. J. Jones, J. Strachan, R. Edgecock, J. K. Pozimski, R. J. L. Fenning, A. Khan, I. S. K. Gardner, D. J. Kelliher, S. Machida, M. A. Hill, C. Johnstone, B.

- Jones, B. Vojnovic, and R. Seviour (2010). “PAMELA : overview and status”. In: *Proceedings of the 1st International Particle Accelerator Conference IPAC 2010*. Kyoto, Japan: JACoW, pp. 112–114. URL: <http://eprints.hud.ac.uk/id/eprint/15286/> (cit. on p. 17).
- Pedroni, E., R. Bacher, H. Blattmann, T. Bohringer, A. Coray, A. Lomax, S. Lin, G. Munkel, S. Scheib, and U. Schneider (1995). “The 200-MeV proton therapy project at the Paul Scherrer Institute: conceptual design and practical realization.” In: *Med Phys* 22.1, pp. 37–53 (cit. on pp. 20, 21).
- Pedroni, E., S. Scheib, T. Bohringer, A. Coray, M. Grossmann, S. Lin, and A. Lomax (Feb. 2005). “Experimental characterization and physical modelling of the dose distribution of scanned proton pencil beams.” eng. In: *Phys Med Biol* 50.3, pp. 541–561 (cit. on p. 10).
- Phillips, M. H., E. Pedroni, H. Blattmann, T. Boehringer, A. Coray, and S. Scheib (1992). “Effects of respiratory motion on dose uniformity with a charged particle scanning method.” eng. In: *Phys Med Biol* 37.1, pp. 223–234 (cit. on p. 24).
- Pinto, M., D. Dauvergne, N. Freud, J. Krimmer, J. M. Létang, C. Ray, F. Roellinghoff, and É. Testa (2014). “Design optimisation of a TOF-based collimated camera prototype for online hadrontherapy monitoring”. In: *Physics in Medicine and Biology* 59.24, p. 7653. URL: <http://stacks.iop.org/0031-9155/59/i=24/a=7653> (cit. on p. 36).
- “Real-time monitoring of the Bragg-peak position in ion therapy by means of single photon detection.” (2010). eng. In: *Radiat Environ Biophys* 49.3, pp. 337–343. doi: 10.1007/s00411-010-0276-2 (cit. on p. 12).
- Richard, M.-H. (2012). “Design study of a Compton camera for prompt-gamma imaging during ion beam therapy”. PhD thesis. Université Claude Bernard - Lyon I (cit. on p. 32).
- Rietzel, E., D. Schardt, and T. Haberer (2007). “Range accuracy in carbon ion treatment planning based on CT-calibration with real tissue samples”. In: *Radiation Oncology (London, England)* 2, pp. 14–14. doi: 10.1186/1748-717X-2-14. URL: <http://www.ncbi.nlm.nih.gov/pmc/articles/PMC1858700/> (cit. on pp. 22, 23).
- Ritt, S. (2009). *9 Channel, 5 GSPS Switched Capacitor Array DRS4*. Revision 0.9. Paul Scherrer Institut (cit. on p. 38).
- Rogers, J. G., R. Nutt, M. Andreaco, and C. W. Williams (Aug. 1994). “Testing 144- and 256-crystal BGO block detectors”. In: *IEEE Transactions on Nuclear Science* 41.4, pp. 1423–1429. doi: 10.1109/23.322926 (cit. on pp. 57, 83).
- Ronsivalle, C., M. Carpanese, C. Marino, G. Messina, L. Picardi, S. Sandri, E. Basile, B. Caccia, D. M. Castelluccio, E. Cisbani, S. Frullani, F. Ghio, V. Macellari, M. Benassi, M. D’Andrea, and L. Strigari (2011). “The TOP-IMPLART project”. In: *The European Physical Journal Plus* 126.7, p. 68. doi: 10.1140/epjp/i2011-11068-x. URL: <https://doi.org/10.1140/epjp/i2011-11068-x> (cit. on p. 17).
- Rossi, B. B. (1952). *High-energy particles*. Prentice-Hall physics. New York, NY: Prentice-Hall. URL: <https://cds.cern.ch/record/99081> (cit. on p. 10).

- Rutherford, E. (1911). "The scattering of α and β particles by matter and the structure of the atom". In: *Phil. Mag. Ser.6* 21, pp. 669–688. DOI: 10.1080/14786440508637080 (cit. on p. 10).
- Saint Gobain (2016). *BGO Bismuth Germanate Scintillation material - Datasheet*. Saint Gobain Ceramics & Plastics (cit. on p. 72).
- Saint Gobain (2017). *Plastic Scintillating Fibers - Product brochure*. Saint Gobain Ceramics & Plastics (cit. on pp. 42, 47).
- Sandjong, S., M. Fontana, and É. Testa (2017). "Compton camera prototype for ion beam therapy monitoring: characterization of the BGO scintillators and simulation of the scintillating fiber beam hodoscope". Master internship report (cit. on pp. 38, 87).
- Schaffner, B. and E. Pedroni (1998). "The precision of proton range calculations in proton radiotherapy treatment planning: experimental verification of the relation between CT-HU and proton stopping power". In: *Physics in Medicine and Biology* 43.6, p. 1579. URL: <http://stacks.iop.org/0031-9155/43/i=6/a=016> (cit. on p. 22).
- Schall, I., D. Schardt, H. Geissel, H. Irnich, E. Kankeleit, G. Kraft, A. Magel, M. F. Mohar, G. Münzenberg, F. Nickel, C. Scheidenberger, and W. Schwab (1996). "Charge-changing nuclear reactions of relativistic light-ion beams ($5 \leq Z \leq 10$) passing through thick absorbers". In: *Nuclear Instruments and Methods in Physics Research Section B: Beam Interactions with Materials and Atoms* 117.3, pp. 221–234. ISSN: 0168-583X. DOI: [https://doi.org/10.1016/0168-583X\(96\)00325-4](https://doi.org/10.1016/0168-583X(96)00325-4). URL: <http://www.sciencedirect.com/science/article/pii/0168583X96003254> (cit. on p. 11).
- Schardt, D., T. Elsässer, and D. Schulz-Ertner (Feb. 2010). "Heavy-ion tumor therapy: Physical and radiobiological benefits". In: *Rev. Mod. Phys.* 82 (1), pp. 383–425. DOI: 10.1103/RevModPhys.82.383. URL: <https://link.aps.org/doi/10.1103/RevModPhys.82.383> (cit. on pp. 5, 13, 19, 21, 23, 24).
- Schardt, D., P. Steidl, M. Krämer, U. Weber, K. Parodi, and S. Brons (2008). "Precision Bragg-curve measurements for light-ion beams in water" (cit. on pp. 11, 12).
- Schneider, U. and R. Hälg (2015). "The Impact of Neutrons in Clinical Proton Therapy". In: *Frontiers in Oncology* 5, p. 235. DOI: 10.3389/fonc.2015.00235. URL: <http://www.ncbi.nlm.nih.gov/pmc/articles/PMC4617104/> (cit. on p. 13).
- Schneider, U., E. Pedroni, and A. Lomax (1996). "The calibration of CT Hounsfield units for radiotherapy treatment planning". In: *Physics in Medicine and Biology* 41.1, p. 111. URL: <http://stacks.iop.org/0031-9155/41/i=1/a=009> (cit. on p. 22).
- Schöne, S., G. Shakirin, T. Kormoll, C. M. Herbach, G. Pausch, and W. Enghardt (Oct. 2010). "A common approach to image reconstruction for different applications of Compton cameras". In: *IEEE Nuclear Science Symposium Medical Imaging Conference*, pp. 2292–2293. DOI: 10.1109/NSSMIC.2010.5874192 (cit. on p. 28).

- Schulz-Ertner, D., O. Jakel, and W. Schlegel (2006). “Radiation therapy with charged particles.” In: *Semin Radiat Oncol* 16.4, pp. 249–259. DOI: 10.1016/j.semradonc.2006.04.008 (cit. on p. 20).
- Serber, R. (Dec. 1947). “Nuclear Reactions at High Energies”. In: *Phys. Rev.* 72 (11), pp. 1114–1115. DOI: 10.1103/PhysRev.72.1114. URL: <https://link.aps.org/doi/10.1103/PhysRev.72.1114> (cit. on p. 11).
- Sethi, R. V., D. Giantsoudi, M. Raiford, I. Malhi, A. Niemierko, O. Rapalino, P. Caruso, T. I. Yock, N. J. Tarbell, H. Paganetti, and S. M. MacDonald (2014). “Patterns of Failure After Proton Therapy in Medulloblastoma; Linear Energy Transfer Distributions and Relative Biological Effectiveness Associations for Relapses”. In: *International Journal of Radiation Oncology *Biology *Physics* 88.3, pp. 655–663. DOI: 10.1016/j.ijrobp.2013.11.239. URL: <https://doi.org/10.1016/j.ijrobp.2013.11.239> (cit. on p. 14).
- Sheehy, S. L. (2017). “Fixed-Field Alternating-Gradient Accelerators”. In: *Proceedings, CAS-CERN Accelerator School: Accelerators for Medical Applications: VÃ¶sendorf, Austria, May 26 - June 5, 2015*, pp. 321–336. arXiv: 1604.05221 [physics.acc-ph]. URL: <https://inspirehep.net/record/1448340/files/arXiv:1604.05221.pdf> (cit. on p. 16).
- Singh, M. (1983). “An electronically collimated gamma camera for single photon emission computed tomography. Part I: theoretical considerations and design criteria”. In: *Medical Physics* 10.4, pp. 421–427. ISSN: 2473-4209. DOI: 10.1118/1.595313. URL: <http://dx.doi.org/10.1118/1.595313> (cit. on p. 92).
- Sonoda, S., Y. Ichimura, H. Kimura, S. Kabuki, A. Takada, T. Mizmoto, H. Kubo, S. Miyamoto, S. Komura, T. Takemura, T. Sawano, T. Kishimoto, Y. Matsuoka, Y. Mizumura, and T. Tanimori (2015). “Application of Electron Tracking Compton Camera (ETCC) in medical imaging”. In: *2015 IEEE Nuclear Science Symposium and Medical Imaging Conference (NSS/MIC)*, pp. 1–3. DOI: 10.1109/NSSMIC.2015.7582015 (cit. on p. 112).
- Spieler, H. (1998). “Semiconductor Detectors Part 2”. Lectures on Detector Techniques, Stanford Linear Accelerator Center , September 1998 - February, 1999 (cit. on p. 55).
- Steinsträter, O., R. Grün, U. Scholz, T. Friedrich, M. Durante, and M. Scholz (2012). “Mapping of RBE-Weighted Doses Between HIMAC- and LEM-Based Treatment Planning Systems for Carbon IonTherapy”. In: *International Journal of Radiation Oncology *Biology *Physics* 84.3, pp. 854–860. DOI: 10.1016/j.ijrobp.2012.01.038. URL: <https://doi.org/10.1016/j.ijrobp.2012.01.038> (cit. on p. 23).
- Stone, R. S. (June 1948). “Neutron therapy and specific ionization.” eng. In: *Am J Roentgenol Radium Ther* 59.6, pp. 771–785 (cit. on p. 15).
- Stone, R. S., J. H. Lawrence, and P. C. Aebersold (1940). “A Preliminary Report on the Use of Fast Neutrons in the Treatment of Malignant Disease”. In: *Radiology* 35.3, pp. 322–327. DOI: 10.1148/35.3.322. eprint: <https://doi.org/10.1148/35.3.322>. URL: <https://doi.org/10.1148/35.3.322> (cit. on p. 15).

- Tajima, T., D. Habs, and X. Yan (2009). “Laser Acceleration of Ions for Radiation Therapy”. In: *Reviews of Accelerator Science and Technology* 02.01, pp. 201–228. DOI: 10.1142/S1793626809000296. URL: <https://doi.org/10.1142/S1793626809000296> (cit. on p. 17).
- Takeda, S., T. Takahashi, S. Watanabe, H. Tajima, T. Tanaka, K. Nakazawa, and Y. Fukazawa (Jan. 2008). “Double-sided silicon strip detector for x-ray imaging”. In: (cit. on p. 33).
- Terasic (2009). *SFP HSMC Terasic Board User Manual*. Revision 1. Terasic Technologies Inc. (cit. on p. 40).
- Terasic (2015). *SoCKit User Manual*. Revision F. Terasic Technologies Inc. (cit. on p. 40).
- Thörnqvist, S., L. P. Muren, L. Bentzen, L. B. Hysing, M. Håyer, C. Grau, and J. B. B. Petersen (2013). “Degradation of target coverage due to inter-fraction motion during intensity-modulated proton therapy of prostate and elective targets”. In: *Acta Oncologica* 52.3, pp. 521–527. DOI: 10.3109/0284186X.2012.752860. URL: <https://doi.org/10.3109/0284186X.2012.752860> (cit. on p. 24).
- Thun, M. J., J. O. DeLancey, M. M. Center, A. Jemal, and E. M. Ward (Jan. 2010). “The global burden of cancer: priorities for prevention”. In: *Carcinogenesis* 31.1, pp. 100–110. DOI: 10.1093/carcin/bgp263. URL: <http://www.ncbi.nlm.nih.gov/pmc/articles/PMC2802672/> (cit. on p. 4).
- Tobias, C. A., E. A. Blakely, E. L. Alpen, J. R. Castro, E. J. Ainsworth, S. B. Curtis, F. Q. H. Ngo, A. Rodriguez, R. J. Roots, T. Tenfordf, and T. C. H. Yang (1982). “Molecular and cellular radiobiology of heavy ions”. In: *International Journal of Radiation Oncology*Biology*Physics* 8.12. Particle Accelerators in Radiation Therapy, pp. 2109–2120. ISSN: 0360-3016. DOI: [https://doi.org/10.1016/0360-3016\(82\)90554-5](https://doi.org/10.1016/0360-3016(82)90554-5). URL: <http://www.sciencedirect.com/science/article/pii/0360301682905545> (cit. on pp. 5, 14).
- Tobias, C. A., J. H. Lawrence, J. L. Born, R. K. McCombs, J. E. Roberts, H. O. Anger, B. V. A. Low-Beer, and C. B. Huggins (1958). “Pituitary Irradiation with High-Energy Proton Beams. A Preliminary Report”. In: *Cancer Research* 18.2, pp. 121–134. eprint: <http://cancerres.aacrjournals.org/content/18/2/121.full.pdf>. URL: <http://cancerres.aacrjournals.org/content/18/2/121> (cit. on pp. 5, 15).
- Tobias, C. A., J. E. Roberts, J. H. Lawrence, B. V. A. Low-Beer, H. O. Anger, and J. L. Born (1955). “Irradiation Hypophysectomy and related studies using 340 MeV protons an 190 MeV deuterons”. In: *Lawrence Berkeley National Laboratory. LBNL Report UCRL-2907* (cit. on pp. 5, 15).
- Tornai, M. P., G. Germano, and E. J. Hoffman (Aug. 1994). “Positioning and energy response of PET block detectors with different light sharing schemes”. In: *IEEE Transactions on Nuclear Science* 41.4, pp. 1458–1463. ISSN: 0018-9499. DOI: 10.1109/23.322931 (cit. on pp. 57, 83).
- Uribe, J., H. Li, T. Xing, Y. Liu, H. Baghaei, Y. Wang, M. Aykac, R. Ramirez, and W.-H. Wong (June 2003). “Signal characteristics of individual crystals in high resolution BGO detector designs using PMT-quadrant sharing”. In: *IEEE Transactions on Nuclear Science* 50.3, pp. 355–361. DOI: 10.1109/TNS.2003.812478 (cit. on p. 72).

- Uzawa, A., K. Ando, S. Koike, Y. Furusawa, Y. Matsumoto, N. Takai, R. Hirayama, M. Watanabe, M. Scholz, T. Elsässer, and P. Peschke (2009). “Comparison of Biological Effectiveness of Carbon-Ion Beams in Japan and Germany”. In: *International Journal of Radiation Oncology*Biology*Physics* 73.5, pp. 1545–1551. ISSN: 0360-3016. DOI: <https://doi.org/10.1016/j.ijrobp.2008.12.021>. URL: <http://www.sciencedirect.com/science/article/pii/S0360301608039175> (cit. on p. 23).
- Vallois, Y. (2016). “Test d’un hodoscope de faisceau à fibres scintillantes”. Master internship report (cit. on pp. 78, 86).
- Vavilov, P. V. (1957). “Ionization losses of high-energy heavy particles”. In: *Sov. Phys. JETP* 5. [Zh. Eksp. Teor. Fiz. 32, 920(1957)], pp. 749–751 (cit. on p. 9).
- Veksler, V. I. (1944). “A new method of accelerating relativistic particles.” In: *Comptes Rendus (Dokal'dy) de l'Academie Sciences de l'URSS* 43.8, pp. 329–331 (cit. on p. 16).
- Webb, S. (2009). “The contribution, history, impact and future of physics in medicine”. In: *Acta Oncologica* 48, pp. 169–177. DOI: 10.1080/02841860802244158 (cit. on p. 4).
- WeissTechnik (2017). *Products brochure*. rev. Jan 2017. Weiss Technik North America, Inc. (cit. on p. 55).
- Wideröe, R. (July 1928). “Über ein neues Prinzip zur Herstellung hoher Spannungen”. In: *Archiv für Elektrotechnik* 21.4, pp. 387–406. ISSN: 1432-0487. DOI: 10.1007/BF01656341. URL: <https://doi.org/10.1007/BF01656341> (cit. on p. 15).
- Wilson, R. (2004). *A brief history of the Harvard cyclotrons*. Harvard University Press (cit. on p. 15).
- Wilson, R. R. (1946). “Radiological Use of Fast Protons”. In: *Radiology* 47.5. PMID: 20274616, pp. 487–491. DOI: 10.1148/47.5.487. eprint: <https://doi.org/10.1148/47.5.487>. URL: <https://doi.org/10.1148/47.5.487> (cit. on pp. 5, 14).
- Wroe, A. J., I. M. Cornelius, and A. B. Rosenfeld (n.d.). “The role of nonelastic reactions in absorbed dose distributions from therapeutic proton beams in different medium”. In: *Medical Physics* 32.1 (), pp. 37–41. DOI: 10.1118/1.1824194. eprint: <https://aapm.onlinelibrary.wiley.com/doi/pdf/10.1118/1.1824194>. URL: <https://aapm.onlinelibrary.wiley.com/doi/abs/10.1118/1.1824194> (cit. on p. 12).
- Yan, X., U. Titt, A. M. Koehler, and W. D. Newhauser (2002). “Measurement of neutron dose equivalent to proton therapy patients outside of the proton radiation field”. In: *Nuclear Instruments and Methods in Physics Research Section A: Accelerators, Spectrometers, Detectors and Associated Equipment* 476.1. Int. Workshop on Neutron Field Spectrometry in Science, Technology and Radiation Protection, pp. 429–434. ISSN: 0168-9002. DOI: [https://doi.org/10.1016/S0168-9002\(01\)01483-8](https://doi.org/10.1016/S0168-9002(01)01483-8). URL: <http://www.sciencedirect.com/science/article/pii/S0168900201014838> (cit. on p. 13).
- Yang, M., G. Virshup, J. Clayton, X. R. Zhu, R. Mohan, and L. Dong (2010). “Theoretical variance analysis of single- and dual-energy computed tomography methods for calculating proton

stopping power ratios of biological tissues”. In: *Physics in Medicine & Biology* 55.5, p. 1343. URL: <http://stacks.iop.org/0031-9155/55/i=5/a=006> (cit. on p. 22).

Zoglauer, A., R. Andritschke, and F. Schopper (2006). “MEGAlib The Medium Energy Gamma-ray Astronomy Library”. In: *New Astronomy Reviews* 50, pp. 629–632. doi: 10.1016/j.newar.2006.06.049 (cit. on p. 96).

Zoglauer, A., E. S. Boggs, M. Galloway, M. Amman, N. P. Luke, and R. Kippen (Oct. 2011). “Design, implementation, and optimization of MEGAlib’s image reconstruction tool Mimrec”. In: 652, pp. 568–571 (cit. on p. 28).

Zografos, A. et al. (2013). “Development of the Dielectric Wall Accelerator”. In: *Proceedings, 4th International Particle Accelerator Conference (IPAC 2013): Shanghai, China, May 12-17, 2013*, THOAB201. URL: <http://JACoW.org/IPAC2013/papers/thoab201.pdf> (cit. on p. 17).

Index

- Abbassi, L., 149
Abe, M., 151
Abellán, C., 47, 143
Adam, L. E., 36, 143
Adam, L.-E., 146
Aebersold, P. C., 160
Ainsworth, E. J., 160
Akagi, T., 151
Albertini, F, 24, 143
Alonso, Jose, 156
Alpen, E. L., 160
Altera, 34, 40, 45, 47, 143
Amaldi, U., vii, 17, 143, 147
Amemiya, N., 152
Amman, M., 162
Ancukiewicz, Marek, 157
Ando, Koichi, 161
Andreaco, M., 158
Andritschke, R., 162
Anger, H. O., 92, 144, 160, 161
Antoine, S., 17, 144
Aslaninejad, M., 157
Aspen Aerogels, 35, 144
Aswath, N., 155
Aulin, B., 144
Aykac, M., 161
Böttcher, S., 148
Baba, Masayuki, 155
Bacher, R., 157
Baghaei, H., 161
Barlow, R., 157
Barrio, J., 149
Barth, R. F., 15, 144
Basile, E., 158
Baskar, R., 5, 144
Basko, R., 28, 144
Bauer, J., 25, 144
Bauer, Julia, 150
Beard, C. D., 157
Becher, W., 150
Beddar, S., 154
Beeckman, W., 144
Belkić, D., 13, 144
Bellemann, M. E., 143, 146
Benassi, M., 158
Bentzen, Lise, 160
Bentzen, S. M., 5, 144
Berger, M. J., 151
Berra, P., 143
Bert, Christoph, 24, 145, 150
Bes, A., 149
Bethe, H., 8, 145
Bhat, M. R., xiii, 94, 145
Bichsel, H., 13, 145
Biegun, A. K., 151
Blakely, E. A., 5, 145, 160
Blakely, Eleanor A., 14, 145
Blattmann, H., 157
Blattmann, H., 157
Bliss, N., 157
Bloch, F, 8, 145
Blue, T. E., 144
Boehringer, T, 157
Boggs, E. S., 162
Bohlen, Till, 150
Bohr, N., 9, 145
Bohringer, T., 157
Bones, P. J., 147
Bonomi, R., 143
Born, J. L., 160, 161
Bortfeld, T., 157
Bosson, G., 149
Bothe, W., 10, 145
Boukhémiri, A., 149
Braccini, S., 14, 143, 145
Bragg, W. H. M. A., 6, 9, 146
Brahme, A., 5, 146
Breton, D., 58, 146
Brill, A. B., 156
Brix, G., 36, 143, 146
Bronk, Lawrence, 150
Brons, S., 159
Brun, R., viii, 50, 52, 60, 146
Brunner, S. E., 84, 146
Bui, F., 147
Buvat, I., 151
Cabal, Gonzalo, 150
Caccia, B., 158
Cachemiche, J- P., 143
Cachemiche, J.-P., 47, 146
Candela Juan, C., 149
Cantor, D., 4, 146
Caponetto, L., 153
Caporaso, G. J., 17, 146

- Carpanese, M., 158
Caruso, Paul, 159
Castelluccio, D. M., 158
Castro, J. R., 160
Catterall, M., 15, 147
Cecchin, D., 104, 147
Center, M. M., 152, 160
Cerutti, F., 156
Chang, P. Y., 145
Chen, X., 35, 45, 147, 153
Chen, Y.-J., 146
Chevallier, M., 153
Cicardi, C., 143
Ciocca, Mario, 149
Cisbani, E., 158
Clayton, J., 162
Clinthorne, N., 151
Cobb, J. H., 157
Coderre, J. A., 144
Collot, J., 144, 149
Combs, S. E., 144
Conjat, M., 144
Coray, A., 157
Coray, A., 157
Cornelius, I. M., 161
Coudurier, V., 75, 86, 147
Craft, David, 149
Crandall, K., 143
Crandall, K. R., 151
Cree, M. J., 28, 147
Crescenti, M., 143
Crespo, P., 148
Crozes, T., 149
Curtis, S. B., 160
Curtis, Stanley B., 145
Curtoni, S., 149

D'Andrea, M., 158
Dahoumane, M., 34, 35, 147
Dauvergne, D., 147–149, 153, 154, 157
Davino, D., 143
De Marchi, S., 147
De Martinis, C., 143
De Nolf, W., 149
De Rydt, M., 153
Debus, J., 152
Debus, J., 144
Debus, Jurgen, 150
Degiovanni, A., 14, 143, 147
Delagnes, E., 146

DeLancey, J. O., 160
DeLaney, T. F., 157
Dendooven, P., 151
Deng, S.-M., 45, 147, 153
DeSantis, C., 152
Despeignes, V., 4, 148
Dexheimer, D., 156
Dinh, Jeffrey, 150
Doll, J., 146
Dong, L., 162
Dong, Lei, 148
Duck, F. A., 4, 148
Durante, M., vii, 5, 7, 10, 11, 13, 14, 18, 148, 149, 156
Durante, Marco, 150, 160
Duval, P. Y., 146

Easton, M. J., 157
Edgecock, R., 157
Eley, John Gordon, 150
Elftmann, R., 36, 148
Elsässer, T., 149
Elsässer, Thilo, 161
Elsässer, T., 159
Endo, M., 155
Engelsman, Martijn, 24, 148
Enghardt, W., 25, 148, 151, 159
Evans, T. C., 4, 148
Everett, D. B., 92, 148

Fenning, R. J. L., 157
Ferrari, A., 156
Fiedler, F., 148, 151
Field, S. B., 147
Fischman, A. J., 157
Fleming, J. S., 148
Fontana, M., 91, 148, 149, 158
Foray, N., 4, 149
Forest, F., 144
Fossati, Piero, 23, 149
Fourrier, J., 144
Frandes, M., 155
Freud, N., 154, 157
Frey, Kathrin, 150
Friedrich, T., 5, 149
Friedrich, Thomas, 160
Froidefond, E., 144
Frullani, S., 158
Fujimoto, T., 152
Fujita, T., 152

- Fukazawa, Y., 160
 Fukumura, A., 154
 Furukawa, T., 152
 Furusawa, Yoshiya, 161
 Futami, Y., 155
 Gaglione, R., 75, 86, 149
 Gallin-Martel, L., 149
 Gallin-Martel, M.-L., 85, 149
 Galloway, M., 162
 Gardner, I. S. K., 157
 Garlasché, M., 143
 Garonna, A., 143
 GE Healthcare, 92, 98, 149
 GeckoDrive, 75, 149
 Geissel, H., 158
 Germano, G., 161
 Gerweck, Leo E., 157
 Ghio, F., 158
 Giantsoudi, Drosoula, 14, 149, 159
 Gillam, J. E., 28, 149, 156
 Giovannini, Giulia, 14, 150
 Giove, D., 143
 Goitein, Michael, 157
 Golnik, C., 57, 83, 150, 151
 Gorecki, A., 149
 Gottschalk, B., 10, 13, 150
 Gottshalk, B., 18, 150
 Grözinger, Sven O., 145
 Graeff, Christian, 24, 150
 Grassberger, C., 12, 150
 Grassberger, Clemens, 149
 Grau, Cai, 160
 Grosshans, David R., 150
 Grossmann, M., 157
 Gruber, L., 146
 Grün, Rebecca, 160
 Guan, Fada, 14, 150
 Gullberg, G. T., 144
 Gunzert-Marx, K., 12, 150
 Hüfner, J., 11, 152
 HÃyer, Morten, 160
 Haberer, T., 153
 Haberer, T., 20, 144, 150
 Haberer, Thomas, 158
 Haberkorn, U., 146
 Habs, D., 160
 Hachon, F., 146
 Haettner, E., 12, 150, 151
 Halperin, E. C., 5, 151
 Hamamatsu, 42, 73, 75, 80, 151
 Hamm, R. W., 17, 151
 Han, L., 92, 93, 95, 110, 151
 Hartmann, G H, 152
 Hasegawa, Azusa, 149
 Hattori, K., 153
 Heidel, K., 151
 Herbach, C. M., 159
 Herfarth, K., 144
 Herfarth, Klaus, 145
 Herk, Marcel van, 155
 Higashi, A., 155
 Hilaire, E., 54, 151
 Hill, M. A., 157
 Hinz, R., 148
 Hirasawa, M., 28, 151
 Hirayama, Ryoichi, 161
 Hirtl, A., 146
 Hishikawa, Y., 25, 151
 Hoffman, E. J., 161
 Holder, David, 156
 Hostachy, J. Y., 149
 Hostachy, J.-Y., 149
 Hubbell, J. H., 99, 111, 151
 Hueso-González, F., 37, 57, 83, 151
 Hug, E B, 143
 Huggins, C. B., 160
 Huh, S. S., 151
 Hysing, Liv B., 160
 Hälg, R., 159
 Ichimura, Y., 159
 ICRU, 13, 22, 152
 Imai, Reiko, 149
 Inada, T., 153
 Inaniwa, T., 22, 152
 Inaniwa, Taku, 23, 152
 Irnich, H., 158
 Iwase, H., 150, 151
 Iwata, Y., 21, 152
 Jäkel, O, 23, 152
 Jacob, C, 152
 Jakel, O, 22, 23, 152, 153
 Jakel, O., 159
 Jemal, A., 4, 152, 160
 Johnstone, C., 157
 Jones, B., 157
 Jones, Bleddy, 14, 153

- Jones, T. J., 157
Kabuki, S., 112, 153, 159
Kagawa, K., 151
Kamada, Tadashi, 149, 152, 155
Kanai, T., 155
Kanai, T., 20, 153, 154
Kanai, Tatsuaki, 152, 153, 155
Kanematsu, N., 152
Kanematsu, Nobuyuki, 22, 152, 153, 155
Kankeleit, E., 158
Karger, C P., 152
Kastan, M. B., 155
Kato, Hirotoshi, 155
Kawachi, K., 153
Keevil, S. F., 4, 153
Kelliher, D. J., 157
Kereiakes, J. G., 4, 153
Kerr, Matthew D., 150
Khan, A., 157
Kimura, H., 159
Kippen, R., 162
Kirsch, D. G., 155
Kishimoto, T., 159
Kleeman, R., 146
Knoll, G. F., 32, 153
Knopf, A., 157
Koehler, A. M., 150, 162
Kohara, R., 153
Kohno, Ryosuke, 153
Kohno, T., 154
Koike, Sachiko, 161
Komori, M., 154
Komura, S., 159
Kormoll, T., 151, 159
Krämer, M., 152
Krämer, M., 150, 159
Kraft, G., 153
Kraft, G., 150, 158
Kramer, M., 23, 153
Krimmer, J., 43, 147, 149, 153, 157
Kubiak, Tomasz, 24, 153
Kubo, A., 153
Kubo, H., 153, 159
Kuchment, P., 112, 154
Kulkarni, S. R., 148
Kunieda, E., 153
Kurz, C., 144
Létang, J. M., 148, 154, 157
Lacasta, C., 149, 156
Lacoste, A., 149
Lancelot, J. L., 144
Landau, L., 9, 154
Larsson, B., 15, 154
Lawrence, E. O., 15, 154
Lawrence, J. H., 160, 161
Le Gac, R., 146
Lee, K. A., 144
Lennox, A. J., 17, 154
Levy, R. P., 22, 154
Ley, J.-L., 33, 35, 55, 83, 95, 147, 148, 153, 154
Li, H., 161
Liebsch, N. J., 157
Lin, S., 157
Lin, Steven H., 150
Liu, Y., 161
Livingston, M. S., 154
Llosá, G., 149, 156
Locher, G. L., 15, 154
Loeffler, J. S., 148, 157
Loeffler, Jay S., 157
Lojacono, X., 28, 54, 96, 151, 154
Lomax, A J., 143
Lomax, A., 157, 159
Lomax, A. J., 13, 154
Lorenz, W., 146
Low-Beer, B. V. A., 160, 161
Lu, G.-N., 147
Luke, N. P., 162
Lüchtenborg, Robert, 150
Méot, F., 144
Maalmi, J., 146
MacDonald, Shannon M., 159
Macellari, V., 158
Machida, S., 157
MacKay, Ranald, 156
Mackin, D., 28, 154
Magel, A., 158
Magrin, G., 143
Mairani, Andrea, 149, 150
Malhi, Imran, 159
Mandrillon, J., 144
Mandrillon, P., 144
Marcatili, S., 149
Marino, C., 158
Martin, C., 148
Marton, J., 146

- Masullo, M. R., 143
 Mathez, H., 147, 153
 Matsufuji, N., 22, 155
 Matsufuji, N., 12, 154
 Matsufuji, Naruhiro, 23, 152, 153, 155
 Matsufuji, Naruhiru, 149
 Matsumoto, Yoshitaka, 161
 Matsuoka, Y., 159
 Matsuzawa, H., 153
 Maxim, V., 28, 54, 148, 151, 154, 155
 McCombs, R. K., 160
 McIntosh, P. A., 157
 McKenzie, Alan L., 24, 155
 McMillan, E. M., 16, 155
 McNamara, Aimee L., 14, 155
 Mellace, C., 143
 Messina, G., 158
 Michaud, S., 157
 Mijnheer, Ben, 155
 Minohara, S., 155
 Minohara, Shinichi, 153
 Mirandola, Alfredo, 149
 Mirkovic, Dragan, 150
 Miuchi, K., 153
 Miyamoto, S., 159
 Miyamoto, Tadaaki, 155
 Mizmoto, T., 159
 Mizoe, Jun-Etsu, 155
 Mizoe, Junetsu, 149
 Mizumura, Y., 159
 Mizushima, K., 152
 Moding, E. J., 5, 155
 Mohan, R., 162
 Mohan, Radhe, 150
 Mohar, M. F., 158
 Molinelli, Silvia, 149
 Molière, G., 10, 155
 Morel, C., 143
 Mori, S., 152
 Mori, Y., 144
 Morse, J., 149
 Motte, J.-F., 149
 Munkel, G., 157
 Munzenrider, J. E., 157
 Murakami, M., 151
 Murakami, T., 152
 Muraz, J. F., 149
 Muraz, J.-F., 149
 Muren, Ludvig P., 160
 Münzenberg, G., 158
 Nagayoshi, T., 153
 Nakahara, T., 153
 Nakazawa, K., 160
 National Instruments, 75, 155
 Nedunchezian, K., 15, 155
 Neuvéglise, D., 144
 Newhauser, W. D., vii, 8, 11–13, 156, 162
 Newport, 46, 156
 Ngo, F. Q. H., 160
 Ngo, Frank Q.H., 145
 Nickel, F., 158
 Niemierko, Andrzej, 149, 157, 159
 Nightingale, J. M., 148
 Nill, S., 156
 Nishimura, H., 153
 Noda, K., 152
 Noda, Koji, 152
 NuPECC, 13, 156
 Nurdan, K., 156
 Nurdan, T. C., 93, 156
 Nutt, R., 158
 Obana, T., 152
 Oberdorfer, F., 146
 Ogitsu, T., 152
 Ohmori, C., 144
 Okada, Y., 153
 Oliphant, M. O., 16, 156
 Oliver, J. F., 156
 Oreccchia, Roberto, 149
 Oriksa, T., 152
 Orito, R., 153
 Ortega, P. G., 37, 156
 Ostertag, H., 143, 146
 Owen, H. L., 157
 Owen, Hywel, 21, 156
 Paganetti, H., 24, 156
 Paganetti, H., vii, 7, 13, 15, 148, 150, 156, 157
 Paganetti, Harald, 22, 149, 155, 157, 159
 Parodi, K., 25, 144, 148, 157, 159
 Parodi, Katia, 150
 Parra, L. C., 28, 157
 Pasternak, J., 144, 157
 Pattalwar, S. M., 157
 Pausch, G., 151, 159
 Pawelke, J., 148

- Peach, K. J., 17, 157
Pearce, P., 143
Pedroni, E., 157
Pedroni, E., 10, 20, 21, 150, 157–159
Peeler, Christopher R., 150
Peschke, Peter, 161
Petersen, JÅrgen B. B., 160
Peterson, S., 154
Petzoldt, J., 151
Peyrin, F., 151
Phillips, M H, 24, 157
Picardi, L., 158
Pinto, M., 36, 157
Pittà, G, 143
Planche, T., 144
Poggiali, D., 147
Polf, J., 154
Potter, J. M., 151
Pozimski, J. K., 157
Prost, R., 154, 155
Puggioni, P., 143
Pönisch, F., 148

Römer, K. E., 151
Réthoré, F., 143
Rademakers, F., 146
Rafecas, M., 149, 156
Raiford, Michael, 159
Ramirez, R., 161
Rapalino, Otto, 159
Rarbi, F. E., 149
Ray, C., 147, 153, 154, 157
Reithinger, V., 153
Riccardin, L., 147
Richard, M.-H., 32, 154, 158
Rietzel, Eike, 22, 23, 145, 158
Ritt, S., 38, 158
Robert, C., 151
Roberts, J. E., 160, 161
Rodriguez, A., 160
Roellinghoff, F., 157
Rogers, C., 147
Rogers, J. G., 57, 83, 158
Rogers, W. L., 151
Ronsivalle, C., 17, 158
Roots, R. J., 160
Rosenfeld, A. B., 161
Rossetto, O., 149
Rossi, B. B., 10, 158
Rosso, E., 143

Rusquart, P., 146
Rutherford, E., 10, 158
Réthoré, F., 146

Saint Gobain, 42, 47, 72, 158
Sakai, H., 151
Sala, P R., 156
Salomé, M., 149
Sampayan, S. E., 146
Sandjong, S., 38, 87, 158
Sandri, S., 158
Sarrut, D., 151
Sawano, T., 159
Schäfer, K., 152
Schöne, S., 28, 159
Schürmann, B., 152
Schaart, D. R., 146
Schaffner, B., 22, 158
Schall, I., 11, 158
Schardt, D, 152, 153
Schardt, D., vii, 5, 11–13, 19, 21, 23, 24, 150, 151, 158, 159
Schardt, Dieter, 158
Scheib, S, 157
Scheib, S., 157
Scheidenberger, C., 158
Schlegel, W., 159
Schneider, R. J., 150
Schneider, U., 13, 22, 157, 159
Scholz, M., 149
Scholz, Michael, 160, 161
Scholz, U., 149
Scholz, Uwe, 160
Schopper, F., 162
Schuemann, Jan, 155
Schulz-Ertner, D., vii, 20, 159
Schwab, W., 158
Schwarz, Marco, 148
Schwengner, R., 151
Sekiya, H., 153
Serber, R., 11, 159
Sethi, Roshan V., 14, 159
Seviour, R., 157
Shakirin, G., 159
Sheehy, S. L., 16, 157, 159
Shih, H. A., 157
Shirahata, T., 153
Shirai, T., 152
Shirai, Toshiyuki, 152
Shouda, K., 152

- Simon, R. S., 150
Singh, M., 92, 159
Sisterson, J. M., 150
Smith, S. L., 157
Sobieski, Mary, 150
Solevi, P., 149, 156
Sommerer, F., 144
Sonoda, S., 112, 159
Spieler, H., 55, 160
Steidl, P., 159
Steinsträter, Olaf, 23, 160
Stephan, Clifford, 150
Stone, R. S., 15, 160
Strachan, J., 157
Strigari, L., 158
Suit, Herman D., 157
Suzuki, K., 146
Szeless, B., 143

Tajima, H., 160
Tajima, T., 17, 160
Takada, A., 153, 159
Takahashi, T., 160
Takai, Nobuhiko, 161
Takami, S., 152
Takayama, S., 152
Takeda, S., 33, 160
Takemura, T., 159
Taleei, Reza, 150
Tammen, J., 148
Tanaka, T., 160
Tanimori, T., 153, 159
Tarbell, Nancy J., 159
Tashima, H., 152
Tenfordf, T., 160
Terasic, 40, 160
Terzioglu, F., 154
Tessonniere, Thomas, 150
Testa, É., 147–149, 153, 154, 157, 158
Thörnqvist, Sara, 24, 160
Thirugnanamurthy, S., 155
Thiruppathy, M., 155
Thomlinson, R. H., 147
Thun, M. J., 4, 160
Titt, U., 156, 162
Titt, Uwe, 150
Tobias, C. A., 5, 14, 15, 160, 161
Tobias, Cornelius A., 145
Todd, R. W., 148
Toet, D., 143

Tomitani, T., 151
Tomura, H., 155
Tornai, M. P., 57, 83, 161
Torres-Espallardo, I., 149, 156
Trofimov, Alexei, 149
Trojan, H., 143, 146
Tsuji, Hiroshi, 152
Tsujii, Hirohiko, 149, 152, 155
Turco, P., 147
Tygier, S. C., 157
Tzenov, S. I., 157

Ueno, K., 153
Unholtz, D., 144
Uribe, J., 72, 161
Uzawa, Akiko, 23, 161

Vaccaro, V., 143
Vallois, Y., 78, 86, 161
Van Luijk, P., 156
Vavilov, P. V., 9, 161
Veksler, V. I., 16, 161
Verdú Andrés, S., 143
Vicente, M. G. H., 144
Virshup, G., 162
Vojnovic, B., 157
Vretenar, M., 143
Vuiart, R., 149

Wagner, A., 151
Wagner, M. S., 150
Walenta, A. H., 147, 156
Wang, Y., 161
Ward, E. M., 152, 160
Watanabe, Masahiko, 161
Watanabe, S., 160
Webb, S., 4, 161
Weber, U., 153
Weber, U., 159
Wegner, R., 143
Weiss, M., 143
WeissTechnik, 55, 161
Welzel, T., 144
Wideröe, R., 15, 161
Williams, C. W., 158
Wilson, R., 15, 161
Wilson, R. R., 5, 14, 161
Wimmer-Schweingruber, R., 148
Witte, H., 157
Wong, W.-H., 161

- Wroe, A. J., 12, 161
Xing, T., 161
Yamada, Shigeru, 155
Yamashita, H, 155
Yamouni, M., 149
Yan, X., 13, 156, 160, 162
Yang, M, 22, 162
Yang, T. C. H., 160
Yeo, R., 144
Yeoh, K.-W., 144
Yock, Torunn I., 159
Yokoi, T., 157
Zaers, J., 143, 146
Zeng, G. L., 144
Zennaro, R., 143
Zhang, R., 156
Zhu, X R, 162
Zhu, X. Ronald, 150
Zoccarato, Y., 147, 153
Zoglauer, A., 28, 96, 162
Zografos, A., 17, 162

Acknowledgements